Nucleon-knockout Reactions from Neutron-deficient Carbon Isotopes
and
Characterization of a Particle Detector Combination for the Super-FRS at FAIR

Vom Fachbereich Physik der Technischen Universität Darmstadt zur
Erlangung eines Doktors der Naturwissenschaften (Dr. rer. nat.)
genehmigte Dissertation von Steffen Erich Schlemme aus Büdingen
Tag der Einreichung: 17.12.2018, Tag der Prüfung: 28.01.2019
Darmstadt — D 17

1. Gutachten: Prof. Dr. Joachim Enders
2. Gutachten: Prof. Dr. Thorsten Kröll

TECHNISCHE
UNIVERSITÄT
DARMSTADT

Fachbereich Physik
Institut für Kernphysik - AG Enders

Nucleon-knockout Reactions from Neutron-deficient Carbon Isotopes
and
Characterization of a Particle Detector Combination for the Super-FRS at FAIR

Genehmigte Dissertation von Steffen Erich Schlemme aus Büdingen

1. Gutachten: Prof. Dr. Joachim Enders
2. Gutachten: Prof. Dr. Thorsten Kröll

Tag der Einreichung: 17.12.2018
Tag der Prüfung: 28.01.2019

Darmstadt — D 17

Bitte zitieren Sie dieses Dokument als:
URN: urn:nbn:de:tuda-tuprints-88439
URL: http://tuprints.ulb.tu-darmstadt.de/8843

Erklärung zur Dissertation

Hiermit versichere ich, die vorliegende Dissertation ohne Hilfe Dritter nur mit den angegebenen Quellen und Hilfsmitteln angefertigt zu haben. Alle Stellen, die aus Quellen entnommen wurden, sind als solche kenntlich gemacht. Diese Arbeit hat in gleicher oder ähnlicher Form noch keiner Prüfungsbehörde vorgelegen.

Darmstadt, den 05.05.2019

(S. Schlemme)

Abstract

Nuclear structure far from stability show unpredicted and very interesting effects, like deformation and halos. A thorough and unified understanding of these observations is needed to comprehend the nuclear many-body problem and the force between the nuclear constituents.

Since the middle of the 20th century the nuclear shell model is used to describe nuclear structure. Single-nucleon removal cross sections depend on the state in which the removed nucleon resided. Thus, the quality of a model prediction can be probed by comparing theoretical cross sections with experimental results. Previous measurements indicate that the reduction factor between theoretical and experimental cross sections decreases for an increasing asymmetry between proton and neutron number. Cross sections of one-neutron removal from $^{10-12}$C and one-proton removal from ^{9}C were determined in inverse kinematics. At the fragment separator FRS at GSI Helmholtzzentrum für Schwerionenforschung at about 1670 MeV/nucl. reaction residues were separated and identified The removal reactions yielded the cross sections σ_{exp} of $\sigma_{\text{-n}}(^{12}\text{C}) = (49.44 \pm 0.88)\,\text{mb}$, $\sigma_{\text{-n}}(^{11}\text{C}) = (24.44 \pm 0.21)\,\text{mb}$, $\sigma_{\text{-n}}(^{10}\text{C}) = (20.21 \pm 0.28)\,\text{mb}$, $\sigma_{\text{-p}}(^{9}\text{C}) = (51.10 \pm 1.35)\,\text{mb}$ and reduction factors $R_s = \frac{\sigma_{\text{exp}}}{\sigma_{\text{th}}}$, when compared to theoretical values obtained using the eikonal approximation, of $R_s(^{12}C) = (0.51 \pm 0.01)$, $R_s(^{11}C) = (0.47 \pm 0.01)$, $R_s(^{10}C) = (0.46 \pm 0.03)$, $R_s(^{9}C) = (1.00 \pm 0.03)$. With the exception of the one-proton removal R_s is almost independent from the neutron-to-proton ratio. Beyond the reduction factor, shell model eikonal approximation describe the data well. While a decreasing trend for increasing neutron deficiency was found, the evolution is still flat. Comparisons of the theoretical momentum transfer from the removed nucleon to the reaction residue showed a consistency when compared to the experimentally measured momentum distribution of the residues, proving the eikonal approximation to be correct for modeling the knock out process.

At GSI a new accelerator facility, the facility for antiproton and ion research (FAIR), is under construction aiming at the delivery of higher beam energies and intensities. That will allow to investigate more exotic ions, hitherto not accessible in experiments or only at low statistics. Higher intensities lead to higher demands on the future detectors, placed along the beam line near the production target in front of the Super-FRS. Particle detector combinations (PDC) consisting of different detectors for different ion-intensity levels are used to monitor the ion flux.

In the framework of this dissertation, prototypes of an ionization chamber (IC) and a secondary-electron monitor (SEM) constructed for FAIR, as well as different designs of single- and polycrystalline diamond detectors were studied. Functionality and performance of all detectors were investigated with a quasi-continuous ^{12}C beam at 62 MeV/nucl. at intensities in the order of $10^5 - 10^7$ particles per second. A spilled ^{124}Xe beam at 200 MeV/nucl. with intensities in the order of $10^3 - 10^6$ ions per spill was used to investigate the lowest reachable uncertainty when calibrating the IC-prototype. All investigated detectors showed full functionality and a linear response with respect to different beam intensities. A calibration of the IC-prototype within an uncertainty of below 1 % was possible. The SEM shows a linear response when compared to intensities of the carbon beam down to 150 kHz. A direct calibration of the

SEM, using a single-crystal diamond detector as reference, yielded an uncertainty of about 5.1 %. The single-crystal diamond detector features a count efficiency of 100 % versus a plastic scintillator. No signs of radiation damage were visible before absorbing a dose of about 25 kGy. The polycrystalline diamond detectors exhibits a counting efficiency of (95 ± 2) % at intensities up to 700 kHz and a rate-dependent decrease of counting efficiency at higher intensities. On the other hand no significant signs of radiation damage were found after depositing a dose of above 4 MGy.

Thus, all of the investigated detectors are suitable to be used as part of a FAIR-PDC. Using a polycrystalline diamond detector as reference detector for the calibration process will reduce the frequency of physical access of the beam line for maintenance. Periodic efficiency checks of the polycrystalline diamond detector, using a single-crystal diamond detector, will guarantee a low uncertainty of the obtained count rates. A calibration of the IC to high accuracy has been demonstrated. The accuracy of the rate determined from the SEM was limited due to the low charge of the beam used in the tests and is expected to improve with the high-Z beams at FAIR.

Zusammenfassung

Die Kernstruktur fern der stabilen Isotope zeigt nicht vorhersagbare und sehr interessante Effekte, wie Deformation und Halo-Kerne. Ein vollständiges und einheitliches Verständnis dieser Beobachtungen ist benötigt um Viel-Körper-Effekte und die Kräfte zwischen nuklearen Komponenten besser zu verstehen.

Seit Mitte des 20. Jahrhunderts wird das nukleare Schalenmodell benutzt um Kernstruktur zu beschreiben. Die Wirkungsquerschnitte von Ein-Nukleon Knockout Reaktionen hängen vom Zustand ab in dem sich das Nukleon vor der Reaktion befand. Daher kann die Aussagekraft von theoretischen Modellen überprüft werden, indem theoretische und experimentell gemessene Ergebnisse verglichen werden. Frühere Messungen deuten darauf hin, dass der Reduktionsfaktor zwischen theoretischen und experimentellen Wirkungsquerschnitten mit zunehmender Asymmetrie zwischen Protonen- und Neutronenzahl abnimmt. Wirkungsquerschnitte von Ein-Nukleon Knockout von $^{10-12}$C und Ein-Proton Knockout von ^{9}C wurden in inverser Kinematik bestimmt. Im Fragment Separator FRS im GSI Helmholtzzentrum für Schwerionenforschung Reaktionsprodukte wurden separiert und identifiziert bei Energien von etwa 1670 MeV/nukl. Die untersuchten Reaktionen lieferten die Wirkungsquerschnitte σ_{exp}: $\sigma_{\text{-n}}(^{12}\text{C}) = (49.44 \pm 0.88)$ mb, $\sigma_{\text{-n}}(^{11}\text{C}) = (24.44 \pm 0.21)$ mb, $\sigma_{\text{-n}}(^{10}\text{C}) = (20.21 \pm 0.28)$ mb, $\sigma_{\text{-p}}(^{9}\text{C}) = (51.10 \pm 1.35)$ mb. Im Vergleich mit theoretischen Werten die auf der Eikonal Näherung basieren, wurden folgende Reduktionsfaktoren $R_s = \frac{\sigma_{\text{exp}}}{\sigma_{\text{th}}}$ bestimmt: $R_s(^{12}C) = (0.51 \pm 0.01)$, $R_s(^{11}C) = (0.47 \pm 0.01)$, $R_s(^{10}C) = (0.46 \pm 0.03)$, $R_s(^{9}C) = (1.00 \pm 0.03)$.

Mit Ausnahme des Ein-Proton Knockouts ist R_{s} nahezu unabhängig vom Proton-Neutron-Verhältnis. Abgesehen vom Reduktionsfaktor beschreiben die Schalenmodell Berechnungen in der Eikonal Näherung die Daten gut. Zwar wurde ein leicht abnehmender Trend des Reduktionsfaktors für zunehmenden Neutronenmangel gefunden, aber die Entwicklung der Faktoren ist weiterhin flach. Vergleiche des Impulsübertrags vom entfernten Nukleon zum Reaktionsprodukt zeigten eine Übereinstimmung mit der experimentell gemessenen Impulsverteilung und bestätigen damit, dass die Knockout-Reaktion mit den Annahmen der Eikonal Näherung korrekt modelliert wird.

Bei der GSI ist eine neue Beschleunigeranlage, die Facility for Antiproton and Ion Research (FAIR), im Bau. Diese Anlage zielt auf höhere Strahlenergien und Intensitäten ab. Dadurch soll die Erforschung von exotischen Ionen ermöglicht werden, die zum jetzigen Stand in Experimenten nicht oder nur bei sehr niedriger Statistik erzeugt und identifiziert werden können. Höhere Strahlintensitäten verlangen von den Detektoren entlang der Strahlführung beim Produktionstarget am Eingang des Super-FRS höheren Anforderungen stand zu halten. Teilchen Detektor Kombinationen (PDC), bestehend aus verschiedenen Detektoren, die jeweils bei verschiedenen Intensitäten arbeiten, werden benutzt um den Ionenfluss zu messen.

Innerhalb des Umfangs dieser Dissertation wurden Prototypen einer Ionisationskammer (IC) und eines Sekundärelektronen Monitors (SEM), die für FAIR entwickelt wurden, als auch mono- und polykristalline Diamant Detektoren getestet. Die Funktionalität und Leistungsfähigkeit aller Detektoren wurde untersucht im Fall der Bestrahlung mit einem quasi-kontinuierlichen ^{12}C Strahl mit 62 MeV/nukl. und

Intensitäten in der Größenordnung von $10^5 - 10^7$ Teilchen pro Sekunde. Ein gespillter ^{124}Xe Strahl mit 200 MeV/nukl. und Intensitäten von $10^3 - 10^6$ Teilchen pro Spill wurde genutzt um die niedrigst mögliche Unsicherheit der Kalibrierung des IC-Prototypen zu bestimmen. Alle untersuchten Detektoren bewiesen ihre volle Funktionalität und eine lineare Antwort in Abhängigkeit zu verschiedenen Strahlintensitäten. Eine Unsicherheit der IC-Kalibrierung von unter 1 % wurde erreicht. Der SEM zeigte eine lineare Antwort für Intensitäten des Kohlenstoffstrahls größer als 150 kHz. Eine direkte Kalibrierung des SEM mit einem monokristallinen Diamant Detektor als Referenz lieferte eine Unsicherheit von etwa 5.1 %. Der monokristalline Diamant Detektor bewies eine Zähleffizienz von 100 % im Vergleich mit einem Plastik Szintillator. Erste Zeichen von Strahlungsschäden wurden nach Absorbieren einer Dosis von etwa 25 kGy sichtbar. Der polykristalline Diamant Detektor zeigte eine Zähleffizienz von (95 ± 2) % bei Intensitäten bis zu 700 kHz und eine intensitätsabhängige Abnahme der Effizienz für höhere Intensitäten. Andererseits zeigte dieser Detektor keine Strahlungsschäden nach Absorption einer Dosis von über 4 MGy.

Zusammenfassend haben alle untersuchten Detektoren ihre Eignung als Bestandteil einer FAIR-PDC bewiesen. Die Nutzung des polykristallinen Diamond Detektors als Referenz Detektor für die Kalibrierung von IC und SEM wird die Häufigkeit des Zutritts der Stahlführung für Instandhaltungsarbeiten reduzieren. Regelmäßige Überprüfungen der Effizienz des polykristallinen Diamant Detektors mit einem monokristallinen Diamant Detektor wird eine niedrige Unsicherheit der gemessenen Zählraten gewährleisten. Weiterhin wurde gezeigt, dass die Kalibrierung des IC-Prototypen mit einer hohen Genauigkeit möglich ist. Die Genauigkeit der Zählraten, die mit dem SEM gemessen wurden, war durch die niedrige Ordnungszahl des im Testexperiment genutzten Kohlenstoffstrahls limitiert. Eine höhere Genauigkeit ist erwartet, wenn der SEM mit Ionen höherer Ordnungszahlen bestrahlt wird.

Summary of Abbreviations

While all shortcuts are explained in each chapter at least once, all of them and their meaning can still be found on this page if necessary:

ADC	Analog/amplitude-to-digital converter
AoZ, AoQ	Mass over charge ratio, Z=Q, if ions are fully stripped
CCE	Charge collection efficiency
CD	Current digitizer
CFD	Constant fraction discriminator
CVD	Chemical vapor deposition, a procedure to produce artificial diamonds
DAQ	Data acquisition system
DBA	Diamond broadband amplifier
FAIR	Facility for Antiproton and Ion Research
FRS	In-flight fragment separator at GSI
Go4	GSI Object Oriented On-line Off-line system
GSI	Gesellschaft für Schwerionenforschung
IC	Ionization chamber
IFC	Current to frequency converter, same as CD
LMD	List-mode data
MBS	Multi Branch System, GSI Data Acquisition System, output = LMD-files
MW, MWPC	Multi wire proportional chamber; gas-filled position sensitive detector
PADI	PreAmplifier-DIscriminator
PC-DD, pcCVD-DD	Poly crystalline diamond detector, produced by means of CVD
PDC	Particle detector combination
PMT	Photo-multiplier tube
QDC	Charge-to-digital converter
SC-DD, scCVD	single-crystal diamond detector, produced by means of CVD
SCI, scint.	Scintillator, in this work always a plastic scintillator
SEM, SEETRAM	Secondary electron transmission monitor
Super-FRS, SFRS	Superconducting In-flight fragment separator foreseen for FAIR
TAC	Time-to-amplitude converter
TDC	Time-to-digital converter
ToF	Time of flight
TPC	Time projection chamber

Contents

1 General Introduction

It was the 5th century B.C. when the ancient Greek philosopher Leucippus and his pupil Democritus postulated their theory that all matter consisted of smallest, indivisible, particles - the atoms. Not being believed by their colleagues in their own time, it took until the beginning of the 19th century before philosophers and natural scientists started to take the idea of atoms seriously. In the following years the existence of the atom was proven and in 1911 Ernest Rutherford demonstrated the existence of a nucleus within the atom [1]. In 1919 Rutherford reported about another experiment of his, in which he demonstrated the nucleus to consist of a multiple number of Hydrogen cores - the proton. One year later he proposed the existence of a neutral core component. Shortly after Chadwicks discovery of the neutron in 1932 [2], Werner Heisenberg developed a model, describing the interaction of protons and neutrons by means of quantum physics. In his theory he gave the first description of binding nucleons in the nuclear core through nuclear exchange forces. Still in the same year Dmitri Ivanenko introduced the basis of the nuclear shell model, describing the structure of the nucleons by occupying certain energy levels. This model got strongly advanced in 1949 by several independently working physicists citebib:goeppert, bib:hans. Major contributions were given by the work of Maria Goeppert-Mayer and J. Hans D. Jensen, earning them a share of the Nobel prize in physics in 1963. In the following years the nuclear shell model and its input parameters were in continuous development and still are in on-going refinement up to today.

The nuclear shell model is a common model in nuclear physics, to describe nuclear states of nucleons in a nucleus. The nuclear states or orbits in the shell model are uniquely described by a set of quantum numbers, including spin, angular momentum and total angular momentum. Depending on which orbit the nucleon occupies the binding energy and its wave function differs. The predictions of the shell model can be probed by performing dedicated experiments, used to determine observables calculated using the shell model. Some approaches to compare the predictions with reality are to study the momentum transfer in nucleon-nucleon scattering, performing quasi elastic scattering experiments or investigate the energy levels of shells using nuclear spectroscopy. Especially valuable results can be obtained when investigating nuclei with extreme properties not used before to determine the parameters of the interaction potential in the model calculation. If discrepancies can be observed in this case, it is clear that this model can not fully describe these properties, yet. Such discrepancies are usually rarely seen when studying nuclei in the near of the valley of stability. Thus, exotic nuclei with very large or very small proton-to-neutron ratios need to be produced first. After their production reactions performed with these nuclei can provide crucial information regarding the quality of the model calculation and if input parameters need to be adjusted. One possible way to probe shell model predictions are nucleon-knockout reactions. This reaction type has been proposed to provide information, that allow to determine absolute spectroscopic factors and thereby occupation probabilities of nucleons in a specific shell [3, 4]. This reaction is usually modeled at very high energies to reduce interaction times between the interacting particles. When modeled at energies in the order of GeV/nucl. the reaction is assumed to happen in very short time scales and the sudden and eikonal approximations can be used to simplify the reaction process. Nevertheless, it was shown, that calculations using the eikonal approximation yielded good results down to energies of 20 MeV/nucl. [5,6]. To obtain a qualitative statement about the spectroscopic factor of the reaction, the final states of all reaction residues have to be identified. Another way is to study isotopes, that possess sufficiently few final states, that a direct comparison of experimental results and theoretical predictions is possible. Reasonable candidates for performing such a comparison are very light nuclei with a simple structure, undergoing reactions at very high energies.

In the first part of this dissertation, results from the FRS experiment S341 are presented, aiming at the precise determination of nucleon-knockout reactions from light carbon isotopes. One-neutron knock-out reactions from $^{10-12}$C and one-proton knock-out reactions from ^{9}C are discussed. Specifically, the experimental procedure, results and their comparison with theoretical predictions are presented

Dedicated facilities are needed to produce and accelerate exotic isotopes. Two archetypes of devices, used to produces radioactive ion beams (RIB), are the isotope separation on line (ISOL) technique and the in-flight separation technique. The prior method produces radioactive isotopes by hitting a production target with a light primary beam and induce fission reaction residues. Thus, the choice of the production target determined the range of produced ion. This target is very hot and gaseous reaction residues get transported to the next stage at which they get ionized using ion sources, a hot plasma or high energy photons. In the last steps the ions get separated by their mass using magnets and experience a re-acceleration, before their transfer to dedicated reaction targets or other experimental setups. The second method, the in-flight separation, produces the ions for the investigation of further reactions by hitting a thin production target with a primary beam. In most cases the ions, desired for further reaction studies, get produced by fragmentation in the production target. A combination of magnets and degraders is placed after the production target, used to separate the desired ions from any contamination of other fragments while traversing the separator (in-flight separation). The identification the produced ions is done by measuring the time of flight, energy loss and magnetic rigidity of each ion along its path through the separator. The ISOL method provides RIBs of high quality but low energy. The in-flight method provides beam of lower quality compared to the ISOL method but ions of much higher energy and shorter lifetimes can be produced and used for dedicated reaction studies. At GSI Helmholtzzentrum für Schwerionenforschung GmbH in Darmstadt, Germany [7], the investigation of very exotic beams is of profound interest. Particle separation is carried out using in-flight separation of ions. A scheme of GSI is shown in Figure 1.1. The heavy ion synchroton at GSI is able to deliver ion beams up to a magnetic bending power of 18 Tm [8]. In the case of N=Z this leads to maximal energies of about 1.9 GeV/nucl.. The in-flight fragment separator - FRS - allows to conduct experiments using beams with ions of very short life times and has a maximum bending power up to 18 Tm [9]. The FRS is not only used to produce RIBs for separate experiments. Different kinds of scattering experiments, like the determination of the reaction cross sections can be performed at the FRS itself. Experiments aimed at investigating cross sections need a good accuracy when monitoring the number of traversing ions. Furthermore dedicated experiments can have strict conditions on the delivered ion rate. Thus, beam diagnostics, delivering a good accuracy regarding the number of traversing ions and covering a wide range of intensities, are necessary. For this reason particle detector combinations (PDC) are used at GSI. They consist of three detectors, each covering a certain range of ion rates. At lowest intensities usually a plastic scintillator (SCI) is used to deliver an absolute particle count. The medium and high rate ranges are covered by an ionization chamber (IC) and secondary electron monitor (SEM), respectively.

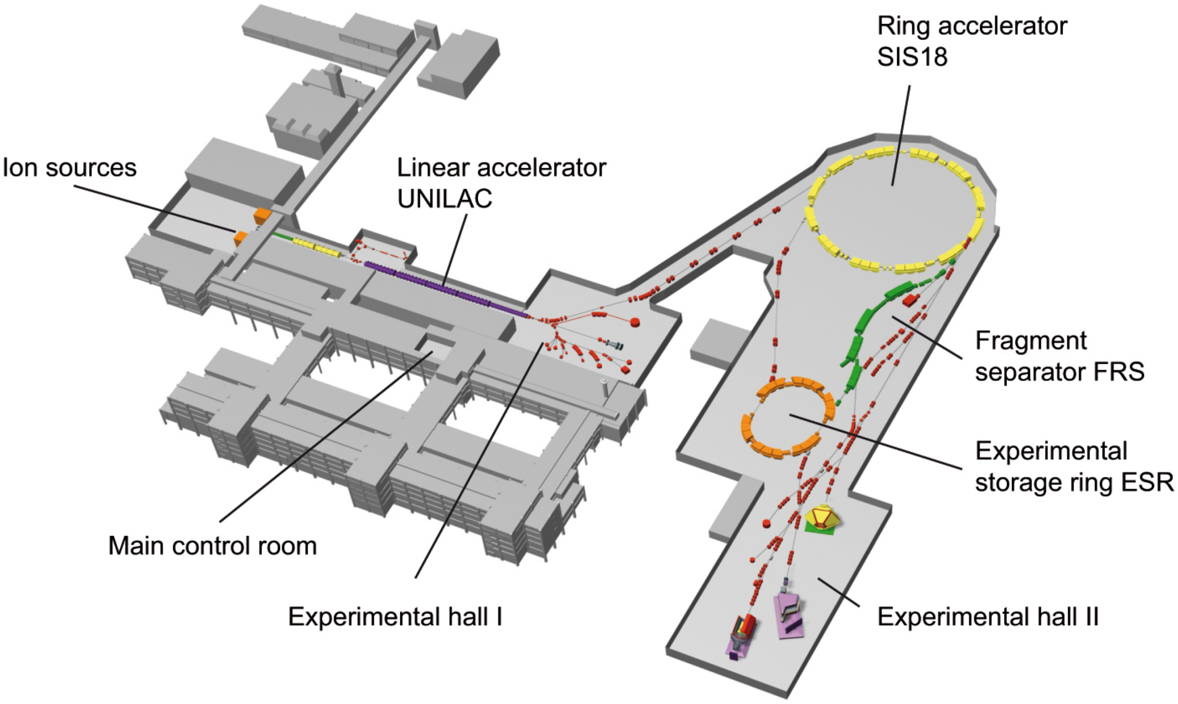

Figure 1.1.: Layout of the components and setups at the accelerator facility at GSI [7].

To increase the yield of nuclides far from stability, an extension of GSI is underway, the Facility for Antiproton and heavy Ion Reaseach - FAIR [10]. A layout of the existing GSI in blue and the future FAIR components in red is shown in Figure 1.2. In the first stage of construction, FAIR's main accelerator stage will be the heavy ion synchroton SIS100, having a bending power of 100 Tm. Besides the increase in energy and many other improvements of beam properties, the facility aims at an increase of ion intensity by a factor of up to 10-1000, dependent on the specific ion. The in-flight separator, to be used at this ambitious project is the superconducting fragment separator (Super-FRS) [11]. Some of the most significant characteristics improved at the Super-FRS are shown in Table 1.1. Due to these

Facility	Max. magnetic bending power $B\rho_{\max}$ [Tm]	Momentum acceptance $\Delta p/p$	Angular acceptance Φ_x [mrad]	Angular acceptance Φ_y [mrad]
FRS	18	1 %	7.5	7.5
Super-FRS	20	2.5 %	40	20

Table 1.1.: Maximum magnetic bending power of the existing fragment separator FRS and the future separator Super-FRS and their momentum and angular acceptance. For the example of ^{50}Ca-ions the increase in bending power translates to an energy increase of 1421 MeV/nucl. to 1644 MeV/nucl.

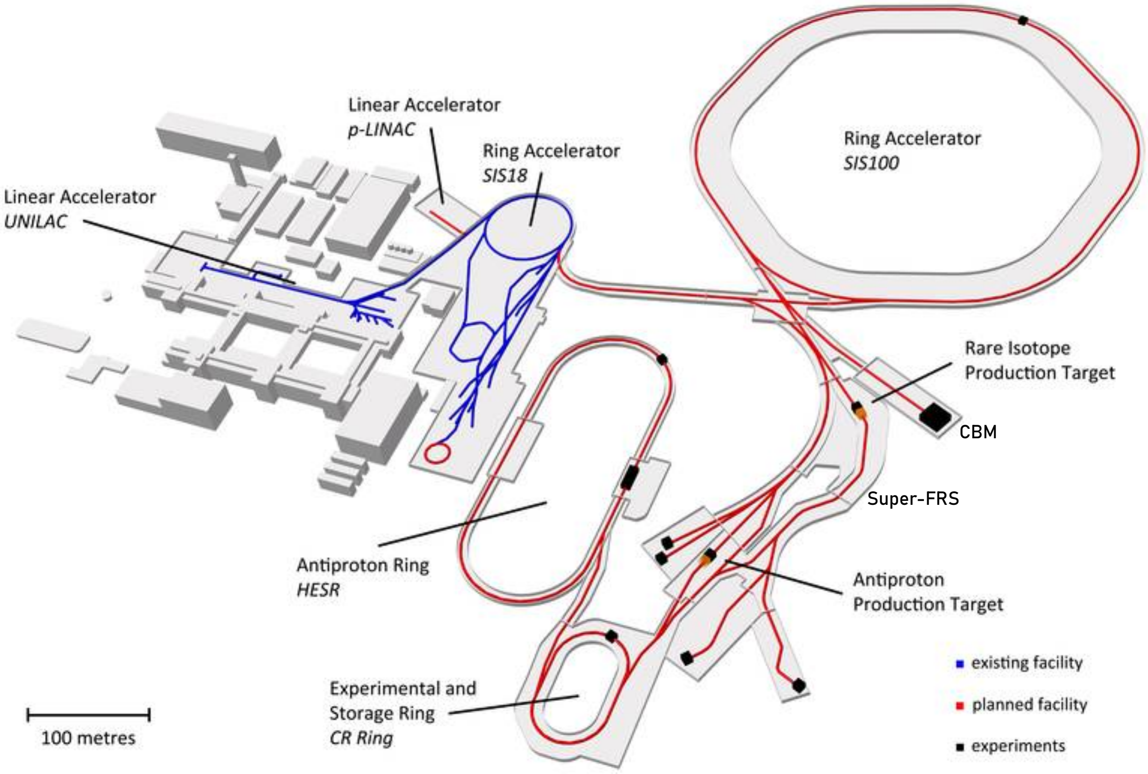

Figure 1.2.: Layout of future research facility FAIR [10].

improvements the ion transmission rate through the Super-FRS will be significantly larger than in the FRS and consequently beam diagnostics will require improvements, to adapt to the conditions in the Super-FRS.

The second part of this dissertation reports about the development and tests of prototypes regarding a particle detector combination to be placed in the high-intensity area near the production target in front of the Super-FRS and in front of the main separator of the Super-FRS. Detectors in the beam at those positions are expected to receive large doses. Even when removed from the immediate beam line, detectors at those positions will be significantly irradiated. At the same time physical access to those areas will be restricted, due to radiation safety. Hence, detectors to be used as part of PDCs in those areas will not only need to deliver intensity measurements at low enough uncertainties to satisfy experimental demands, but also have a high radiation hardness, to be operational even after long periods of beam time with high intensities.

Within the framework of this work single and polycrystalline diamond detectors, expected to have a much higher radiation hardness compared to classical particle monitors like a plastic scintillator, and an IC- and SEM-prototype designed for the use at FAIR were studied and results concerning their performance, radiation hardness and efficiency are presented.

I. One-Nucleon Removal Reaction Cross Sections from Carbon Isotopes

1 Introduction

Nuclear spectroscopy is interested in the description of the structure of nuclei. One common model to describe energy levels of nuclear states, binding energies, etc., in the nucleus is the shell model. Many body shell model calculations open the access to calculate nuclear states, nuclear wave functions and thus the occupation probabilities and binding energies of nucleons in the core in different nuclear states. In the shell model the quantum-mechanical state of a nucleus is described by the sum of all configurations, which describe the occupation of a single-particle orbital by single nucleons in this nucleus. But the model uses the nucleon to fill up the possible configurations by starting with the lowest energy levels. Thus, when calculating the quantum-mechanical state of a nucleus, contributions of higher energetic orbits get neglected. In reality nucleons have an occupation probability in these higher energetic levels, too. A measure for the occupation probability of higher energetic orbits can be found by comparing the respective nucleus with a neighboring nucleus, with one or more or less nucleus. Modeling the overlap of two wave functions, describing a nucleus before and after the transfer of one nucleon

$$\langle \Psi_{A+1} | S \cdot \Psi_A \rangle, \tag{1.1}$$

the spectroscopic factor S can be found, which is an absolute measure for the overlap of the wave functions. The same transfer can be experimentally studied by performing one-nucleon removal reactions. If a good theoretical description of the reaction process is possible a proportionality between the spectroscopic factor and the cross section of one-nucleon removal σ_{-1N} can be found:

$$\sigma_{-1N} \propto S \tag{1.2}$$

Still comparisons of the theoretical calculations of the cross sections and experimental results of the same cross sections an inequality was found

$$\sigma_{-1N,exp} < S \cdot \Sigma, \tag{1.3}$$

where Σ is a factor related to the theoretical cross section of removing a single particle from a specific state. The scale of this inequality presents the accuracy of the theoretical model. Another scale for the quality of the used model is the momentum distribution of the reaction residue. The momentum distribution of the residues carries information about the angular momentum of the state, the single nucleon had been removed from. Thus, the scale of agreement between the angular momentum derived from the experimental momentum distribution and the angular momentum of the modeled state from which the nucleon is removed is a good measure for the quality of the model, too.

Hence, an experimental approach needs to be modeled in a way that the measurements allow to derive the experimental reaction in the nucleus. The energies of the reacting particles have to be sufficiently high, that a suitable reaction theory can be applied onto the results and statistics and precision of the data need to be high enough, that a significant comparison with the theoretical model is possible.

These conditions were fulfilled by performing an experiment in inverse kinematics. The reaction projectiles with mass number A were impinged at a reaction target. After removal of one nucleon they were forward transmitted and the number of projectiles undergoing an one-nucleon removal compared with the total number of projectiles in front of the reaction target. The projectiles were hitting the target at energies above 1.6 GeV/nucl. at the focal plane F2 of the FRS. This led to a highly forwarded angle of the reaction residues and allowed to easily separate the reaction residues from any contamination and thereby provide high statistics. A set of position and energy sensitive and time of flight detectors provided a precise identification of the projectiles and residues. Conducting the reaction at relativistic energies also guaranteed a very short interaction time and thereby, fulfilled the condition to use the sudden eikonal approximation to describe the reaction theory. The nucleon removal was studied by performing one-neutron removal from $^{10-12}$C and one-proton removal from $^{10-12}$C. These nuclei had a simple nuclear structure and a comparison of theoretical predictions of the eikonal model and the experimental results were achievable.

In the following chapters, theoretical foundations of the experiment, its procedure and results are presented. In the first part, basic principles of the shell model and the reaction theory of the nucleon-removal are described. In the second part, the setup and procedure are described. The third part explains the procedure of particle identification and the determination of reaction probabilities. Lastly the obtained results are presented and discussed.

2 Theoretical description of knockout reactions

2.1 Shell-model description of nuclei

In the nuclear shell-model a the wave function of a nucleus Ψ can be described as a combination of the corresponding nucleons single-particle wave functions ϕ_i [12]. To satisfy the demands of the Pauli-principle on a multi-fermionic system the wave function of the nucleus is found by constructing the Slater determinant of the individual single-particle wave functions

$$\mathbf{\Psi} = \frac{1}{\sqrt{N!}} Det|\phi_i(\vec{r}_N)| \tag{2.1}$$

Vice versa the wave function Ψ can be obtained by solving the Schrödinger-equation

$$\boldsymbol{H}\mathbf{\Psi} = E\mathbf{\Psi}, \tag{2.2}$$

where the Hamiltonian is given by the sum of the individual nucleons contributions

$$\boldsymbol{H} = \sum_{i=1}^{A} \boldsymbol{T}_i + \sum_{\substack{i,j=1 \\ i<j}}^{A} \boldsymbol{V}_{i,j}, \tag{2.3}$$

with

$$\boldsymbol{T}_i = \frac{\hbar^2}{2m_i}\Delta_i. \tag{2.4}$$

The nucleons potential with respect to each other is governed by the two-body interaction potential $V_{i,j}$. The sum rules were chosen in a manner, that each possible pairing of two nucleons only appears once. Introducing an average interaction with respect to one nucleon V_i, the Hamiltonian can be broken down into two therms

$$\boldsymbol{H} = \boldsymbol{H}_0 + \boldsymbol{V}_r, \tag{2.5}$$

where $\hat{H}_0$ refers to the average interaction

$$\boldsymbol{H}_0 = \sum_{i=1}^{A} (\boldsymbol{T}_i + \boldsymbol{V}_i) \tag{2.6}$$

and $\hat{V}_r$ refers to a residual interaction. Nucleons are fermions. Hence, when following the approach to describe the nuclear core as a combination of independent nucleons lying within a central potential induced by all other nucleons, each nucleon occupies single-particle states, as allowed by the Pauli-principle. The average potential V_i was found to be well described by

$$\boldsymbol{V}_i = \boldsymbol{V}(\boldsymbol{r}) + \boldsymbol{V}_{ls}(\boldsymbol{r})(\vec{l} \cdot \vec{s}). \tag{2.7}$$

Here, $\boldsymbol{V}(\boldsymbol{r})$ is described by a Woods-Saxon-potential

$$\boldsymbol{V}(\boldsymbol{r}) = -V_0 \left[1 + e^{\frac{r-R}{a}} \right]^{-1}, \tag{2.8}$$

where a and R are parameters describing the blur of the nucleus' radius and the potential's turning point, respectively. The second therm of V_i is given by a radial potential function and the spin-orbit coupling leading to the orbit energy-level splitting with respect to the total angular momentum $\vec{j} = \vec{l} + \vec{s}$. Using the interaction potential from Equation (2.7) the experimentally observed shell closures, also known as the magic numbers, of nuclei were reproduced. Still, theoretical nucleon-removal cross sections calculated within this structure model showed discrepancies compared to experimental results. To correctly model the reaction process the residual interaction has to be taken into consideration. The removal-reactions describes within this dissertation all treat the removal of nucleons from the p-shell. The residual interaction and thereby the Hamiltonian for the p-shell was established by Warburton and Brown. They considered all known data of energy levels in the mass region A=10-20 to develop two types of potential model fits, the WBT and the WBP. A description of their work and how they modeled these Hamiltonians can be found in [13]. Since then these models were improved and additional models developed. The experimental results of this dissertation were compared with theoretical removal cross sections from [14]. In the case of the one-neutron removal from ^{12}C and ^{11}C the theoretical spectroscopic factors were calculated within the WBP and PJT [15] interaction models, respectively, were presented. In the case of ^{10}C and ^{9}C spectroscopic factors were calculated using the WBP, PJT, Cohan and Kurath [16] and PWT [13] shell-model predictions.

2.2 One-nucleon knockout

In one-nucleon knockout experiments an ion beam of known energy and particle composition impinges on a reaction target and residues are identified at 0°. Target materials preferably consist of light nuclei like ^{9}Be or ^{12}C. Their low charge number reduces the influence of Coulomb interaction in the reaction mechanism. Lighter targets also have a smaller number of possible fragments as well as a lower stopping power, and thus, a lower absorption of the particle beam and reaction residues in the target.

At GSI studies of exotic, short lived isotopes are carried out in inverse kinematics, where reactions on the projectiles are investigated. A scheme of a nucleon knockout reaction is shown in Figure 2.1. The projectile hits the target. After the knock-out of a single nucleon, the former projectile has a forward-focused trajectory due to the high incident beam velocity. This allows to identify almost all reaction residues in an in-flight fragment separator and study their mass, charge and energy by positioning detectors behind the separator. The main benefit of this method are the short time scales of the whole process. The fragment separator (FRS) at GSI has a path-length of about 70 m. Particles flying at velocities near to the speed

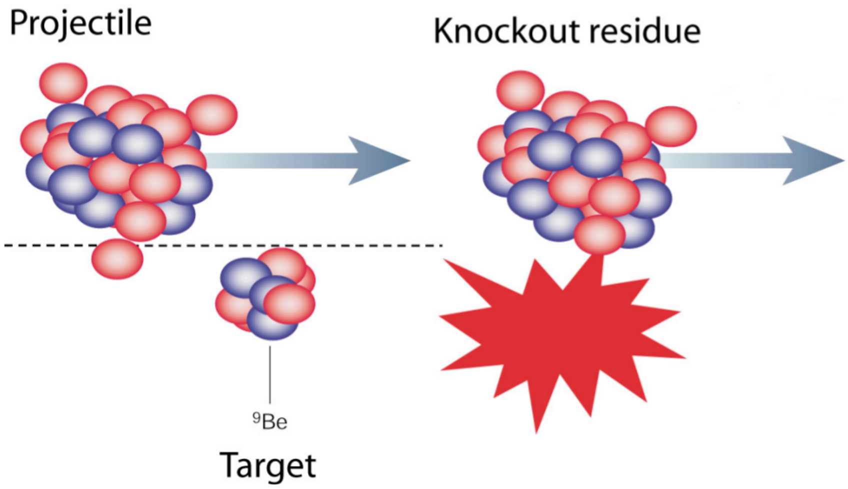

Figure 2.1.: Scheme of an one-nucleon removal reaction in inverse kinematics. The projectile passes the target and a nucleon gets removed. In the eikonal model only one nucleon of the projectile overlaps with the target nucleus and the former projectile follows its trajectory without significant changes in energy. Plot taken from [17]. Reprinted with permission from *Nature Publishing Group*, order number: 4543010800324)

of light need less than 1 μs to pass the FRS. Thus, it is safe to assume, that even ^{9}C[1], the shortest lived of the investigated isotopes passes the fragment separator without major losses due to decay. Therefore, reaction studies utilizing inverse kinematics are a strong tool to investigate exotic isotopes. Knockout experiments in inverse kinematics at relativistic energies may be described within the sudden and eikonal approximations to model the reaction process. Detailed descriptions of the eikonal model can be found in [18–20]. Calculations using the sudden and eikonal approximations describe the removal of a nucleon assuming the projectile core to be separated into two geometrical regions. As indicated in Figure 2.1 the projectile has a region overlapping with the target nucleus and within the approximations only the nucleon to be removed is assumed to occupy this overlapping region. The removal reactions studies within the framework of this dissertation were carried out at energies above 1600 MeV/nucl. and consequently the nuclei's high velocity led to highly forwarded angles of the residues due to the lorentz boost. The time scales of the interaction can be assumed to be very short (sudden approximation), so that no interaction between the projectile core and the target nuclei is to be expected. Consequently the reaction mechanism only depends on the state of the removed nucleon. The relative momentum distribution of the remaining reaction residue originates from the intrinsic momentum distribution of the removed nucleon.

The reaction process itself can be divided into two regimes, the elastic breakup (diffraction dissociation) and absorption (stripping) of the single nucleon [21]. Diffractive reactions describe the scattering of the single nucleon due to interaction with the target nucleus. No energy is transferred in the process, which therefore proceeds elastically. While the target nucleus stays in the ground-state, the removed nucleon is scattered at highly forwarded angles at the same velocity as the beam. Stripping describes all reactions in which a transfer of parts of the single nucleons energy or even the absorption of the whole nucleon leads to an excitation of the target nucleus [18]. The following de-excitation can happen by

---

[1] $T_{1/2}(^9C) = 125$ ms

particle ejection as well as through γ-radiation. In general a third process, the Coulomb dissociation, contributes to the total single nucleon removal. In most cases it provides a negligible contribution to the total cross section. Even the diffractive contribution is usually small compared to the stripping process. The only exception, leading to larger diffractive contributions, are nucleon removal reactions, considering the removal of a halo nucleon [18]. In both of the relevant processes secondary particles and radiation are produced. In a kinematic analysis of the reaction process all of these by-products had to be analyzed. But as the determination of cross sections was the main goal of the experiment, the detection of the reaction residues and the primary projectile intensity was sufficient. Thus, the only requirement of the experiment allowing to analyze the knockout cross sections was to be able to count and identify projectiles and reaction residues. The calculation of the theoretical one-nucleon knockout cross section uses the ansatz that σ_{th} can be divided into two factors described by the reaction and the structure input. They are given by the calculation of the single-particle-removal cross section σ_{sp} and the spectroscopic factor C^2S, respectively.

The relevant contributions to the single particle cross section are knockout due to diffraction $\sigma_{\mathrm{sp}}^{dif}$ and stripping $\sigma_{\mathrm{sp}}^{str}$

$$\sigma_{\mathrm{sp}} = \sigma_{\mathrm{sp}}^{str} + \sigma_{\mathrm{sp}}^{dif}, \tag{2.9}$$

that can not be distinguished when only detecting residues. Individual contributions to the cross sections can be calculated using the eikonal model [22]. Some assumptions about the removed nucleon have to be applied. In the projectile the particle is described by a normalized single-particle wave function with a specific set of quantum numbers (n,l,j). The single particle is moving relative to the remaining nucleons in the core in a state $c = j^{\pi}$ [21]. For a quantitative description wave functions like $|\Phi_{JM}^{c}\rangle$ are used, with J and M the magnitude and projection of the total angular momentum $\vec{J} = \vec{I} + \vec{j}$ of the projectile's ground state. Finally the single-particle cross sections can be described as integrals over the projectiles center-of-mass impact parameter $\vec{b}$ [22]

$$\sigma_{\mathrm{sp}}^{str} = \frac{1}{2J+1} \int d\vec{b} \sum_{M} \langle \Phi_{\mathrm{JM}}^{c} | (1 - |\boldsymbol{S_n}|^2) |\boldsymbol{S_c}|^2 | \Phi_{\mathrm{JM}}^{c} \rangle, \tag{2.10}$$

$$\sigma_{\mathrm{sp}}^{dif} = \frac{1}{2J+1} \int d\vec{b} \left[\sum_{M} \langle \Phi_{\mathrm{JM}}^{c} | (1 - \boldsymbol{S_c S_n})^2 | \Phi_{\mathrm{JM}}^{c} \rangle - \sum_{\mathrm{M,M'}} \langle \Phi_{\mathrm{JM'}}^{c} | (1 - \boldsymbol{S_c S_n})^2 | \Phi_{\mathrm{JM}}^{c} \rangle \right]. \tag{2.11}$$

Here, $\boldsymbol{S_n}$ and $\boldsymbol{S_c}$ denote the elastic S-matrices describing the scattering of the removed nucleon and the remaining core of the projectile, respectively, at the target. Both S-matrices are expressed as functions of their individual impact parameters and can be calculated using the optical limit of Glauber theory [23]. The single-particle cross section is obtained by calculating the reaction cross section if a certain state with given quantum numbers is occupied. It allows the determination of the cross section if a particle in this state is removed.

The second factor contributing to the calculation of σ_{th} is the spectroscopic factor $S(\alpha, j^{\pi})$. Those factors provide information about the occupation probabilities of specific states and are derived from nuclear shell-model calculations using the approaches to describe the Hamiltonian, which were mentioned in chapter 2.1. The spectroscopic factor describes the transition probability of the initial state of a projectile's wave function to a specific final state α in the residue. In other words the spectroscopic factor $S(\alpha, j^{\pi})$ tells us about the occupation probability of a particle in the initial state j^{π}, the nucleon is removed from and the probability the residue is in the final state α after the nucleon removal. Thus, it expresses the parentage of an initial state, with given single-particle configuration j^{π} in the projectile, with respect to a specific final state α of the reaction residue after removal of exactly this single-particle [21]. The spectroscopic factor can be found by calculating the overlap of two wave functions, describing the initial state of the projectile and the final state of the residue after nucleon removal.

$$\langle \Psi^{f}_{\text{A-1}} | \Psi^{i}_{\text{A}} \rangle = \sum_{j} c^{if}(\alpha, j^{\pi}) \Phi_{j} \tag{2.12}$$

The spectroscopic amplitudes for the observed reactions are given by the factors $c^{if}(\alpha, j^{\pi})$. Taking the square of the spectroscopic amplitudes the spectroscopic factors $S(\alpha, j^{\pi})$ are obtained.

$$S(\alpha, j^{\pi}) = |c^{if}(\alpha, j^{\pi})|^{2} \tag{2.13}$$

If the isospin configurations of the initial and final state and thus, the Glebsch-Gordan coefficients C are known, one writes usually C^2S for the spectroscopic factor [24]. Finally an expression for the theoretical cross sections can be found by applying the assumption of the eikonal approximation, by treating the theoretical removal cross section as a mixture of the single-particle-removal cross section and the corresponding spectroscopic factor [25].

$$\sigma_{\text{th}}(\alpha) = \frac{A_p}{A_e} C^2 S(\alpha, j^{\pi}) \sigma_{\text{sp}}(S^{*}_{\alpha}, j) \tag{2.14}$$

Here, A_p and A_e are the mass number of the projectile and ejectile nuclei and their ratio poses a center-of-mass correction, necessary for many body calculations based on harmonic oscillator forces [26]. In the case of one-nucleon knockout from p-shell nuclei the mass numbers can be described as $A_e = A_p - 1$. Furthermore, $S^{*}_{\alpha} = S_{\text{n,p}} + E^{*}_{\alpha}$ is the effective separation energy for the reaction residue to reach the final excited state α at excitation energy E^{*}_{α} with the ground-state to ground-state separation energy $S_{\text{n,p}}$. A given single spectroscopic factor and single-particle cross section only describe a partial cross section of a transition from a specific state into a specific final state after nucleon-removal. Depending on the structure of the nucleus multiple combinations regarding the transition from a specific initial to a specific final state can describe the one-nucleon removal reaction. The experimental observation only counts the number of reaction residues and cannot distinguish which transition led to its production. It only sees the sum of all possible contributions. Thus, for comparisons of theoretical and experimental cross sections the total theoretical cross section, being the sum of all partial cross sections has to be calculated.

$$\sigma_{\text{th}} = \sum_{\alpha} \sigma_{\text{th}}(\alpha) \tag{2.15}$$

2.3 Momentum distributions

As mentioned above the eikonal model describes the nucleon removal from a specific state j^{π}. Looking at shell model calculations and consequently the spectroscopic factors a set of possible states, occupied by the single nucleon at different probabilities, can be found. At the moment of the nucleon's removal a momentum transfer to the reaction residue occurs, strictly correlated to the orbital angular momentum l of the involved nucleon [27]. This momentum transfer leads to an observable distribution of the longitudinal momentum $p_{||}$ of the reaction residue. Vice versa this means, measuring the distribution of $p_{||}$ allows to draw conclusions about the orbital angular momentums of the removed nucleons, their binding energy and thus, about the structure of the studied nucleus. All considered cores presented in this dissertation deal with nucleon-knockout from the p-shell. Therefore the extraction of the longitudinal momentum distribution serves as cross check with the reaction description within the eikonal approach and the experimental analysis method. Furthermore, it allows the estimation of events outside of the spectrometer acceptance.

2.4 Reduction of theoretical compared to experimental cross sections

Theoretical descriptions always aim at improving their models and their conformity with experimental results. Since the spectroscopic factors derived from the shell-model calculations are no experimental observable a direct comparison is not possible. The same goes for the input parameters, like effective interaction ranges, nucleon radial overlaps and further inputs used to model the residual interaction of the nucleons in the p-shell. The total theoretical cross section on the other hand can be compared with experimental results. A commonly used comparison between the theoretical and experimental cross section is the reduction factor

$$R_s = \frac{\sigma_{\text{exp}}}{\sigma_{\text{th}}}. \tag{2.16}$$

For comparisons of different isotopes the reduction factor is plotted versus the asymmetry of neutron and proton binding energies of the removed nucleon. In the case of proton removal the asymmetry is given by $\Delta S = S_p - S_a$ and for neutron removal by $\Delta S = S_n - S_p$. The original surmise that knockout reactions could possibly be sensitive to spectroscopic factors even on an absolute scale comes from the observation that R_s in stable nuclei agrees with results from quasi-elastic (e,e'p) reactions [18]. This reaction is believed to be sensitive to the wave function of individual nucleons due to the weakness of the electromagnetic interaction. In Figure 2.2 a collection of neutron knockout data is presented. A detailed description of the data points and their origin can be found in [25]. It is obvious that a large discrepancy between theory and experiment can be found for large positive binding energy asymmetries and thereby for nucleon removal of strongly bound nucleons. At large negative asymmetries and low binding energies of the removed nucleon the reduction factor is nearly unity. These discrepancies show that the description of the nuclear states needs still improvement in some cases. Especially the description of the short-range interaction of the nuclear force, dominant in the removal of nucleons in low lying shells, is not yet fully understood. Therefore, it is most valuable to study the reduction factors between theoretical and experimental cross sections, to further increase the amount of data, relevant for

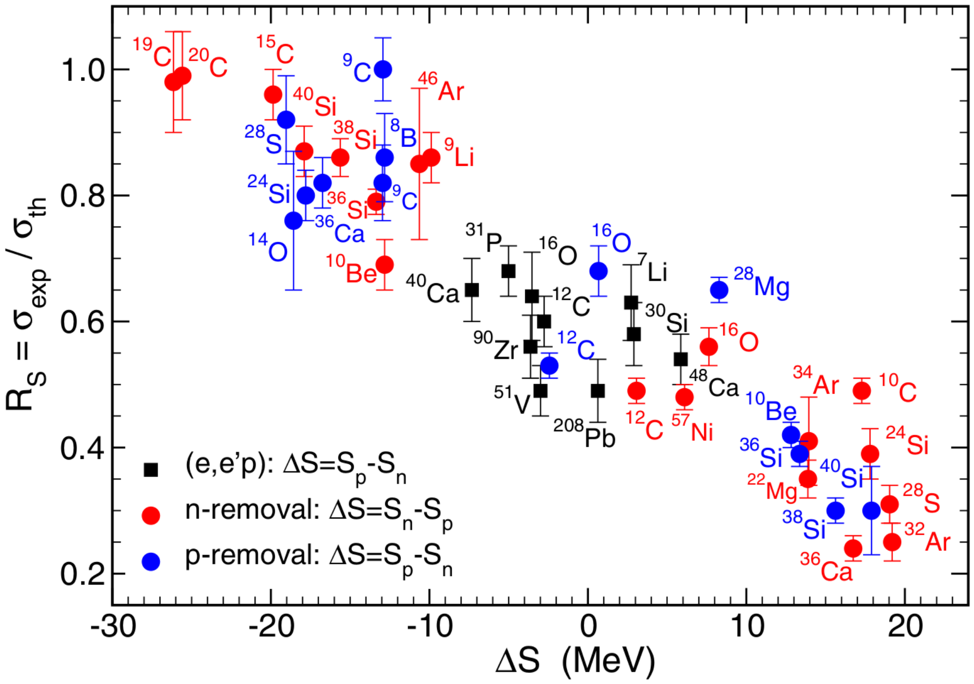

Figure 2.2.: Compilation of various reduction factors obtained by calculating the ratio of experimental and theoretical one-nucleon cross sections. In most cases the decrease of R_s is highly sensitive to an increase of the difference between neutron and proton separation energy ΔS. Plot taken from [25] with permission from the author J.A. Tostevin.

improving the many body nuclear shell model and get a better understanding of the nucleon-nucleon interaction at short ranges.

A series of studies regarding the cross section of one- and two-nucleon knockout and charge-exchange reactions of neutron-poor carbon isotopes was performed at the in-flight fragment separator (FRS [9,28, 29]) at GSI in Darmstadt from July 24-28, 2008. The reactions reported about in this dissertation were one-neutron knockout of $^{10-12}$C and one-proton knockout from ^{9}C

$$^{9}\mathrm{Be}\left(^{12}\mathrm{C},{}^{11}\mathrm{C}\right)\mathrm{x}, \tag{3.1}$$

$$^{9}\mathrm{Be}\left(^{11}\mathrm{C},{}^{10}\mathrm{C}\right)\mathrm{x}, \tag{3.2}$$

$$^{9}\mathrm{Be}\left(^{10}\mathrm{C},{}^{9}\mathrm{C}\right)\mathrm{x}, \tag{3.3}$$

$$^{9}\mathrm{Be}\left(^{9}\mathrm{C},{}^{8}\mathrm{B}\right)\mathrm{x}. \tag{3.4}$$

The projectiles of these reactions were produced from a primary beam of ^{12}C-ions at 1670 MeV/nucl. The secondary beam was identified event by event and hit a secondary target, thus producing the corresponding ejectiles after nucleon-knockout.

The short lived isotopes discussed in this dissertation have been produced, separated and identified in the fragment separator FRS. Drawings, pictures and a list of all detectors and electronics used at the different areas of the FRS can be found at [29, 30]. A layout of the FRS, surrounding devices and beam connections is shown in Figure 3.1. The ion beam is fed to the FRS after acceleration in the heavy ion synchrotron SIS18 [8]. At the beginning of the FRS, different production targets can be inserted. The main part of the FRS consists of four sections, S1-S4, to separate ions with respect to their magnetic rigidity. The FRS consists of large dipole magnets for beam deflection and higher-order magnetic systems, like quadrupole or hexapole magnets, that are used to focus the beam along the beam line through the separator. Additionally aluminum wedges at S1 and S4 and a dedicated degrader system

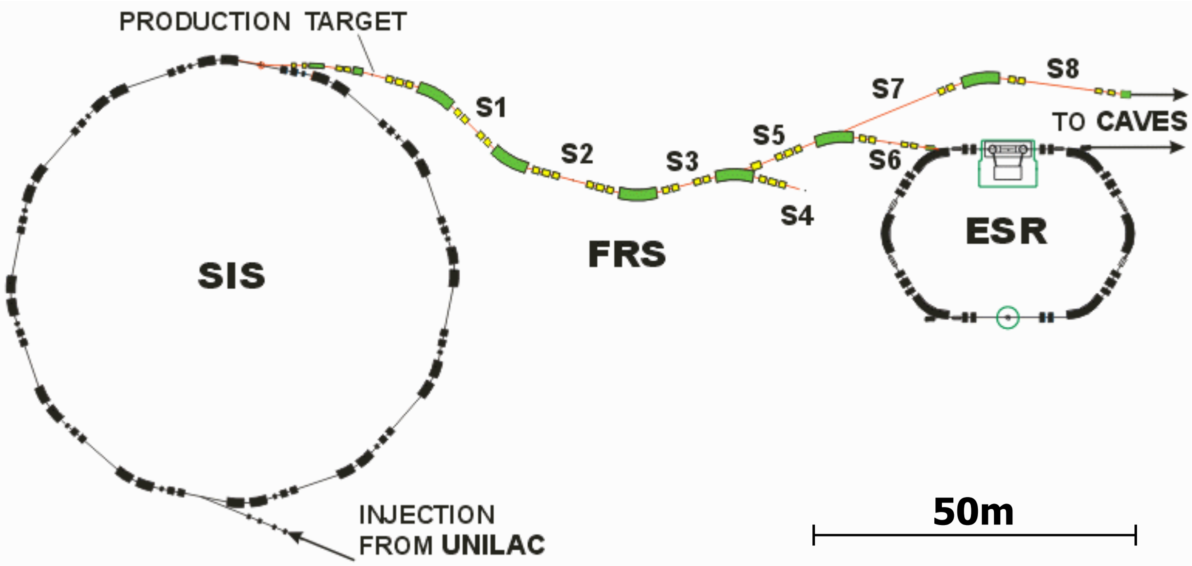

Figure 3.1.: Layout of the FRS and surrounding devices. Dipole stages are green, higher order magnetic systems for ion optical corrections are yellow [30].

at S2 allow a further separation of the ions with regard to their charge. Along the focal planes detectors can be mounted to perform experiments with the FRS itself. Otherwise the separated ion beam can be transported to different experimental sites or to the heavy-ion storage ring ESR [31]. Separation of ions in the FRS principally happens in two major steps, separation by magnetic rigidity in dipole magnets and due to their charge in a degrader system. Both steps are working most efficiently, if the ions are fully stripped, meaning charge and atomic number are the same $q = Z \cdot e$. The dipole magnets of the FRS used for the separation concerning the ions magnetic rigidity are shown as green parts in Figure 3.1 and 3.2. The traversing charged particles feel a magnetic dipole field and as a consequence the resulting Lorentz force acts as centripedal force

$$\vec{F}_L = \vec{F}_Z, \tag{3.5}$$

with

$$\begin{aligned} \vec{F}_L &= q(\vec{v} \times \vec{B}) && (3.6) \\ \vec{F}_Z &= m\omega \times (\omega \times r). && (3.7) \end{aligned}$$

Thus, the particles are forced to move along a circular path through the magnetic dipole field and from Eq. 3.5 their magnetic rigidity can be calculated

$$B\rho = \frac{\beta\gamma uc}{Ze} \cdot \frac{A}{Z}. \tag{3.8}$$

Here, $m = \gamma uA$ denotes the relativistic mass of the ions, A and u are the atomic mass number and atomic mass unit, respectively, $\beta = \frac{v}{c}$ is the ion's velocity in units of the speed of light, $q = Ze$ is the charge of the ions and γ is the Lorentz factor. The individual contributions of the magnetic rigidity is the magnetic field strength B and the ions bending radius in the dipole field ρ. In the case of the reactions presented in this work the mass-over-charge (A/Z or AoZ) separation was sufficient to identify the incident carbon isotopes. Since the projectiles and the production target (beryllium) consisted of light ions the variety of contamination in the projectile beam, having the same mass-over-charge ratio as the separated carbon isotopes, was small. An exclusion of the contaminating isotopes in the data analysis was easily performed, using a plastic scintillator as a charge-sensitive detector in front of the secondary reaction target. If a larger contamination is expected, possibly leading to increased dead times of the detectors and thus reducing the number of obervations of the desired isotopes, or a better spatial separation of the ions is needed, another method is added, the degrader system. By introducing material - the degrader - in the beam line [9] ions can be separated by their charge. Heavy charged particles traversing matter loose energy due to inelastic scattering processes. The mean energy loss dE per unit length dx can be described, using the Bethe-Bloch equation [32]

$$-\langle\frac{\mathrm{d}E}{\mathrm{d}x}\rangle = KZ^2\frac{\tilde{Z}}{\tilde{A}}\frac{1}{\beta^2}\left[\frac{1}{2}ln\left(\frac{2m_e c^2\beta^2\gamma^2 W_{\max}}{I^2}\right) - \beta^2 - \frac{\delta(\gamma\beta)}{2}\right]. \tag{3.9}$$

$\tilde{Z}$ and $\tilde{A}$ are the atomic charge and mass of the traversed matter, $K = 4\pi N_A r_e m_e c^2$ a constant, $W_{\max}$ the maximum energy transfer in a single collision and I the mean excitation energy of the materials nuclei. For a generalized view and qualitative discussion of the energy loss of an ion beam in matter the formula can be reduced to

$$-\left\langle\frac{\mathrm{d}E}{\mathrm{d}x}\right\rangle \propto Z^2. \tag{3.10}$$

This means, in first order the energy loss of the beam in any material only depends on the charge of the ions. The introduced matter is a wedge. Due to the wedge shape of the degrader an achromatic ion optical system is generated. Ions of one species but different momentum will traverse the wedge at different points of thickness. Consequently ions of larger momentum will suffer a larger energy loss and vice versa. Hence, all ions of one species but different momenta in front of the wedge can ideally be focused into one point and momentum after the wedge. Thus, a separation of the ions by their charge is possible, as well as improving the separation of the ions in the next dipole stage after the degrader system, since now all ions of one species have a lower relative momentum spread.

3.1 Experimental setup

To measure the knockout cross section of different isotopes they had to be produced first and the ion beam delivered to the secondary reaction target, ideally without contamination of other isotopes. The schematic of the experimental setup is shown in Figure 3.2. A primary ^{12}C beam was impinged on ^{9}Be-production target in front of the FRS to produce the required projectiles, consisting of neutron poor carbon isotopes. The only exception was the neutron knockout from ^{12}C, where the primary beam was directly transmitted to the reaction target after attenuation in the production target. The thicknesses of the production and reaction targets are shown in Table 3.1. The exact composition of the reaction target, relevant for the cross section calculation, can be found in appendix A.1.

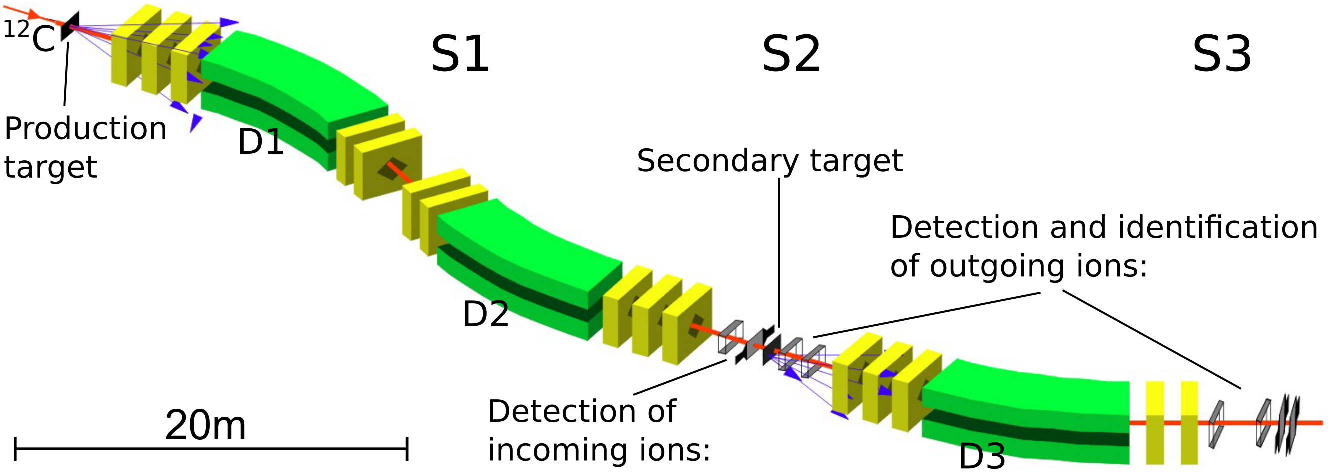

Figure 3.2.: Schematic overview of the experimental setup at the FRS [33]. The desired projectiles coming from the production target were separated at the dipole stages D1 and D2. Reaction residues produced in the secondary target were separated at D3. At the focal planes S2 and S3 detectors for the particle identification and intensity measurements were placed.

	Thickness $t \cdot \rho$ [mg cm^{-2}]
Production target	4011 $\pm$ 1
Reaction target	4925.9 $\pm$ 21.4

Table 3.1.: Properties of the production and reaction target.

Following secondary beam production, the separation of this particle cocktail was achieved along the first and second stage of the FRS in dipoles D1 and D2, using the ions mass-over-charge ratio (A/q). Nearly all particles produced at this very high energy were fully stripped (q=Z). At S2 the particles hit a secondary reaction target. The particles of interest were separated by their A/Z ratio in the third stage of the FRS in dipole D3 and transmitted to S3. Detectors dedicated to the identification of the reaction residues were placed at S2 after the reaction target and at S3. The magnet settings of the FRS regarding the ion transmission in the measurements are shown in Table 3.2. For each reaction four measurements

Reaction	TA→S2	$B\rho_0$[Tm]	#Events	S2→S3	sec. TA	$B\rho_0$[Tm]	Trigger	scale	T [min]
(^{12}C,^{11}C)	^{12}C	16.33	382004	^{12}C	in	16.02	SCI2.1	1	19
"	"	"	340589	"	out	16.02	SCI2.1	1	21
"	"	"	320153	^{11}C	in	14.64	SCI2.1	1	44
"	"	"	396611	"	out	14.80	SCI2.1	1	39
(^{11}C,^{10}C)	^{11}C	14.97	394544	^{11}C	in	14.65	Comb.	2	14
"	"	"	116295	"	out	14.65	Comb.	256	8
"	"	"	57358	^{10}C	in	13.25	Comb.	256	129
"	"	"	119027	"	out	13.44	Comb.	256	64
(^{10}C,^{9}C)	^{10}C	13.57	109619	^{10}C	in	13.23	SCI 2.1	1	16
"	"	"	45092	"	out	13.45	SCI2.1	1	6
"	"	"	134397	^{9}C	in	11.91	Comb.	256	246
"	"	"	142492	"	out	12.08	Comb.	256	156
(^{9}C,^{8}B)	^{9}C	12.22	384	^{9}C	in	11.93	Comb.	256	12
"	"	"	338	"	out	12.11	Comb.	256	10
"	"	"	1229	^{8}B	in	12.73	Comb.	256	42
"	"	"	7334	"	out	12.90	Comb.	256	115

Table 3.2.: Settings of the FRS for the transport of the ions from the production target to S2 and for the transport of the ions from S2 to S3. The magnetic rigidity $B\rho$ was calculated using the magnetic field strength, provided by Hall-probes and the effective bending radius ρ_0=11.396 m obtained by calibration (see chapter 4.2.2). The corresponding trigger signals for the DAQ were either coming from the SCI 2.1 only or from a trigger box (combined). The box triggered the DAQ whenever a coincidence between SCI 2.1 and the scintillators at S3 was measured or at every nth signal from the SCI 2.1, with n given by the downscale factor (scale). The number of events relates to the number of identified carbon ions at S2 in front of the reaction target (normalization constraints from chapter 4.3.1 applied). The number of events has to be multiplied with the downscale factor to get the real number of projectiles traversing SCI 2.1. The number or residues is given by signals recorded by both SCI 3.1 and 3.2.

were performed to obtain a background corrected reaction probability. The procedure is explained in chapter 4.3.3, Equation (4.12). The table also includes the trigger settings of each measurement. The trigger procedure is explained in detail in chapter 3.2. The final identification was placed at S3 to maximize acceptance and transmission. While the resolving power at S4 would have been higher, the number of contaminants was small enough at S3 when using a relativistic light ion beam like carbon at energies in the range of more than 1 GeV per nucleon. Ultimately a clear particle identification at S3 was possible, while reducing the number of corrections due to transmission losses at the fourth stage of the FRS. Hence, setting up the particle identification detectors at S3 allowed to record data at much larger statistics and lower systematic uncertainties, compared to mounting the detectors at S4.

For the final calculations of the reaction probability various detectors had been used to determine the charge, position and number of particles. A scheme of the detector positioning at S2 can be seen in Figure 3.3. The incoming beam traversed a plastic scintillator (SCI) [30, 34], measuring the energy loss, and a multi-wire proportional chamber (MW) [35], measuring x- and y-position of the particles, before hitting the reaction target. The measured energy loss was later used to calculate the charge of the particles. The x- and y-positions of the outgoing beam were recorded by two TPCs [36] after

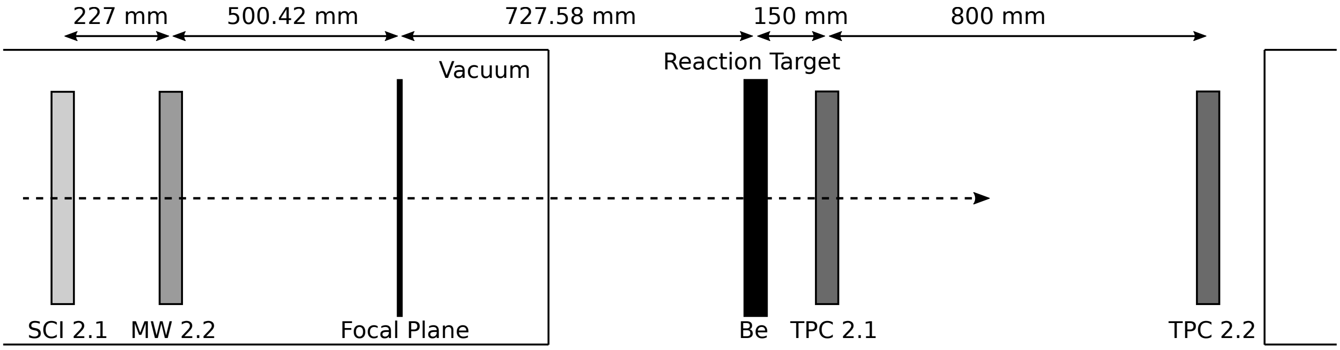

Figure 3.3.: Schematic drawing of the detector setup at S2. Plastic scintillator SCI 2.1 and multiwire proportional chamber MW 2.2 measured charge and position of the incoming particles in front of the reaction target, while the time projection chambers TPC 2.1 and TPC 2.2 measured the position information of the outgoing particles.

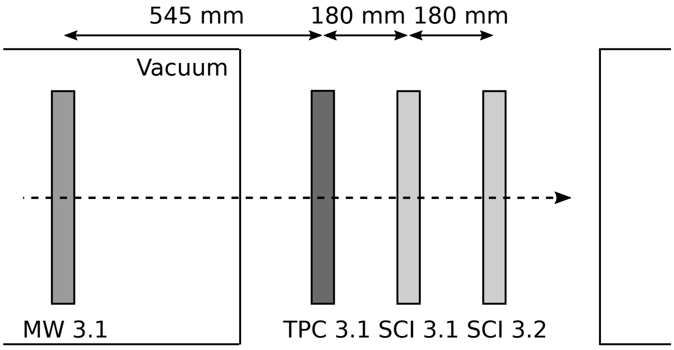

Figure 3.4.: Schematic drawing of the detector setup at S3. The multiwire proportional chamber MW 3.1 and time projection chamber TPC 3.1 measured the position of the ions, while the scintillators SCI 3.1 and 3.2 measured the charge of the reaction residues. The focal plane at S3 in the optical settings is located 80 cm in front of MW 3.1, shortly after the last quadrupole magnet.

the reaction target, also allowing to calculate the angle of the particle trajectory. This information was especially important for the calculation of the x-position in the focal plane of S2 and thereby for the particle identification of the reaction residues (see chapter 4.2).

A further set of detectors was placed at S3. A scheme of the detector positioning is shown in Figure 3.4. Two SCIs individually measured the energy loss of the reaction residues. For later calculations the average of the measured pulse heights, after conversion into charge, was used

$$Z_{\mathrm{S3}} = \frac{Z_{\mathrm{SCI3.1}} + Z_{\mathrm{SCI3.2}}}{2}. \tag{3.11}$$

The x- and y-positions of the particles at S3 were recorded by a MW and a TPC. The focal plane at S3 was behind the last quadrupole magnet of the third stage and 80 cm in front of the MW-chamber.

3.2 Data acquisition and analysis

The standard data acquisition (DAQ) system at GSI, the multi branch system (MBS) [37], was used running on a RIO server had been used to record the data of all detectors. Before these data could be recorded, the measured signals had to be digitized. This was done by various electronics modules, mainly based on the VME framework. Time-to-digital converters (TDC) linked the timing information of the delay lines and anodes of the TPCs and MWs to the DAQ. Charge to digital converters (QDC) linked the energy loss measured at the SCIs to the DAQ. The time of flight (ToF) was measured by a time to analog converter (TAC), started and stopped by SCI 2.1 and SCI 3.1.

Different trigger schemes have been employed during the experiment. For the determination of the nucleon-knockout cross section the ratio of number of residues and the number of incident ions (projectiles) must be known. Trigger option one analyzed all ions incident at S2, although only a small fraction of them undergo the desired reaction. In this case the trigger signal was directly coming from the SCI 2.1. Trigger option two made use of a coincidence of the scintillators at S2 and S3 (i.e. SCI 2.1 $\wedge$ (SCI 3.1 $\vee$ SCI 3.1)) to tag a possible reaction and a reduced (downscaled) S2 trigger for normalization purposes. The S2 trigger (with possible downscale factors of 2^n, with n=[0,8], and the used factors presented in Table 3.2) and the combined S2 and S3 trigger (without downscale) were fed to the input of a dedicated trigger electronics module [38]. Trigger type one at high incident beam intensities leads to significant dead time. For trigger type two the number of reduced triggers coming from SCI 2.1, but without any trigger from S3, are represented in channel 2 and 3 of the histogram shown in Figure 3.5. Triggers coming from S3 in coincidence with a trigger at S2 are represented in channel 4 to 7. Triggers coming from S3 in coincidence with the reduced trigger from SCI 2.1 are displayed in channel 6 and 7. To calculate the actual number of particles that traversed SCI 2.1, the events in channel 2, 3, 6 and 7 had to be summed and multiplied by the reduction factor. All data recorded by MBS were saved in list-mode-data files (LMD). To unpack these files and sort them, the GSI Object Oriented On-line Off-line system (Go4) [39] was used. Go4 is usually set to perform four sub routines. The first one unpacks the data, the second one sorts them, the third performs their calibration and the forth is dedicated to the final analysis of the data. Go4 was connected directly to MBS during the experiment, to perform an online analysis of the data. This way, the detector responses, beam position, calibration settings, etc. had

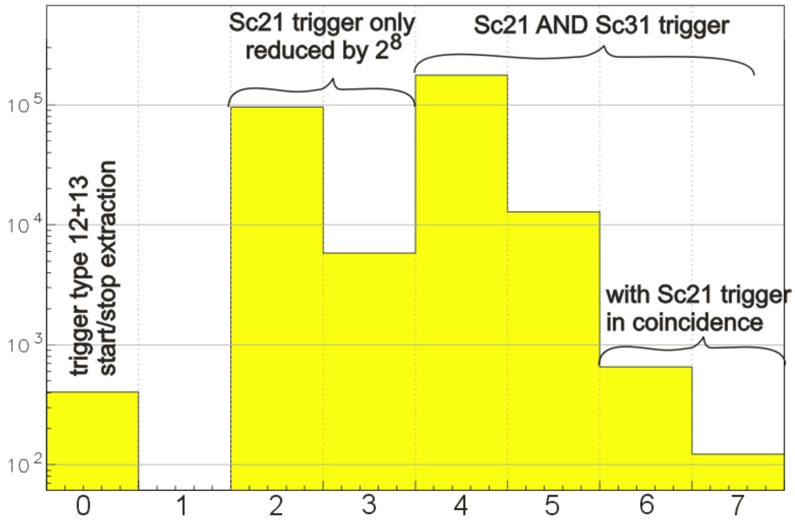

Figure 3.5.: Sample histogram of the trigger types produced by the trigger box.

been checked, while the data were recorded. For the final offline presented in this work, Go4 was used, too. Each of the subroutines creates a tree-branch, which can be saved as .root files. For the analysis of the presented data only the unpack and sort routines of Go4 were used. The sorted files were saved in a .root file. For the full calibration and analysis of the sorted data self-developed and customized ROOT [40] macros were used.

3.3 Detectors and calibration procedure

3.3.1 Plastic scintillator

Ions traversing material suffer energy loss due to inelastic scattering with shell electrons of the atoms. Scintillation materials have excited states which decay by electromagnetic radiation in the visible spectrum. Thus, by exciting the atoms of the detector material and the following de-excitation light is emitted. Photomultiplier tubes (PMT) are used to convert the emitted light into an electronic signal. The scintillators were used for charge determination and to measure the time of flight between two positions. The charge is determined from the energy loss of the ion beam in the material, which is proportional to pulse height delivered by the PMT. The energy loss of ion beams in matter is given by the Bethe Formula and is proportional to the charge and velocity of the traversing particles

$$\frac{\mathrm{d}E}{\mathrm{d}x} \propto \frac{Z^2}{\beta^2}, \tag{3.12}$$

with the particle charge $Z \cdot e$ and the velocity in units of the light speed β. If the energy loss of the particles in the detector and the velocity of the particles are known, their charge can be calculated. To each scintillator, two PMTs are connected for signal read-out on each side of the scintillator material. The

PMT signals are subsequently digitized. The left and right side gain were manipulated simultaneously while conserving the sum of the square of the gain parameters g_l and g_r

$$g_l^2 + g_r^2 = 1. \tag{3.13}$$

The final energy loss value was given by the geometric mean of both PMTs

$$dE_{\text{SCI}} = \sqrt{dE_{\text{SCI-L}} * dE_{\text{SCI-R}}}. \tag{3.14}$$

The second purpose of the SCIs, to measure the time of flight, was realized using a time to analog converter (TAC), with the scintillator timing signals feeding into it as start and stop signals. The output signal of the TAC was digitized using an ADC. Absolute timing was determined from a pulser measurement, shown in Figure 3.6. The calibration was performed independently for the connections of each side of the PMTs. Two sets of timing spectra were generated for the left and the right PMTs of the scintillators in the setup. The final time of flight, used in the data analysis, is given by the mean time of the left and right side

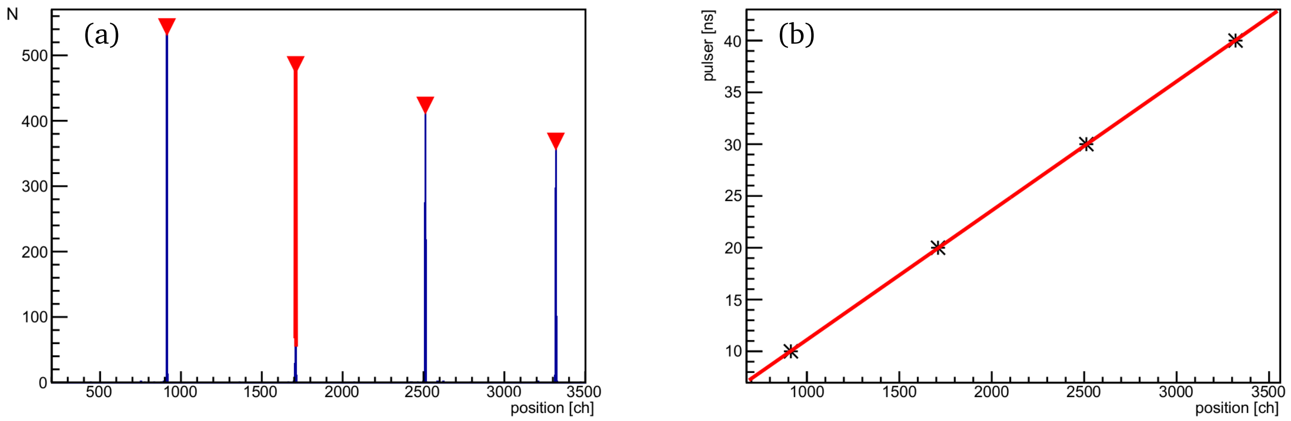

Figure 3.6.: Calibration of the TAC, using a pulser as reference to calibrate the channel numbers with respect to absolute time scales. The distance between the four peaks (a) refers to a time difference of 10 ns. Fitting the time vs. channel number (b) delivers the calibration.

$$t_{\text{ToF}} = \frac{t_{\text{ToF, L}} + t_{\text{ToF, R}}}{2}. \tag{3.15}$$

3.3.2 Time projection chamber

Time projection chambers are gas-filled ionization chambers. P10-gas (90% Argon, 10% Methan) was used during the experiment as fill gas. A scheme of the used TPC can be seen in Figure 3.7. The ions of the primary beam traversing the chamber induce secondary electrons by inelastic scattering. The secondary electrons drift towards the anode due to the high voltage applied at the cathode. The inner

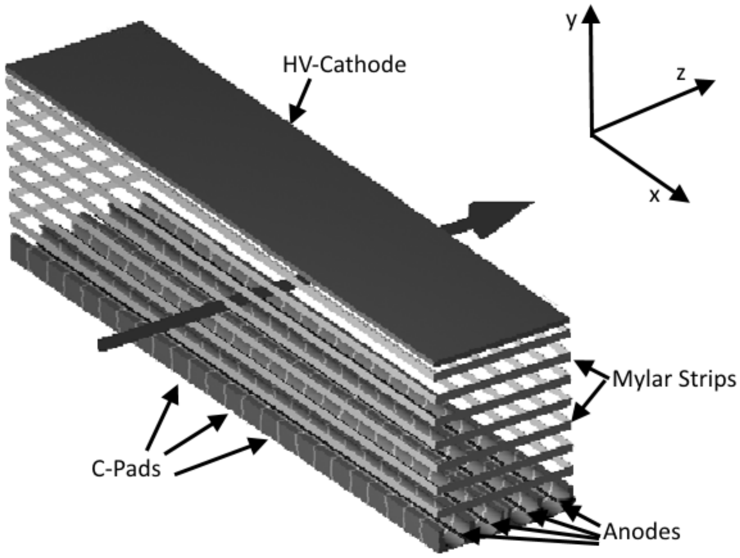

Figure 3.7.: Scheme of a TPC [36]. Scales of the active area (x×y×z) are 200 mm×80 mm×50 mm.

chamber is surrounded by metalized Mylar strips to provide an uniform electric field within the drift volume [36]. The anode wires are placed in C-pads. Each of these C-pads is connected to an integrated passive delay-line. Every TPC has two independent delay-lines, used to calculate the x-position of the traversing particle. Measuring the time, the signal takes to reach the right and left side of the delay-line, the x-position can be determined

$$x = w_{\text{del}} \cdot (t_l - t_r) + x_{\text{off}}. \tag{3.16}$$

Here, w_{del} is the propagation velocity of the signal in the delay-lines in $\text{mm}\,\text{ch}^{-1}$ (mm per channel), and x_{off} a simple offset value in mm. Both values are found experimentally by performing a calibration measurement. If both delay-lines delivered a good signal, the average x-position is calculated, otherwise only the x-position of the valid signal is provided. The y-position of the particle can be calculated using its drift time given by the anode

$$y = w_{\text{dri}} \cdot t_{\text{dri}} + y_{\text{off}}, \tag{3.17}$$

where w_{dri} is the electron drift velocity in $\text{mm}\,\text{ch}^{-1}$ and y_{off} an offset value on mm. Both values are provided by a calibration measurement. The start signal for the time measurements of the TPC is given by the FRS trigger. A time to digital converter (TDC) is used to digitize the time signals coming from the TPC and provides a channel number proportional to the time difference. Calibrating the channel number to obtain the actual position information is done using a scintillator mask. The mask is a grid with well known lattice spacing. For the calibration measurements only events were recorded, when the scintillator mask and the TPC both showed a signal. This measurement was performed with defocused ion beam. A large beam spot allowed to irradiate the whole mask at once and clearly see the lattice, needed to calibrate the TPC. The resulting x-y distribution is shown in Figure 3.8. The final calibration of the TPC channels was performed individually for each dimension. Figure 3.9(a) shows the projection

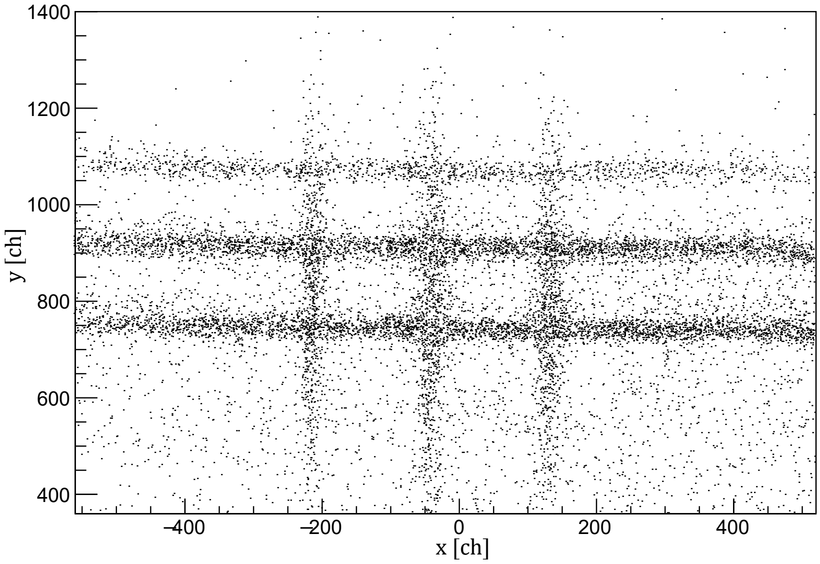

Figure 3.8.: Calibration of the TPC channels using a scintillator mask with known lattice distances. Events were only considered when TPC and scintillator mask both showed a signal.

of the x-y distribution on the x-axis. The position of the peaks refer to the x-positions of the grid, which are well known. Plotting channel number vs. x or y, respectively, provides the calibration factor of the TPC channels in $\mathrm{mm\,ch^{-1}}$, see Figure 3.9(b).

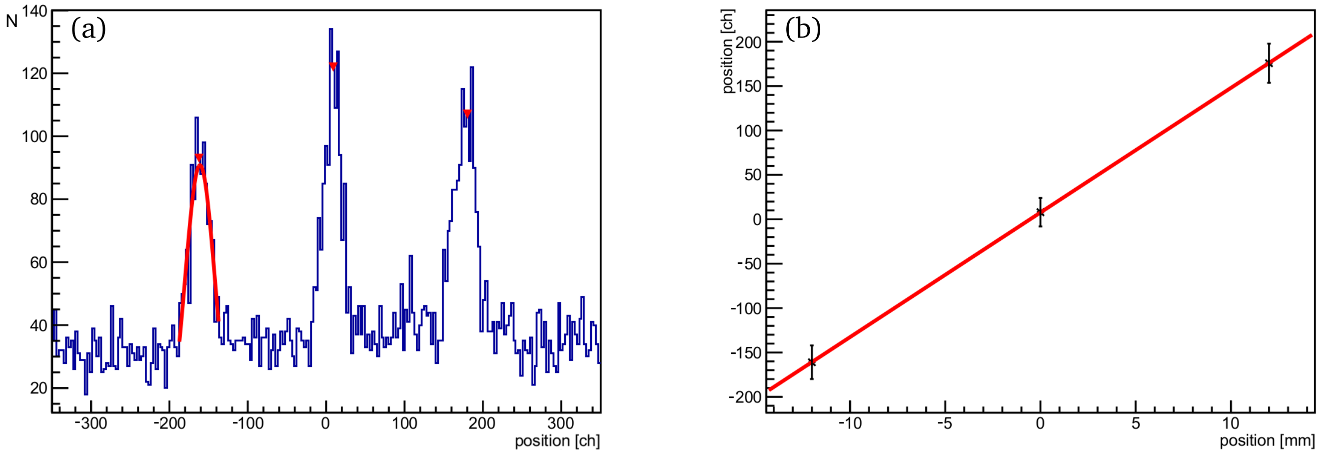

Figure 3.9.: In (a) the x-projection of the TPC counts of the calibration measurement from Figure 3.8 is shown. The channel numbers of the peaks were determined and in (b) plotted vs. the known distances of the mask. The slope delivered a calibration factor in $\mathrm{mm\,ch^{-1}}$. The calibration process of the multi-wire chamber was performed analog.

To reduce the number of bad signals due to back scattered ions or electrons or other influences inducing noise a control sum is used in the analysis. It can be calculated for each delay-line and anode as given by

$$t_{\mathrm{CS}} = t_l + t_r - 2t_{\mathrm{dr}}. \tag{3.18}$$

Commonly four control sums are calculated for the TPC. The first two are calculated with the first delay-line and the first and second anode, respectively. The other two are calculated using the second delay-line and the third and fourth anode, respectively. Before the measurement, each control sum was calibrated, using the data of the calibration measurements with the ^{12}C-beam. The x- and y-positions of a TPC event were only calculated if the control sum was lying within a certain range of the calibrated control sum. A control sum of the TPC at S3, recorded during a calibration measurement can be seen on the in Figure 4.5(a).

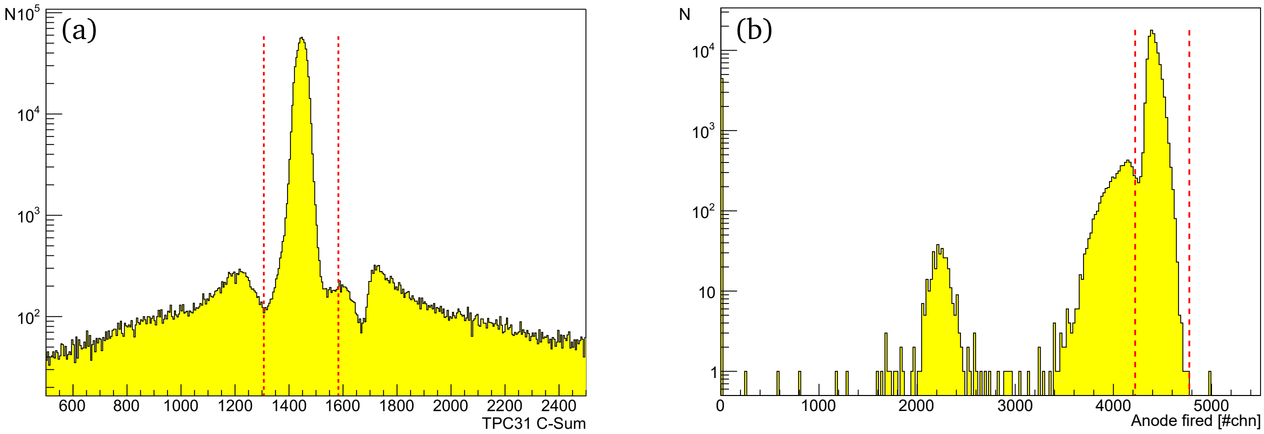

Figure 3.10.: Control sums of the TPC (a) and MWPC (b) at S3. The control sums were recorded during a calibration measurement, using a ^{12}C beam. The red dotted lines roughly outline the 3-σ environment around the Gaussian fitted peaks.

3.3.3 Multi-wire proportional chamber

A schematic sketch of a multi-wire layer can be seen in Figure 3.11. Two planes of wires, each rotated by 90° serve as anode. High voltage is applied to metalized Mylar foils, positioned in coplanar planes above and below the wires. These foils serve as cathode planes. Similar to the TPC readout, the wires were connected to delay-lines and the x-position calculated by using the time the signal needed to reach the

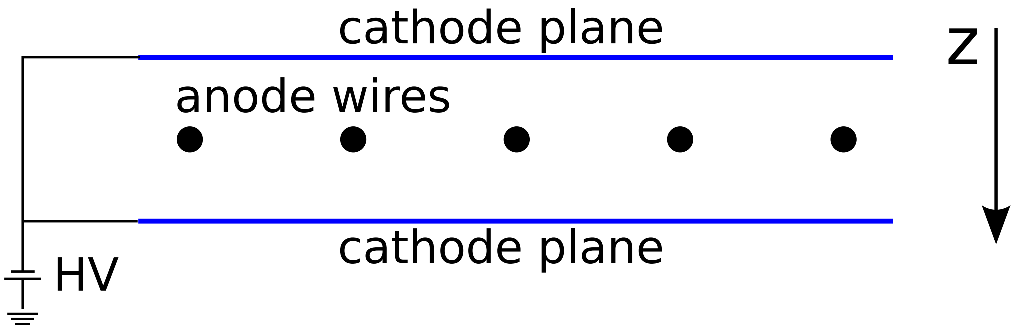

Figure 3.11.: Layout of a multi-wire chamber. Two planes of metalized Mylar foil serve as cathode for the wires.

left and right side of the line. Contrary to the TPC the y-position was not calculated using a drift time, but also from the wire position. A control sum was introduced by the sum of the left and right delay-line times.

$$t_{\mathrm{CS}} = t_l + t_r \tag{3.19}$$

As long as the sum of the delay-line signals was in the valid range of the control sum, the position of the traversing ion was calculated. A control sum of the MW at S3, recorded during a calibration measurement can be seen in Figure 4.5(b).

4.1 Position tracking

For the correct identification of the reaction residues, of their momentum distribution, and for assessing possible angular acceptance losses, the trajectory of the residues must be known. In particular, the positions at the focal planes of S2 and S3, $x_{tr}(S2)$ and $x_{tr}(S3)$ and the angles of the particles when crossing these planes provide the required information in combination with the known magnet settings. The values of $x_{tr}(S2)$ and $x_{tr}(S3)$ were determined by position tracking. An example of this procedure is shown in Figure 4.1 for $x_{tr}(S2)$. TPC 2.1 and TPC 2.2 were used to determine the (horizontal) x-position of the particles at two different positions in beam direction. With distances d_1 and d_2 between the focal plane and the TPCs, see Figure 4.1, the tracked position at the focal plane was obtained

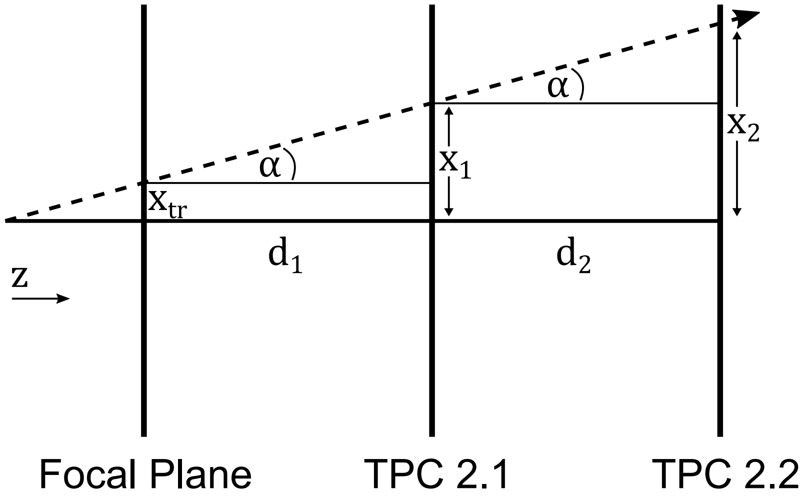

Figure 4.1.: Schematic representation for determining the x-position $x_{tr}(S2)$ of a particle in the focal plane of S2 using TPC 2.1 and 2.2. The x-position in the focal plane of S3 has been calculated similarly, using MW 3.1 and TPC 3.1.

$$x_{\mathrm{tr}}(S2) = x_1 - d_1 \cdot \tan(\alpha) = x_1 - \frac{d_1}{d_2}(x_2 - x_1)\,. \tag{4.1}$$

For S3 the detectors MW 3.1 and TPC 3.1 were used to calculate $x_{tr}(S3)$.

4.2 Particle Identification - Reaction Residues

For identification of the reaction residues two methods were applied in the data analysis. The comparison of results allows one to assess systematic uncertainties in the cross-section determination. In addition to plotting the charge of the ions versus the mass-over-charge ratio (AoQ or AoZ, if $Q = Z$), the charge versus the horizontal position at MW 3.1 (Z vs. x) was used, thereby reducing the number of required detectors.

4.2.1 Time of Flight, β and γ

The Time of Flight (ToF)

$$t_{\text{tof}} = t_{\text{S3}} - t_{\text{S2}}, \tag{4.2}$$

for particles transmitted from S2 to S3 determined from the scintillator signals SCI 2.1 and SCI 3.1 with the start signal given by SCI 3.1. To obtain the real ToF the measured one was corrected

$$t_{\text{tof}} = t_{\text{delay}} - t_{\text{tof, measured}}, \tag{4.3}$$

including a delay factor t_{delay} that was experimentally determined using a centered ^{12}C-beam without target. From the time of flight of the particles and their path length from S2 to S3, their velocity β in units of the speed of light and the Lorentz factor γ were calculated

$$\beta \cdot c = v = \frac{L_{\text{S2}\rightarrow\text{ S3}}}{\Delta t_{\text{S2}\rightarrow\text{ S3}}}, \tag{4.4}$$

$$\gamma = \frac{1}{\sqrt{1-\beta^2}}. \tag{4.5}$$

4.2.2 Identification by Z vs. AoZ

If the bending radius ρ and the velocity β of the particles in the dipole magnets are known, AoZ is calculated from

$$\frac{A}{Z} = \frac{B\rho}{\beta\gamma} \cdot C, \tag{4.6}$$

where C is a constant. The magnetic field strength B was measured by Hall probes for each FRS-setting during the experiment. The product $B\rho$ is also known as magnetic rigidity. For the transition of a particle from S2 to S3, $B\rho$ is obtained from

$$B\rho = B\rho_0 \cdot \left(1 + \frac{x_{\text{tr}}(S3) + M_{\text{S2}\,\rightarrow\,\text{S3}}\, x_{\text{tr}}(S2)}{D_{\text{S2}\,\rightarrow\,\text{S3}}}\right), \tag{4.7}$$

where $M_{\text{S2}\,\rightarrow\text{S3}}$ is the ion optical magnification factor between S2 and S3. It was determined using the ion optical simulation program GICOSY [41] and found to be $M_{\text{S2}\,\rightarrow\text{S3}} = 0.59$. The horizontal positions at the focal plane, $x_{tr}(S2)$ and $x_{tr}(S3)$, are determined with respect to the central beam. As further quantities enter $D_{S2\rightarrow S3}$, the dispersion between S2 and S3 and ρ_0=11.396 m, the effective bending radius of this dipole stage. The latter was found transmitting a ^{12}C-beam from S2 to S3 and set the magnetic rigidity of D3 to center the ion beam in both focal planes, so that

$$\rho_0 = \frac{(B\rho)_{\text{FRS-setting}}}{B_{\text{measured}}}. \tag{4.8}$$

The dispersion in an ion optical transfer system is defined as the change of beam position vs. a change in the relative momentum of the particle

$$D = \frac{x}{\Delta p/p}. \tag{4.9}$$

To measure the dispersion between S2 and S3 experimentally, the horizontal positions of the beam in the focal plane at S3 $x_{tr}(S3)$ of a ^{12}C-beam was measured for different momenta. A change of momentum was induced by scaling the magnetic rigidity of D3 in 1% steps from -5% to +5%. $x_{tr}(S3)$, see Figure 4.2. Finally, $D_{S2\rightarrow S3}$ was obtained by performing a linear fit of all $x_{tr}(S3)$.

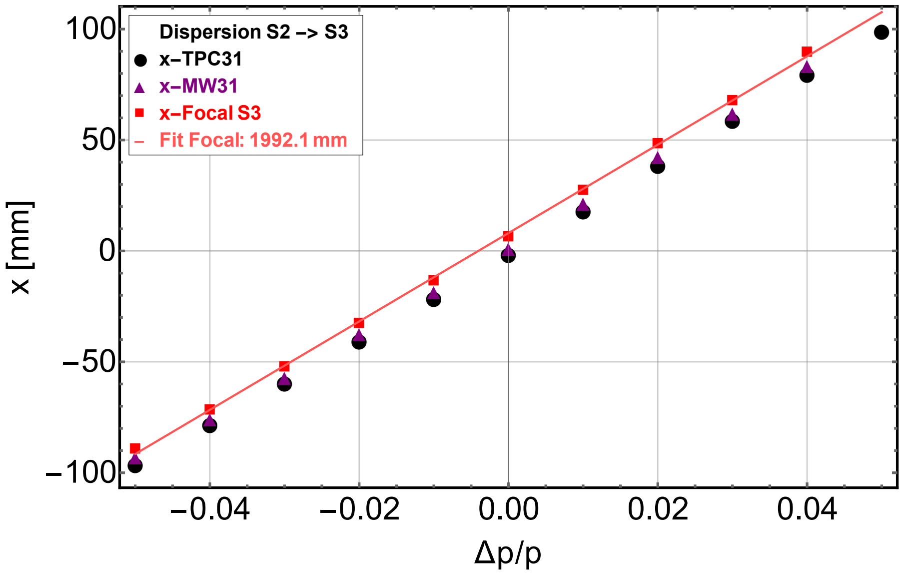

Figure 4.2.: Dispersion curve for the ion transmission between S2 and S3. It was obtained by scaling the Bρ values of D3 in 1% steps around the centered ^{12}C-beam setting and performing a linear fit of the different $x_{tr}(S3)$.

The charge of the particles vs. the A/Z ratio is plotted in Figure 4.3. The shown distributions resulted from delivering a ^{11}C-beam to S2, impinging it on the reaction target and setting dipole stage D3 to transmit ^{11}C. In the data analysis ^{11}C was selected by drawing a graphical cut in the plot that was applied as logical constraint to other identification plots. Events whose position in the Z vs. AoZ plot had

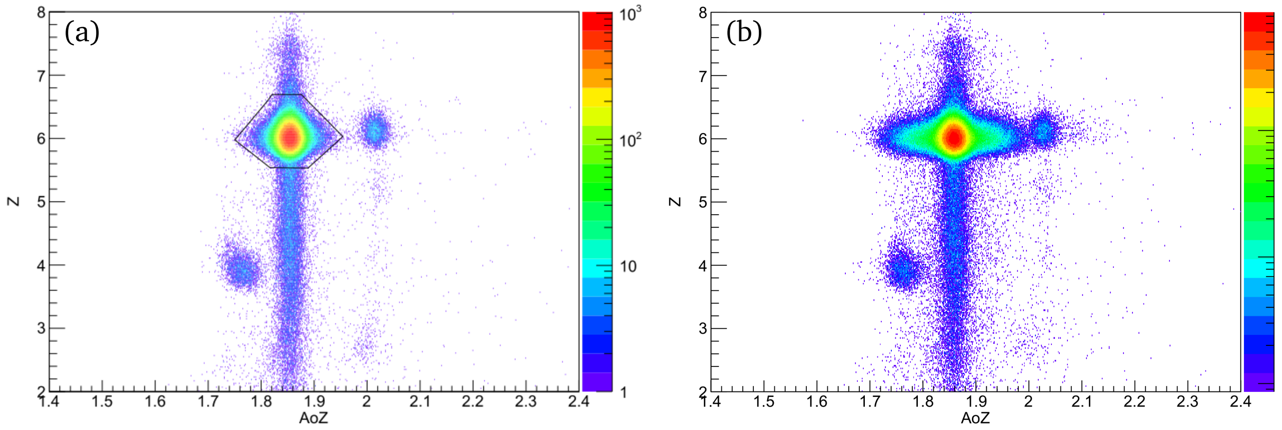

Figure 4.3.: Two dimensional histograms displaying the Z vs. A/Z distribution at S3. ^{11}C is selected by performing a graphical cut on the distribution. In (a) the x-position to determine $B\rho$ was directly taken from TPC 3.1. In (b) the calculated x-position at the focal plane x_{tr}(S3) was used.

not been within the graphical selection were excluded. Figure 4.3(b) was obtained from the calculated horizontal position in the focal plane of S3, Figure 4.3(a) from the horizontal position as given by the TPC 3.1 without any corrections or back-tracing. In the case of this experiment, the calculation of the x position in the focal plane led to a less resolved identification plot compared to directly using the x position of the TPC. It is note fully clear why the identification plot using the focal plane to determine A/Z had a lower resolution than the plot using the TPC. In the data analysis it was observed that the multiwire chamber MW 3.1 was not working properly. Additionally, the focal point was determined by a reverse calculation using two detectors, which conserved the correct horizontal position but blurred out the x-distribution. In the data analysis all identification plots using the A/Z ratio calculated with the x-TPC position provided a better resolution and was therefore used for determining the reaction probabilities.

4.2.3 Identification by ToF and Z vs. x

The identification by A/Z involves good detector signals from all four position-sensitive detectors, or at least all three TPCs and the plastic scintillators. To reduce efficiency-issues and get insight into statistical uncertainties in the residue identification, the residue charge Z and x position at MW 3.1 (closest position detector to the focal plane at S3) were used to identify the residues. In Figure 4.4(a) the Z vs. x distribution of the particles at S3 is shown. The particles of interest are framed by a graphical cut, the black line. A cross check to see if this cut selected the correct isotopes was performed by plotting Z vs. A/Z after applying this graphical cut as logical constraint. This plot is shown in Figure 4.4(b). The consistency check revealed that still some ^{12}C isotopes contaminated the ion beam selection. These were probably leftovers from the primary beam hitting the production target in front of the FRS and having the right energy to be transmitted from the target to S2 and further to S3. At S2 the only property measured for identification had been the charge. Hence, the data analysis at S2 did not allow a discrimination

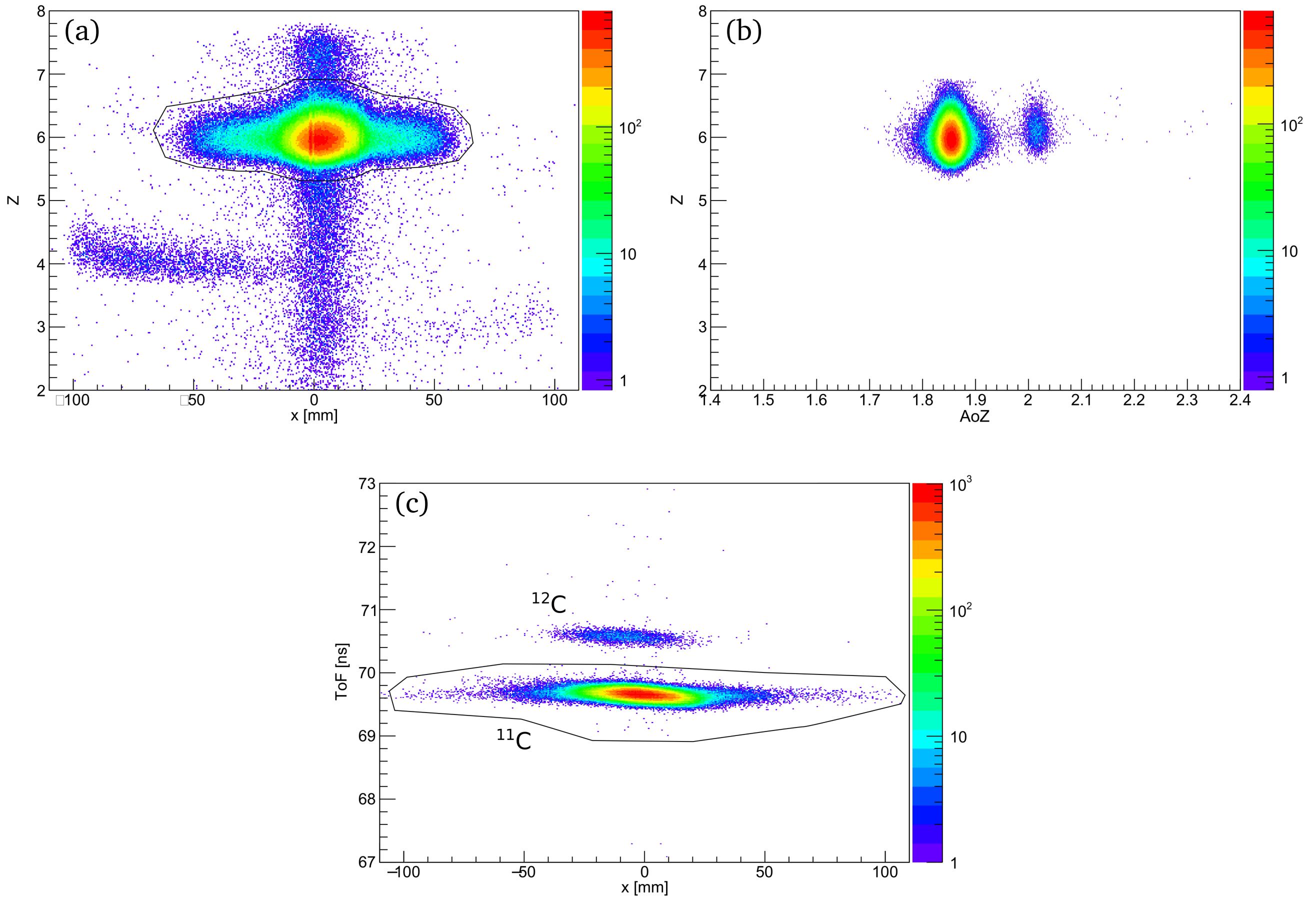

Figure 4.4.: In (a) ^{11}C was selected by performing a cut on the Z vs. $x_{\mathrm{MW3.1}}$ position. A Z vs. A/Z identification plot, provided by using the TPC, is shown in (b) after applying the logical constraint from the selection in (a). Leftovers of the primary ^{12}C-beam are visible. In (c) the cut from a was applied onto a ToF vs. $\mathrm{x}_{\mathrm{MW3.1}}$ distribution. By adding the ToF information the ^{12}C-ions were successfully removed from the selection.

between isotopes. Thus, the minimum number of detectors for the identification process had to be increased by adding the time of flight of the particles. In Figure 4.4(c) the ToF vs. x distribution for the same data as in Figure 4.4(b) is shown. After additionally excluding the slower satellite, a repetition of the cross check confirmed that the ^{12}C-ions were removed and thereby, identifying the satellite as ^{12}C. Hence, particle identification by Z and x alone was not possible, but required at least the time of flight information of the particles.

4.2.4 Identification method: AoZ vs. MW

Both methods described in the last two sections allowed the identification of the isotopes. Hence, the cross sections of all reactions were calculated twice, using each method independently to identify the particles. However, significant fluctuations in the sensitivities of the two delay lines in MW 3.1 were observed. In addition, graphical cuts in the two-dimensional histograms of Z vs. x-MW3.1 for the $^9\mathrm{Be}\left(^9\mathrm{C},^8\mathrm{B}\right)\mathrm{x}$ reaction, see Figure 4.5, proved to be error-prone because the residues could not be unambiguously separated. Including the time of flight information did not improve the resolution of the identification plot. Hence, the AoZ identification method was preferred. It allowed a cleaner identification in the two-dimensional histogram and more importantly did show considerably less efficiency fluctuations. The AoZ-identification plots of each reaction residue are presented in chapter 4.3.

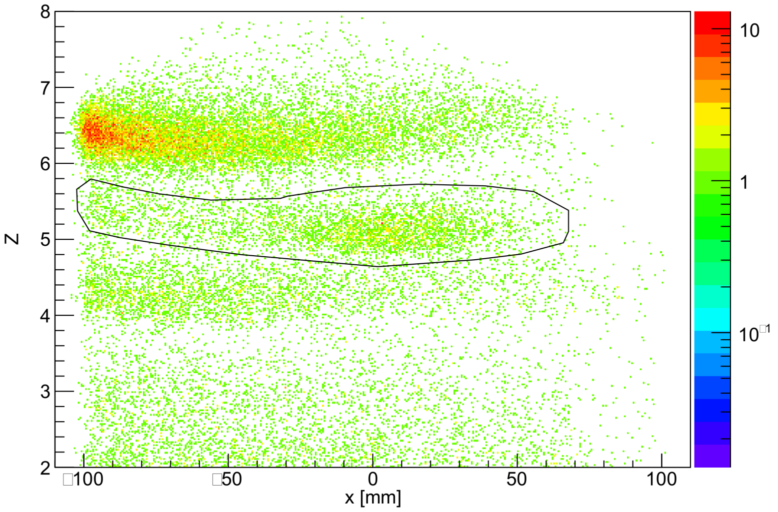

Figure 4.5.: Residue identification from Z vs. x (MW 3.1) for selecting ^{8}B from the ^{9}Be$\left(^{9}\text{C},{}^{8}\text{B}\right)$x reaction. Larger systematic uncertainties arise from placing the boundaries of a graphical cut.

4.3 Determination of Reaction Probabilities

The reaction cross section σ is determined by three factors: The number of incoming particles n_p, the number of produced ejectiles n_e and the number of atoms per unit area in the reaction target n_t

$$\sigma = \frac{n_e}{n_p \cdot n_t} = \frac{p_r}{n_t}, \tag{4.10}$$

with the reaction probability p_r. For a precise determination of n_e, reactions in material other than the target, acceptance losses and detector efficiency need to be known or to be determined experimentally.

4.3.1 Beam normalization

The reaction probabilities were determined after normalization to the number of carbon isotopes measured at S2 in front of the target. The incident secondary beam was solely identified by its charge. In addition a cut on the x distribution was performed, to make sure all ions passed the reaction target. The Z vs. x distribution in front of the reaction target is shown in Figure 4.6. All residues were normalized to the incident particles lying within the constraints of the black box in the distribution. The selection plot of ions at S2 was the same for all carbon isotopes, except for some minor adjustments of the central Z-value due to some shifts of the scintillator output.

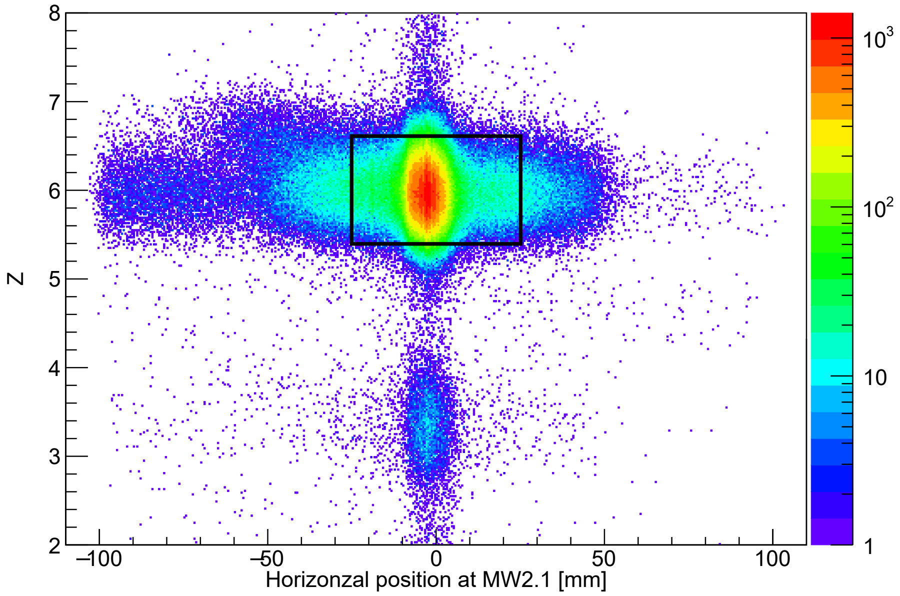

Figure 4.6.: Two dimensional histogram displaying Z vs. x of the incoming carbon beam at S2. All identification plots were normalized to the incoming beam, restricted in Z and x of the black box.

4.3.2 Final selection of reaction residues

After applying the S2-normalization and the correct trigger-ID for events at S3 as constraint on all Z vs. A/Z identification plots, the reaction residues of all investigated reactions were identified in a two-dimensional Z vs. A/Z representation as discussed above. The calculation of the corrected reaction probability (see Equation (4.12)) required to estimate the number of surviving projectiles and the number of residues with reaction target in and out, each. An example of these four identification histograms of one reaction is shown in appendix A.2. Shown below in Figure 4.7 - 4.10 are the identification plots of each reaction residue with reaction target in. The number of particles within a graphical cut, and consequently the cross section, depends on the shape of it. While the individual isotopes were clearly resolved, a small uncertainty still remained. Each cut was drawn by human estimation and no algorithm. To estimate this uncertainty, a second, more strictly confining cut was drawn. Both selections, the normal and the strict one, were used to calculate the cross section and thus, study the influence of the choice of the cut on the systematic uncertainty of the cross section.

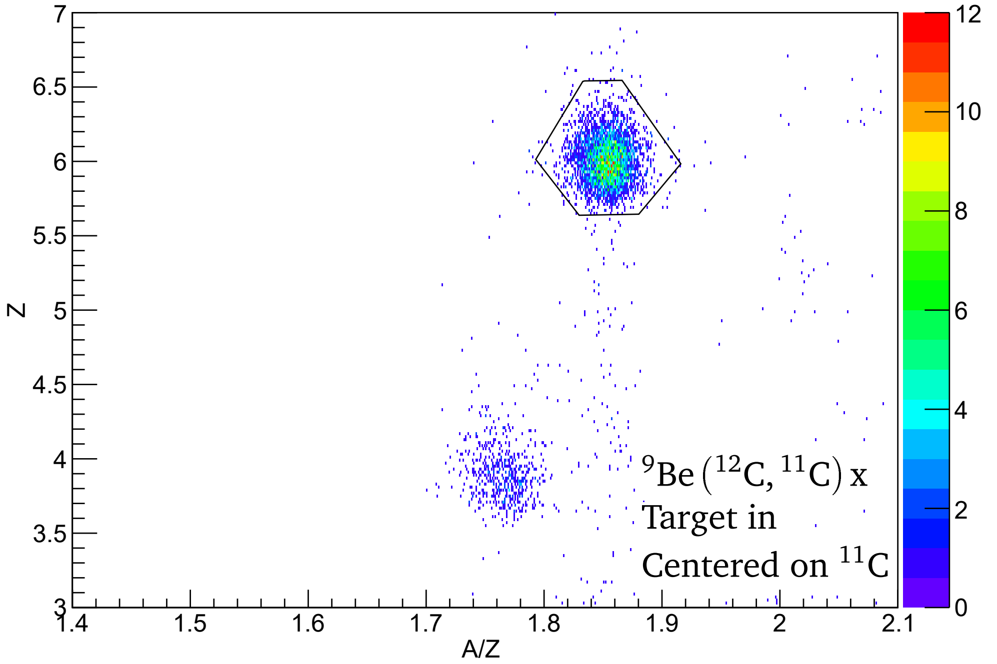

Figure 4.7.: Particle identification histogram showing the Z vs. AoZ distribution at S3 for the reaction ^{9}Be (^{12}C, ^{11}C) x with secondary target in. The magnetic field setting of dipole D3 was centered on the ^{11}C reaction residues. The polygon indicates the graphical cut selecting ^{11}C

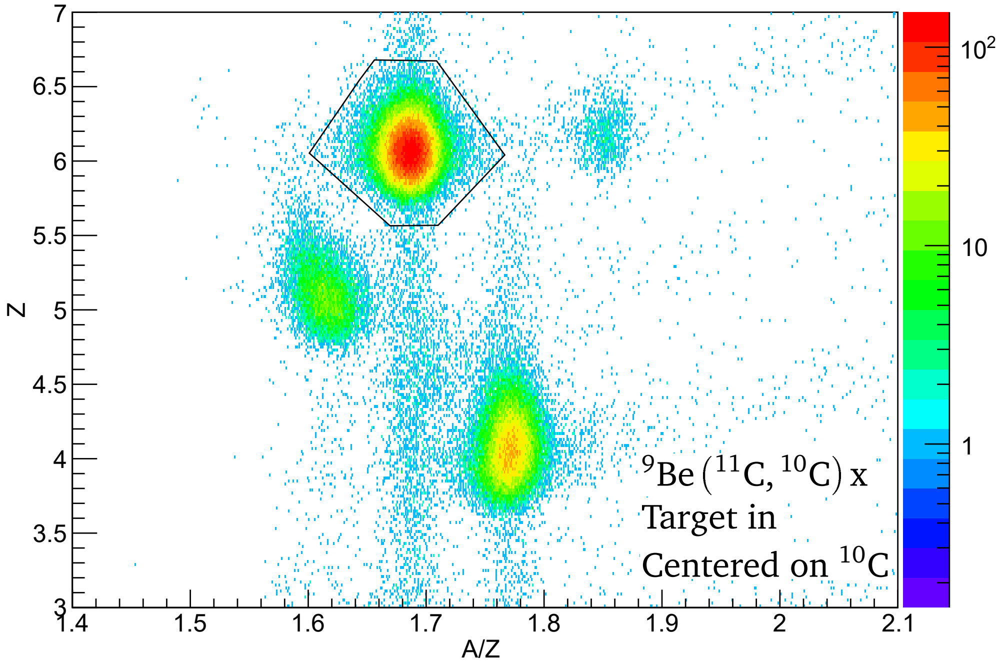

Figure 4.8.: Particle identification histogram showing the Z vs. AoZ distribution at S3 for the reaction ^{9}Be (^{11}C, ^{10}C) x with secondary target in. The magnetic field setting of dipole D3 was centered on the ^{10}C reaction residues. The polygon indicates the graphical cut selecting ^{10}C

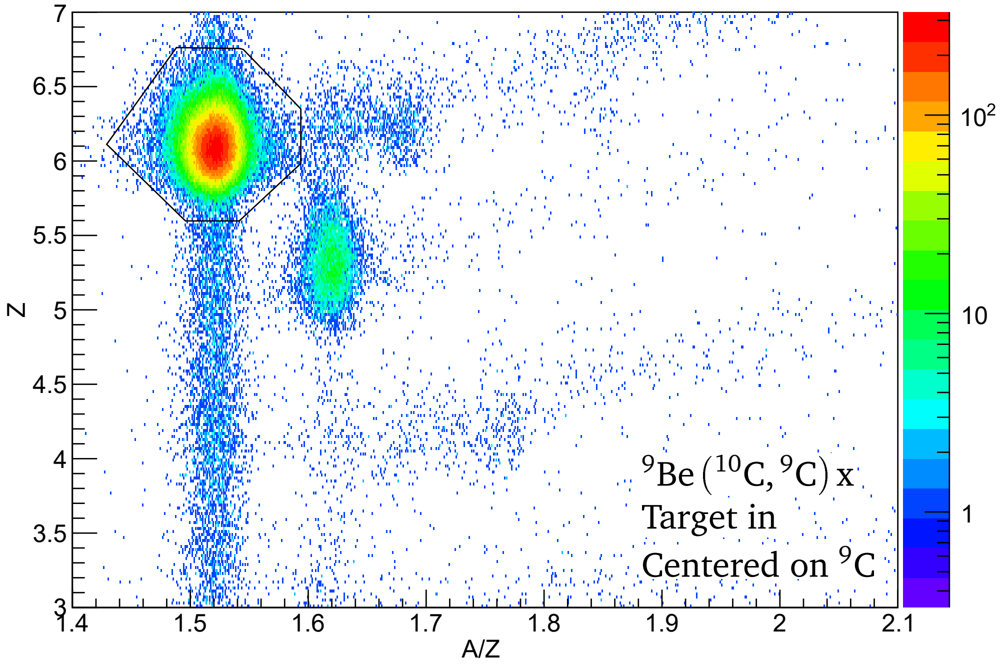

Figure 4.9.: Particle identification histogram showing the Z vs. AoZ distribution at S3 for the reaction ^{9}Be (^{10}C, ^{9}C) x with secondary target in. The magnetic field setting of dipole D3 was centered on the ^{9}C reaction residues. The polygon indicates the graphical cut selecting ^{9}C

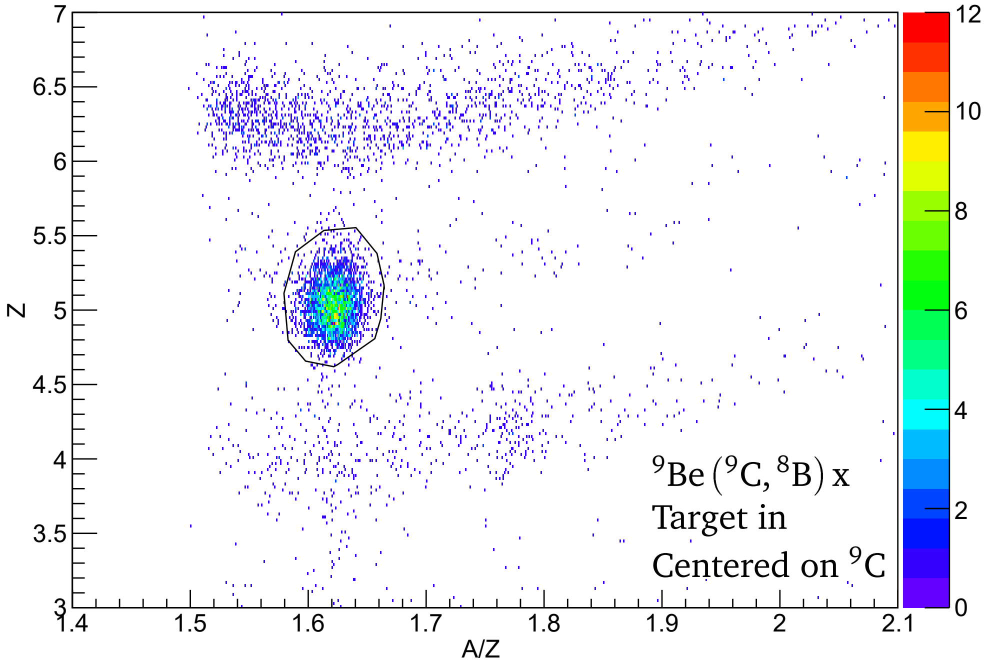

Figure 4.10.: Particle identification histogram showing the Z vs. AoZ distribution at S3 for the reaction ^{9}Be (^{9}C, ^{8}B) x with secondary target in. The magnetic field setting of dipole D3 was centered on the ^{8}B reaction residues. The polygon indicates the graphical cut selecting ^{8}B

4.3.3 Reaction probability

Equation (4.10) neglects several factors: The reaction residues measured at S3 have not necessarily been produced in the reaction target. In any matter along the beam line, for example detectors or air, knockout reactions have occured, contributing to the total number of measured reaction residues. The same holds for the reaction residues already produced in the secondary reaction target at S2. A fraction of them undergo a further reaction before reaching S3. Some projectiles measured at S2 in front of the reaction target have been absorbed in the reaction target or before they even reached the target. The corrected reaction probability, accounting for those effects, is calculated from

$$p_{\mathrm{cor}} = \frac{p_{\mathrm{t}}(\mathrm{reaction})}{p_{\mathrm{t}}(\mathrm{survival})} - \frac{p_0(\mathrm{reaction})}{p_0(\mathrm{survival})}. \tag{4.11}$$

The different p_i were calculated with Equation (4.10). In Equation (4.11) p_t refers to probabilities measured with the reaction target in the beam line, p_0 refers to probabilities measured without reaction target, to determine the background due to reactions in other matter than the reaction target. In both cases the numerators refer to the probability of a reaction residue, produced in a knockout reaction. The denominators refer to the probability of the projectiles, measured at S2 in front of the reaction target, to survive to S3. For the example of one-neutron knockout of ^{11}C Equation (4.11) takes the form

$$p_{\mathrm{cor}} = \frac{p_{\mathrm{t}}(^{11}\mathrm{C} \rightarrow {}^{10}\mathrm{C})}{p_{\mathrm{t}}(^{11}\mathrm{C} \rightarrow {}^{11}\mathrm{C})} - \frac{p_0(^{11}\mathrm{C} \rightarrow {}^{10}\mathrm{C})}{p_0(^{11}\mathrm{C} \rightarrow {}^{10}\mathrm{C})}. \tag{4.12}$$

Hence, for the correct calculation of the corrected reaction probability, four measurements were necessary for each reaction.

While Equation (4.11) determines the reaction probability incorporating the most significant corrections,further corrections are needed. The determination of the final reaction probability

$$p_{\mathrm{f,\,cor}} = E \cdot T_{\mathrm{cor}} \cdot \left(K \cdot \frac{p_{\mathrm{t}}(\mathrm{reaction})}{p_{\mathrm{t}}(\mathrm{survival})} - \frac{p_0(\mathrm{reaction})}{p_0(\mathrm{survival})} \right) \tag{4.13}$$

contains the correction factor E, treating different detection efficiencies of the projectiles and ejectiles in the detectors involved in the particle identification. If the efficiencies for the detection of ejectiles - for example ^{10}C in Equation (4.12)) and projectiles ^{11}C in Equation (4.12)) - are not the same, $E \neq 1$. The factor K takes the mass-dependent absorption in matter into account. The total interaction cross section of the particles and therefore absorption in matter depends on A. This effect has a non-negligible contribution only for the first term in Equation (4.12). Finally, T_{cor} considers transmission losses between S2 and S3, due to the acceptance of the third stage of the FRS.

The detection system has a specific detection efficiency, depending on the investigated nuclide. Hence, the number of counts measured at S3 needs to be corrected for detection efficiency. For the example of Equation (4.12) the factor E reads

$$E = \frac{\epsilon(^{11}\mathrm{C})}{\epsilon(^{10}\mathrm{C})}. \tag{4.14}$$

The analysis showed no significant differences in detection efficiency for different mass numbers A of the selected carbon isotopes. This means $E = 1$ for all investigated neutron-knockout reactions. The only significant difference was found for the proton knockout from ^{9}C

$$E = \frac{\epsilon(\mathrm{C})}{\epsilon(\mathrm{B})} = \frac{\epsilon_{\mathrm{SCI3.1}}(\mathrm{C}) \cdot \epsilon_{\mathrm{SCI3.2}}(\mathrm{C}) \cdot \epsilon_{\mathrm{TPC3.1}}(\mathrm{C})}{\epsilon_{\mathrm{SCI3.1}}(\mathrm{B}) \cdot \epsilon_{\mathrm{SCI3.2}}(\mathrm{B}) \cdot \epsilon_{\mathrm{TPC3.1}}(\mathrm{B})}. \tag{4.15}$$

None of the involved detectors had a detection efficiency of 100% . Thus, the efficiency of one detector was calculated by normalizing the number of observed events N to another detector.

$$\epsilon_{\mathrm{SCI3.1}} = \frac{N_{\mathrm{SCI3.1} \,\wedge\, \mathrm{SCI3.2}}}{N_{\mathrm{SCI3.2}}} \tag{4.16}$$

$$\epsilon_{\mathrm{SCI3.2}} = \frac{N_{\mathrm{SCI3.1} \,\wedge\, \mathrm{SCI3.2}}}{N_{\mathrm{SCI3.1}}} \tag{4.17}$$

$$\epsilon_{\mathrm{TPC3.1}} = \frac{N_{\mathrm{TPC3.1} \,\wedge\, \mathrm{MW3.1}}}{N_{\mathrm{MW3.1}}} \tag{4.18}$$

By this method the relative efficiency of each detector was determined, independent from the intrinsic efficiency of the detector. All constraints applied to the detector data during particle identification were connected by a logical **AND**. For calculating the corresponding efficiencies of one detector no coincidence was required (logical **OR**) while all others remained in **AND**. The final efficiencies found by this method and the corresponding correction factors E are shown in Table 4.1.

Element	ϵ	E
C	$99.2 \pm 0.2\%$	1
B	$95.4 \pm 1.0\%$	1.040 ± 0.011

Table 4.1.: Detection efficiencies and correction factors for the residue of the corresponding element.

Mass-dependent absorption differences in target

The particles measured for the determination of the survival probability and the particles measured for the reaction probability experience a slightly different absorption in the target matter, due to different mass numbers or charge. While this holds true both terms with and without target, the magnitude of this effect for target-out runs is negligible. The total interaction cross section of the ejectiles σ_e and projectiles σ_p in the reaction target were calculated to estimate the ratio of absorption and thus the correction factor

$$K = \frac{\text{Absorption of projectiles in sec. target}}{\text{Absorption of ejectiles in sec. target}} = \frac{e^{-\sigma_{\mathrm{p}} d_t/2}}{e^{-\sigma_{\mathrm{e}} d_t/2}}, \tag{4.19}$$

with d_t being the thickness of the reaction target. For the calculation of the correction factor, the probability of a neutron knockout was assumed to be homogeneous throughout the target. Hence, the average difference in target thickness, which the incoming projectiles and the reaction residues effectively see, amounts to $d_t/2$. The total reaction cross section σ_R, to estimate the absorption in the reaction target, was calculated using the Kox formula [42]

$$\sigma_R = \pi R^2 \left[1 - B_C/E_{\mathrm{CM}}\right], \tag{4.20}$$

where B_C is the height of the coulomb barrier of the projectile-target system and given by

$$B_C = Z_t Z_p e^2 \cdot \left(r_C \left(A_t^{1/3} + A_t^{1/3}\right)\right)^{-1}. \tag{4.21}$$

In Equation (4.21), Z_p and Z_t are the atomic numbers of the projectile and target nuclei, A_t and A_p are the corresponding mass numbers, e is the elementary charge and $r_C = 1.3\,\mathrm{fm}$ the nuclear radius constant. Due to the high kinetic energy of the carbon beam the second term in the brackets of Equation (4.20) is of the order of 10^{-3} for all investigated reactions. Thus, the contribution of Coulomb repulsion is negligible. The only remaining significant term in Equation (4.20) to calculate σ_R is the interaction radius R. It consists of a volume and a surface term

$$R = R_{\mathrm{vol}} + R_{\mathrm{surf}}. \tag{4.22}$$

The volume term is given by

$$R_{\mathrm{vol}} = r_0 \left(A_t^{1/3} + A_p^{1/3}\right), \tag{4.23}$$

and the term regarding the nuclear surface contribution by

$$R_{\mathrm{surf}} = r_0 \left[a \frac{A_t^{1/3} A_p^{1/3}}{A_t^{1/3} + A_p^{1/3}} - c \right] + D. \tag{4.24}$$

The parameters $r_0 = 1.1\,\text{fm}$, $a = 1.85$ and $c = 1.9$ were found by fitting experimental data [42,43]. The last term D describes the neutron excess [42] and is given by

$$D = \frac{5\,(A_t - Z_t)\,Z_p}{A_p A_t}. \tag{4.25}$$

The final correction factors of each reaction, describing the ratios of the absorption of projectile and ejectile in the reaction target, are shown in Table 4.2. Even in case of the beam transmission with reaction target in the beam line, as described by the first term of Equation (4.13), the total impact on the reaction probability is rather small. Uncertainties of the K-values were $< 0.1\%$ in all cases and did not have any significant impact on the total uncertainty of the knockout reaction cross sections.

Reaction	$^9\text{Be}\,(^{12}\text{C}, ^{11}\text{C})\,\text{x}$	$^9\text{Be}\,(^{11}\text{C}, ^{10}\text{C})\,\text{x}$	$^9\text{Be}\,(^{10}\text{C}, ^{9}\text{C})\,\text{x}$	$^9\text{Be}\,(^{9}\text{C}, ^{8}\text{B})\,\text{x}$
K	99.49%	99.47%	99.44%	99.41%

Table 4.2.: Absorption correction factors K of the investigated reactions.

Transmission losses S2→S3

The transmission of particles from S2 to S3 can be limited due to the ion optical acceptance of the third dipole stage of the FRS. The acceptance of the device describes the limitation in transmission due to relative momentum distribution, angle, and position of the particle's trajectory. If the particle's angle or position or a combination of both is too large, the particle will get cut off while traversing the dipole magnet. To quantify the losses due to the finite acceptance, MOCADI [44] simulations were performed. Position and angle of the particles at the end of S2 were set to match the properties measured by the TPCs. The magnetic rigidity of the dipole in the simulation was set to match the product of the magnetic field strength, measured by the hall probes, and ρ_0. Two-dimensional x-angle vs. x-position distributions at the end of S2 are shown in Figure 4.11 for the example of ^{9}C ions after one-neutron knockout from ^{10}C. In Figure 4.11(a), no constraints were applied. In Figure 4.11(c) only particles not being transmitted to S3 are shown. Especially when the ions had large positive or large negative angles at the end of S3 they were not transmitted through S3. Some losses are also visible for ions with large distances from the beam-line center. To properly estimate the correction value T_{cor} for the performed measurements, the transmission of the reaction residues and the transmission of the surviving projectiles were simulated, each. The factor T_{cor} was calculated in a similar way like the correction value for the detection efficiency, given by the ratio of the transmission value of the surviving projectiles divided by the transmission value of the reaction residues.

$$T_{\text{cor}} = \frac{\tau\,(\text{survival})}{\tau\,(\text{reaction})} \tag{4.26}$$

How well the simulations really represent the actual beam could not be answered with certainty. As an example the x-angle vs. x-position distribution at the end of S2 corresponding to the measured

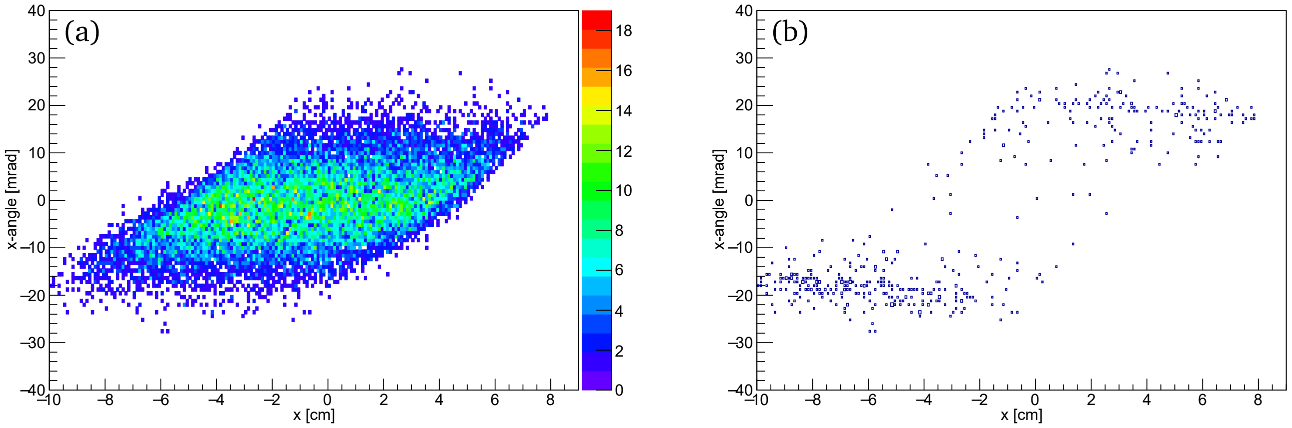

Figure 4.11.: MOCADI simulation of the reaction $^{9}\mathrm{Be}\left(^{10}\mathrm{C},^{9}\mathrm{C}\right)\mathrm{x}$ with reaction target in. The x-angle vs. x-position of ^{9}C at the end of S2 is presented without any constraints (a). When gating on particles not transmitted to S3, distribution (b) results. Mainly ions with large angles were not transmitted to S3. In the case of this example the losses amount to 2.53%. The losses of the other reactions are states further below in Table 4.3-4.5.

data of the $^{9}\mathrm{Be}\left(^{10}\mathrm{C},^{9}\mathrm{C}\right)\mathrm{x}$ reaction is shown in Figure 4.12. The distribution in Figure 4.12(b) was obtained by demanding the ^{9}C ions to be transmitted to S3 and is comparable to the simulation in Figure 4.11(b). A comparison of the measured distribution in Figure 4.12(a) with the simulated distribution in Figure 4.11(a) was not possible. Identification of reaction residues was only possible with detectors positioned at S3. Gating on ^{9}C in the measured distribution would again demand a logical **AND** of the particles being registered at S3 and thereby reproduce the same distribution as in (b). Thus, the distribution shown is a mixture of all particles still present at the end of S2 before passing dipole D3.

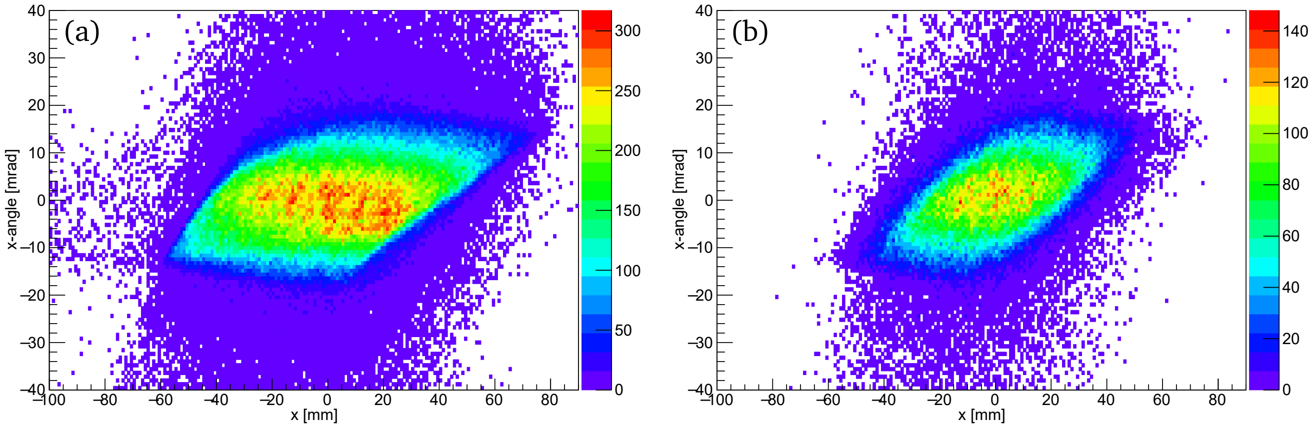

Figure 4.12.: Measured distribution of x-angle vs. x-position for the reaction $^{9}\mathrm{Be}\left(^{10}\mathrm{C},^{9}\mathrm{C}\right)\mathrm{x}$. In (a) the distribution of ^{9}C-ions at the end of S2 is shown under the constraint that they reached S3. The same distribution without any constraint is shown in (b). Gating on ^{9}C alone was not possible, as only ions that reached S3 were identified.

To probe the robustness of the simulation regarding slight changes of the FRS-settings and beam characteristics, multiple combinations of beam and magnet settings were simulated. Should the transmission value not show any major changes by changing some of the input parameters of the simulation, it would lead to the confirmation of the simulated transmission value within a small uncertainty. On the other hand, if small changes of the input parameters lead to larger changes in the transmission value a larger uncertainty had to be taken into account. Without explicitly changing the beam properties in the simulation file, MOCADI works with a straight and centered beam as input. Simulations were performed using the centered beam without adjustment, and the beam with adjustments, to match the experimentally measured properties of the beam at S2 behind the secondary reaction target. For each of the two cases, three settings of the magnetic rigidity were simulated.

The first setting was obtained as described above, by the product $B\rho_0$, using the magnetic field, given by the Hall probes and the ρ_0 determined with help of the calibration measurements. The second setting used slightly lower $\rho_0 = 11.345\,\mathrm{m}$ to calculate the magnetic rigidity. This ρ_0 was determined by analyzing a later measurement with a nearly centered ^{10}C beam. Regarding the particle identification, a small shift of ρ_0 only led to an offset in the identification plots x-axis and did not have any influence on the identification plot or the reaction probability. In the case of the optimal kinetic energy of the ions for highest transmission values through the dipole, it led to a shift of -15 MeV/nucl. compared to the first setting. The third setting was given by matching the magnetic rigidity of D3, to achieve highest possible transmission of reaction residues, having an average kinetic energy at the end of S2, as determined by the MOCADI simulation. This led to a shift of the optimal kinetic energy, transmitted through the dipole, of about -30 MeV/nucl., compared to the first setting. These three settings marked the largest possible range at which the particle energies could have been during the experiment. In summary, the relative energy shift of all three settings was $\lesssim 10^{-3}$ compared to the beam energy of above 1600 MeV/nucl. Further sub-settings of different simulation parameters were given by using the non altered, centered beam parameters and beam parameters adjusted to the actual measured beam properties for each of the three settings of magnetic rigidity. The results of the six different simulations are shown in Table 4.3-4.5. No data are shown for the one-neutron knockout of ^{12}C. In all six cases the transmission of the surviving projectiles and reaction residues were 100%due to the good (primary) beam quality. In the case of the other reactions the relative changes of transmission due to the different magnetic rigidity settings were in the order of a few $10^{-2}\,\%$. A larger impact on the transmission was found when changing the input parameters of the beam properties.

The final correction factor T_f was given by the setting adjusted to the measured beam trajectory and the magnetic rigidity set to match $\rho_0 \cdot B_{\mathrm{Hall}}$ $(x_{\mathrm{S2}}, \alpha_{\mathrm{S2}}, E_1)$, as those properties were directly obtained from the experimental measurements. The uncertainty of the correction factors was given by the standard

(^{11}C,10C)	x_0, α_0			$x_{\mathrm{S2}}, \alpha_{\mathrm{S2}}$				
	E_1	E_2	E_3	x_{S2}[mm]	α_{S2}[mrad]	E_1	E_2	E_3
τ(survival)	100%	100%	100%	1.88	3.07	99.92%	99.92%	99.91%
τ(reaction)	99.49%	99.49%	99.48%	2.84	2.9	99.05%	99.04%	99.04%
T_{cor}	1.0052	1.0051	1.0052			1.0088	1.0089	1.0088

Table 4.3.: Transmission values and correction factor of the reaction probability for different settings of the beam trajectory and magnetic rigidity for the reaction $^{9}\mathrm{Be}\left(^{11}\mathrm{C}, ^{10}\mathrm{C}\right)\mathrm{x}$. The simulation was performed with and without adjusting the angle α_0, α_{S2} and position x_0, x_{S2} to their measured properties at S2. Each setting was simulated at three energy settings for the transmission through the third stage of the FRS.

(^{10}C,9C)	x_0, α_0			x_{S2}, α_{S2}				
	E_1	E_2	E_3	x_{S2}[mm]	α_{S2}[mrad]	E_1	E_2	E_3
τ(survival)	99.96%	99.96%	99.96%	7.98	4.19	98.46%	98.44%	98.43%
τ(reaction)	97.59%	97.64%	97.54%	4.53	0.95	97.59%	97.47%	97.42%
T_{cor}	1.0242	1.0238	1.0248			1.0089	1.0099	1.0104

Table 4.4.: Same as Table 4.3 for the reaction ^{9}Be $\left(^{10}\text{C}, ^{9}\text{C}\right)$ x

(^{9}C,8B)	x_0, α_0			x_{S2}, α_{S2}				
	E_1	E_2	E_3	x_{S2}[mm]	α_{S2}[mrad]	E_1	E_2	E_3
τ(survival)	99.79%	99.78%	99.77%	0.2	2.67	99.16%	99.16%	99.12%
τ(reaction)	94.22%	94.68%	94.69%	0.4	2.51	93.54%	93.62%	93.45%
T_{cor}	1.0591	1.0539	1.0536			1.0601	1.0592	1.0607

Table 4.5.: Same as Table 4.3 for the reaction ^{9}Be $\left(^{9}\text{C}, ^{8}\text{B}\right)$ x

deviation of all correction factors with respect to this T_f, instead of to the average value. For the one-neutron knockout from ^{10}C, shown in Table 4.4, the transmission value of the reaction residue was found to be very robust against changes of magnetic rigidity or beam properties. However, the transmission value of the surviving projectiles was very sensitive to changes of the beam angle. Furthermore the angle of the projectile beam was larger than the variety of magnet settings and slits in the FRS beam line should geometrically allow. It was not possible to entirely identify source of this large angle. The influence on the transmission can be seen in Figure 4.13. The x-angle vs x-position distribution at S2 of the not transmitted ^{10}C ions is shown when using position and angle of the ions as given by the TPCs at S2. Particles of large negative x-angles are cut in the case of the adjusted beam, as can be seen in Figure 4.13(a). Figure 4.13(b) was obtained by keeping the measured x-position, but setting a 0°-angle

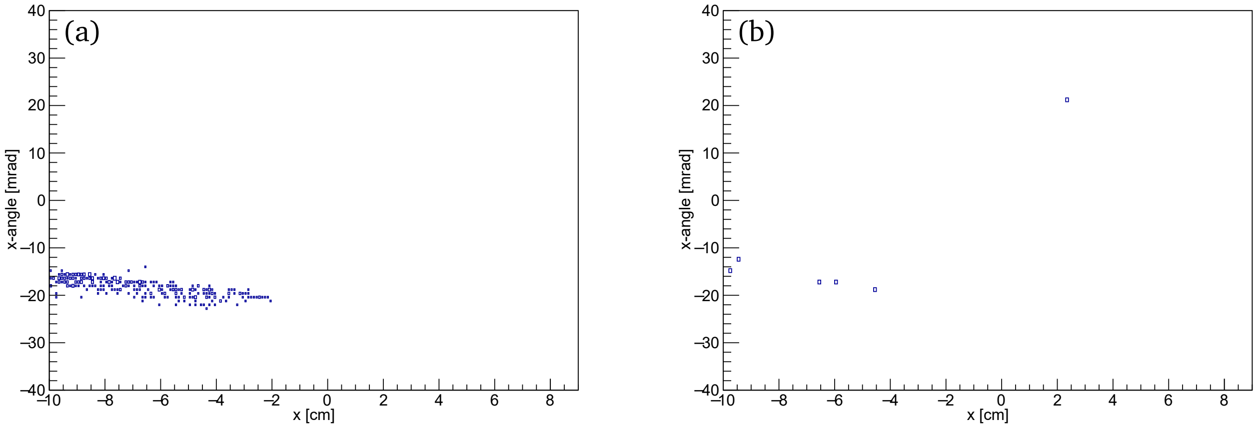

Figure 4.13.: Simulated distribution of ^{9}C-reaction-residues at the end of S2, with beam parameters as experimentally measured (a) and with the beam-angle set to 0° (b). In (a) a significant amount of ions was not transmitted to S3. In (b) some ions at large positive and large negative angles were still not transmitted, indicating that the transmission of the ^{9}C-residues was performed at the limit of the angular acceptance of the third FRS stage.

of the ions as input parameter. Nearly 100% of the particles were transmitted. A further simulation, still keeping the x-position the same but setting a negative beam angle of same magnitude as the measured (positive) angle, showed the same picture as Figure 4.13(a), but mirrored, showing the lost particles at the positive end of the x-angle. This indicated that the surviving ^{10}C projectiles after traversing S2 were barely fitting into the acceptance of D3. The simulated transmission was very sensitive to changes of the beam angle. Furthermore it was not fully clear how such a large angle was observed in the first place or if it just was a measurement error. Therefore, another approach was taken to obtain the transmission correction factor: T_{cor} was calculated by taking the mean value of all possible correction factors given in Table 4.4. The error in this case, given by the standard deviation, yielded a much larger value than in the other cases.

Reaction	$^{9}\mathrm{Be}\left(^{12}\mathrm{C},{}^{11}\mathrm{C}\right)\mathrm{x}$	$^{9}\mathrm{Be}\left(^{11}\mathrm{C},{}^{10}\mathrm{C}\right)\mathrm{x}$	$^{9}\mathrm{Be}\left(^{10}\mathrm{C},{}^{9}\mathrm{B}\right)\mathrm{x}$	$^{9}\mathrm{Be}\left(^{9}\mathrm{C},{}^{8}\mathrm{B}\right)\mathrm{x}$
$T_{\mathrm{cor,\,f}}$	1	1.009 ± 0.002	1.017 ± 0.008	1.06 ± 0.002

Table 4.6.: Final T_{cor} factors for the correction of the reaction probability regarding transmission losses.

Geometrical acceptance of detectors

In the corrected reaction probability of Equation (4.13) no factor concerning potential beam losses due to the geometry of the detectors was considered. The largest impact of geometrical losses at any of the detectors involved in the particle identification would have been at TPC 3.1. The active area of the TPC was limited in x direction by ±100 mm. A rough estimate of losses was performed investigating the x-distribution of the relevant ions at this TPC. If any major losses had occurred, significant cut-offs at the left and right side of the distributions would have been visible. The linearly and logarithmically-scaled x-position distributions of the residues from the reaction $^{9}\mathrm{Be}\left(^{10}\mathrm{C},{}^{9}\mathrm{C}\right)\mathrm{x}$ are shown in Figure 4.14. A similarly looking distribution but narrower was found for the residues of the reaction $^{9}\mathrm{Be}\left(^{9}\mathrm{C},{}^{8}\mathrm{B}\right)\mathrm{x}$. While on the right side of the distribution (large positive values of x) it is not clear whether the detector

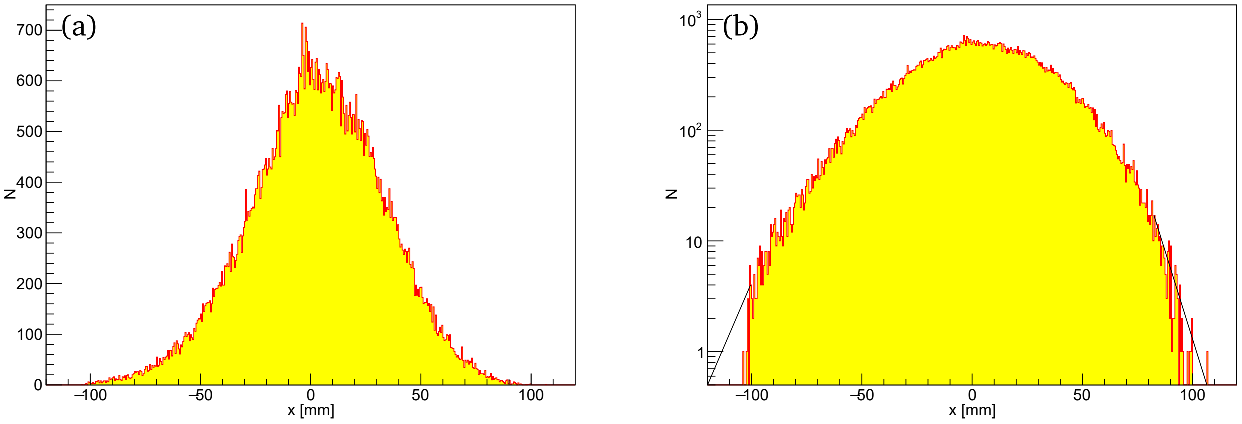

Figure 4.14.: The horizontal position distribution of ^{9}C-residues (from reaction $\left(^{10}\mathrm{C},{}^{9}\mathrm{C}\right)$) at TPC 3.1 is shown. Distributions in linear scale (a) and logarithmic scale (b) are provided. A linear fit of the left and right flank in the log-scaled distribution was performed (black lines), to estimate possible geometrical losses of ions at this detector.

size led to not accepting all residues, events appear to be lost for negative values of $x < -100\,\mathrm{mm}$. The estimated losses have not been taken into account as corrections of the total number of counts but as systematic uncertainty of below 1%. For distributions of the reaction residues of the neutron knockout from ^{12}C and ^{11}C, no geometrical losses were found at all.

5.1 Cross sections and reduction factors

After determining the corrected reaction probability $p_{\mathrm{f,cor}}$ the knockout cross section

$$\sigma_{\mathrm{ko}} = \frac{p_{\mathrm{f,cor}}}{n_t}, \tag{5.1}$$

with the number of atoms per unit area in the secondary reaction target

$$n_t = \frac{N_A \cdot t \cdot \rho}{A}, \tag{5.2}$$

was determined. In Equation (5.2) N_A denotes the Avogadro Constant, t the target thickness, ρ the density of the target and A the target materials molar mass in g per mole. The material properties of the target and its composition, molar mass and target thickness can be found in appendix A.1. The final results of the data analysis are shown in Table 5.1. In chapter 4.3.2 two graphical cuts of the particle identification plots were introduced, the most probable - *normal* - and a more confining - *strict* - cut. For reasons of comparison all cross sections were calculated using either of the cuts, identified by the quantities σ_0 and σ_s, respectively. The theoretical one-nucleon knockout cross sections were obtained using

$$\sigma_{\mathrm{th}} = \frac{A_p}{A_e} \cdot C^2S \cdot \sigma_{\mathrm{sp}}. \tag{5.3}$$

The corresponding single-particle cross sections σ_{sp} and spectroscopic factors C^2S were taken from a compilation by Simpson and Tostevin [14]. Hereby A_p is the projectile mass number and $A_e = A_p - 1$ the mass number of the reaction residues. In the case of the one-neutron knockout from ^{10}C a set of spectroscopic factors was given in [14], obtained by different models of the interaction potential. For the corresponding calculations of the theoretical cross sections their mean value was taken. The resulting

Dataset	$^9\mathrm{Be}\,(^{12}\mathrm{C},{}^{11}\mathrm{C})\,\mathrm{x}$		$^9\mathrm{Be}\,(^{11}\mathrm{C},{}^{10}\mathrm{C})\,\mathrm{x}$		$^9\mathrm{Be}\,(^{10}\mathrm{C},{}^{9}\mathrm{C})\,\mathrm{x}$		$^9\mathrm{Be}\,(^{9}\mathrm{C},{}^{8}\mathrm{B})\,\mathrm{x}$	
	σ_0 [mb]	σ_S [mb]	σ_0 [mb]	σ_S [mb]	σ_0 [mb]	σ_S [mb]	σ_0 [mb]	σ_S [mb]
Experiment	49.442	48.936	24.435	24.381	20.210	19.977	52.100	51.657
$1\sigma_{\mathrm{stat}}$	0.654	0.644	0.075	0.074	0.087	0.086	0.710	0.702
$1\sigma_{\mathrm{sys}}$	0.252	0.249	0.134	0.134	0.191	0.189	0.644	0.638
σ_{th}(Gaus)	97.11		51.81		44.084 ± 1.905		51.183	
σ_{th}(HF)	-		-		44.564 ± 2.149		51.765 ± 0.075	

Table 5.1.: Overview over experimental and theoretical cross section calculations. Hereby σ_0 refers to cross sections calculated with the presented particle identification and σ_s to the cross sections from the more strict graphical cuts. The quantities σ_{stat}, σ_{sys} and σ_{th} refer to statistical and systematical uncertainties and the error margin due to different theoretical approaches.

uncertainty of the theoretical values was given by their standard deviation. In addition, in the case of the one-neutron knockout from ^{10}C and the one-proton knockout from ^{9}C, the single-particle cross sections were given for calculations assuming Gaussian-shaped distributions of the core mass and additionally distributions obtained from a Hartree-Fock (HF) procedure. In the case of the HF-based cross sections a variety of results concerning different input parameters was given. Again, the mean value and standard deviation were taken for further considerations.

In Table 5.2 and 5.3 the corresponding reduction factors with respect to to Gauss and HF-based theoretical predictions are given. The reduction factor of ^{12}C matches prior performed measurements, reported in [24]. Thus, all measurements and calculations presented in this work are assumed to deliver good and precise results. Comparing the cross sections derived from *normal* and *strict* graphical selection cuts, only minor differences are visible and σ_0 and σ_S agree within the systematic uncertainty of the cross-section determination. A similar result can be seen for the comparison of the calculations, performed with theoretical values based on the Gaussian core model and the Hartree-Fock method. The

Gaussian

Normal ID:

Dataset	^{9}Be $(^{12}$C, ^{11}C) x	^{9}Be $(^{11}$C, ^{10}C) x	^{9}Be $(^{10}$C, ^{9}C) x	^{9}Be $(^{9}$C, ^{8}B) x
Reduction	50.91%	47.16%	45.85%	101.79%
$1\sigma_{\text{stat}}$	0.67%	0.14%	0.2%	1.39%
$1\sigma_{\text{sys}}$	0.26%	0.26%	0.43%	1.26%
$1\sigma_{\text{theo}}$	-	-	1.98%	-

Strict ID:

Dataset	^{9}Be $(^{12}$C, ^{11}C) x	^{9}Be $(^{11}$C, ^{10}C) x	^{9}Be $(^{10}$C, ^{9}C) x	^{9}Be $(^{9}$C, ^{8}B) x
Reduction	50.39%	47.06%	45.32%	100.93%
$1\sigma_{\text{stat}}$	0.66%	0.14%	0.19%	1.37%
$1\sigma_{\text{sys}}$	0.26%	0.26%	0.43%	1.25%
$1\sigma_{\text{theo}}$	-	-	1.96%	-

Table 5.2.: Estimated reduction factors based on *normal* and *strict* cuts and Gaussian shaped core models. Given uncertainties are absolute and not relative values with regard to the reduction factor. The quantities σ_{stat}, σ_{sys} and σ_{th} refer to statistical and systematical uncertainties and to the error margin due to different theoretical approaches.

Hartree-Fock

Normal ID:

Dataset	^{9}Be $(^{10}$C, ^{9}C) x	^{9}Be $(^{9}$C, ^{8}B) x
Reduction	45.56%	100.65%
$1\sigma_{\text{stat}}$	0.19%	1.37%
$1\sigma_{\text{sys}}$	0.43%	1.24%
$1\sigma_{\text{theo}}$	2.19%	0.15%

Strict ID:

Dataset	^{9}Be $(^{10}$C, ^{9}C) x	^{9}Be $(^{9}$C, ^{8}B) x
Reduction	44.83%	99.79%
$1\sigma_{\text{stat}}$	0.19%	1.36%
$1\sigma_{\text{sys}}$	0.43%	1.23%
$1\sigma_{\text{theo}}$	2.16%	0.14%

Table 5.3.: Like Table 5.2 based on HF-results to derive the reduction factors.

latter yielded slightly lower reduction factors. Still across the isotopic chain individual values were lying within the error margin of each other. Looking at the evolution of the reduction factors a decreasing trend can be seen. The reduction factors drawn versus the nucleon asymmetry factor ΔS can be seen in Figure 5.1. The reduction factors of the one-neutron removal reactions decrease with increasing nucleon asymmetry, but only very slightly. Including the uncertainties of the theoretical cross sections, the R_s value of the one-neutron removal from ^{10}C overlaps with the reduction factor of the one-neutron removal from ^{11}C. Thus, for neutron-deficient carbon isotopes no dependence of R_s(-1n) may be claimed. The change of $R_s$between one-neutron removal from ^{12}C and ^{11}C is slightly larger than the error bars and amounts to less than 4%, but ΔS hardly changes, as well. The last investigated reaction was the one-proton removal from ^{9}C. The one-proton removal from ^{9}C is on the far negative site of the asymmetry ΔS and similar to the trend of the reductions factors presented in Figure 2.2, a reduction factor near unity was found.

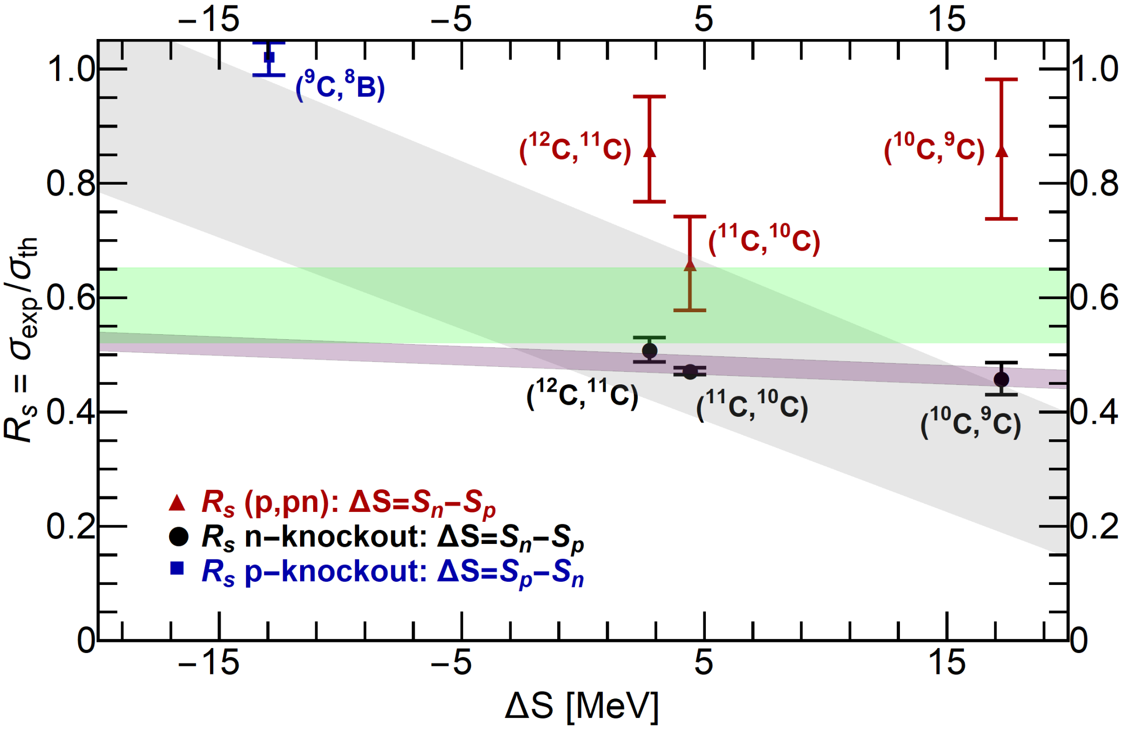

Figure 5.1.: Cross section reduction factors versus the asymmetry factor ΔS. The black circles and the blue square represent the nucleon removal data from this work (Gauss, *Normal*). The purple shaded area presents the estimated dependence of the neutron-knockout related data with respect to ΔS. The dependence differs significantly from the nucleon-removal dependence observed in [25] which is indicated by the gray shaded area. In [45] reduction factors obained from (p,pn)-reactions with the same species of isotopes as in this work were reported, indicated by the red points. Like in the data from this work a rather flat dependence of R_s with respect to ΔS was found. Lastly, the green shaded area indicates the deviation of reduction factors in [25] obtained from (e,e'p) reaction-data. Nucleon separation energies were taken from [46].

The longitudinal momentum distribution of the reaction residues depends on the reaction processes involved in the production of the residues. In a knockout reaction the momentum of the removed nucleon is subtracted from the nucleus and for the relative longitudinal momenta $p_{\parallel}^{rel}$ of the removed nucleon and the reaction residue holds

$$p_{\parallel}^{rel}(residue) = -p_{\parallel}^{rel}(nucleon). \tag{5.4}$$

The longitudinal momentum distribution[2] of the knocked-out nucleon depends on the nucleon's binding energy and its orbital angular momentum. It can be determined from measuring the position distribution in a dispersive section of the beam line, characterized by

$$\frac{\Delta p}{p_0} = \frac{\Delta x_{\mathrm{S3}}}{D \cdot \gamma}. \tag{5.5}$$

Here, Δx_{S3} denotes the relative x-distribution measured at the focal plane S3. The average total momentum and Lorentz factor of the reaction residues are given by p_0 and γ, respectively. The Lorentz factor was introduced to convert the measured momentum distribution in the laboratory system to the center-of-mass framework

$$\Delta p_{\parallel,\mathrm{CM}} = \Delta p = \frac{p_{\mathrm{lab}}}{\gamma}. \tag{5.6}$$

All comparisons of theoretical and measured momentum distributions presented in this dissertation were performed in the center-of-mass system. To correctly determine the relative momentum distribution of the reaction residues the relative x-distribution at S3 had to be corrected.

The incident beam's momentum spread at S2 induced chromatic aberrations at the focal plane S3. This incident spread led to chromatic aberrations at the focal plane of S3. Using the tracking information of the ion beam at S2 and S3, an achromatic distribution was produced by subtracting the influence of the incident beam spread

$$\frac{\Delta p}{p_0} = \frac{x_{\mathrm{S3}} - (x_{\mathrm{S2}} \cdot C)}{D_{\mathrm{S2}\rightarrow\mathrm{S3}} \cdot \gamma}, \tag{5.7}$$

with

$$C = \left(M_{\mathrm{S2}\rightarrow\mathrm{S3}} + \kappa \frac{D_{\mathrm{S2}\rightarrow\mathrm{S3}}}{D_{\mathrm{S0}\rightarrow\mathrm{S2}}} \right). \tag{5.8}$$

In these equations, x_{S3} and x_{S2} are the x-values at the focal planes of S3 and S2, and M and D describe the magnification and dispersion of the ion transfer between the focal planes. κ is a degrader specific factor. The ion-transfer matrix, delivering the magnification and dispersion values, was obtained from simulating the ion transfer through the FRS with GICOSY [41]. These values yielded $C = -0.384$. If

---

[2] For reasons of simplicity all mentioned momenta refer to their longitudinal part.

C is chosen correctly the relative momentum distribution at S3 is independent from the incident beam spread at S2 and reaches its narrowest possible distribution width. Thus, $C = -0.4$ was experimentally determined by adjusting the factor until the width of the resulting momentum distribution reached its minimum and now dependence with respect to the incident beam spread was observed, anymore [33]. Consequently the proportionality between the relative momentum distribution and the corrected x-distribution was described by

$$\frac{\Delta p}{p_0} \propto x_{S3} + 0.4 \cdot x_{S2}. \tag{5.9}$$

The effect of this correction and thereby its correctness can be seen in Figure 5.2. In Figure 5.2(a) x_{S3} vs. x_{S2} is plotted. A clear correlation between the x-position at S3 and S2 can be recognized. In Figure 5.2(b) $x_{S3} + 0.4 \cdot x_{S2}$ vs. x_{S2} is plotted. No correlation between the distribution of $x_{S3} + 0.4 \cdot x_{S2}$ and the incident beam spread x_{S2} is visible. Hence, the description allowed the particle's momentum distribution at S3 to be determined independently from of the incident beam spread at S2. Finally the relative momentum distribution of the reaction residues was given by

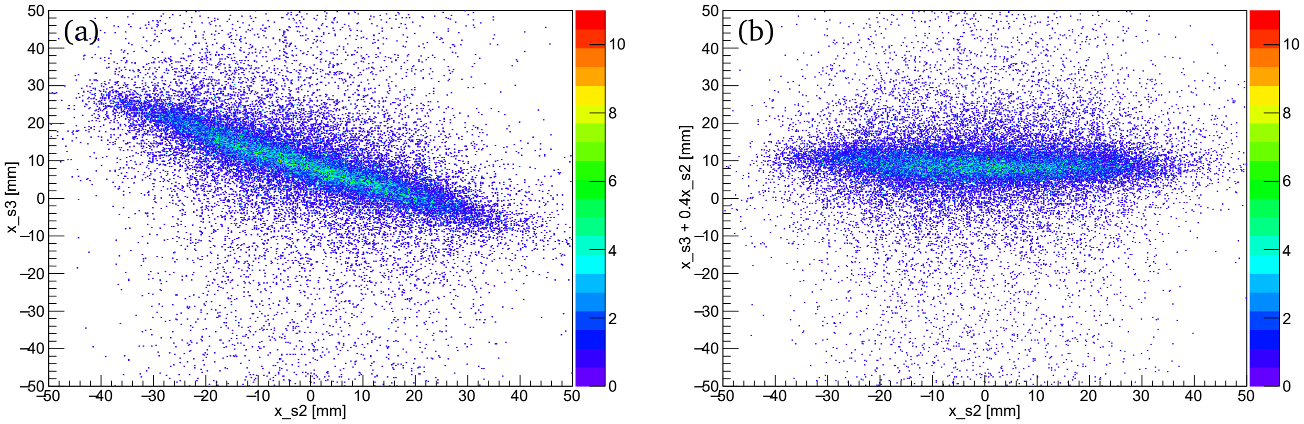

Figure 5.2.: In (a) the back tracked focal-plane x-positions at S2 $x_{tr,S2}$ and S3 $x_{tr,S3}$ are plotted versus each other. In (b) a chromatic correction was applied. The corrected distribution is independent of the initial momentum spread at S2 and depends only on the relative momentum distribution of the residue after the one-nucleon removal.

$$\Delta p = (x_{S3} + 0.4 \cdot x_{S2}) \cdot \frac{p_0}{D_{S2 \to S3} \cdot \gamma} \tag{5.10}$$

To ultimately investigate if the identified reaction residues and thereby the measured momentum distributions were originating from one-nucleon knockout, theoretical calculations of the expected momentum distributions were performed. The theoretical momentum distributions were obtained using MOMDIS [47], a computer program used to "calculate momentum distributions in stripping and diffraction dissociation reactions" ([47], Abstract). The calculation code of MOMDIS bases on formulas of eikonal's theory in sudden approximation. MOMDIS is used to calculate the momentum distribution of reaction residues after knock-out reactions and it was used to calculate the theoretical momentum distributions of the carbon and boron reaction residues[3]. A direct comparison between those distributions could not be performed. The measured distribution is affected by the characteristics and resolution of the detectors involved in the measurement of the momentum distribution. These influences affect the response of the detector. To take these influences into consideration, the theoretical data were convoluted with the data of a response function, or rather a response distribution. The general form of a convolution of a function or distribution with a response function or distribution looks like

$$(f * g)[n] := \sum_{m=-\infty}^{\infty} f[m] \cdot g[n-m]. \tag{5.11}$$

Due to the geometrical limit of the TPC size the actual convolution was cut at $\pm 300\,\mathrm{MeV/c}$ instead of $\pm\infty$. The distribution f is given by the momentum distribution obtained with MOMDIS. The response distribution is given by g. It was obtained by transmitting the unperturbed carbon beam to S3 without traversing the secondary reaction target and recording the momentum distribution. After correction of the momentum distribution regarding the incident momentum spread at S2, the corrected distribution served as response function. For each of the studied reactions the response function was recorded with the corresponding unperturbed carbon beam. In Figure 5.3 the response distribution, given by the unperturbed ^{11}C beam, is shown.

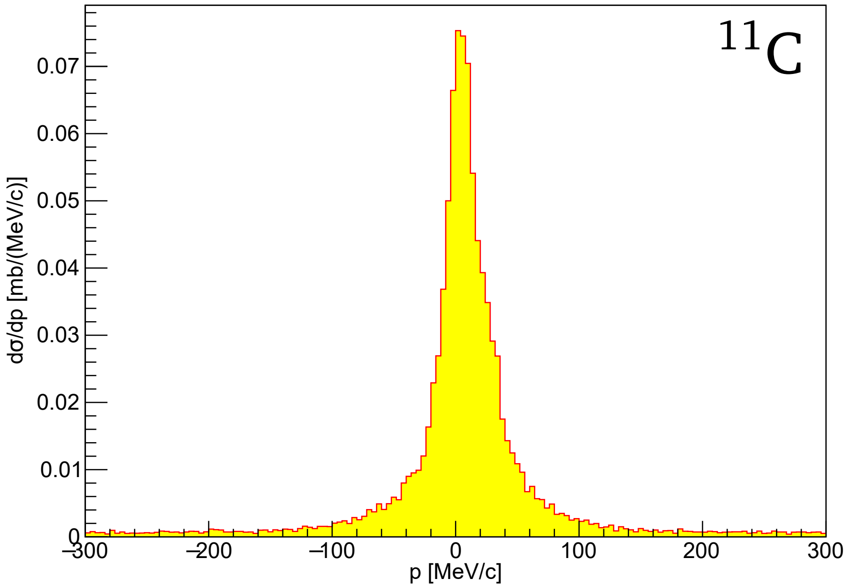

Figure 5.3.: Distribution of ^{11}C at the focal plane without target at S2. The distribution served as response function for the folding with the theoretical momentum distribution.

Finally, the measured distributions of the reaction residues were overlayed with the convolution of the theoretical distributions. The theoretical and convoluted distributions are displayed as the black line in Figures 5.4-5.5. Due to the convolution process the theoretical distributions were broadened and got tails. Comparisons of the real spectra in yellow with the black lines of the convoluted distributions

---

[3] Theoretical calculations performed and kindly provided by Jeff Tostevin, j.tostevin@surrey.ac.uk

delivered a good match in all four cases. Comparisons of the 1-σ environments of the distributions are shown in Table 5.2. Differences of theoretical predictions and experimental values mainly resulted from the large low momentum tails of the measured distribution. After zooming in to ±200 MeV/c around the center of the distributions, the differences between the theoretical and experimental 1-sigma widths decreased to below 1 % in the case of all reactions.

Dataset	^{9}Be (^{12}C, ^{11}C) x 1σ [MeV/c]	^{9}Be (^{11}C, ^{10}C) x 1σ [MeV/c]	^{9}Be (^{10}C, ^{9}C) x 1σ [MeV/c]	^{9}Be (^{9}C, ^{8}B) x 1σ [MeV/c]
Measured	105.77±3.82	109.32±4.33	106.73±6.03	86.72±2.23
Conv. theory	103.18±3.72	105.21±4.32	103.68±5.92	76.61±2.12

Table 5.4.: Widths of the full experimental momentum distributions given by the measurement and the convoluted theoretical momentum distribution.

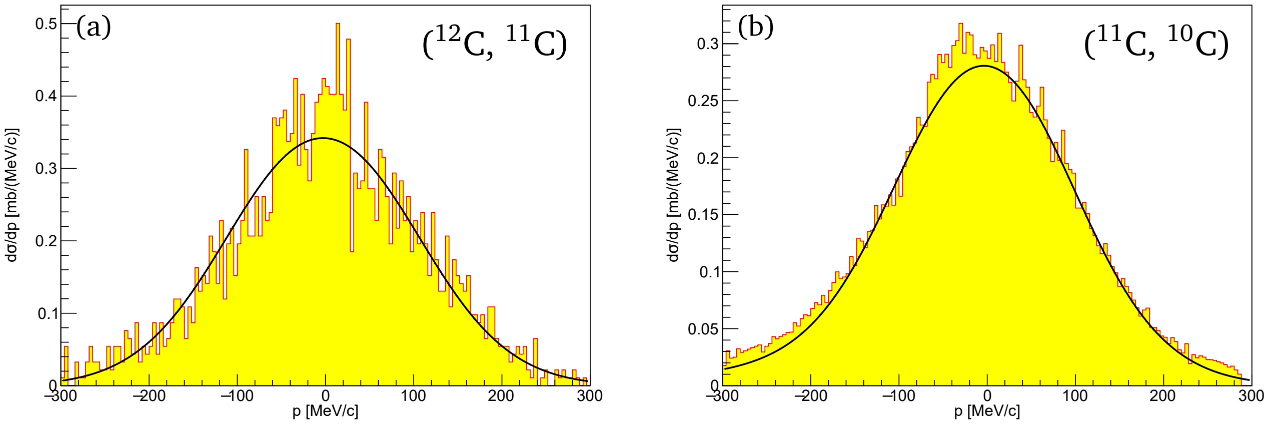

Figure 5.4.: Momentum distribution of ^{11}C after one-neutron knockout from ^{12}C (a) and momentum distribution of ^{10}C after one-neutron knockout from ^{11}C (b).

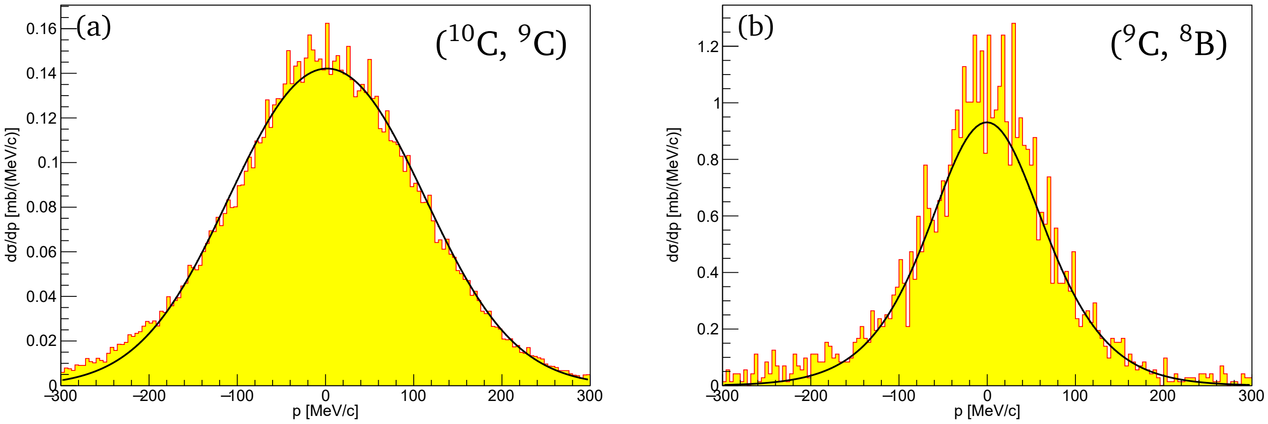

Figure 5.5.: Momentum distribution of ^{9}C after one-nucleon knockout from ^{10}C (a) and momentum distribution of ^{8}B after one-proton knockout from ^{9}C (b).

The experimental cross sections of nucleon removal reactions of ^{12}C, ^{11}C, ^{10}C and ^{9}C as well as the relative longitudinal momentum distributions of their reaction residues were investigated. In the case of the momentum distributions a good agreement between the experimental results and theoretical predictions using the eikonal in sudden approximation model was found. One-nucleon removal cross sections were determined with relative accuracies of typically a few percent and expected differences between experimental and theoretical predictions were found. In Table 6.1[4]. the final results regarding the measured cross sections and the estimated reduction factors are shown. While the measurement did not distinguish in which final state the residue has been, the theoretical estimations from [25] still did. A comparison of the absolute spectroscopic factors ratios from [25] with relative spectroscopic factors provided by (p,pn) transfer reactions [48] showed similar relative fractions. Thus, it can be assumed that the theoretical predictions from [25] regarding the knockout cross sections are a solid source for estimations of the reduction factor R_s.

Reaction	σ_{exp}[mb][4]	R_s	J^{π}-res.	E[keV]	σ_{sp}[mb]	Abs. C^2S_{ko}	Rel. C^2S_{tr}
(^{12}C,^{11}C)	49.44(65)(25)	0.509(7)(3)	$3/2^-$	GS	23.06	3.163	100
			$1/2^-$	2000	20.83	0.577	17.4
			$3/2^-$	4804.2	21.11	0.192	9.7
(^{11}C,^{10}C)	24.44(8)(13)	0.472(1)(3)	0^+ ($p_{3/2}$)	GS	27.50	0.440	
			2^+ ($p_{1/2}$)	3353.7	26.08	0.009	
			2^+ ($p_{3/2}$)	"	25.20	1.380	
(^{10}C,^{9}C)	20.21(9)(19)	0.459(2)(4)(20) 0.456(2)(4)(22)	$3/2^-$	GS	22.9	1.733(75)	100
(^{9}C,^{8}B)	52.10(71)(64)	1.018(14)(13) 1.007(14)(12)(2)	2^+	GS	48.4	0.94	100

Table 6.1.: The table shows the final one-nucleon removal cross sections presented in this work and the reduction factors obtained from comparison with the theoretical single particle cross section σ_{sp} and the spectroscopic factor C^2S_{ko} from [25]. The two reduction values at (^{10}C,^{9}C) and (^{9}C,^{8}B) each relate to determination of the theoretical cross sections with assuming a Gaussian core density distribition and with using the HF-method. The relative spectroscopic factors C^2S_{tr} were provided by (p,pn) transfer reactions [48]. If not explicitly clear the possible final states of the reaction residues J^{π} are complemented by the information from which state the single nucleon was removed. Final states with relative spectroscopic factors below 1 or with energies above the nucleon separation energy are not shown.

The theoretical predictions of the cross sections, based on many-body nuclear shell-model calculations, are in agreement with the expected values for knockout reactions from nuclei of highly negative asymmetric proton-neutron binding energy differences without the need for introducing quenching. Most of the results shown in [25] (cf. Figure 2.2) show a strongly decreasing tendency of R_S with increasingly large positive ΔS. No such trend is visible for one-neutron knockout from ^{12,11,10}C. The studied

---

[4] Ordering of uncertainties - Value(a)(b)(c) - in all presented data: (a=statistical)(b=systematical)(c=uncertainty of theoretical values)

neutron-removal reactions allowed for a weakly decreasing trend with increasing ΔS, but the decrease was significantly less or compatible with ΔS independence for R_s, in contrast to the data of Figure 2.2. While for the investigated carbon removal reactions the nucleons were removed from the $1p$-shells, the reduction factor compilation of [25] show a strongly decreasing evolution with increasing positive ΔS were mostly deduced from knockout reactions of nucleons occupying other shells than the p-shell. Nevertheless for the neutron-knockout reactions from this work reduction factors far below unity were determined. Calculating the theoretical cross section when assuming a Gaussian core density distribution or performing HF-calculations did not lead to significant differences of R_s. Another method to determine the theoretical knockout cross section are ab-initio variational-monte-carlo (VMC) calculations [49–51]. Lapikas et al. [52] found a perfect agreement between the VMC-calculated and measured spectroscopic factors for the reaction ^{7}Li(e,e'p)^{6}He, without applying a quenching factor. Further comparisons of VMC and shell-model calculations and experimentally measured cross sections are presented in [50]. For some reactions VMC calculations describe reality better, for other reactions the SM calculations describe reality better. The reduction factors in Table 6.1 were taken from [25] and were obtained using SM calculations assuming Gaussian and HF core densities. Cross sections obtained from VMC calculations were presented in some cases, too, but, changes of the reduction factor were in the order of a few percent at most, thereby, not removing the need for a quenching factor as in [52].

The results presented here were measured at beam energies above 1.6 GeV/nucl. where the validity of the eikonal model in sudden approximation may be well assumed. Some of the studied removal reactions have been investigated before. In [53] the experimental cross section of one-proton removal from ^{9}C at a beam energy of about 90 MeV/nucl., performed at the National Superconducting Cyclotron Laboratory (NSCL) at the Michigan State University (MSU), was reported, yielding $\sigma_{\text{exp}} = (56 \pm 3)$ mb. Corresponding reduction factors, reported in [50], were found in the range from 0.87 to 1, dependent on the used theoretical model, respectively. Those values show a similar trend as the results reported in this work. Reported cross sections in both cases are in the same region and within each of the error bars an overlap can be found. In the case of the reduction factors an overlap can be found in the region of $R_s \approx 1$.

In [51] results of the one-neutron removal from ^{10}C at a beam energy of 120 MeV/nucl., performed at MSU, were reported. A cross section of $\sigma_{\text{exp}} = (23.2 \pm 1.0)$ mb was found and reduction factors of 0.4 up to 0.5 were estimated. Again the value is only slightly different from the result presented in this work and an overlap of the estimated reduction factors can be seen. In both cases the reaction studies were performed at much lower energies than the ones presented in this dissertation but still the eikonal model yielded the same the reduction factors. Reported statistics of the (^{10}C,^{9}C) experiment at MSU were nearly a factor 10 smaller compared to the statistics reported in this work. Also the relative systematic uncertainties summed up to 5%. Those were in much better control in the framework of the work, namely about 1%. In the case of the NSCL experiment (^{9}C,^{8}B) the systematic uncertainty and the statistics were not discussed separately. Thus, the presented results of the presented cross sections and reduction factors represent the most accurate values, experimentally obtained up to now. Energies and momentum distributions of the reaction residues strongly supported the capability to use the sudden eikonal approximation to deliver theoretical comparisons. Systematic as well as statistical uncertainties were well in control.

It has been questioned that nuclear knockout reactions allows spectroscopic factors to be extracted at an absolute scale because the nuclear probe is short-ranged and only the outermost part of the wave function may be sampled [54–58]. Also the ΔS dependence of R_s has not been observed in other single-particle reactions. Recent arguments proposed intermediate-energy (about 500 MeV/nucl. quasi-free proton scattering (QFS) as better suited to probe the single-particle wave function, since the NN force allows the protons to penetrate into the nuclear interior [54, 59]. Recent results, currently submitted for publication [45] show for ^{12,11,10}C(p,pn)-reactions larger R_s values (red points in Figure 5.1) of $R_s(^{12}C,^{11}C)=0.86(9)(8)^4$, $R_s(^{11}C,^{10}C)=0.66(6)(8)$ and $R_s(^{10}C,^{9}C)=0.86(12)(8)$. These results show no clear trend with respect to ΔS, and [45] also reports - in agreement with results from transfer [60] - different average quenching factors for proton and neutron removal. However, the difference reported by [45] is not as large as the values reported here, and finds larger R_s for neutron removal.

In summary the measured knockout cross sections shown in Table 6.1 present highly precise data. The cross sections were compared to theoretical values from [25] and reduction factors deduced. These reduction factors of the carbon isotopes did not show an as clearly decreasing trend as indicated by the plot in Figure 2.2. A nearly flat behavior of R_s vs. ΔS was observed, similar to the results of QFS studies presented in [45]. The eikonal model showed a robustness with respect to the predictions of theoretical nucleon-removal cross sections presented by MSU in [50, 51, 53] and by Tostevin et al. in [25]. The only observed difference from predictions of the eikonal model in sudden approximation and measured data is visible in the momentum distribution. While in the data of this work a good congruence was observed, in the MSU data slow non-sudden influences can be seen, questioning the correct description of the momentum distribution with the eikonal model at lower energies. Finally, to obtain a quantitative understanding of nuclear knockout and the influence of the underlying structure more precise data at high energies are needed.

II. Development of a Particle Detector Combination for the Super-FRS

1 Introduction

An important part of the beam diagnosis in accelerator facilities is a working online analysis of beam intensity and transmission along the beam line. In the case of facilities like GSI/FAIR the ions are delivered from a synchroton in a spill structure. Thus, another important task of beam diagnostics is to perform highly resolved measurements of the spill structures. Measuring the transmission along the beam line allows the beam operators to optimize the ion transport to the experimental sites as well as the radiation safety staff to identify points of high background radiation [61]. Usually, a combination of different particle detectors is used for those purposes, as the complete range of particle intensities, used in various experiments, cannot be covered by one detector alone. These so-called particle detector combinations (PDC) usually consist of three types of detectors. A first stage dedicated to measure ions at lower intensities, a second for medium intensities and a third for the highest intensities, up to the space-charge limit. In Figure 1.1 theoretical measuring ranges of plastic scintillators (Scint.), diamond detectors (Dia.), ionization chambers (IC) and secondary electron transmission monitors (SEM) are shown. The upper limit of the diamonds is given by rates at which the diamond detectors studied in this work showed significant saturation effects [5].

PDCs are already in use at GSI. The usual combination of detectors is a plastic scintillator (SCI), followed by an IC and a SEM. The SCI is used at lowest intensities. Beyond intensities of 1 MHz the

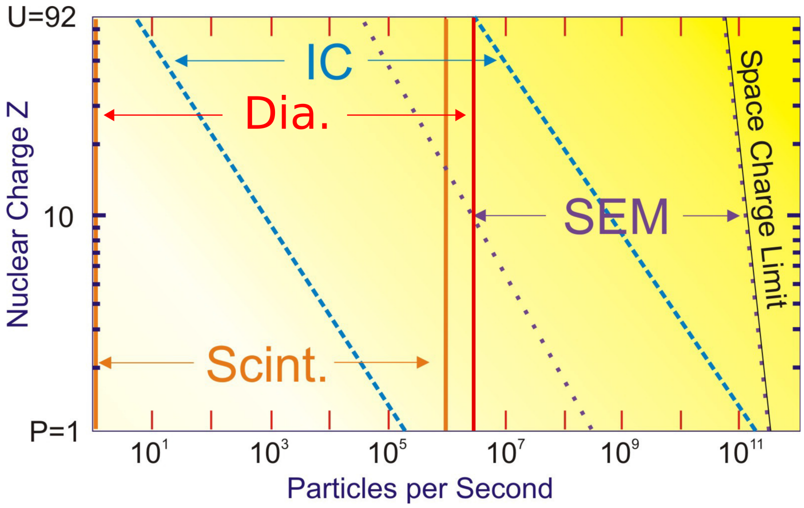

Figure 1.1.: Theoretical work ranges of different particle monitors. The red line was added later from results of the measurements in Catania 2017, which investigated the count behavior of diamond detectors. Furthermore in the same experiment the SEM was found to be operational at lower intensities (10^5–10^6 pps for carbon with $Z = 6$, not indicated in the plot) contrary to the theoretical predictions of this plot. Plot adapted from [62].

---

[5] For reasons of simplicity the units *MHz*, *pps*, *ions per second*, and similar expressions were used in the following chapters but always refer to particles per second if not otherwise specified.

detector is starting to show significant saturation effects. Longer periods of irradiation at intensities in the order of 0.1 MHz to 1 MHz can also damage the scintillation material, and thus, reduce its efficiency. In many cases (undamaged) SCIs are assumed to have a counting efficiency of nearly 100 %. Therefore, they are used to calibrate the second stage of a PDC, the ionization chamber. The PDC-ICs work in current mode. Hence, only a secondary current, proportional to the primary ion beam intensity, is measured. An empirical calibration factor, translating IC-current to absolute counts is found by comparing the measured secondary IC-current and the SCI particle count. After calibration, the IC can be used to monitor beam intensities at much higher intensities than a plastic scintillator. If the intended intensities even exceed the capacities of the IC, SEMs are used. After calibrating the SEM using the IC as reference, a secondary current is measured, that is expected to be proportional to the primary beam intensity.

Ions traversing matter suffer energy loss. The energy loss of the ions traversing the detectors scales with the charge $Z \cdot e$ of the beam ions like

$$dE \propto Z^2. \tag{1.1}$$

In the case of the SCI, this does not significantly impact the signal output, as only the number of measured pulses are of interest. In most cases the amplification of the read-out electronics of the SCI, usually photo multiplier tubes (PMT), are adjusted to obtain measurable pulses for each ion. In the case of the IC and SEM, the induced secondary current strongly depends on the charge of the ions. Figure 1.1 shows that a direct calibration of the SEM using a SCI is possible for heavier ions, but not for ions of low charge number. Consequently a two-step calibration is required in some cases while in other situations a single calibration step may be sufficient. Depending on the charge of the ion beam and the strength of the secondary current, an one-step calibration can yield a lower calibration uncertainty. In the case of medium mass ions a careful evaluation is necessary to achieve lowest possible uncertainties but also to reduce the amount of irradiation deposited at the first-stage detector, potentially damaging it.

At in-flight facilities to produce exotic radioactive ion beams (RIB) very high beam intensities are utilized while due to low production cross sections the number of desired ions reaching the dedicated experiment is still low. Calibration of the particle monitors is often carried out using the primary beam. Therefore, these detectors do not only need to have a high radiation hardness but also a high sensitivity when particle rates of highly exotic beams need to be measured at high precision. This holds even more true for detectors in the super conducting in-flight separator Super-FRS. This machine will be a core component of the future ion research facility FAIR. A scheme of the machine is shown in Figure 1.2. The Super-FRS is designed for high beam intensities and energies delivered by the heavy ion synchroton SIS100 and it will be used to produce and study highly exotic ion beams. PDCs are planned to be utilized as particle intensity monitors in the region of the production target at focal plane *FPF0* and thereby in the target hall [63], and in front of the main-separator at focal plane *FPF4*.

A scheme of the target hall of the Super-FRS is shown in Figure 1.3(a). The beam pipe will be surrounded by an iron shielding, followed by a thick concrete shielding. These huge amounts of shielding material are needed, as the high intensities FAIR is aiming for will induce a high radiation environment. A simulation of the expected dose rate in the vicinity of the production target is shown in Figure 1.4.

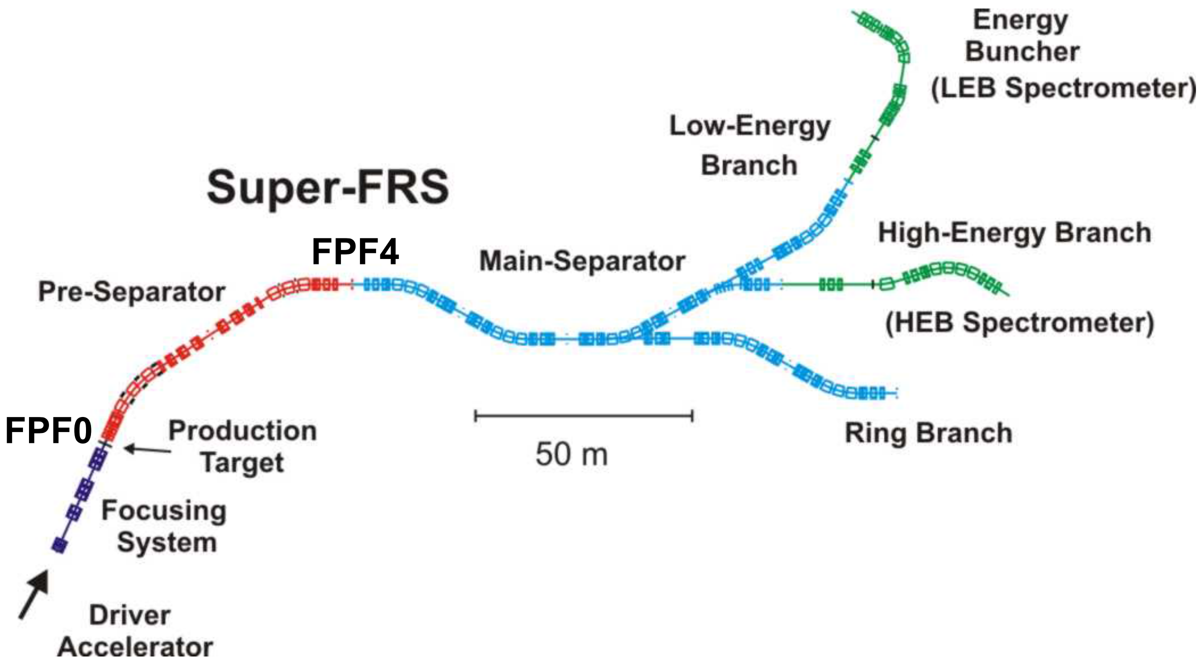

Figure 1.2.: Layout of the Super-FRS [11]. The PDC in development is planned to operate at in front of the target-wheel at FPF0 and in front of the main-separator at FPF4.

These high radiation doses demand a many-meters-thick shielding around the beam pipe. To minimize direct exposure of the detectors to the beam, they will be mounted on ladders, movable by pneumatic drives. These target ladders will be mounted in 2 meter long plugs, having their own iron and concrete shielding and will be able to be pulled into dedicated holes along the inner shielding of the beam-pipe. A profile of the target area, including these plugs is shown in Figure 1.3(b). Above the plugs an outer concrete shielding will be placed, to sufficiently reduce radiation levels to follow radiation protection

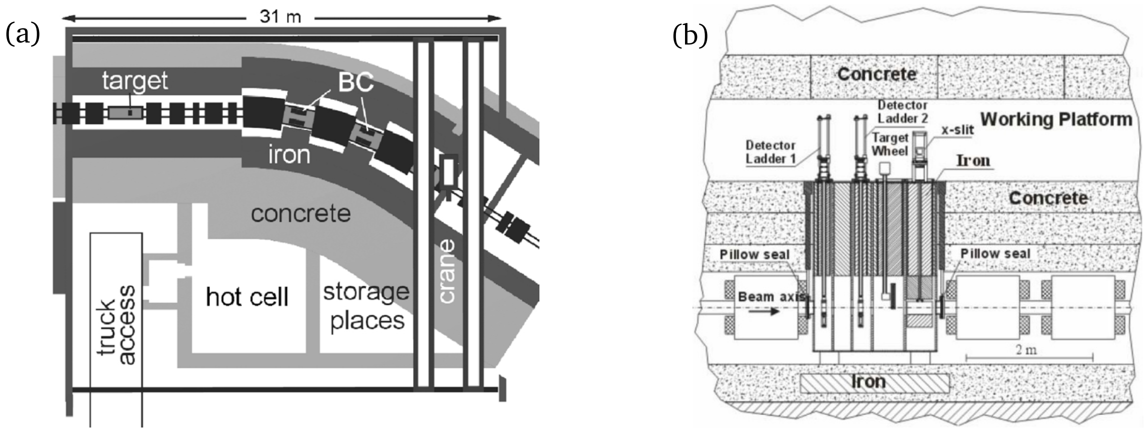

Figure 1.3.: Layout of the target area and beginning of the pre-separator from above (a). Shielding thicknesses will have to be in the order of meters. A hot cell will be used to deposit activated material. Layout of the production target area in front of the Super-FRS including target and detector ladders (b). Figures taken from [63], and reprinted with permission from *Elsevier Science B.V.* order number: 4543011165616, and [11].

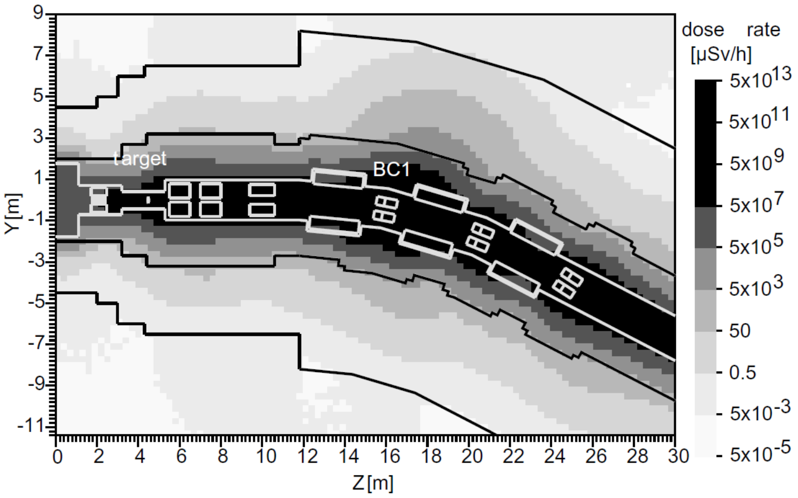

Figure 1.4.: Simulation of the dose rate in the vicinity of the production target at the entrance of Super-FRS. Plot taken from [63], and reprinted with permission from *Elsevier Science B.V.* order number: 4543011165616.

laws for unrestricted access. Consequently if a detector receives a large enough dose to show radiation damage and thus, has to be exchanged, this outer concrete shielding has to be removed first. After removal of the shielding the plug, containing the PDC, can be pulled out. High dose exposures of the detectors in the beam line, even if they are pulled out of the direct beam line, are expected in the target area of the Super-FRS.

The next position, where particle monitors will be needed, is between the pre- and the mainseparator - at focal plane *FPF4*. Although direct ion intensities and background irradiation at this position will be lower compared to the target area, intensities will still be high enough to deposit doses large enough to damage detectors. The development of a new FAIR-PDC, had to be commissioned.

Within the scope of this work, various detector tests were performed, regarding prototypes for a possible operation in the future FAIR-PDC:

- Diamond detectors, consisting of single-crystal and polycrystalline diamond material, were tested regarding their performance and if they are a reasonable replacement for plastic scintillators. In particular a characteristic counting efficiency curve of the diamond detectors and an estimation of their radiation hardness was desired.

- A prototype of a new IC design for use at FAIR (FAIR-IC) was tested. General functionality, achievable counting uncertainties after calibration and operation readiness as particle monitor were studied.

- The same tests were performed for a new SEM prototype, also designed for the use in FAIR.

- The functionality of the data acquisition when using long cable lengths between detectors and read-out electronics, was tested.Part of the front-end electronics may need to be positioned further away from the beam line and consequently from the detectors (about 20–30 m).

These and more tests were performed within three experiments at INFN-LNS Catania in 2015 and 2017, and at GSI in 2016. In the following sections detailed goals and results of the individual experiments are reported. The development of the tested detector typed was beyond the scope of this dissertation. The following sections will, therefore, introduce the operational principles of the detector types as well as the details of the tested prototypes.

2.1 Diamond Detectors

Diamond detectors are planned to be used as first stage of the new FAIR-PDC. Two different types of diamond material were used for the development of the investigated diamond detectors - single-crystal (SC-DD) and polycrystalline (PC-DD) diamond detectors. Single crystal diamond detectors are of superior quality compared to polycrystalline diamond detectors. They have a higher charge collection and counting efficiency. On the other hand they are only available in smaller dimensions and at much higher prices. The single- and polycrystalline material was purchased from Element Six Ltd. (UK). The diamond material was produced using chemical vapor deposition and hence are often called scCVD and pcCVD diamond detectors. For simplicity the abbreviation SC and PC will be used in this dissertation. Further processing of the material to obtain different geometries and structures of the active detecting area had taken place in the detector laboratory of GSI.

Chemical vapor deposition

The first artificial diamonds were produced using a high-pressure high-temperature (HPHT) formation process in the 1950's. Those diamonds were produced at temperatures ranging from 1500 °C to 2000 °C at pressures above 5 GPa [64]. The CVD process was postulated a few years later and was able to deliver sufficiently large growth rates in the 1980's. Among the advantages of this method are the better control of impurities within the diamond and the ability to grow large area diamonds. The CVD process takes place at pressures of $1-27$ kPa. Chemical reactions are utilized to grow the diamond by gas deposition on a solid surface, also called seed. Usually a mixture of hydrogen and methane is used as source gas. The deposition reaction needs a high temperature. This can either be realized by heating the gas with filaments or producing a plasma by means of microwave heating, see Figure 2.1. The substrate is constantly cooled using water. A description of the CVD process can be found in [64].

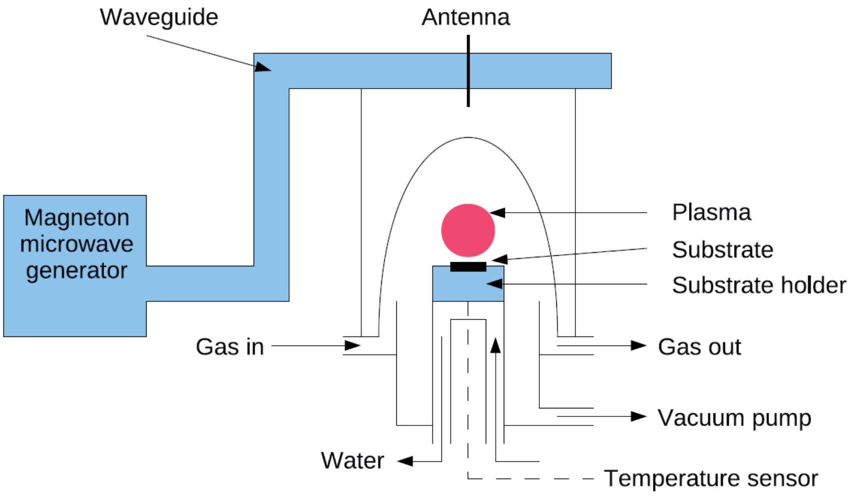

Figure 2.1.: Sketch of a microwave generator, used to grow CVD diamonds. Plot taken from [64].

The quality of the CVD diamonds depends strongly on the quality of the substrate. Two different substrate types can be used, the homo- or heteroepitaxial type. Homoepitaxial substrates have diamond-like crystal structure and are usually the choice if electronic grade diamonds, as needed for detectors, are produced. The main difference when growing SC and PC diamonds is again the substrate. For high-quality SC diamonds an artificial diamond, already produced by means of the HPHT method, is used as substrate. If grown properly, this method delivers a single-crystal structure with negligible impurities. When producing PC diamond material, diamond powder is used. In the growth process of the diamond some of the grains in the powder disappear while others grow bigger. Nevertheless, the grain structure never disappears completely, independent of the diamond's size. While SC material has very few defects, PC material can have different types of defects. Atoms can be displaced from their ideal lattice position, leading to holes at some other positions in the lattice (vacancy), while at some inter lattice spaces additional atoms can be sitting (interstitial). More complex defects, like Frenkel pairs, impurities in the lattice, etc. can occur, too. On the other side, PC diamonds can be grown much bigger than SC diamonds. In general SC diamonds are limited to scales of mm^2 while PC diamonds are available in the order of cm^2.

Signal creation in diamond detectors

Besides their large bandgap energy of $E_{\mathrm{gap}} = 5.47\,\mathrm{eV}$ [65], diamond detectors behave like solid-state semiconductor detectors. Figure 2.2 shows an example of the general principle of signal creation in diamond detectors. When an ion of sufficiently high kinetic energy traverses the diamond material, it ionizes some of the lattice atoms and creates electron-hole pairs. The total amount of produced charge

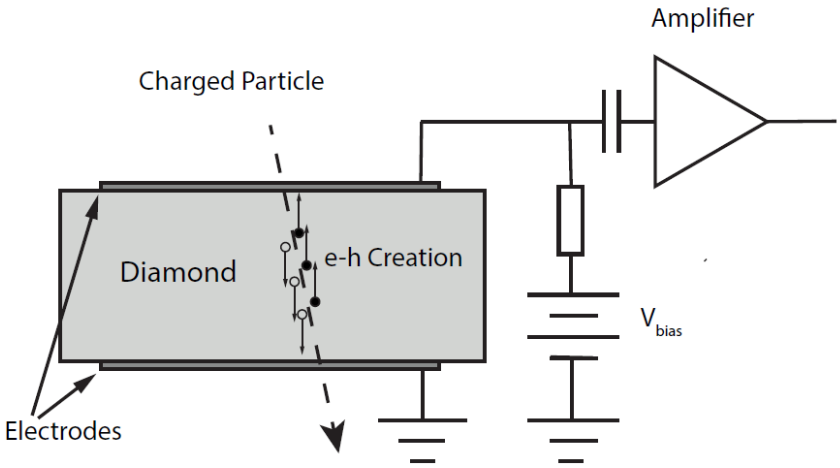

Figure 2.2.: Scheme of the signal generation in an irradiated diamond detector. The ions create electron-hole pairs. Applying high voltage to one electrode and ground potential to the other creates an electrical field, collecting the e-h pairs. Before transferred to further electronics the resulting diamond signal gets amplified. Plot taken from [64].

Q_{tot} depends on the energy loss of the ion in the material dE and an efficiency ϵ describing energy losses of the ionization process

$$Q_{\mathrm{tot}} = \frac{\epsilon \cdot dE}{E_I} e, \tag{2.1}$$

where E_I is the average energy to produce an electron-hole pair. In the case of diamond $E_I = 13\,\mathrm{eV}$ [66]. The high voltage supply, ground potential and signal read-out are connected by electrodes on the top and bottom of the detector. They are usually produced by sputtering chromium or gold onto the diamond. The signal amplitude of diamond detectors is usually in the order of $10^{-4}\,\mathrm{V}$, demanding the use of (pre-)amplifiers before the diamond detector can be read-out by further electronics [67].

The most commonly used description of the signal formation at the electrodes of diamond detector is the Shockley–Ramo theorem [68], which states that the measured signal, induced at the electrode, is not formed by the total amount of collected charge but by the instantaneous motion of the charge carriers. The instantaneous current i due to a single electron's motion $\vec{v}(t)$ for a given electrode is given by

$$i(t) = e\vec{E}(r(t))\vec{v}(t), \tag{2.2}$$

where e is the electron charge. The variable $\vec{E}(r(t))$ describes the component of the electrical field at the position of the electron, without the electron present. Since the geometry of the diamond detectors is similar to a simple plate capacitor, the electric field component is given by $\vec{E}_v = \frac{U}{d}\vec{e}_z$, with $\vec{e}_z$ being the unity vector perpendicular to both electrodes. The drift velocity of the charge carrier is given by $\vec{v}$. Since electron and hole have a different mobility the final induced current is given by the sum of their currents

$$i(t)_{\mathrm{tot}} = i_{\mathrm{e}}(t) + i_{\mathrm{hole}}(t). \tag{2.3}$$

In reality the electrodes themselves have an influence on the measured signal, due to material properties, and in the case of lattice defects or structural damage in the diamond material, the integrated current signal or the measured charge Q_M will differ from Equation (2.1). Additional energy levels in the band gap also increase the probability of thermal excitation and thus, increase the leakage current of the detector, reducing the signal-to-noise ratio. All of these effects lead to a smaller charge collection efficiency (CCE) of the measured charge, compared to the total produced charge

$$CCE = \frac{Q_M}{Q_{\mathrm{tot}}}. \tag{2.4}$$

The charge collection efficiency is linked to the charge collection distance (CCD) and describes the average distance a charge carrier traverses the diamond detector before it hits an impurity

$$CCD = CCE \cdot t, \tag{2.5}$$

where t is the thickness of the diamond. The CCE of SC diamonds is (or very close to) about 100%.

The PC material has more defects than the SC material. The mobility of holes and electrons in PC material is much smaller than in the SC material. Since the drift velocity $\vec{v}$ of the electrons and consequently the instantaneous current $i(t)$, described in Equation (2.2), depends on the charge-carrier mobility μ as described by

$$\vec{v}(E) = \frac{\mu\vec{E}}{1+\frac{\mu E}{v_S}}, \tag{2.6}$$

where $E = |\vec{E}|(r(t)) = |\vec{E}(r(t))|$, an increase of the electrical field strength leads to a larger CCE. Nevertheless, the gain of this approach is limited. If $\mu \cdot E$ reaches large values, the drift velocity approaches its saturation value v_S. Furthermore the strength of the electric field is limited by the breakdown field strength of the material. The latter problem is less important, as diamond material has a large breakdown field strength in excess of $10\,\mathrm{V}/\mu\mathrm{m}$ [65]. However, SC diamond detectors only need relatively small field strengths anyway. Their vanishingly small number of lattice defects allows the charge carries to reach their saturation velocity and consequently their saturation CCE at low field strengths. The PC diamond detectors require larger field strengths to compensate the decrease of CCE due to defects in the crystal lattice. Furthermore, while the SC's CCE shows a steep increase towards its saturation point at low field strengths, the CCE of the pcCVD has a much broader characteristic curve. The CCE of the PC slowly increases with increasing field strength and requires very high field strengths to reach its saturation point. This characteristic behavior of the CCE can be seen in Figure 2.3.

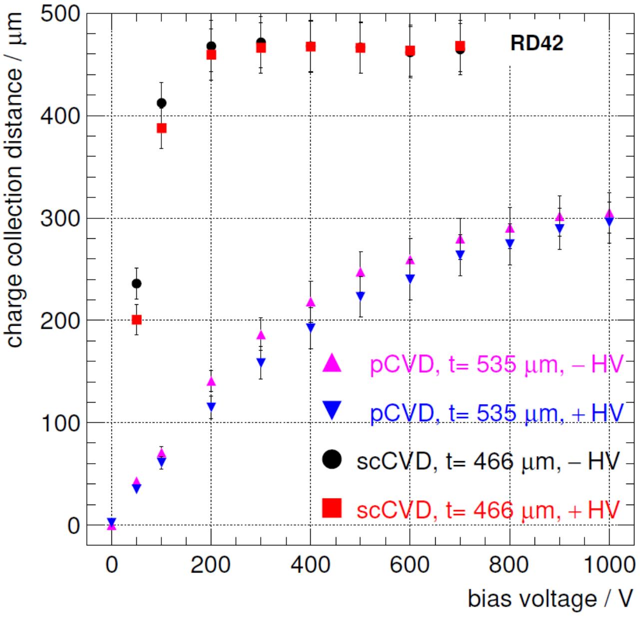

Figure 2.3.: Evolution of the CCD of a SC-DD and a PC-DD versus the applied voltage. Plot taken from [64].

Electrodes

The electrodes of the individual detectors were sputtered onto the diamond material at in the detector laboratory of GSI. The electrodes of all diamond detectors were fabricated by the sputtering method, depositing 50 nm of chromium, to operate as adhesion material for a 150 nm thick layer of gold [69]. This kind of electrode provides an ohmic contact [70]. The backside electrode of all diamond detectors were connected to the HV-supply and provided a fully planar contact. With the exception of two detectors the front-side electrode was also produced as a planar contact. The first exception was a PC-DD, tested in Catania 2015. By applying a shadow mask onto the detector material before performing the sputtering process, four equally sized and electically not connected electrode areas were fabricated on the top of the detector. The other detector having a distinguished structure was a polycrystalline strip diamond detector. Laser photolithography was used to shape the electrodes in a sandwich configuration. The detailed dimensions and shapes of all detectors are presented in the chapters describing the experiments.

2.2 Ionization Chamber

Ionization chambers (IC) are gas-filled detectors. An ion beam traversing the gas ionizes the atoms of the gas and produces electron-ion pairs due to inelastic scattering. A detailed description of the involved processes can be found in [71]. A schematic layout of an IC is shown in Figure 2.4. The active gas volume is confined by electrodes connected to a high-voltage supply. The resulting electric field separates negative and positive charge carriers. The collected ions are measured at the inner electrode. The polarization of the high voltage can be chosen arbitrary, depending on the requirements of the specific detector. The same holds true for the high-voltage and read-out connections. The tested IC-

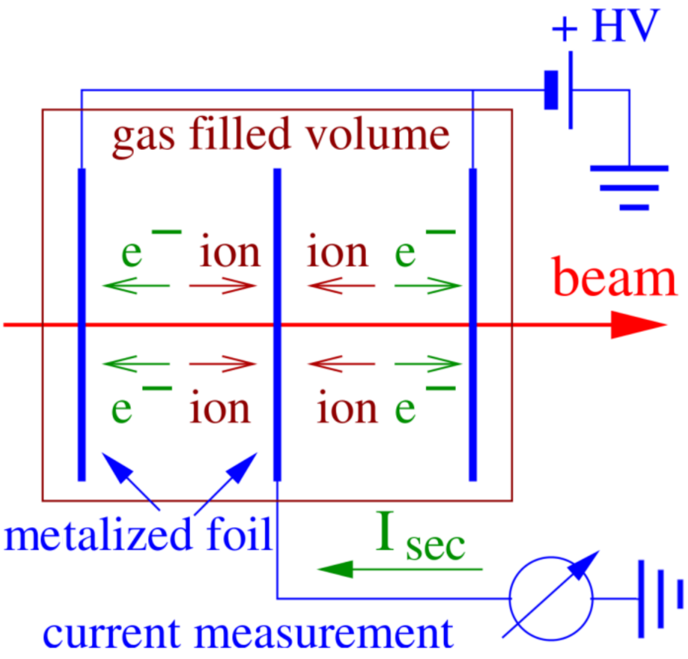

Figure 2.4.: General work principle of an IC. A primary ion beam produces electron-ion pairs which in turn get separated by an electrical field. The resulting secondary current is proportional to the primary beam intensity. Drawing adapted from [62].

prototype was found to be working best when applying a negative voltage to the inner electrode and measure the collected electrons at the outer electrodes.

This configuration was used in all tests presented in this work. Usual IC operation demands an electrical field strength high enough to prevent recombination effects within the gas, but low enough to prevent inducing further ionization along the path of the secondary electron-ion pairs. The resulting current I_{sec}, measured at the electrodes, depends on the average energy needed to produce an electron-ion pair and the energy loss and intensity I_{beam} of the primary ion beam within the active gas volume [62]. Vice versa, the intensity of the primary beam can be calculated, if the secondary current was measured and all of the other variables are known

$$I_{\text{sec}} = \frac{1}{W} \cdot \frac{\mathrm{d}E}{\mathrm{d}x} \Delta x \cdot I_{\text{beam}}, \tag{2.7}$$

where W is the average value needed to produce an electron-ion pair in the gas. These values are given by precise empirical observations and are well known for all commonly used detector gases. P10-gas[6] at atmospheric pressure and a constant flow of about $50\,\text{cm}^3\,\text{min}^{-1}$ was used in all test experiments. In an experiment, the correlation between primary and secondary current is usually not calculated as many factors as signal attenuation in cables and electronics, characteristic behavior of the involved electronics, etc. have an impact on the measured secondary current. Instead, a calibration curve is measured. The general procedure of this calibration is described in chapter 2.6.

Two designs of ionization chambers were considered for the development and test of a PDC. The first, shown in Figure 2.5(a), was an older design, already used at the FRS. This design was more simple than the scheme shown in Figure 2.4 and consisted of only two aluminum foils. The HV-supply and the signal read-out were each connected to one of the foils. A second model, designed for the use at the FAIR Super-FRS and shown in Figure 2.5(b), was produced at the GSI detector laboratory. It consisted of three silver coated ($100\,\mu\text{g/cm}^2$) mylar foils ($d = 1.5\,\mu\text{m}$), forming a circular active area with a diameter of 54 mm. A detailed drawing of this design, already including signal read-out, HV-supply, and gas-

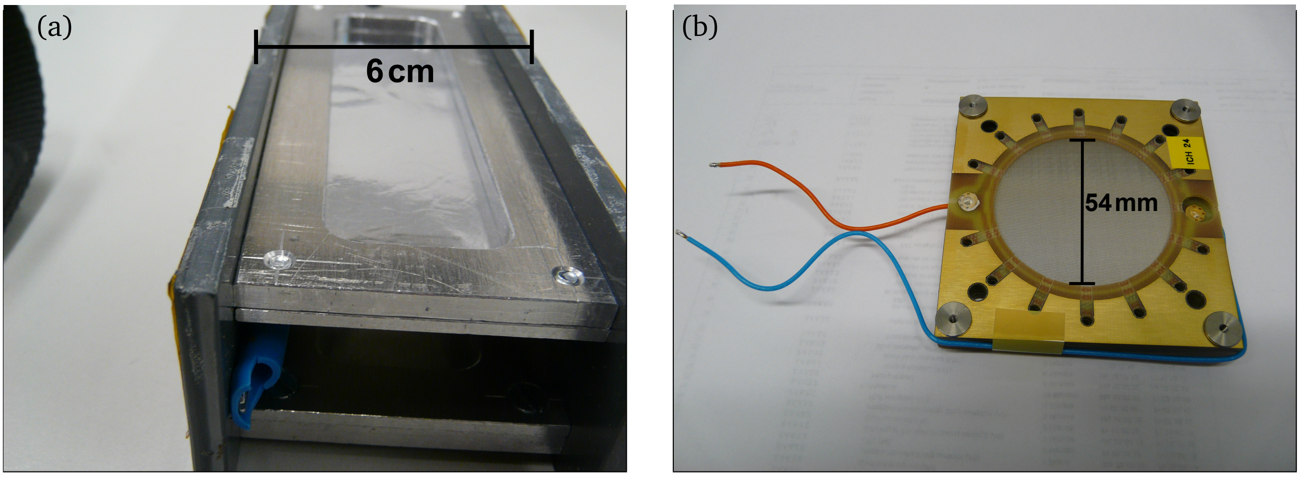

Figure 2.5.: The two foiled (a) and three foiled (b) ionization chamber designs under investigation.

---

[6] 90 % Argon ($W = 26.3$ eV) and 10 % Methane ($W = 29.1$ eV).

supply connections is shown in Figure 2.6. While the displayed resistors at the HV-input usually serve as HV-filter to reduce voltage fluctuations, the actual test experiments featured an external filter inserted between HV-supply and HV-input.

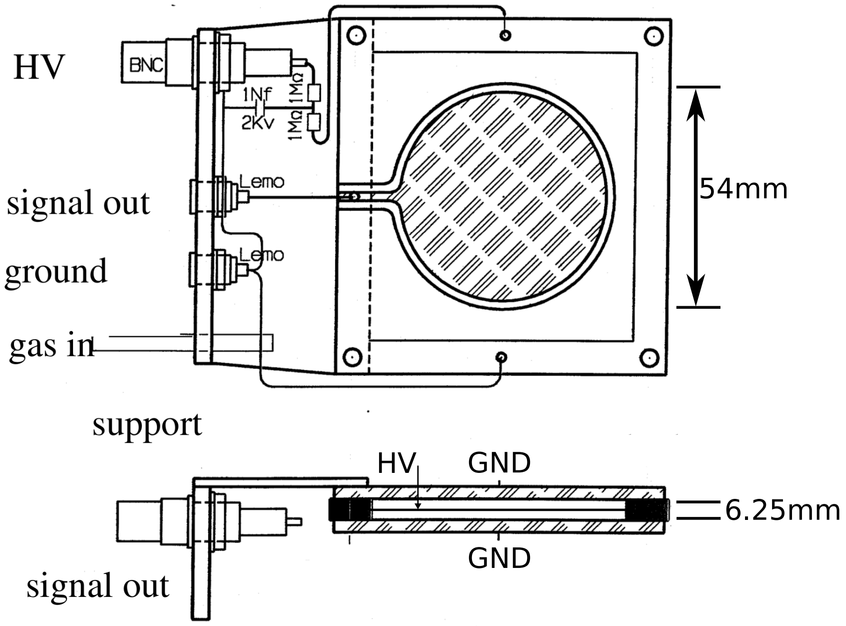

Figure 2.6.: Technical drawing of the IC-prototype, including signal read-out, HV-supply, and gas-supply connections. Three foils separated the active gas valume, introducing gaps between the electrodes of 3.125 mm. A negative HV was applied to the center electrode, signal read-out to the outer electrodes. Drawing adapted from [62].

Because the new design had not yet been tested before additional tests were mandatory before the experiments. Both detectors were put into a gas pocket to confine the P10 supply gas. Detailed drawings and dimensions of this pocket and the mounting of the FAIR-IC design are shown in appendix A.2. Both chambers were tested and compared in the laboratory in advance of the experiments, using a β^-–emitter (^{90}Sr) since it had the highest activity of all available radiation sources. Although several improvements were applied onto the two-foiled design in these tests, this IC model did not show successful operation. Therefore, all experiments were carried out using only the prototype of the FAIR-IC.

Upper operational voltage

The optimal operational voltage was found by measuring the characteristic voltage work function. In the case of the IC-prototype it was measured independently in all experiments. While an ion-beam is needed to record the characteristic curve, the electrical noise of the device in the absence of any kind of energetic ion source at different voltages can at least reveal a tendency regarding the upper limit of voltage, the detector can be operated at. In Figure 2.7 the average electrical noise at voltages up to 1900 V is shown. Each point was determined by observing the measured current for about 100 s. Error bars are caused by fluctuations of the measured current. These fluctuations strongly increase at voltages above 1000 V. In the case of the IC-prototype, having electrode gaps of 3.125 mm, this means to preferably not operate the IC at electrical field strengths of 3200 V/cm or higher.

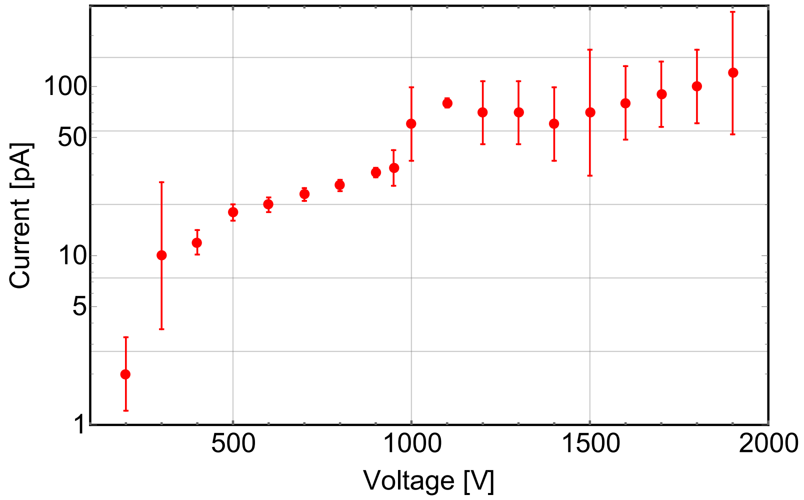

Figure 2.7.: Average electrical noise of the IC-prototype measured without a dedicated radiation source. Starting from voltages of 1000 V and above the noise level and its uncertainty significantly increases.

2.3 Secondary electron transmission monitor

As third stage of the FAIR-PDC, monitoring the highest beam intensities, a secondary-electron transmission monitor (SEM) is foreseen. The general working principle of a SEM can be seen in Figure 2.8. Thin metal foils are placed in vacuum, centered along the ion beam line. Proportional to the energy loss of

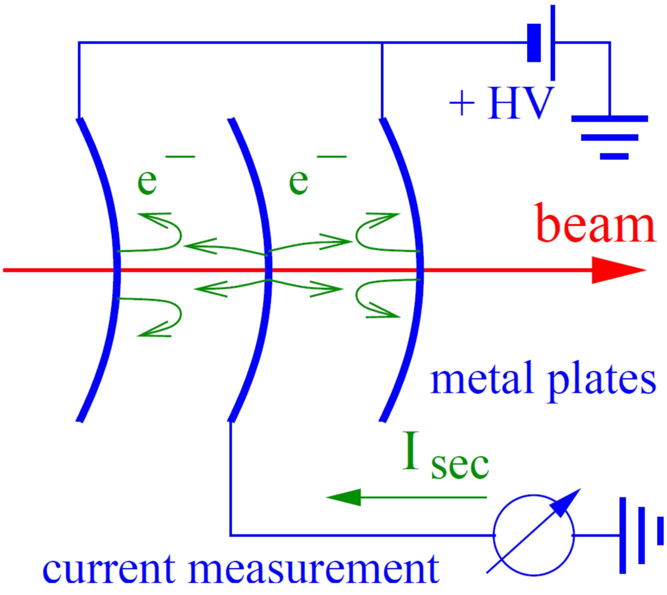

Figure 2.8.: Scheme of the SEM operation. The ion beam knocks out electrons from the metal foils. When applying a positive HV on the outer foils they collect the electrons and a current measured at the inner foil. Drawing adapted from [62].

the ion beam in the metal foils, a number of electrons get emitted from the surface of the metal foils. The exact correlation between secondary electron and primary ion beam current can be calculated using the Sternglass-formula [72]

$$I_{\text{sec}} = Y \cdot \frac{1}{\rho}\frac{\mathrm{d}E}{\mathrm{d}x} \cdot I_{\text{prim}}, \tag{2.8}$$

where Y is the yield factor. It describes the number of electrons emitted from the surface of the metal foil per unit of energy loss. The specific energy loss of the ion beam in the foil $\frac{\mathrm{d}E}{\mathrm{d}x}$ is proportional to the square of the ion charge Z

$$\frac{\mathrm{d}E}{\mathrm{d}x} \propto Z^2. \tag{2.9}$$

At GSI titanium is usually used to construct the detector foils. In the test experiment at the LNS in Catania 2017 a prototype of a SEM consisting of aluminum foils was tested. Production is easier and cheaper than when using titanium but it is not clear how well a SEM consisting of aluminum performs. A picture of this aluminum prototype is shown in Figure 2.9. The active area of the detector is a circle with a diameter of 107 mm [73] and thereby larger than the previous GSI-SEM with had an active area of $80 \times 80\,\text{mm}^2$. The new FAIR-PDC-SEM is built from three $24\,\mu$m-thick aluminum foils mounted on ceramic insulators at a gap size of 5 mm between the foils. The foils are not plane but slightly shaped to suppress mechanical vibrations. HV-supply and read-out connections were applied in the same manner as the schematic drawing in Figure 2.8 implies.

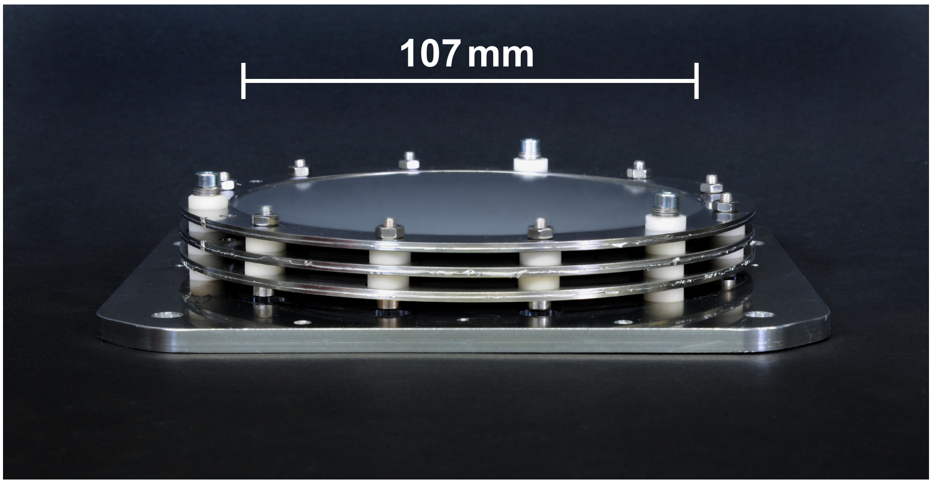

Figure 2.9.: Picture of the FAIR-PDC-SEM-prototype. It consists of three $24\,\mu$m thick circular aluminum foils with a diameter of 107 mm and a gap size of 5 mm between the foils. Picture adapted from [73].

2.4 Readout Electronics

Different sets of electronics and read-out systems were used during the test experiments. Schemes of the explicit detector–readout-electonic connections are presented in the corresponding sections, presenting the experiments. In the following a list of the most important read-out electronic used in the experiments is given.

Current digitizers (CD), Diamond Broadband Amplifiers (DBA), PADI-7-boards (PreAmplifier-DIscriminator), leading edge discriminators (LED), VME Universal Logic Module v.3 (VULOM3) scaler modules, and a digital oscilloscope were the core components of the signal read-out. Current digitizers were used to read out the IC and the SEM and convert the measured secondary current into an equivalent of digital pulses. DBAs were used to amplify the analog signals coming from the diamond detectors. The amplified (still analog) diamond signals were either sent to a digital oscilloscope or to a LED. The digital oscilloscope (LeCroy WaveRunner 620Zi [74]) was used to record the waveforms of the analog signals. The scope has a bandwidth of 2 GHz and a maximum resolution of 10 Gs/s or 20 Gs/s, when operating in four or two channel mode, respectively. The LED (CAEN Mod. N841 [75]) converts an incoming analog signal into a logical pulse if the analog signal's amplitude exceeded a manually set threshold. The threshold of the LED is variable in a range from 1 mV to 255 mV. Pulse widths of the logical output signals were variable adjustable in the range from 5 ns to 40 ns. The diamond strip detectors were installed on an integrated PADI-7 electronic board [76, 77], which already featured an internal amplifier and discriminator, and thereby, directly provided logical pulses for each of the 16 channels. Finally, a VULOM3 scaler module [78], which was developed at GSI, was used to count the number of logical pulses coming from the CD, the LED, and the PADI7. The VULOM3 module had an external and internal 200 MHz clock regarding the timing of the read-out cycles.

Current digitizer

IC and SEM were operated in current mode. The measured current was converted into digital signals by the use of a current digitizer (CD), sometimes also referred to as current-to-frequency converter (IFC). The rate or frequency of the generated pulses depends on the measured current and the charge sensitivity of the device. The maximum current which can be converted, without inducing any saturation effects in the electronics, is called the full-scale (FS) reading. The digitizer model used during the test experiments was a CD1012-module [79, 80]. Full-scale reading sensitivity settings range from 10^{-10} A to 10^{-4} A and can be adjusted in steps of one order of magnitude. In the case of this device the full-scale current translates to a frequency of 10 kHz at the digital output. If the frequency of the output exceeds the full-scale value or is very low, the sensitivity needs to be reduced or increased to avoid non-linear effects and keep uncertainties as low as possible.

DBA and PADI7 - diamond signal amplification

The studied diamond detectors have signal amplitudes, pulse widths and rise times in the order of about 100 μV, about 1 ns and about 100 ps, respectively. Dedicated diamond broadband amplifiers (DBA), to satisfy the demands of such signal shapes, were developed at GSI [67]. DBAs are low noise, current-sensitive pre-amplifiers. For the test experiments the model DBA-III was used. It has a bandwidth of 2 GHz and a variable gain up to +53 dB. A BNC-output at the DBA provides the amplified analog signal.

The diamond strip detectors were were directly mounted on a preamplifier-discriminator ASIC (PADI7) [76, 77], which can be seen in Figure 2.10. This electronic board was designed and developed at GSI and features an internal amplifier and discriminator. Each of the 16 diamond strips is treated independently and conclusively the board features a 16-channel output. The PADI7 board has signal rise times of <500 ps and an intrinsic electronic resolution of $\sigma_{\mathrm{te}} < 15$ ps.

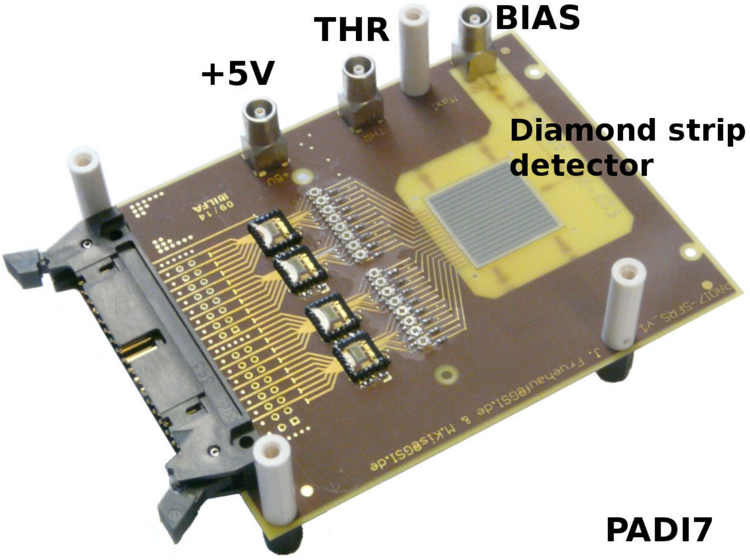

Figure 2.10.: Five DBA boxes connected to diamond detectors (a) and a PC-strip diamond detector (gray squared area, dimensions about $20 \times 20\,\mathrm{mm}^2$) mounted on a PADI7 board (b). In the experiments a different detector of similar design was used. Picture provided by [70].

2.5 Data aquisition

Number of counted pulses coming from the memory of the VULOM3 scaler module were read-out using GSI's standard data aquisition system (DAQ), the multi branch system (MBS) [37]. MBS was running on a RIO4 server. MBS creates list-mode-data files (lmd), containing data of all electronic modules, connected to and read out by the DAQ. These data were monitored online, while recording the data, and later in an offline analysis by using Go4 [39]. The Go4 data analysis framework was running on a computer directly connected to MBS. For the offline analysis Go4 was used to convert the lmd-files into raw root files. In the offline analysis the raw data were analysed and subsequently presented using dedicated ROOT [40] macros, Origin [81] and Mathematica [82].

2.6 Calibration of IC and SEM

When an ion beam traverses an IC or SEM, only a current signal but no actual information about the absolute number of ions can be measured. Linear calibration coefficients for the IC and SEM currents with respect to the incoming particle intensities as measured with SCI and SC-DD were determined over over a large range of incident particle rates. Higher-order contributions describe the saturation characteristics of the reference detector or the detector system that is to be calibrated. Therefore, the most robust calibrations are obtained at particle rates below the saturation point of the reference particle monitor but above the minimum rate it takes to induce a secondary current. If these conditions are fulfilled, a linear dependence between the measured particle counts and the secondary current is found.

3 Radiation Hardness of a PC Diamond Detector and Test of the FAIR-IC – LNS Catania 2015

The first test experiment presented in this dissertation was carried out at the LNS in Catania, Italy. It was dedicated to:

- Study the radiation hardness of a polycrystalline diamond detector: Investigate the evolution of detector characteristics during on-going irradiation.
- Test the functionality of the IC-prototype.
- Perform a calibration of the IC with respect to a single-crystal diamond detector.
- Use the calibrated IC to determine the amount of dose deposited in the polycrystalline diamond material.

These tests were carried out in the first chamber of the 0°-beam-line at the LNS accelerator facility. A primary ^{12}C beam at an energy of 62 MeV/nucl. was used to irradiate the detectors. The beam was delivered by the superconducting cyclotron, capable of providing ion energies between 8 and 100 MeV/nucl.

3.1 Detector Design

In the test experiment a single-crystal diamond detector (SC-DD), a polycrystalline diamond detector (PC-DD), two polycrystalline diamond strip detectors (strip-DD) and an ionization chamber (IC) were used. For each of the diamond-related test experiments new detectors of different designs were constructed. The explicit SC-DD design used in this experiment was an electronic-grade single-crystal CVD diamond plate and had an active area of dimensions $2\times2\times0.09\,\mathrm{mm}^3$. The material was mounted on a PCB board. The electrodes were fabricated by sputtering a layer of 50 nm Cr followed by 100 nm of Au and had a full planar contact on both sides of the detector and were operated at 100 V. In Fig-

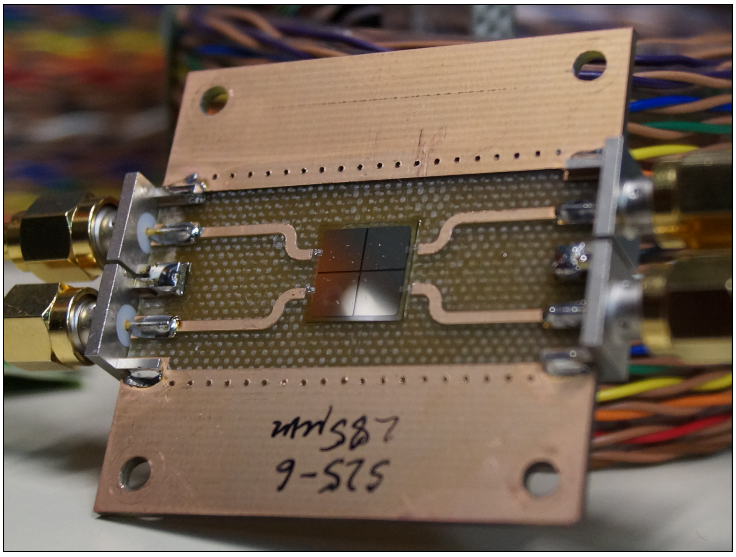

Figure 3.1.: Photograph of the used PC-DD, connected via four SMA-cables. The diamond material and the four electrically separated electrode-quadrants sit in the center. The complete active area has a size of $10\times10\,\mathrm{mm}^2$.

ure 3.1 the used PC-DD is shown. An electronic-grade polycrystalline CVD diamond plate of dimensions $10\times10\times0.3\,\mathrm{mm}^3$, mounted on a PCB board, provided it's active area. The PC-DD electrodes were produced with the same method as the SC-DD's electrodes. Additionally, a cross-shaped shadow mask was placed above the diamond material during the sputtering process to create four equally sized electrode quadrants. Each of the quadrants was individually connected to read-out electronics. The lower electrode consisted of a full planar contact. A voltage of 300 V was applied to the contact, generating about the same intrinsic electric field as in the SC-DD. The segmentation of the upper electrode of the PC-DD allowed an independent read-out of the signals of each quadrant. Both detectors, SC-DD and PC-DD, were connected to pre-amplifiers using shielded coaxial-SMA cables. These cables allowed to transport the signals and the high voltage supply without interference in one cable. The third type of the used diamond detectors was a diamond strip detector. The base of the detector was an electronic-grade polycrystalline CVD diamond plate of dimensions $20\times20\times0.3\,\mathrm{mm}^3$. The electrodes were also produced using the sputtering method. The final geometry was obtained by using laser photolithography to shape the electrodes in a sandwich configuration. The resulting active area consisted of 16 strips of dimensions $18\times1\,\mathrm{mm}^2$ with a gap of 0.15 mm between each strip. The backside electrode of the strip detector consisted of a full planar contact. A picture of a strip detector mounted on a PADI7-board used to read out the detector was presented in Figure 2.10.

3.2 Experimental setup and procedure

All detectors were centered along the beam line and irradiated using a primary ^{12}C-beam at 62 MeV/nucl.. The physical calculator in LISE++ [83] was used to estimate the energy loss of the carbon ions in the detectors. The energy loss calculations from LISE base on the atima code [84] developed at GSI. The energy loss of ^{12}C at 62 MeV/nucl. was calculated to be about 5.2 times larger compared to ^{12}C at 1500 MeV/nucl. - a possible ion beam for future FAIR NUSTAR operation - in the tested PC diamond material. Since the difference is not too large, results obtained using this carbon beam are still comparable to results one expects to obtain from the referred uranium beam. Furthermore, the ions were predicted to traverse all detectors. Simulations predicted a total energy loss of less than 10 MeV/nucl. after passing all detectors. Still, the energy loss at each detector was expected to be large enough to have sufficiently large signals to test the detectors. Another important issue was a sufficient particle rate to deposit a significant dose of radiation at the diamond material. A large number of ions traversing the PC-DD was required to investigate the detector properties with on-going large dose absorption. The LNS-cyclotron delivered primary-beam currents up to about 2 enA to the 0° beam line, satisfying the intensity demands. Beam attenuation by factors of 10, 100 and 1000 allowed to vary the ion intensity and to perform measurements requiring lower or a variety of ion intensities. Additionally, the opening size of slits along the beam line could be adjusted to further vary the beam intensity.

The experiment took about 80 hours of irradiation time in total and was divided into two runs, each having a slightly different setup. Runs 1 and 2 had a duration of 18 h and 62 h, respectively. Schemes of the corresponding setups are shown in Figure 3.3 and 3.6.

In the first run all of the introduced detectors had been used. The detectors were mounted in the small vacuum chamber, shown in the center of the photograph in Figure 3.2. In the picture the beam was traversing from the right to the left. A detailed technical drawing of the chamber can be found in appendix A.1. A schematic drawing of the setup is shown in Figure 3.3. The studied PC-DD was mounted on a grey plastic board at the entrance of the vacuum chamber. This board was fixed to the entrance of the vacuum chamber and can be seen at the right entrance of the chamber in Figure 3.4. After the PC-DD two strip diamond detectors were placed, rotated by 90° with respect to each other, allowing

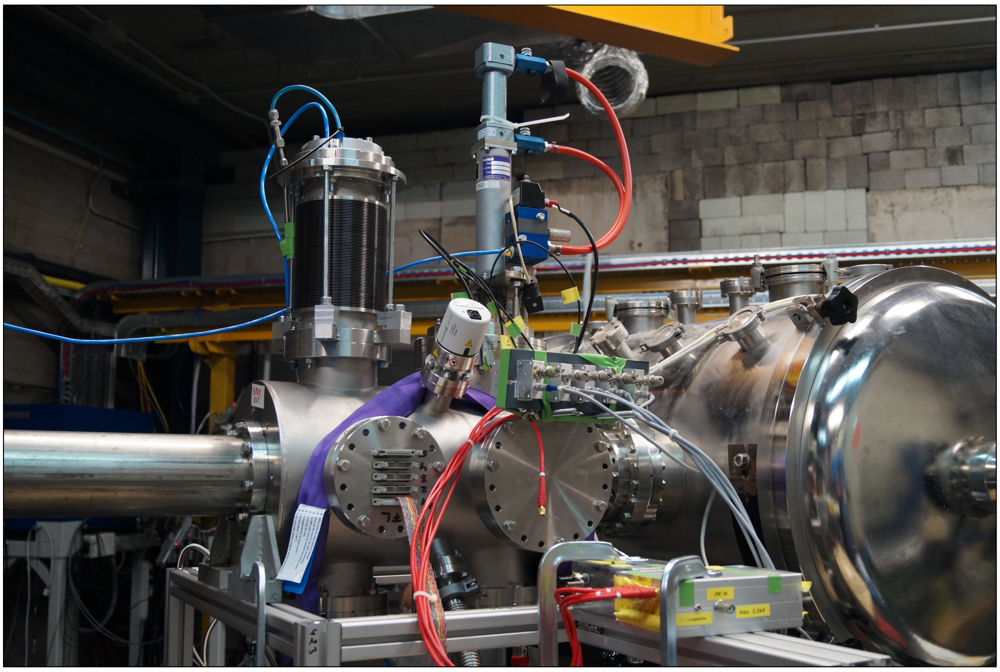

Figure 3.2.: The vacuum chamber housing all detectors sits in the center of the photograph and has a length of 51 cm. On the top of the chamber the gas pocket of the IC (l.) and the pneumatic pump (r.), moving SC-DD and strip-DD in/out, can be seen. The beam entered from the right.

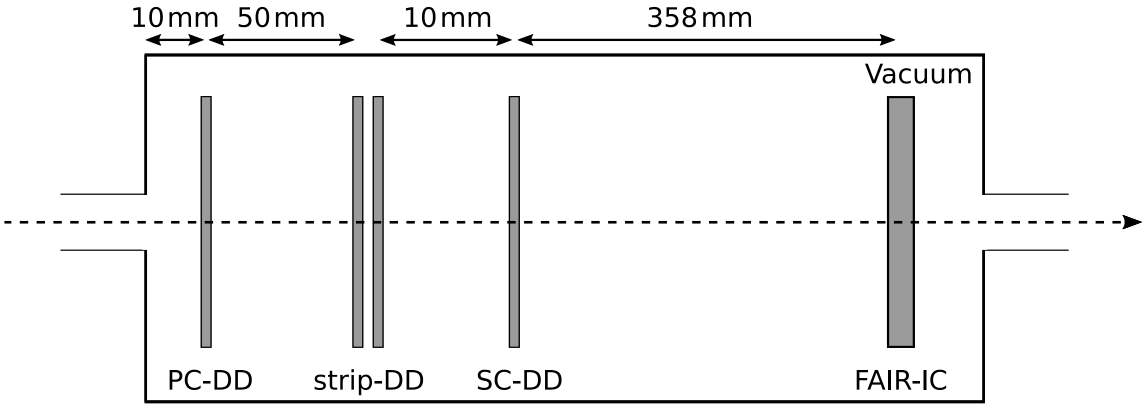

Figure 3.3.: Schematic layout of the first run. All diamond detectors and the IC inside a gas pocket were placed in a vacuum chamber.

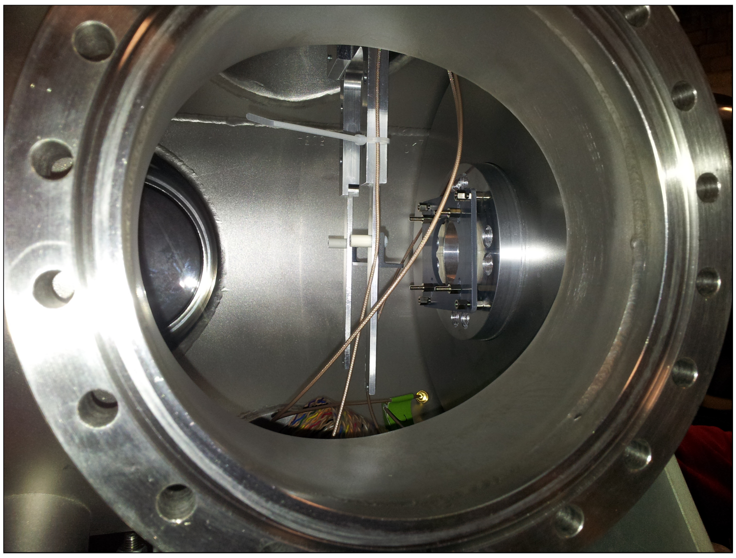

Figure 3.4.: Inside the vacuum chamber (the flange in the front has a diameter of about 20 cm). The beam entered from the right. On the right of the picture a grey plastic board (width about 10 cm), used to mount the PC-DD, is visible.

the position of a traversing particle to be determined in x- and y-direction. Next in line a SC-DD was mounted. The SC-DD served as reference detector, delivering the absolute particle count[7]. SC-DD and strip detectors were mounted on the same holder, shown in Figure 3.5. The holder was attached to a pneumatic pump, visible on the top right of the vacuum chamber in Figure 3.2. It allowed to remotely pull out the strip detectors and the SC-DD from the beam line at any time. At the last position the gas pocket housing the IC-prototype had been placed. A constant flow of P10 was provided to the pocket, sustaining a homogeneous and continuous distribution of the detector gas within the IC. The beam time was split into phases of long irradiation at the highest possible intensity and into short phases to record

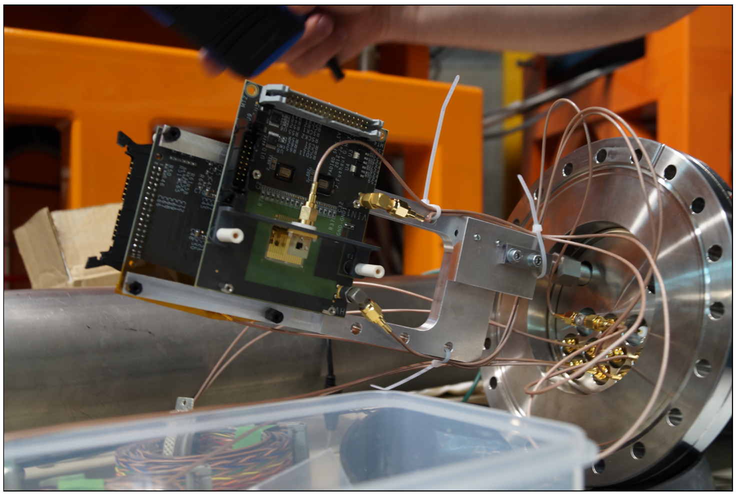

Figure 3.5.: SC-DD and strip-DDs mounted on an aluminum holder (length about 30 cm, width of flange about 20 cm). The holder was connected to a pneumatic pump. On the right the precise alignment of the detectors using a laser adjustment tool is shown.

---

[7] The count efficiency of a SC-DD was assumed to be 100 %. This was confirmed in a later test, described in chapter 5.4

data at a wide range of intensities. The long phases aimed at depositing the largest possible radiation dose at the PC-DD to investigate its radiation hardness. In the short phases of varying beam intensity SC-DD and strip-DD were inserted into the beam line, too. Count-rate records of all detectors were taken at different beam intensities for a calibration of the IC current vs. the SC-DD count rate. Additionally, the waveforms of the SC-DD and PC-DD were recorded to analyze their signal shape and thereby the detector properties with on-going irradiation.

The deposited dose at the PC-DD was maximized by transmitting the maximal possible ion intensity to the 0° beam-line and simultaneously reducing the irradiated area at the detector. In the experiment the spot size was reduced by focusing the ion beam at the third quadrant (Q3). The focus was improved by using the position information of the strip detectors and the PC-DD quadrants.

Second Run

During the first run, beam fluctuations and electronics problems did not allow all data to be analyzed in an unambiguous way. A second run was carried out, which used a simplified and better controllable setup, shown in Figure 3.6. The second setup refrained from using strip detectors. Instead, a brass collimator, with a diameter of 2.6 mm and a thickness of 30 mm, was fitted into the entrance of the vacuum chamber. Because of the collimator, the maximal intensity possibly traversing the detectors decreased but the beam spot position and diameter at the detectors was fixed. Similar to the first run, the PC-DD was mounted on a plastic board, directly attached to the entrance of the vacuum chamber, but slightly off-centered to allow the beam to impinge on Q4 only.

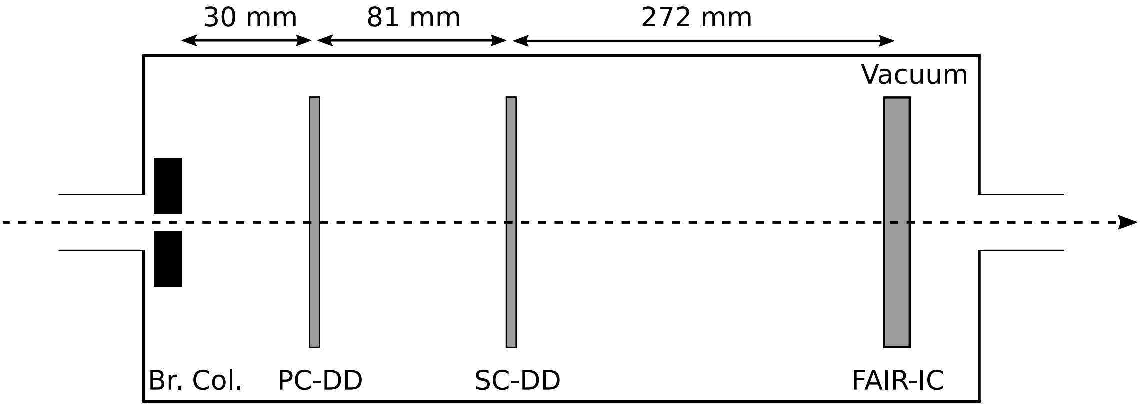

Figure 3.6.: Schematic layout of the second run. A brass cylinder was placed into the entrance windows serving as collimator. On the other hand the strip detectors were removed.

However, the mounts only allowed a positioning with a precision of ±1 mm at best. The exact extrapolation of the quadrant positions was later performed by matching experimental results and LISE++ beam simulations.

The general experimental procedure of the second run again combined long irradiation phases to deposit large doses of irradiation at Q4 with short phases of varying beam intensities. In those short phases count rates of all detectors and waveforms of the PC-DD and SC-DD were recorded at different ion-beam intensities.

In Figure 3.7 a schematic layout of the diamond detector read-out is shown. The SC-DD and each quadrant of the PC-DD were connected to diamond broadband amplifiers[8]. The amplified analog signal was sent to a signal-splitter. While one copy of each signal was sent to a digital oscilloscope[9] to record the signal's waveform, another copy was sent to a leading edge discriminator (LED), converting the analog signals into logical pulses. These pulses were counted by a VULOM3 scaler module.

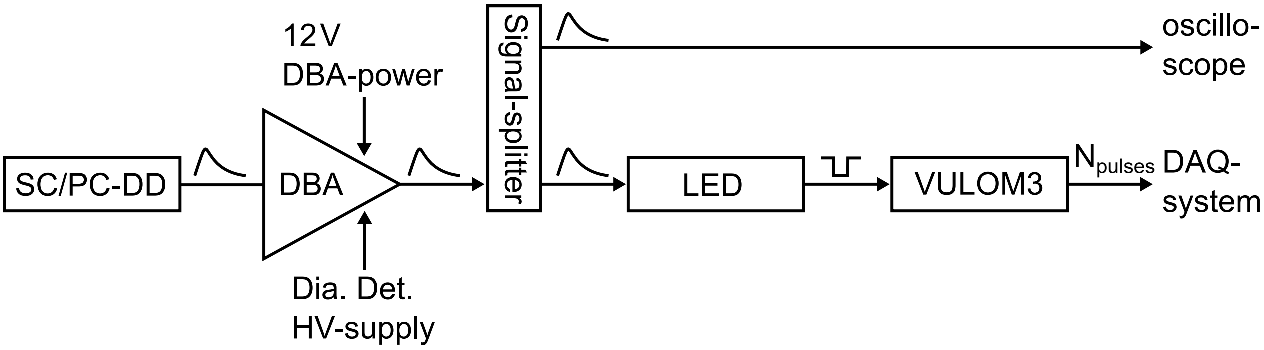

Figure 3.7.: Schematic layout of the read-out electronics connected to the SC/PC-DD.

In Figure 3.8 a schematic layout of the ionization chamber read-out is shown. The measured current is concerted into logical pulses in a current digitizer (CD). The pulses were counted using a scaler module (Run 1: VULOM3, Run 2: CAEN V830).

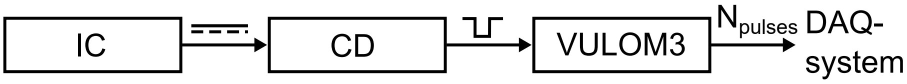

Figure 3.8.: Schematic layout of the read-out electronics connected to the IC.

In Figure 3.9 a schematic layout of the strip diamond detector read-out is shown. The detector is mounted on a PADI7-board featuring internal signal amplification and discrimination. The logical signals from the strip-DD were fed to the same scaler module like the logical signals from IC and SC/PC-DD.

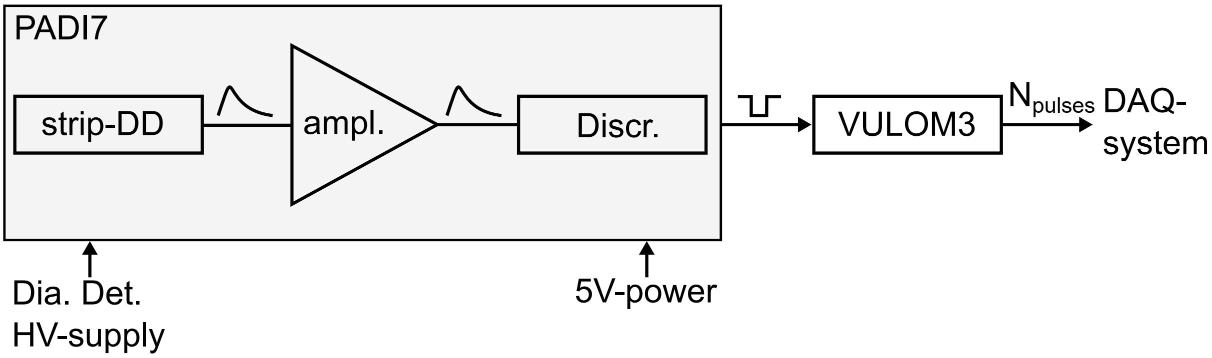

Figure 3.9.: Schematic layout of the read-out electronics connected to the strip-DD.

---

[8] Model: DBA-III [67]

[9] Model: LeCroy WaveRunner 620Zi [74]

The scaler modules were read out by a MBS-based data acquisition to record the number of pulses each time the DAQ was triggered. In both runs a 10 Hz clock had been used to trigger the DAQ. The trigger initiated the read-out of the count values saved in the memory of the scaler module. While minimizing dead time, this simplified trigger system merged a large number of events, without assigning any event specific IDs. No data, except the number of counts within the 10 Hz period were saved. Hence, it was impossible to only analyze events fulfilling specific conditions.

3.4 Test and Characterization of the Ionisation Chamber

The first step of studying the functionality of the ionization chamber was to observe the measured current at different values of applied voltage was recorded while keeping the ion intensity constant. This characteristic voltage line of the detector is shown in Figure 3.10. Within the error bars the IC showed current independence from the applied voltage. The voltage of the IC for the experimental measurements was set to 560 V, since the number of counts of the digitizer output was stable at this voltage. At the same time the measured noise was low and no electrical breakthroughs were observed. Because later measurements of the beam intensity including the diamond detectors showed beam intensity fluctuations, it is not clear if the secondary IC current really was independent from the voltage or if the fluctuations observed later did also occur during the current measurement, and therefore, no statistically significant statement about the characteristic voltage line of the IC can be made[10].

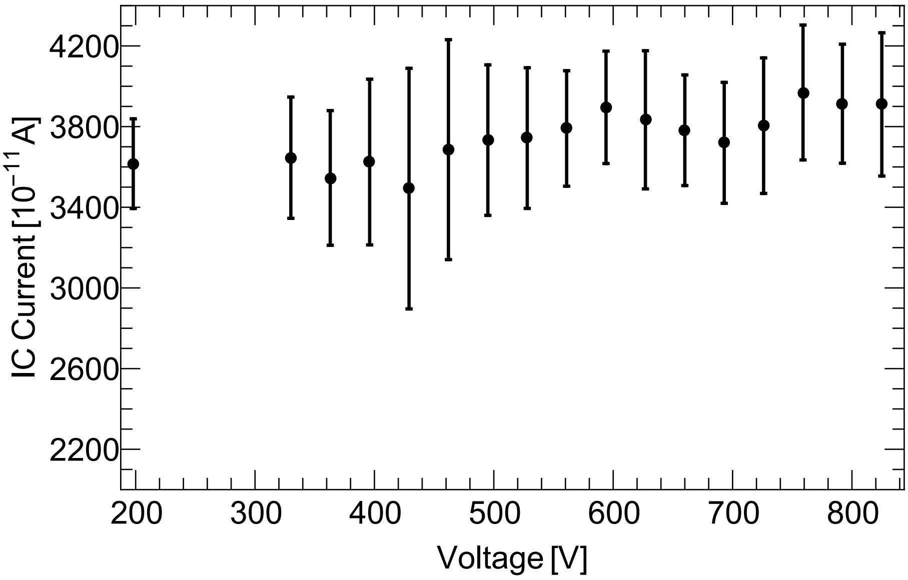

Figure 3.10.: Measured IC current at different supply voltages.

When comparing the counts of each detector a correlation between the counts measured by each detector was found. In Figure 3.11(a)-(c) excerpts of count spectra regarding SC-DD, PC-DD and digitized IC current counts are shown. These spectra were recorded in the first run. Because the beam

---

[10] Another record of the characteristic line, presented in chapter 4.3, confirmed a voltage independent behavior at 500 V to 1000 V.

spot size was larger than the active area of the SC-DD, the PC-DD recorded more counts per second, despite having a lower count efficiency. For the shown spectra ratios of $N_{\mathrm{PC}}/N_{\mathrm{SC}}=2.85\pm0.17$ and $N_{\mathrm{IC}}/N_{\mathrm{SC}}=(2.10\pm0.14)\cdot10^{-2}$ were found. For regions of approximately constant ion-rates the ratio is constant. Fluctuations of the ratio are only visible at times the intensity significantly changes. Later measurements in the experiment showed a beam spot size varying with intensity. Furthermore, the beam spot size was larger than the SC-DD's active area. Hence, the ratio can be assumed to have been constant except when intensity changes induced varying geometrical losses. Based on the observed linearity it can be assumed that the detectors were working properly.

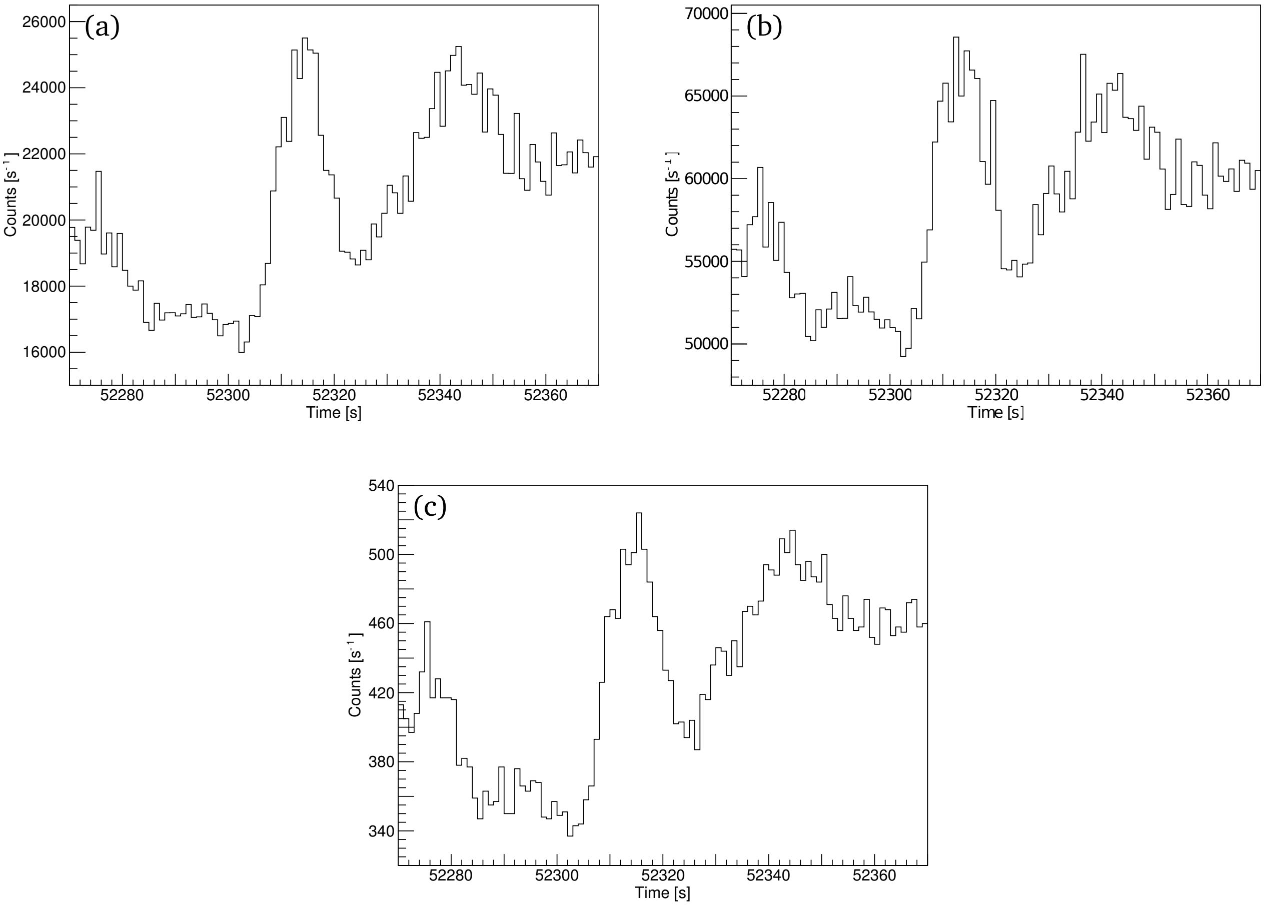

Figure 3.11.: Count spectra of the SC-DD (a), of the PC-DD (b), and of the digitized IC current(c). The SC-DD recorded less counts than the PC-DD due to a smaller active area and a large beam spot size. Spectra recorded in the first run with the VULOM3 scaler. Binning: 1 s.

In the second run, the digitized IC current was read out by a different scaler module. A malfunction of this CAEN scaler compromised the possibility to identify beam fluctuations in the IC and induced systematic uncertainties in the calibration. Another possible source for systematic uncertainties was electrical noise. The noise led to non-zero count rates for the IC current during beam-off periods and was found to be of negligible magnitude.

3.5.1 Run #1 - Calibration of the ionization chamber without collimator

The calibration of the ionization chamber was performed using the SC-DD as reference detector for the absolute particle count. The records of the strip detectors showed a random and not controllable change of the beam spot size at all times. Especially, when the intensity of the beam was changed by varying the slit sizes along the beam line or changing the attenuation factor large fluctuations occurred. As no collimator was placed in front of the detectors in the first run, the fluctuations led to varying geometrical losses at the smaller active area of the SC-DD. When comparing the counts of the SC-DD with the counts of the larger PC-DD a ratio of about 4 was found at lowest intensities. At increasing intensities the ratio decreased, which indicated that the PC-DD suffered geometrical losses, too. The data acquisition of the setup recorded the number of counts at each detector per trigger cycle of the clock. No detector was triggering the DAQ and thus, no event-by-event evaluation of the data was possible. In Figure 3.12 the beam spot recorded by the strip detector at high intensity is shown. The outer and inner yellow box are the projections of the PC-DD's and SC-DD's active areas, respectively. To produce a calibration plot of the SC-DD counts with respect to the IC current the ratio of counts, lying in and out of the inner box, was used to correct the SC-DD counts. A calibration of the ionization chamber, using the PC-DD was not possible. At medium to high intensities, large leakage currents caused shut downs of the HV-supply in irregular and not controllable intervals. The measured current of the IC was not corrected since it's diameter was significantly larger than the beam diameter. The final calibration plot of the IC using the

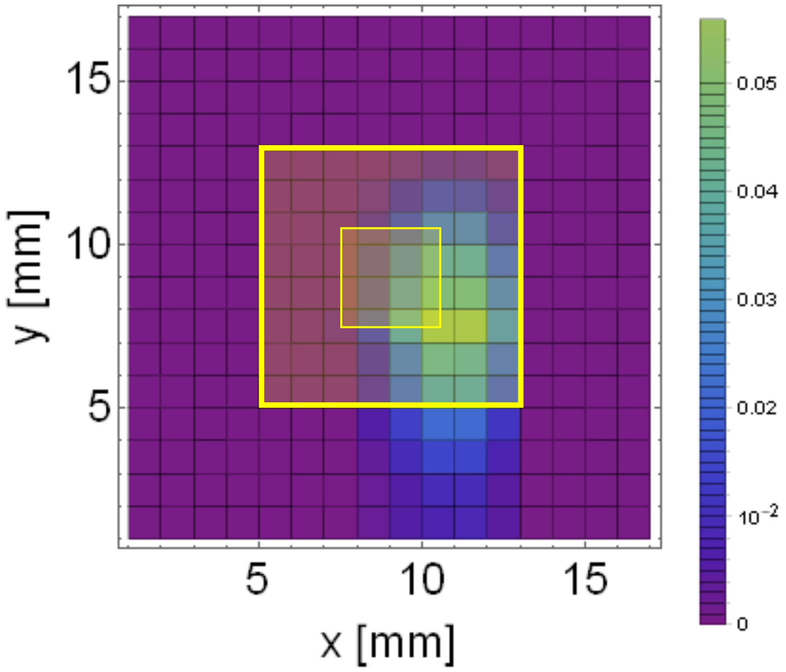

Figure 3.12.: Relative intensity distribution of the ion beam at rates in the order of a few MHz. The outer yellow box is the projection of the PC-DD, the inner box is the projection of the SC-DD.

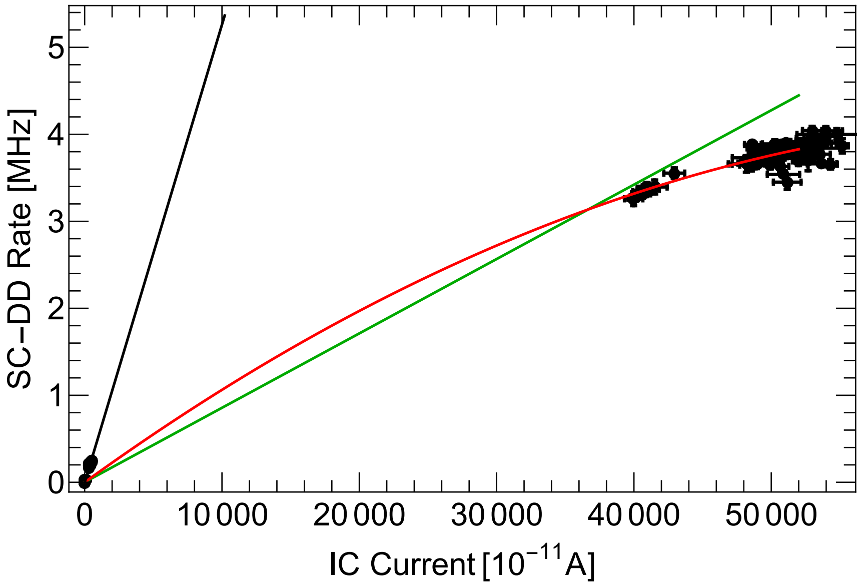

Figure 3.13.: IC calibration plot: SC-DD count rates vs. the digitized secondary IC current. No usable data records with data in the intermediate region between 1 MHz and 3 MHz were obtained.

SC-DD as reference can be seen in Figure 3.13. Linear and second-degree polynomial fit functions as

$$f_{\text{lin}}(I_{\text{IC}}) = b_1 I_{\text{IC}} + c_1, \tag{3.1}$$

$$f_{\text{pol}}(I_{\text{IC}}) = a I_{\text{IC}}^2 + b_2 I_{\text{IC}} + c_2, \tag{3.2}$$

were fitted to the data to find the linear calibration factor b, delivering the ion rate at all intensities with respect to the current measured at the IC

$$N_{\text{total}} = b \cdot I_{\text{IC}}. \tag{3.3}$$

The green line presents a linear approach including all data, the black line presents a linear approach limited to data below 1 MHz and the red line a polynomial approach limited to data above 1 MHz. Their linear coefficients b are presented in Table 3.1. While the black fit was able to describe the data points of lower rates, the red the data points of high rates and the green fit provided an average linear fit, none of the fits was able to describe the whole data range, and thereby the characteristic current-to-count curve of the IC correctly. The problem was aggravated by the absence of any usable data records, having

Fit	Fit function	Linear factor [10^{11}ions/A]
Black	lin. (fit only data < 2.5 MHz)	527 ± 6
Red	pol. (fit only data > 2.5 MHz)	114 ± 6
Green	pol. (fit all data)	86 ± 4

Table 3.1.: Different linear factors of the fit functions, applied to the calibration plot of run1.

data in the intermediate region between 1 MHz and 3 MHz. Further fit functions applied to the data were a polynomial fit, a root function, and a linear fit including exponential dampening, using multiple variations of lower and upper rate limits of the data in all cases. However, none of them was able to match the data.

3.5.2 Run #2 - Calibration of the ionization chamber with collimator

In the second run a collimator was put at the entrance of the vacuum chamber, leading to a constant size and position of the beam spot at the detectors. Still the area of the collimator bore was larger than the active area of the SC-DD and a fraction of the ion beam was passing the SC-DD without traversing the diamond material. Hence, the counts measured by the SC-DD had to be corrected for these geometrical losses.

$$N_{\text{total}} = G \cdot N_{\text{SC}}. \tag{3.4}$$

This correction factor G was given by the inverse of the fraction of ions traversing the active area

$$G = T_{\text{aa}}^{-1}. \tag{3.5}$$

The value of T_{aa} was obtained by simulating the ^{12}C transmission through the experimental setup, using *LISE++* [83]. A Faraday cup was inserted into the last possible position before the setup and yielded an ion current of (2.1 ± 0.1) nA. The other two parameters, variable in the input of the simulation, were the beam diameter and the angular divergence. These two were adjusted to match the given experimental constraints. Primary not scattered ions behind the collimator could not have a larger angle than 86.8 mrad due to a bore diameter of 2.6 mm and a bore length of 30 mm. The fraction of ions traversing the active part of the SC-DD was also fixed by the actual number of ions measured by the SC-DD itself. The last constraint was the actual count distribution of the individual PC-DD quadrants, shown in absolute and relative scales in Figure 3.14(a) and (b), respectively. The area of the beam spot size, which determines the number of counts per mm^2 was calculated in the LISE++ simulation. As men-

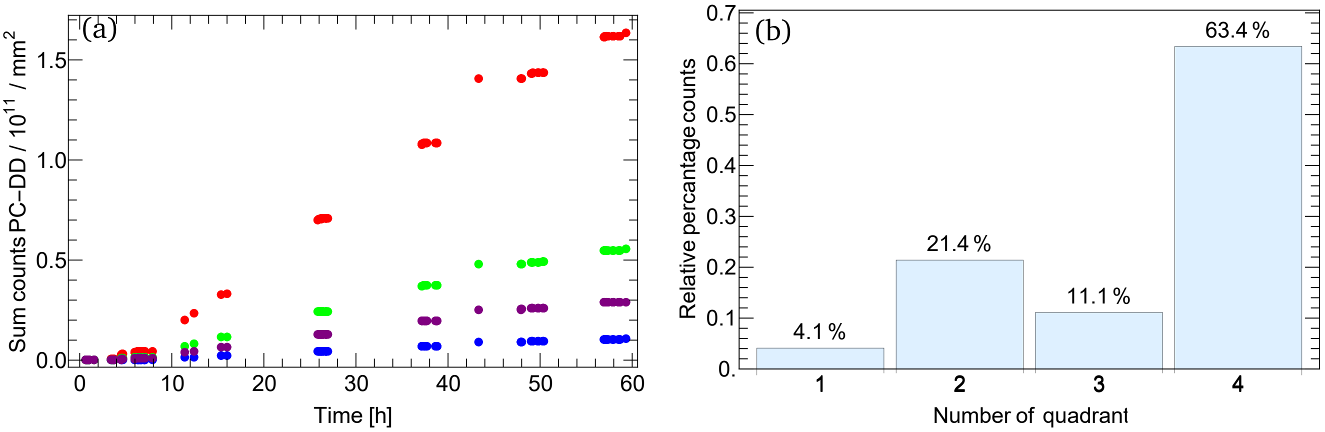

Figure 3.14.: Integrated number of counts of the PC-DD quadrants Q1 (blue), Q2 (green), Q3 (purple), and Q4 (red) in (a). Their relative fractions are shown in (b).

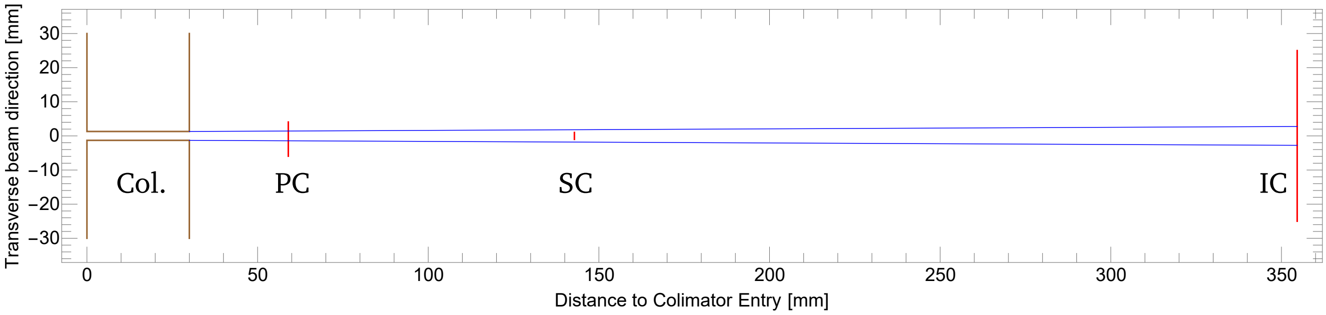

Figure 3.15.: Geometry of the setup in the second run. The blue line presents the FWHM of the beam envelope obtained with the beam simulation. The SC-DD suffered geometrical beam losses.

tioned above the positioning of the PC-DD had not been very precise. Thus, the position of the PC-DD, and thereby of the quadrants, was another variable to be varied simultaneously with the other input parameters of the simulation. Finally the simulation was recursively adjusted until the input parameters led to an exact description of the experimental constraints and measured values. A scheme of the FWHM environment of the simulated beam envelope is shown in Figure 3.15. PC-DD and IC completely cover the beam spot, while the SC-DD suffers geometrical losses. In Figure 3.16 the estimated spot size and position on the PC-DD are shown. Beam parameters were obtained by varying each quadrant's position in the simulation until the simulated and recorded count distributions matched. The beam spot had a diameter of 2.7 mm leading to an irradiated area of about 5.73 mm^2. The center position of the beam spot changed between the individual measurements by less than 100 μm and the spot itself was completely hitting the PC-DD at all times. Since the fluctuations of the beam spot center were homogeneously distributed in time and position around its central value, the average center of all beam spots was later used

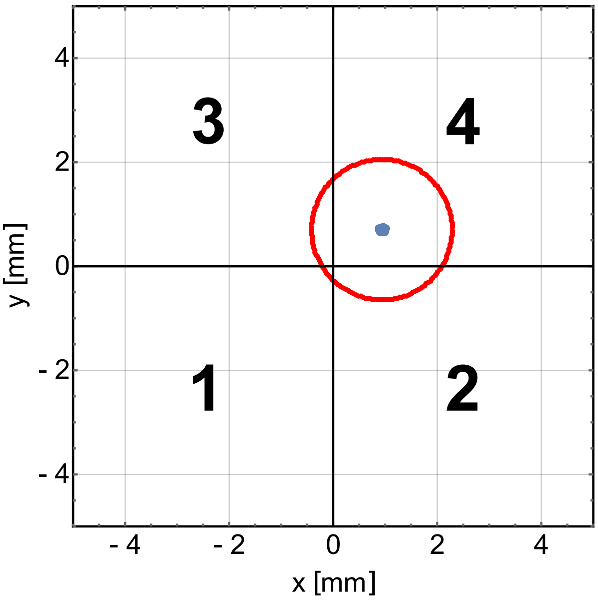

Figure 3.16.: Beam spot at the PC-DD during each of the measurements in the second run. The red circle describes the maximum diameter allowed by the setup's geometry, the blue dots the center of the beam spot.

to estimate the dose deposition on the individual quadrants. The resulting uncertainty was negligible compared to the uncertainties of the geometrical loss factor at the SC-DD and the linear factor of the calibration fit. After the simulation was adjusted to match the measured data as good as possible, the geometrical losses of the ion beam at the SC-DD were simulated. The transmission ratio through the active area of the SC-DD was determined to be $T_{\text{aa}} = (54.58 \pm 0.03)\,\%$ and the geometrical correction factor to $G = (1.832 \pm 0.001)$.

A better understanding and control of the beam characteristics and intensity in the second run compared to the first run also allowed to correctly adjust the current digitizer to one sensitivity setting through the whole experiment. The setting was high enough to deliver current counts at attenuated beam intensities, but the counts did not exceed the full scale of the CD while operating at full beam intensity. Hence, all measurements were performed without changing the settings of the CD. In Figure 3.17 the final calibration of the IC current vs. the SC-DD counts are shown. A linear and a second-degree poly-

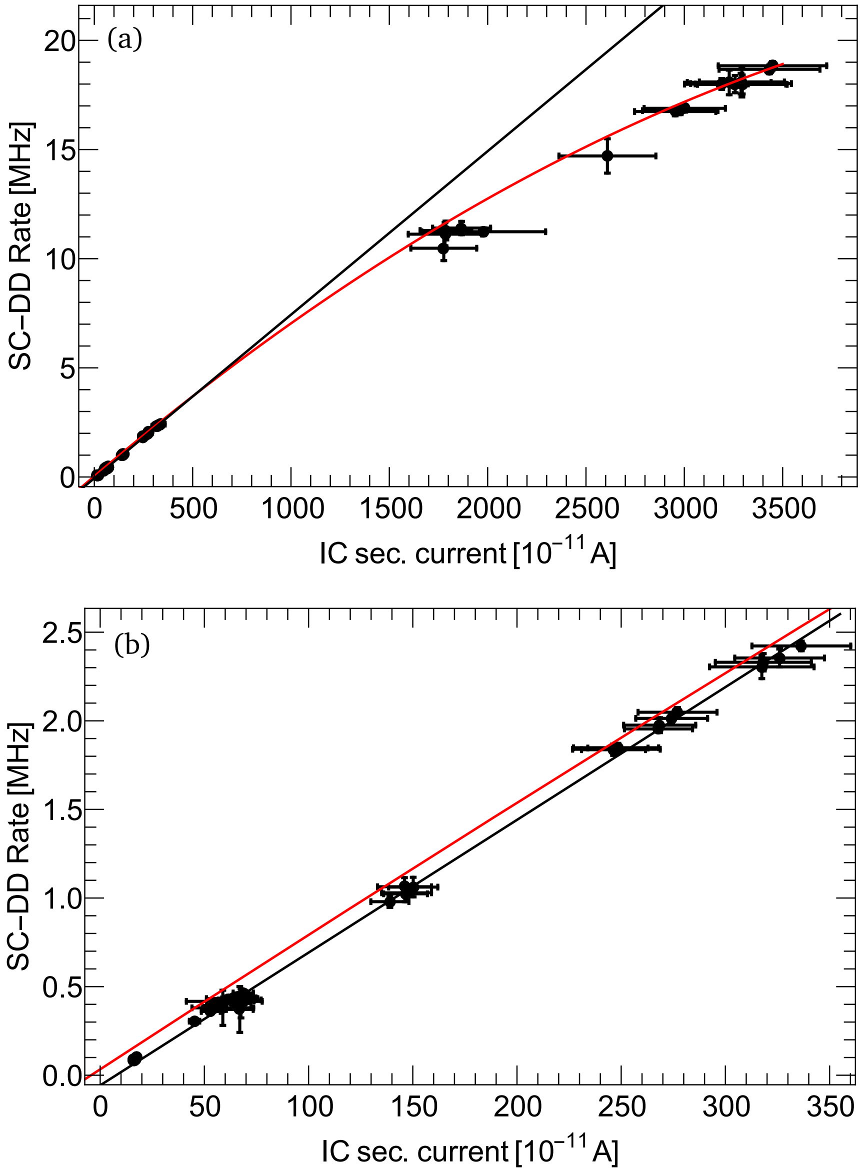

Figure 3.17.: Loss corrected count rates of the SC-DD vs. the digitized IC current. The red line is a polynomial fit including all data. The black line is a linear fit only including data below 2.5 MHz.

nomial fit function, as in Equation (3.2), were applied to the data. The whole data range and an excerpt zooming into rates below 2.5 MHz are shown in Figure 3.17(a) and (b), respectively. The determined linear factors are presented in Table 3.2. The polynomial fit delivered a linear parameter with an uncertainty of about 5.9%. Data points with rates above 10^7 Hz showed non-linear count decreases due to saturation of the diamond material and pile-up of the signals delivered to the discriminator. Furthermore the ion current, delivered by the cyclotron, grew more unstable for higher beam intensities, and thus, caused larger current and count-rate uncertainties. Most of the recorded data were at rates below 2.5 MHz, while the few data at rates above 10 MHz were separated by a large intensity gap. Hence, to improve the uncertainty of the linear factor a second fit in the more stable and less pile-up affected region below 2.5 MHz was performed. The linear factor of this fit had an uncertainty of 2.4%. The deduced linear factor was found to be within the uncertainty of the linear factor of the polynomial fit. Hence, for all further considerations the linear factor of the linear fit was taken.

Fit	Fit function	Linear factor $[10^{11}\text{ions/A}]$
Black	lin.	7491 ± 181
Red	pol.	7645 ± 452

Table 3.2.: Different linear factors of the fit functions, applied onto the calibration plot.

3.6 Total dose deposited at the diamond detectors

The calibration of the IC was necessary to estimate the accumulated counts and thus the deposited dose at the PC-DD. After determining the number of ions N traversing the detector, the deposited dose was calculated as

$$D = N \cdot \frac{E_{\text{loss}}}{A \cdot d}. \tag{3.6}$$

In Equation (3.6) A is the size of the irradiated area at the diamond material, d is the areal density or thickness of the material in units of $[\frac{g}{cm^2}]$, E_{loss}=36.59 MeV is the average energy loss of the carbon ions in the material and was given by LISE++ simulations. The accumulated counts per area from the first run are shown in Figure 3.18(a). In the first run the uncontrollable beam intensity and spot size, the frequent failures of the PC-DD HV-supply, and the large uncertainty of the IC calibration prevented a precise count estimation and only a lower and upper limit of the calibration factor of the IC were obtained. Thus, the change of diamond detector characteristics with increasing dose was only studied for the data of the second run. The counts of the first run provided a minimum dose estimation absorbed by the PC-DD in the first run. Data were provided by the IC current, translated to counts with the lower limit calibration factor ($86 \cdot 10^{11}$ ions/A, green fit in Table 3.1). The irradiated area was given by the strip-DD, if data were available, and else by the largest measured area of the beam spot. Finally a lower limit of about 0.9 MGy deposited at the PC-DD in the first run was found.

The accumulated counts per area from the second run are shown in Figure 3.18(b). Black dots represent the counts given by the calibrated IC, orange dots represent the counts given by the PC-DD itself. The irradiated area was given by the LISE++ beam simulation and had a constant value of about 5.73 mm^2

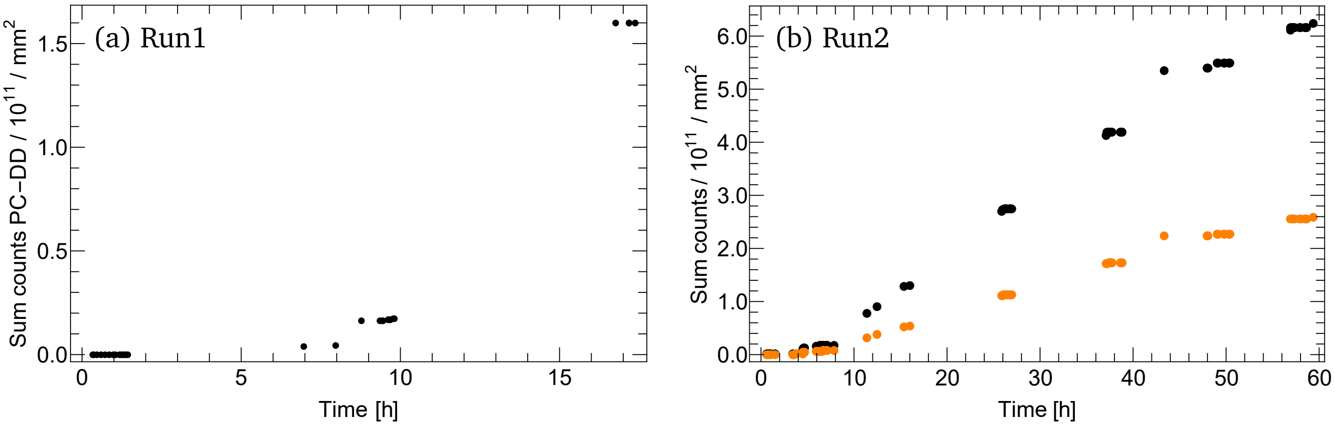

Figure 3.18.: Estimated number of ions that have traversed the PC-DD. In run1 the IC with the lower limit calibration factor ($86 \cdot 10^{11}$ ions/A, green fit in Table 3.1) provided the counts (a). In run2 counts were provided by the PC-DD itself (orange) and the calibrated IC (black) (b).

as can be seen in Figure 3.16. Furthermore the simulation showed a nearly uniform distribution of the beam intensity in the area of the irradiated beam spot, suggesting a flat distribution of the deposited dose over the whole irradiated spot. Taking only the counts delivered by the PC-DD itself, the total dose, delivered to the PC-DD during the second run, resulted to (1.43 ± 0.13) MGy. Using instead the counts delivered by the calibrated IC, the total dose of the second run resulted to (3.46 ± 0.31) MGy. As described above, the IC, contrary to the PC-DD, did not suffer from any losses or count inefficiencies. Hence, for all further considerations regarding the deposited dose the results based on the calibrated IC were used.

While the main goal of the experiment had been the investigation of the PC-DD, counts and waveforms of the SC-DD were recorded in the second run, too. Hence, the change of detector characteristics with on-going irradiation was studied for the PC-DD and the SC-DD. The SC-DD was pulled out during the long high-rate phases. Still a non-negligible amount of ions traversed the detector during the short phases. The number of carbon ions, measured by the SC-DD in the first and second run, is shown in the left and right of Figure 3.19, respectively. Since the beam spot size had been larger than the active area

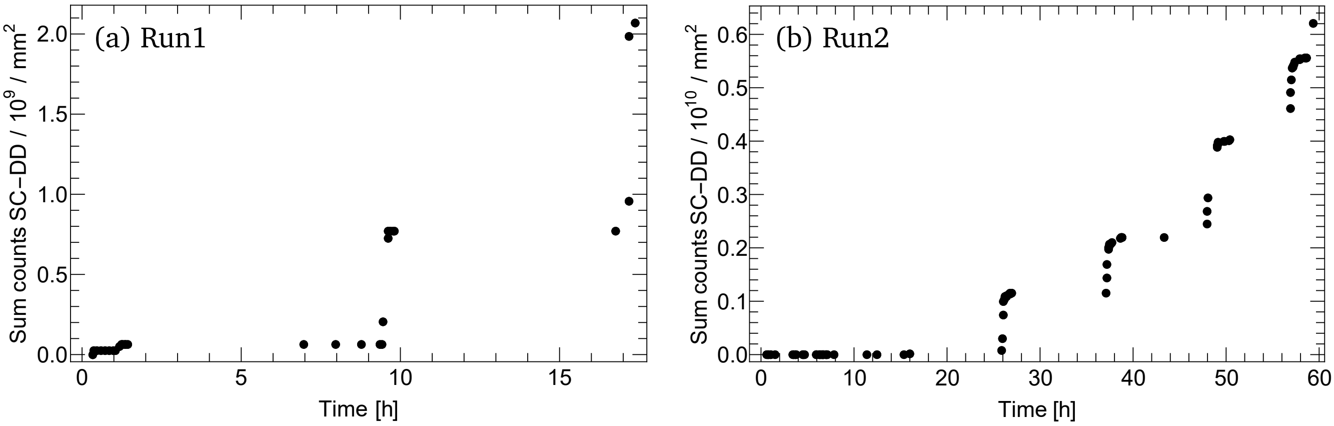

Figure 3.19.: Integrated counts of the SC-DD from run1 (a) and run2 (b). The SC-DD was only inserted in the short phases of varying beam intensities. The irradiation phases are best visible in (b).

of the SC-DD at all times, the irradiated area taken for the dose calculation was the detector area itself ($2\times2\text{mm}^2$). The average energy loss of the carbon ions in the SC diamond material was estimated by LISE++ simulation to be 19.39 MeV. Conclusively, doses of about 11.5 kGy and about 35.5 kGy were deposited in the SC diamond in the first and second run, respectively. Similar to the analysis of the PC-DD, the dose deposited at the SC-DD in the first run delivered an offset regarding the dose the SC-DD already absorbed before the second run.

3.7 Properties of the diamond detector after irradiation

In the second run the diamond detectors were analysed by recording waveforms at 18 points of irradiation over a period of 62 hours. Most of the points were taken at beam attenuation factors of 100 and 1000, to reduce the time the SC-DD was exposed to higher intensities, and thus, prevent to potentially damaging it. Each of the recorded points contained about 10000 waveforms. Before analyzing the signal shape itself, the waveforms were cleared of any background noise by performing a baseline adjustment (BLA). In Figure 3.20 two already corrected waveforms are shown. Waveform (a) was recorded before any irradiation and waveform (b) at the end of the experiment. Due to BLA the determined diamond properties, for example the signal amplitude or rise time, were independent from the background and comparable for all data points. Two waveforms, shown in Figure 3.20, were recorded at the beginning and at the end of the test experiment, respectively. Before performing a detailed analysis of the diamond properties, they already allowed a first guess of the evolution of the PC-DD properties, after receiving a large radiation dose. Between the upper and the lower waveform a dose of about 3.5 MGy was deposited at the PC-DD. Still both waveforms look nearly the same, suggesting a non-significant damage of the PC material.

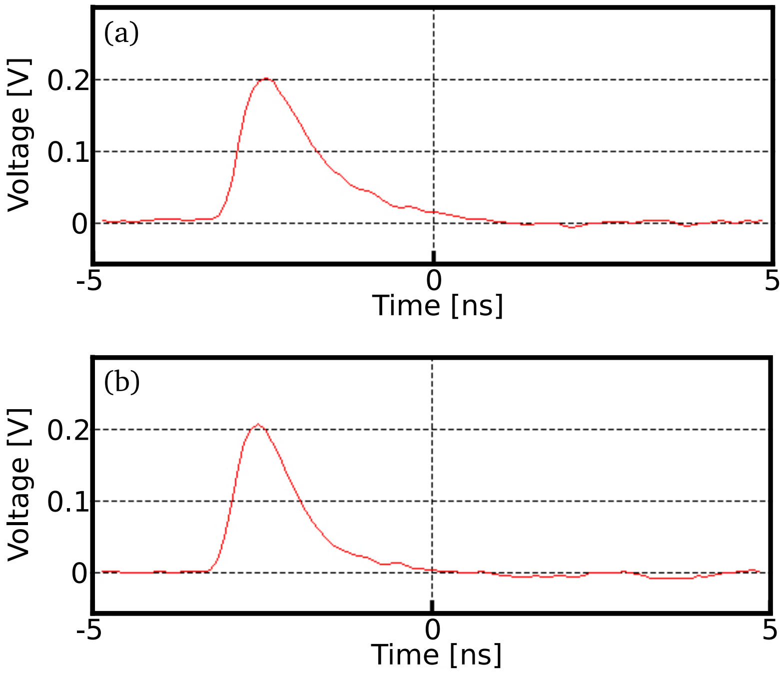

Figure 3.20.: Waveforms of the PC-DD quadrant after subtraction of the background. Waveforms of Q4 before (a) and after (b) irradiation are shown. No significant change is visible.

The detailed analysis showed similar results. After performing the BLA, the waveforms were analysed with regard to their signal amplitude, total collected charge, signal rise time, and signal slope at the leading edge. The amplitude was given by the signal peak. The collected charge was obtained by fully integrating the waveform signal. The signal rise time was determined by measuring the time the signal took in the leading edge to climb from 10% to 90% of the signal peak and the leading-edge slope was determined by a linear fit applied to the edge between the 10% and 90% points.

If the PC-DD diamond detector had been damaged due to the irradiation, this should have led to a visible change in the signal shape. Damage would have led to charge losses and a broader signal shape, observable by a lower signal amplitude, less collected charge, a decrease of the slope and an increase of the rise time if the signal width grows faster than the amplitude decreases. These values were determined by the same procedure, as described above, for each of the 10000 waveforms of each point. The resulting values showed a Gaussian-shaped distribution for each of the properties. The final average values were given by the median of Gaussian fits, applied to these distributions. Given uncertainties of the PC-DD properties relate to the 1σ environment of the Gaussian fits. The evolution of the PC-DD properties during the second run versus the absorbed dose is shown in Figure 3.21. The presented values refer to waveforms recorded at ion rates in the range of 10 kHz to 100 kHz. Signal amplitude and collected charge, shown in the left plot, stayed constant within the uncertainty of the data points during the whole irradiation. The amplitude even showed an increasing trend[11] before it started to decrease at about 1.5 MGy. Rise time and slope of the PC-DD, shown in the right of the figure, stayed constant within the uncertainty. These properties also showed a rather improving, instead of an aggravating, trend. The rise time slightly decreased, and the slope increased over time. The data, regarding the evolution of the diamond properties, were all plotted versus the dose received during the second run, as provided by the IC. In the first run the PC-DD already absorbed a dose of at least about 0.9 MGy. Hence, the minimum dose deposited in total during the two runs was (4.4 ± 0.3) MGy. Judging from the evolution of the

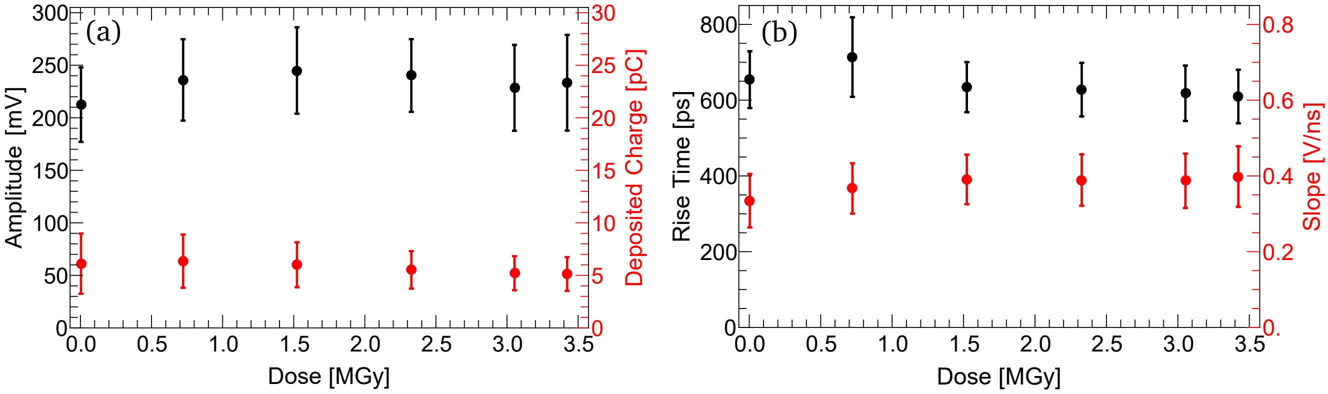

Figure 3.21.: PC-DD properties with increasing dose. Data recorded at rates of 10 kHz to 100 kHz during the second run. The x-error bars, all having a relative width of about 9% of the dose values, were left out for better perception of the evolution of the detector properties.

---

[11] An increasing quality of the PC material is eventually induced by "pumping" [64, 70]. The carbon beam fills up deep holes in the diamond material, eventually faster repairing than destroying the material at the beginning of irradiation. However, the effect is not well understood, yet.

detector properties it can be safely stated that polycrystalline diamond detectors are properly operating, even after having received a dose in the order of MGy.

The properties of the SC-DD, on the other hand, were observed to decrease. Figure 3.22(a) shows the amplitude distribution of the SC-DD before any irradiation. After absorbing a dose of 10 kGy up to 80 kGy all distributions looked similar to Figure 3.22(b). Finally, Figure 3.22(c) shows the distribution after absorbing a dose of more than 80 kGy is presented. Distribution (a) shows the behavior of the undamaged SC-DD. After receiving a certain amount of radiation some parts of the SC-DD were probably damaged. Distribution (b) is a mixture of signals completely generated in the damaged area (peak at 280 mV and signals passing the partly damaged area (amplitude straggling). The assumption about the 280 mV-peak is supported by the third distribution. After absorbing a large dose only the small peak is visible. The further decrease of amplitudes slowed at this point and showed a behavior with slight similarities to the evolution of the PC-DD properties. All doses mentioned above were the values received in the second run and did not include the dose received in the first run. The absorbed dose

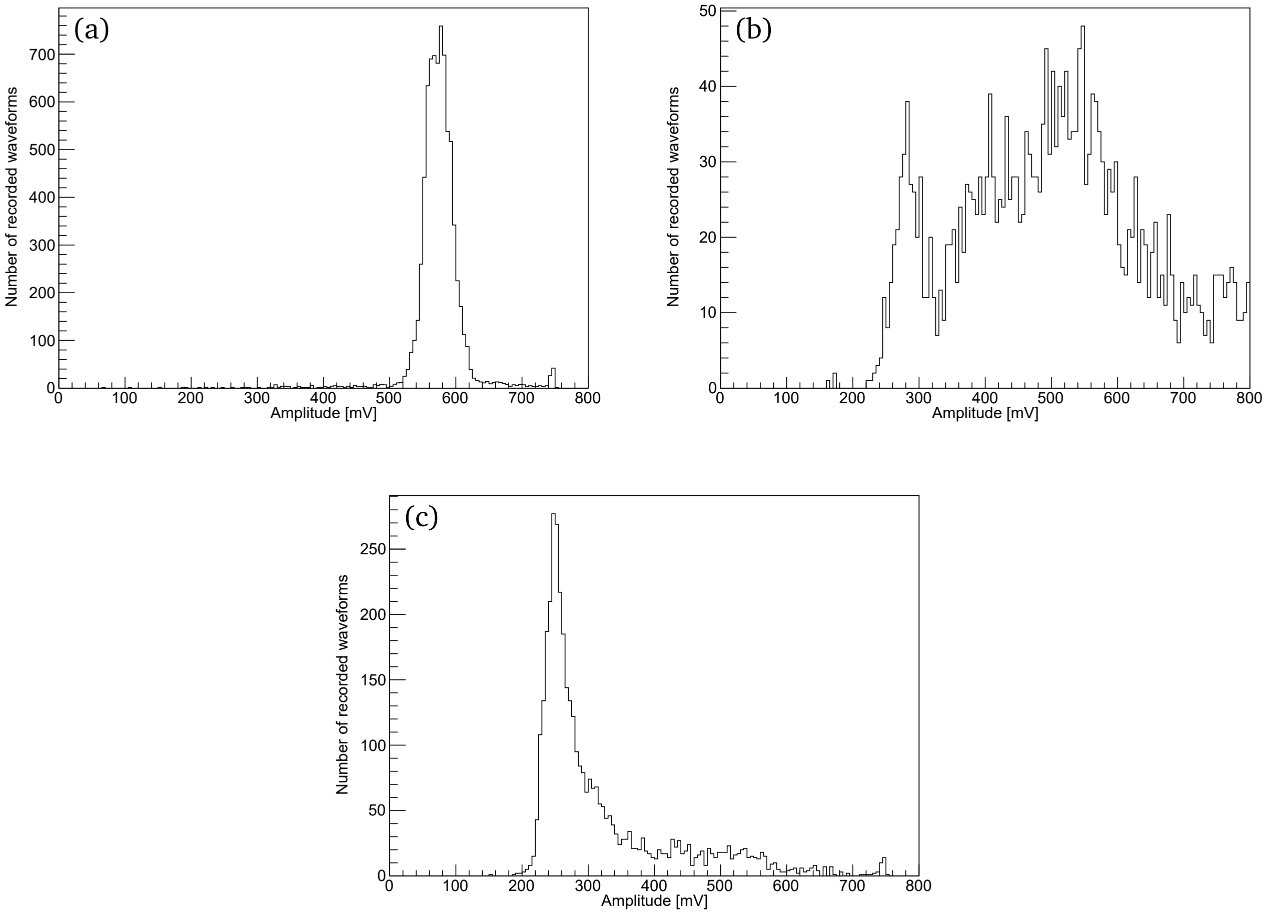

Figure 3.22.: SC-DD amplitude distributions in the second run. The first was recorded before any irradiation (a). Records between 10 and 80 kGy were all similar to distribution (b). Distribution (c) was recorded after absorbing more than 80 kGy. The integrated number of recorded waveforms is 10000 in all three histograms.

during the first run was calculated to be at least 11.5 kGy. Conclusively this means, the SC-DD started to show deteriorating properties after absorbing a dose of at least 21.5 kGy and featured a homogeneously reduced signal output after at least 91.5 kGy.

3.8 Time of Flight

The time-of-flight resolution can be a measure of radiation hardness, too, when discriminator thresholds are kept the same. A stable distribution of the measured time of flight with on-going irradiation is correlated to a high radiation hardness. The time of flight between the SC-DD and the PC-DD recorded at the beginning and at the end of run2 is shown in Figure 3.23(a) and (b), respectively. The distribution was recorded with the scope introduced in chapter 3.3 and provided a binning of 100 ps. Start and stop time were determined by the time when the height of the signals at the leading edge reached 50% of the amplitude. Hence, any damage leading to a significant change of the signal shape of SC-DD or PC-DD has an impact on the measured resolution of the ToF distribution.

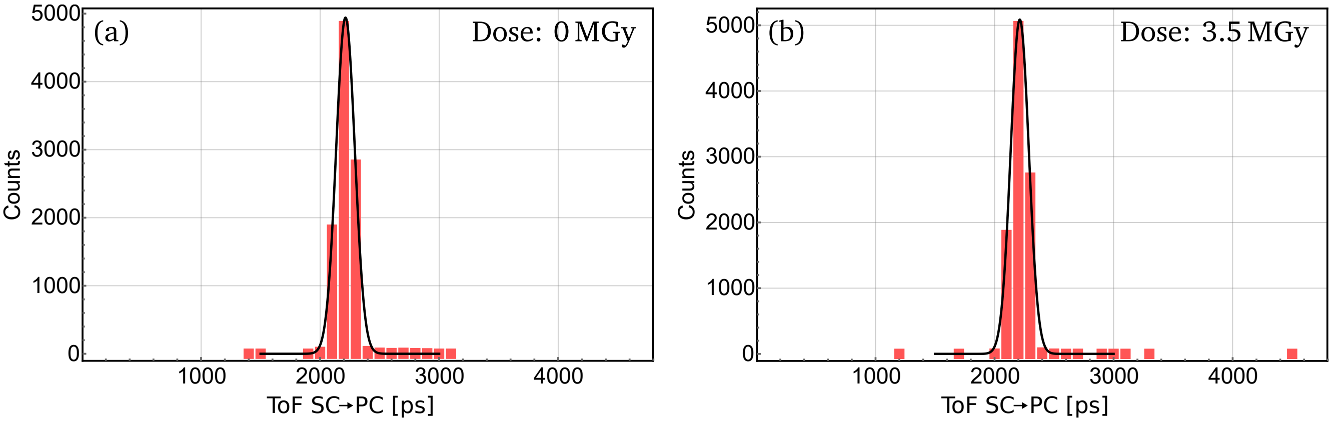

Figure 3.23.: Time of flight of the carbon ions between the SC-DD and the PC-DD. The distributions were recorded before irradiation (a) and the end of the experiment (b) after the PC-DD received a dose of about 3.5 MGy. Recorded at a binning of 100 ps with a scope.

Distribution (a) and (b) were recorded at the beginning and the end of the second run, respectively. Examples of the corresponding signal shape of the PC-DD were given above in Figure 3.20. The ToF-resolution of distribution (a) amounted to $\sigma_{\text{tof}}=(78 \pm 7)$ ps, the resolution of distribution (b) to $\sigma_{\text{tof}}=(76 \pm 8)$ ps. As expected from the results discusses above no significant difference of the measured resolutions was observed. This further confirmed the high radiation hardness of the PC-DD and the capability of using diamond detectors even after large doses of irradiation as time of flight detectors. However, the ToF-resolution from this experiment is no benchmark for the achievable best resolution since setup and electronics were not optimized for time-of-flight measurements[12].

---

[12] Dedicated time of flight measurements performed at the GSI in 2015 obtained $\sigma_{\text{ToF}} = 45$ ps [69]

3.9 Summary

The test experiment performed at the LNS in 2015 delivered several data sets regarding the IC-prototype performance and the radiation hardness of the single- and poly-crystalline diamond detectors. All data were recorded using a ^{12}C beam at 62 MeV/nucl.

Comparisons between the single-crystal diamond detector, polycrystalline diamond detector and the ionization chamber yielded the following results:

- At all rates the IC-prototype showed a linear correlation with respect to the other detectors[13].
- A linear correlation of the SC-DD counts with respect to the secondary IC current was found for all recorded rates[13].
  → At ion rates above 2.5 MHz, non-linear count effects of the SC-DD were visible.
- A calibration of the IC using the SC-DD as reference detector was possible within an uncertainty of about 2.4%
- The PC-DD signal properties were nearly unchanged after 4.4 MGy

These results show that the IC-prototype was working properly and at a reasonably small enough uncertainty to be used as part of a particle detector combination at the Super-FRS. Furthermore, the properties of the PC diamond detectors, extracted from the waveform records, did not show a significant decrease of quality over the period of irradiation. A high radiation hardness of these detectors was proven, allowing them to be operated in high-radiation environments over extended time periods. This makes them a suitable choice as particle monitor along the Super-FRS beam line. Further test experiments dedicated to investigate if the uncertainty of the IC-prototype can be further improved and to measure the absolute count efficiency of the PC-DD were conducted at GSI in 2016 and at LNS in 2017, respectively. These experiments are presented in the following chapters.

---

[13] Rates at which the diamond detectors showed saturation effects were excluded

4 Precise Calibration of the Ionisation Chamber - GSI Darmstadt 2016

The measurements in Catania 2015 succumbed to various assumptions like a SC-DD counting efficiency of 100 %[14] and a simulated correction factor regarding the geometrical losses of the beam at the SC-DD. An additional test of the same IC-prototype was proposed and performed at GSI in 2016. This time the reference counting detector was a plastic scintillator which was mounted behind the ionization chamber. This test aimed at the following measurements:

- Study the response of the IC-prototype versus a ^{124}Xe-beam at 200 MeV/nucl., slowly extracted from the SIS18-synchrotron.
- Determine the most accurate calibration of the IC at rates in the order of 10^4 to 10^6 ions per spill.
- Investigate the influence of cable lengths to the current digitizer on the accuracy of the measurement.

The experiment was carried out at the HTC beam line in cave C at GSI. Hence, the detectors were irradiated with a beam with spill structure, contrary to the test at the LNS, at which the detectors were irradiated by a quasi-continuous ion beam.

4.1 Experimental setup

The setup was completely mounted in air. After the beam-pipe exit the IC was positioned, inserted into the same gas pocket (see appendix B.2) that was used in the experiment at LNS. A plastic scintillator (SCI), operating as reference detector for the absolute particle count, was mounted directly behind the gas-pocket. The BC 420 scintillation material had an active area of $220 \times 100\,\mathrm{mm}^2$, with the long side aligned along the horizontal direction. The plastic scintillator was connected to photomultiplier tubes (PMT) on both horizontal sides.

The ionization chamber and the plastic scintillator were irradiated by a ^{124}Xe-beam at 200 MeV/nucl. The spill length varied between 4 and 5 s with breaks of about 10 s between each spill. Intensities in the order of $10^4 - 10^6$ ions/spill had been delivered to the experiment. The highest intensity was about one order of magnitude smaller compared to the intensity in the previous experiment at the LNS. On the other hand the charge number of xenon $Z = 54$ is significantly larger than the charge number of carbon $Z = 6$. LISE++ simulations predicted an average energy loss of about 10 MeV for the xenon ions in the IC, compared to 0.3 MeV for the carbon ions during the LNS experiment. Thus, the current was expected to be larger compared to the first test experiment, despite lower intensities. The LISE++ simulations also confirmed that neither plastic scintillator nor IC suffered any geometrical losses.

4.2 Data Acquisition

Schematic layouts of the SCI and IC read-out electronics are shown in Figure 4.1 and 4.2, respectively. The light produced in the SCI was converted into analog electrical signals in the PMT. The analog signals

---

[14] This was shown to be correct in a later experiment, presented in chapter 5, but not known for certain at this time.

were forwarded to a leading edge discriminator (LED) and converted into digital signals. All digital output pulses of the discriminator were splitted and the copies were sent to a VULOM3 scaler module and - after pulse stretching in a gate generator - to the same scaler module. Finally, the scaler module was read out by a MBS-based data acquisition. The stretched pulses were used to check if the pulse widths of the signals directly coming from the LED were too short to be properly registered by the electronics. If this had been true the channel counting the narrower signal would have counted less signals than the channel counting the stretched signals. The IC was connected to two CD1012 current digitizer (CD) modules at different sensitivity settings. One was adjusted to a full-scale setting of 10^{-7} A and the other to 10^{-8} A. The module at higher sensitivity should guarantee a high resolution during lower beam intensities. The module at lower sensitivity was set up in the case the beam intensity and consequently the measured IC current should exceed the linear region of the first module. Later measurements showed no differences of their counting behavior, at any beam intensity. The only exception was a constant offset, not affecting the calibration of the IC. Hence, for all further considerations the counts coming from the current digitizer set to the higher sensitivity was used to reduce statistical uncertainties. In this experiment a 10 Hz clock, a 100 Hz clock and all signals from the left-side PMT were used to trigger the DAQ.

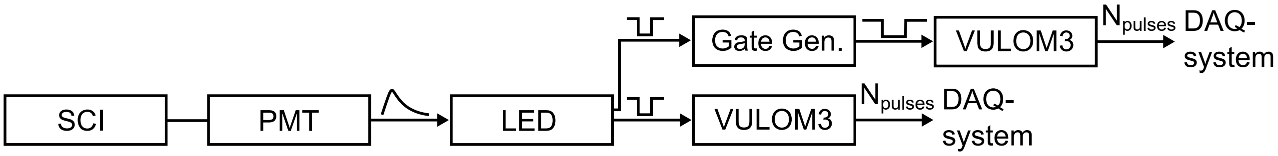

Figure 4.1.: Schematic layout of the SCI read-out electronics.

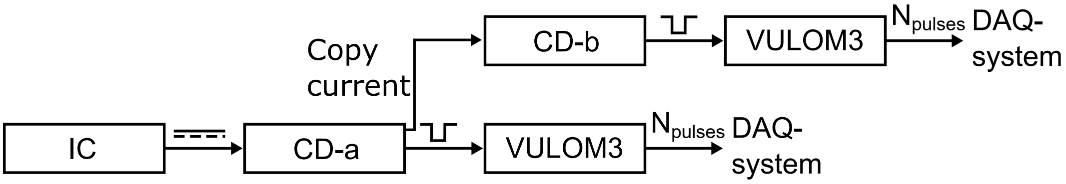

Figure 4.2.: Schematic layout of the IC read-out electronics.

4.3 Test and characterization of the ionization chamber

For comparing the measured current with the absolute particle count obtained by the plastic SCI, Figure 4.3(a) shows the digitized IC current, and Figure 4.3(b) the corresponding SCI counts. The IC current was recorded with a current digitizer sensitivity of 10^{-8} A FS, meaning, one digitizer count estimated to a measured current of 1 pA. The shown IC spectrum is already noise corrected. The spill structure of the beam provided a measurement of the noise. In the time between two spills the SCI did not count anything and thus, only the clock triggered the DAQ. The IC spectra on the other hand showed a nearly constant amount of counts at each clock trigger in this period. These counts were related to electrical noise and the average noise level was estimated. Measured noise levels were in the order of 150 pA s^{-1}. The spectra yielded a similar response of IC current and SCI counts. Scintillators and current sensitive

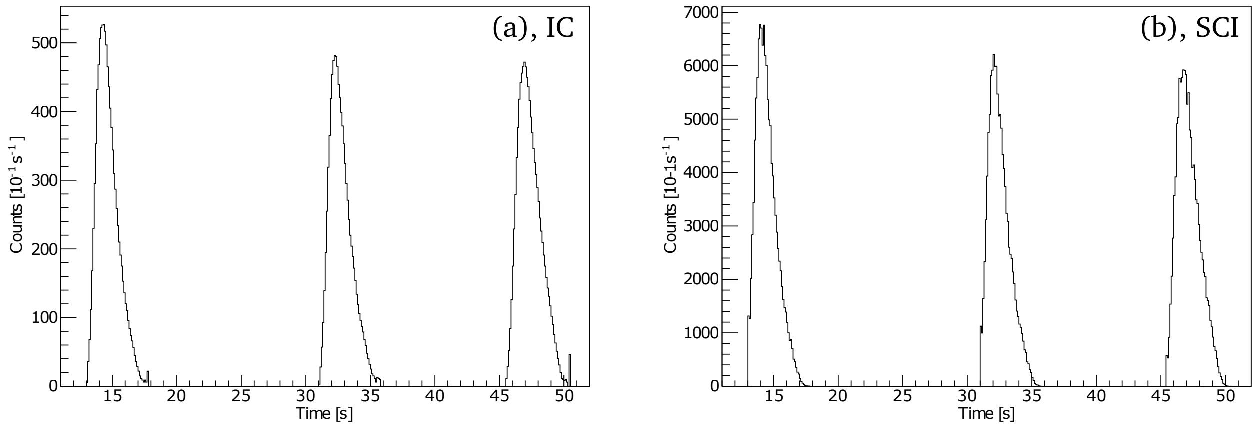

Figure 4.3.: Count rate of ion spills as given by the SCI (a) and the digitized IC current (b). Binning is 10 Hz, digitizer sensitivity is 10^{-8} A FS. The IC-spectrum is already noise corrected.

detectors have a slightly different shape of the signal response when operated in a spilled beam. Therefore, usually not the integrated counts of specific time intervals but the integrated counts of each spill are compared [85, 86]. A rough comparison of the count ratio in Figure 4.3 yields $N_{\mathrm{SCI}}/N_{\mathrm{IC}} = 12.5 \pm 0.2$ for each spill and thereby a first proof of the linearity of the detectors with respect to each other. A detailed comparison of IC current and SCI counts is shown later in chapter 4.4.

The next step was to determine the characteristic work function of the ionization chamber, see Figure 4.4. It shows the average IC current per ion traversing the SCI. Count rates of SCI and IC were simultaneously recorded at different stages of voltage applied to the IC. Measurements were taken in steps of 100 V between 400 V and 1500 V. At each step the measured IC current, background counts due

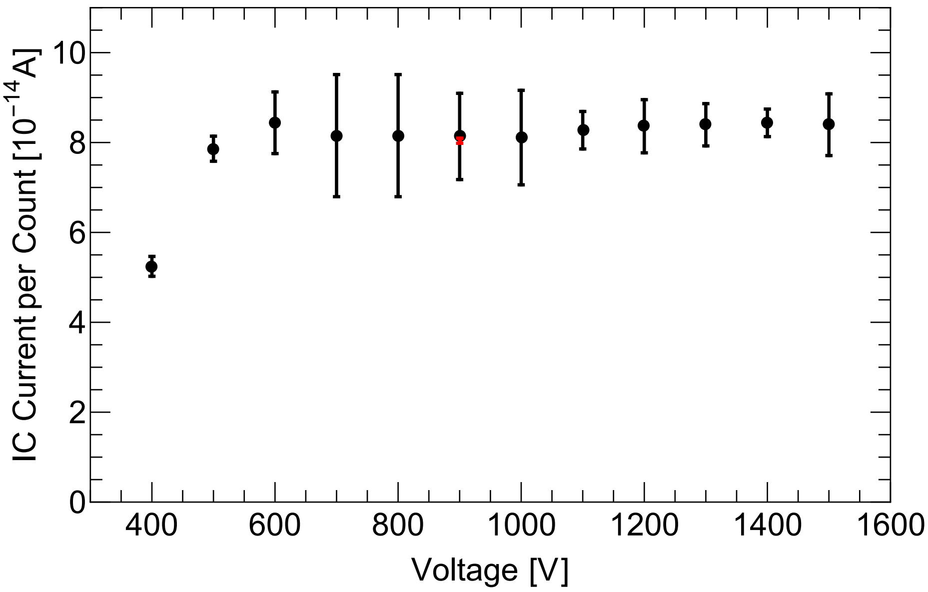

Figure 4.4.: Characteristic work function of the IC. Each step was measured for 5-10 min. The later calibration runs were performed at 900 V. One of these longer (about 200 min) runs is indicated by the red point. It had a significantly lower uncertainty but yielded the same current yield per ion as the short measurement.

to electrical noise and the frequency at which electrical breakthroughs occurred in the IC were observed. Between 600 V and 1500 V a constant current per count yield was observed. Nevertheless, at voltages above 1000 V the current showed a slightly increasing trend, an increasing noise level and electrical breakthroughs occurred more often. This observation is in accordance with the prior measurements regarding the behavior of the IC-prototype noise, which was reported in chapter 2.2, Figure 2.7. The region between 700 V and 1000 V was more stable and had a nearly constant current-per-ion yield. Hence, 900 V was chosen as operational voltage for the detector, since this point showed the lowest uncertainty. Besides the small statistics when recording the characteristic voltage line (each voltage step was recorded for about 5-10 minutes), the resulting uncertainty of the yield was also effected by instabilities of the spill structure and intensity. These instabilities were resolved in later measurements. The red point at 900 V in Figure 4.4 shows the current-per-ion yield for one of the later - and longer (about 200 minutes) - calibration runs. The uncertainty is negligibly small.

4.4 Calibration of the IC and influence of a long cable

After the characterization of the IC three independent and dedicated measurements were performed to obtain a more detailed analysis of the IC-prototype and the achievable precision of its calibration. The setup was unchanged in the case of all three measurements, except for the cable connecting CD and IC. A 3 m BNC cable was used in the first two cases. In the last measurement a 50 m BNC-ecoflex cable was used to examine if a long cable had any significant impact on the measured IC current and if a reasonable calibration of the IC was still possible. Before those measurements were performed the counts from the current digitizer were recorded over a longer period of time without beam. This long measurement allowed to precisely determine the electrical noise, and noise fluctuations. An average noise value of about 150 pA s^{-1} was found. In Figure 4.5 the fluctuations from the average noise value are shown. Observed fluctuations of the electrical noise were in the dimension of $\lesssim 0.2\%$ compared to the current

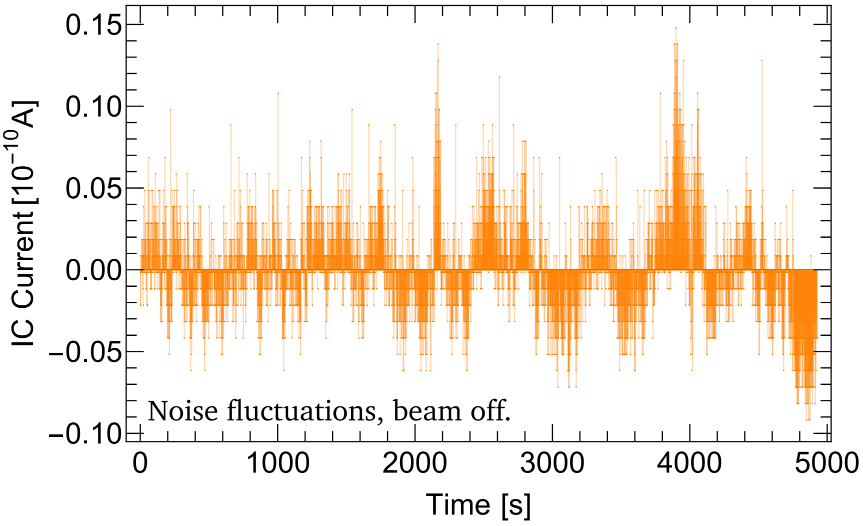

Figure 4.5.: Electrical noise from the IC after subtracting the average noise level. Recorded in a phase without beam. The same distribution after subtracting the average noise value, showing the fluctuations of the electrical noise, can be seen in (b). Binning: 1 s.

values in the calibration plots shown in Figures 4.6(a)–(c). The fluctuations did not have any significant impact on the uncertainty of the calibration fits.

After correcting the IC-current count values for the electrical noise, the calibration plots of the three measurements were produced. The general calibration procedure was described in chapter 2.6. The calibration plots shown in Figures 4.6(a)–(c) show the integrated counts of each spill as given by the SCI versus the integrated counts of each spill as given by the IC, similar to a method previously used at GSI to calibrate current sensitive detectors [85, 86]. Statistical uncertainties and the uncertainty of the current digitizer contributed to the error bars of the IC current. In the case of the number of SCI counts only statistical uncertainties were taken into consideration. The calibration factors were obtained by assuming a linear behavior

$$f\left(I_{\mathrm{IC}}\right) = bI_{\mathrm{IC}} + c. \tag{4.1}$$

All calibration plots, the corresponding fit functions and the obtained linear calibration factors are presented in Figure 4.6 and Table 4.1, respectively. The final calibration factor was given by the linear slope b. The parameter c just indicates an offset of the digitizer calibration. In the results and uncertainties of the linear calibration fits are shown. The first and the second measurement yielded the same calibration factors. Relative uncertainties of $\lesssim$1 % were achieved. While the second more precise measurement had a larger χ^2-value, the Pearson correlation coefficient[15] still supported a very good linear description of the data. In the third measurement a 50 m long BNC-ecoflex cable was used as connection between the IC and it's current digitizer. Also the synchrotron delivered intensities up to factor of 7 higher compared to run 1 and 2. The IC-current was still measured without any problems, proving the feasibility of IC read-out even though electronics were connected by a very long cable. One noticeable difference was a slightly different calibration factor. The third run had a much larger range of rates compared to run 1 and 2. But with increasing rates the SCI, rather than the IC, suffers from saturation effects, consequently leading to a decrease of the linear factor from the fit function. Instead the linear factor increased. Probably because of the longer cable the current signal was slightly more attenuated than in the short cable. Measuring the same rates at the SCI but with smaller IC currents leads to a steeper slope of the linear factor of the fit. Another difference in run 3 was the larger scattering of the data points. In the third run the internal spill structure showed an alternation of very high-intensity bins, randomly followed by very low-intensity bins. These fluctuations indicated instabilities of the beam extraction from the SIS18 at the time of the third measurement. These rapid and random alternations of beam intensity on a time scale of about 10 ms led to an unstable counting efficiency of the detectors and consequently to a smeared-out distribution of the data points within the calibration plot. Nevertheless, these instabilities were occurring

Run	Relative cal. factor [10^{10} ions/A]	χ^2 / ndf	R-Value
1	1290 ± 13 (1.0%)	117/59	0.998
2	1290 ± 8 (0.6%)	1498/397	0.999
3	1325 ± 10 (0.8%)	38439/345	0.998

Table 4.1.: Calibration factors given by the slope of the linear fits applied onto the calibration plots.

---

[15] A straight line without any variance of the data points has a Pearson correlation coefficient of 1.

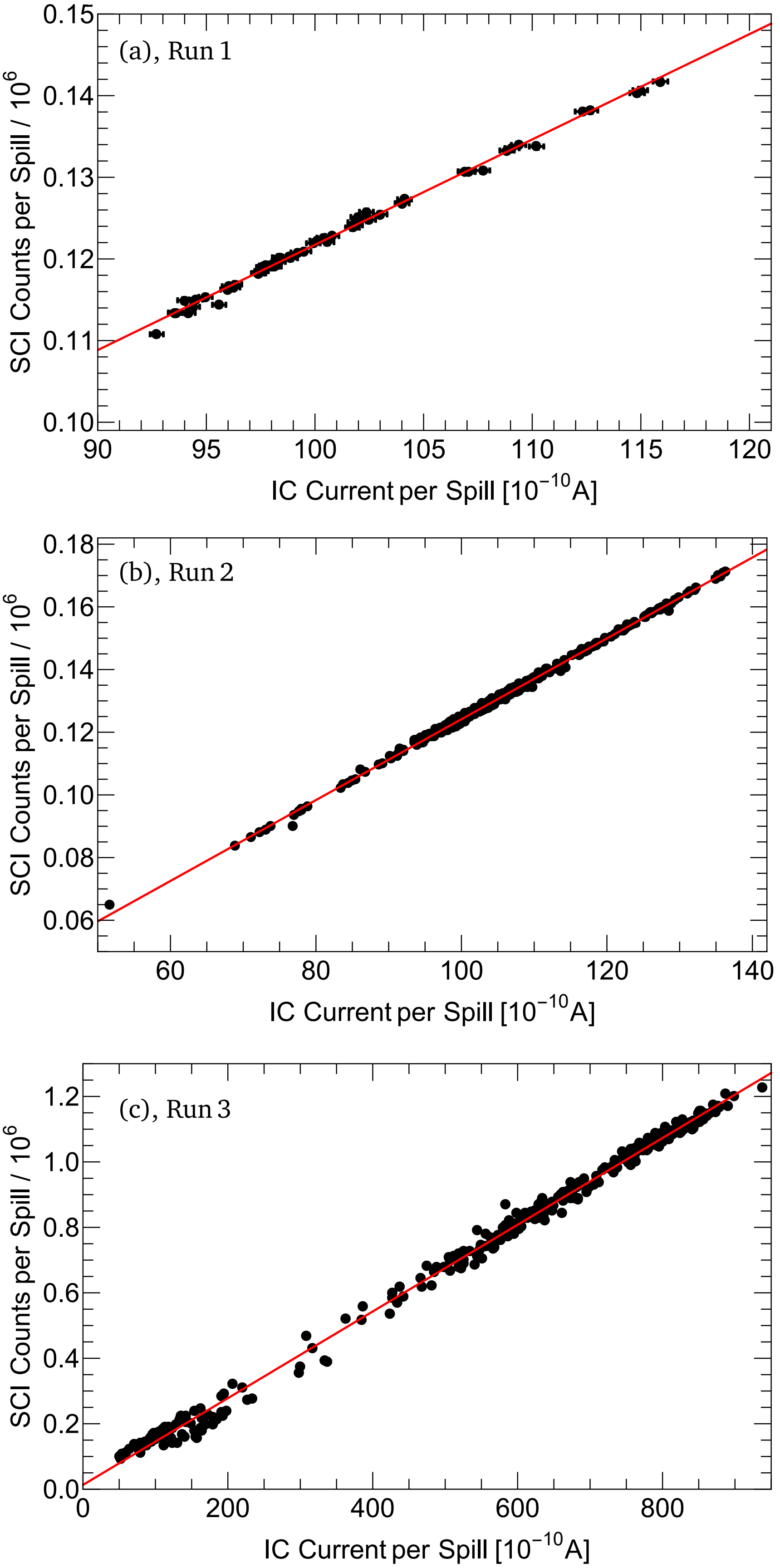

Figure 4.6.: (a): First calibration run of the IC-prototype, including 61 spills. Cable length: 3 m.
(b): Second cal. run, including 399 spills. Same setup as in run 1. Cable length: 3 m.
(c): Third cal. run, including 347 spills. The 3 m cable connecting IC and CD was replaced with a 50 m BNC-ecoflex cable. The linear factor is slightly larger compared to before.

on a random basis. At rates below 200 kHz this effect was smearing out the data sufficiently strong that no statistically significant fit was possible. Hence, no direct comparison with run 1 and 2 in the same data range was possible. When analyzing the full data range a statistically significant fit was possible, but due to the smeared-out data points the fit had a larger χ^2- value compared to run 1 and 2. A Pearson correlation coefficient of nearly 1 still indicated a good description of the data by a linear fit, which provided an uncertainty of the linear factor of below 1 %and a deviation of the calibration factor from previous runs by less than 3 %.

Comparing the data obtained with the *original* trigger signal and the stretched one showed that the number of counted pulses was independent from the used signal.

4.5 Summary

The measurement at GSI 2016 aimed at testing and further investigating the IC-prototype at typical GSI beam conditions. Following results were obtained:

- The IC-prototype was fully functioning with a ^{124}Xe-beam at 200 MeV/nucl., slowly extracted from a synchrotron.
- A calibration of the IC with an uncertainty $\lesssim$1 % was achieved.
- A longer cable did not affect the accuracy of the IC calibration.

Further improvement is anticipated because the CD is foreseen to be replaced by an optimized design[16] for FAIR.

---

[16] Charge-Frequency-Converter: **P**rofile **A**cquisition **D**igitizer (POLAND) [87]

The third test experiment was performed at the LNS in Catania, Italy, in 2017, aiming at the determination of the characteristics of an aluminum-based SEM-prototype as well as further investigations of the single- and polycrystalline diamond detectors. The setup was positioned in the first chamber of the 0° beam line at the INFN-LNS. Fully stripped ^{12}C-ions at 62 MeV/nucl. were delivered by the LNS cyclotron. Following measurements and tests were planned for the experiment:

- Test functionality of the SEM-prototype at intensities in the range of 10^4 pps to 10^7 pps.
  → Arguing from the theoretical particle range of the SEM for $Z = 6$, as given by Figure 1.1, the SEM can be reliably operated at intensities of 10^7 pps and above. Hence, study how well the SEM performs at lower intensities.
- Study proportionality of secondary current of SEM with respect to different beam intensities.
  → Perform, if possible, a direct calibration of the SEM, using the SC-DD as absolute intensity monitor.
- Study the lowest reachable uncertainty of the SEM calibration.
- Examine the absolute efficiency of a SC-DD.
- Measure the absolute efficiency of a large area PC-DD.
- Quantify the influence of long cables connecting SEM and SC-DD with their read-out systems.

5.1 Experimental setup and procedure

Initially a three-step calibration, by calibrating the IC-prototype with the single-crystal diamond detector and subsequently the SEM-prototype with the IC, was planned. Because of time constraints the IC was not integrated in the setup. The setup shown in Figure 5.1 was realized to study the SEM-prototype and deduce the efficiency curves of the diamond detectors with respect to a secondary electron transmission

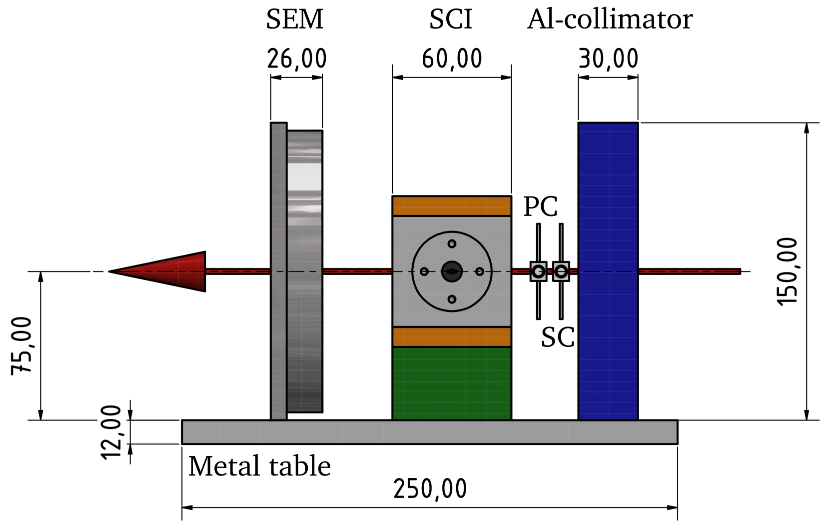

Figure 5.1.: Exp. setup: The beam entered from the right and traversed an Al-collimator, SC- and PC-DD, a scintillator, and last the SEM. Drawing provided by A. Kratz from the FRS-dept. at GSI.

monitor. All detectors were irradiated by a fully stripped ^{12}C-beam at an energy of 62 MeV/nucl. The intensity of the ion beam was controlled by a series of attenuation factors (1, 10, 100, 1000) and the opening size of slits along the beam line. The detectors were mounted on a metal table and were centered along the beam-line. In Figure 5.1, the beam enters from the right side. An aluminum collimator with a bore diameter of 2.5 mm was positioned in front of a single-crystal and polycrystalline diamond detector. Further downstream a light-shielded box, containing a plastic scintillator and photomultiplier tubes on both horizontal sides of the SCI, was placed. The SCI operated as reference detector. At the last position of the setup the SEM was mounted. LISE++ simulations confirmed that none of the detectors suffered any geometrical losses. Hence, a comparison of all detectors without any assumptions or corrections was possible. A picture of the setup is shown in Figure 5.2. All detectors were mounted on a metal table placed in a vacuum chamber. During the experiment the setup was slightly changed and a second configuration with the SEM mounted in front of the collimator was used.

Figure 5.2.: The experimental setup was mounted in a vacuum chamber, which was shown on the far right of the photograph in Figure 3.2. Experimental setup from right to left: Beam entry, Al-collimator, SC-DD, PC-DD, plastic SCI, SEM. The metal table has a length of 250 mm, the collimator a height of 150 mm.

5.2 Detector designs

The diamond detectors were mounted on printed circuit boards (PCBs). Drawings and pictures of the diamond detectors are shown in appendix B.3. The active area of SC-DD and PC-DD consisted of electric grade single-crystal CVD and polycrystalline CVD diamond plates, respectively and both their electrodes were constructed as one planar contact.

Such an unsegmented large area PC-DD is planned to operate as part of a PDC at the Super-FRS. Since the ion-beam is usually focused on the production target and not the detectors using a large area detector secures to detect all relevant parts of the beam. The plastic scintillator used in the experiment was provided by the GSI detector laboratory. PMTs designed to work in vacuum were attached to the SCI. The exact dimensions of the active area of the diamond detectors and the plastic scintillator and the simulated ion beam energy in front of each detector are shown in Table 5.1.

Detector	h×v×t [mm^3]	Incident average ion energy [MeV/nucl.]
SC-DD	3.23×3.23×0.160	62
PC-DD	18×18.25×0.3	60.39
SCI	60×60×0.2	57.27
SEM (circ.)	$r = 107/2$ mm, t=24 μm	56.58

Table 5.1.: Dimensions of the detectors. The rectangular dimensions in horizontal (h), vertical (v), and target thickness (t) direction are given. In the case of the circular SEM foils the radius (r) is given. The thickness of the SEM relates to one of the three foils mounted in the SEM. The energy of the ions in front of each detector was given by LISE++ simulations.

5.3 Read-out and data acquisition

Schematic layouts of the read-out electronics of the SC/PC-DD, the SCI, and the SEM are shown in Figure 5.3-5.5, respectively. The diamond detector signals were amplified by diamond broadband amplifiers[17]. The amplified signals were either fed to a digital oscilloscope to record the signal waveforms or to a leading-edge discriminator (LED). The digital pulses were counted by a VULOM3 scaler module. The SCI's PMT signals were also digitized and counted by the VULOM3 scaler module. The secondary current of the SEM was fed into a CD1012 current digitizer (CD), whose signals were also counted by the VULOM3. The scaler modules were read out by a MBS-based data acquisition to record the number of pulses each time the DAQ was triggered. A 10 Hz was used to trigger the data acquisition.

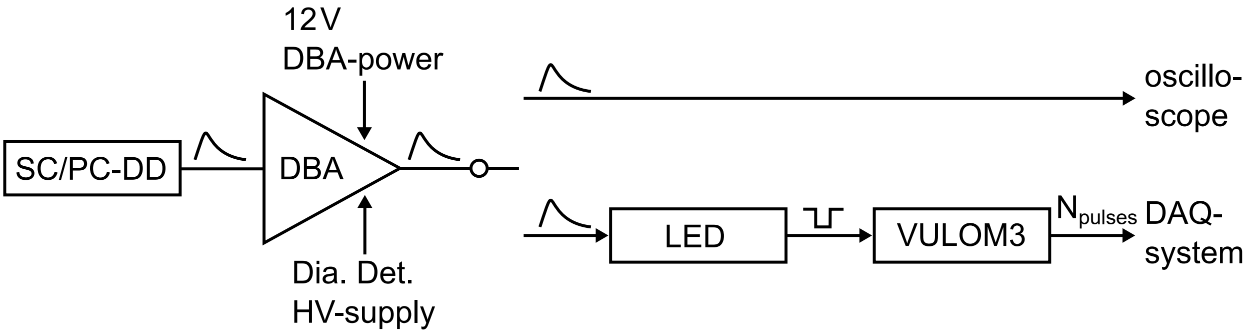

Figure 5.3.: Schematic layout of the read-out electronics connected to the SC/PC-DD.

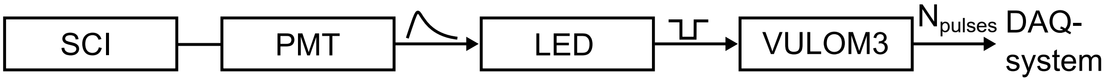

Figure 5.4.: Schematic layout of the read-out electronics connected to the SCI.

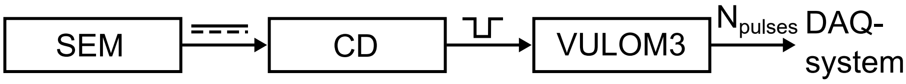

Figure 5.5.: Schematic layout of the read-out electronics connected to the SEM.

---

[17] Model: DBA-III

5.3.1 Functionality of all detectors

Observing the raw number of counts of the digitized SEM current showed that all detectors had a similar response with regard to the beam intensity. Particle rates in the order of 10 MHz and below were expected to traverse the collimator. For $Z=6$, theoretical predictions [62] estimated a minimum rate to operate the SEM reliably of 10^7 MHz. Thus, the current digitizer was operated at its highest sensitivity setting of 10^{-10} A FS. This means, one logical pulse of the digitizer corresponded to a secondary current of 10 fA. The recorded scaler spectra of SCI and SEM are shown in Figure 5.6(a) and (b), respectively. A comparison of the scaler spectra for SCI, SC-DD, PC-DD, and SEM for the same time period as in Figure 5.6 is presented in Figure 5.7. The count rates of each detector were multiplied by an arbitrary

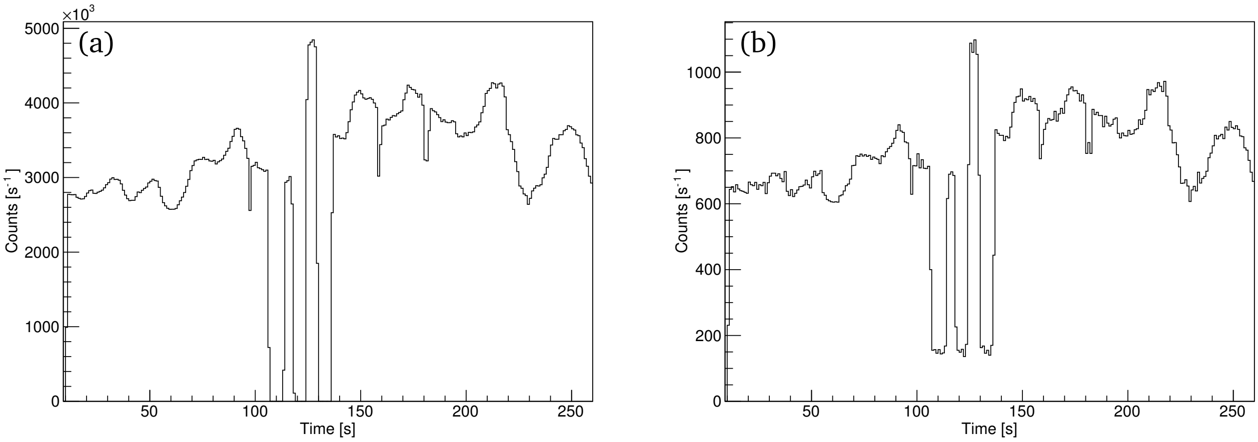

Figure 5.6.: SCI counts (a) and digitized SEM current (b). One SEM count translates to 10 fA at the CD input. A similar response is clearly visible. Binning: 1 s.

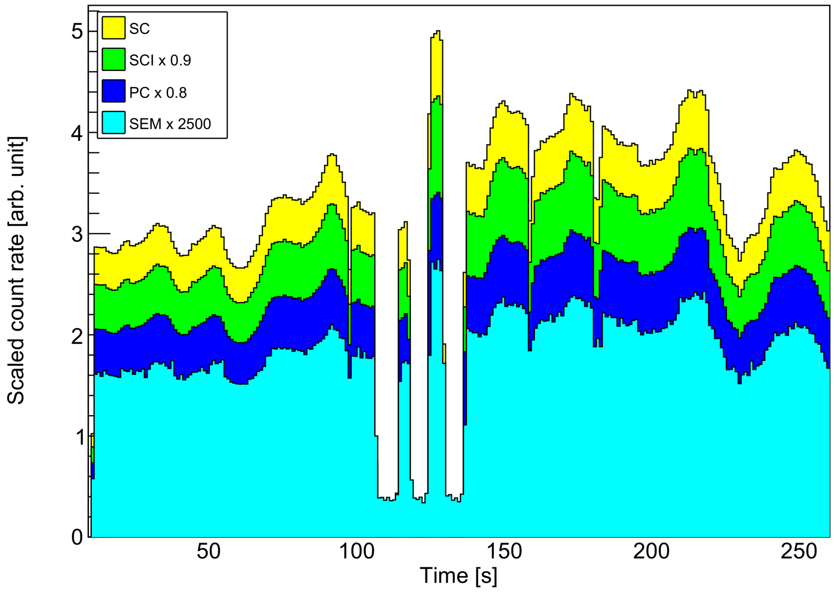

Figure 5.7.: Count-rate distributions of a single run. Detector rates have been scaled for better comparison. All detectors showed a linear response regarding the beam intensity. Binning: 1 s

factor to allow a good comparison. The histograms show the same response for all detectors. Further tests at lower intensities showed that the SEM was able to measure secondary currents proportional to the beam intensity and distinguishable from electronic noise down to intensities of 100-200 kHz, i.e. nearly two orders of magnitude better than anticipated. The scaler spectrum also shows that the intensity delivered by the cyclotron was strongly fluctuation within a few seconds. Later performed measurements with the SEM positioned in front of the collimator showed that not the intensity of the beam was fluctuating, but the beam spot position at the collimator. Despite an approximately constant beam intensity, the beam-spot shifts led to varying beam intensities measured by the detectors mounted further downstream behind the collimator. Hence, a calibration of the SEM with respect to the SC-DD was only carried out for the first configuration of the setup.

5.4 Calibration of the Single-Crystal Diamond Detector

SC-DDs are discussed to replace SCIs as reference detectors at high intensity regions of the Super-FRS. To guarantee comparable efficiencies the efficiencies of SCI and SC-DD were compared. A linear response of SCI and SC-DD was found for data up to 1.25 MHz. Hence, the linearity between SC-DD and SCI was studies below 1.1 MHz.

$$N_{\mathrm{SC}} = bN_{\mathrm{SCI}} + c \tag{5.1}$$

The linear relationshop is evident from Figure 5.8. Within the uncertainty of the fit, the slope b of the SC-DD counts vs. the SCI counts was found to be 1. Thus, the SC-DD can be used was reference for the calibration of the SEM. After an irradiation with $3.6 \cdot 10^9$ ions/mm^2 (this translates to an absorbed dose

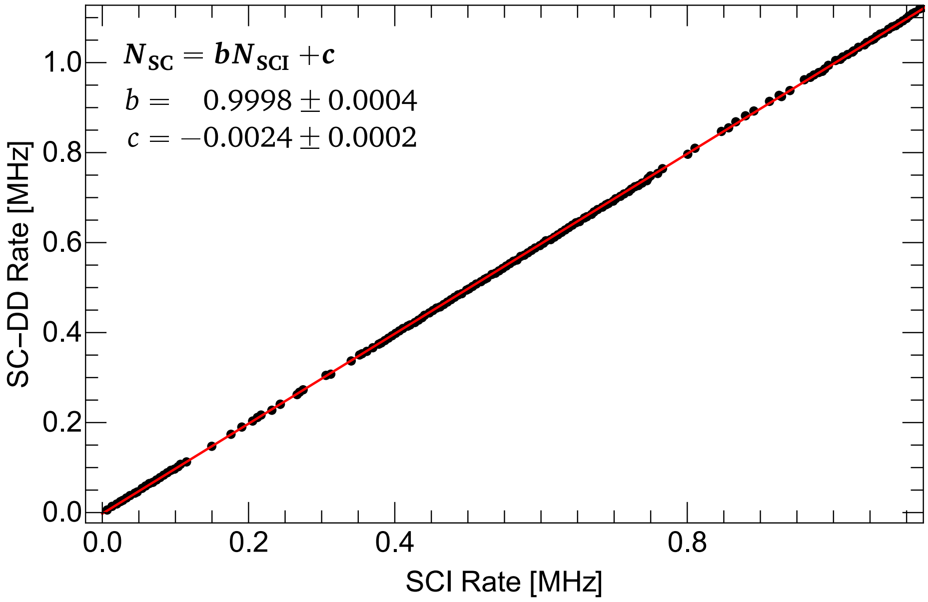

Figure 5.8.: SC-DD count-rate vs. the SCI count-rate before irradiation. Within the uncertainty of the linear fit the SC-DD showed a counting efficiency of 100 %.

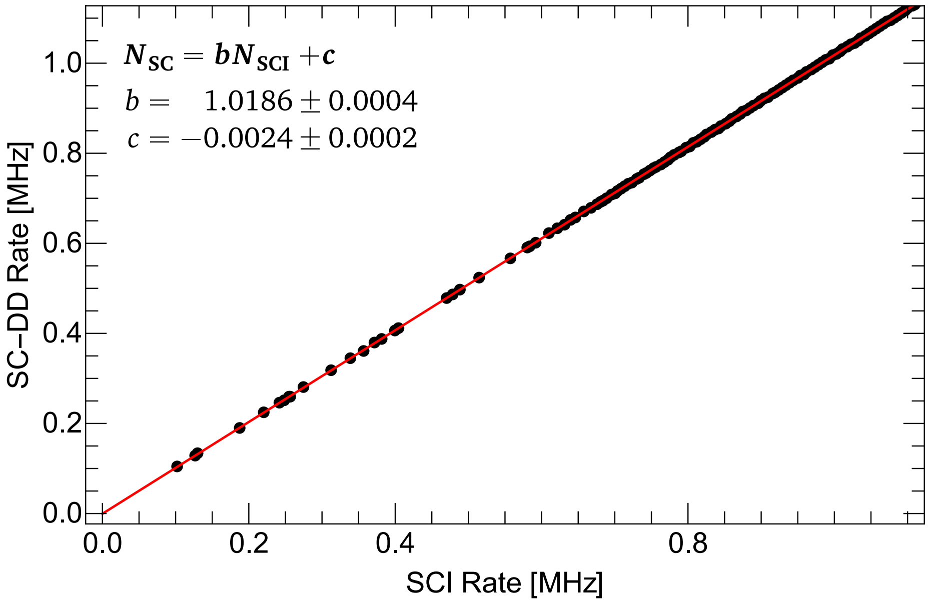

Figure 5.9.: SC-DD count-rate vs. the SCI count-rate after irradiating the detectors with $3.6 \cdot 10^9$ ions/mm^2 (D_{SC} = 19.98 kGy, D_{SCI} = 23.48 kGy). The data indicate a decreasing efficiency of the SCI.

of 19.98 kGy at the SC-DD and 23.48 kGy at the SCI) Figure 5.9 shows that a linear slope coefficient $b > 1$ was found, indicating a decrease of the efficiency of the SCI. This assumption was confirmed by the behavior of the SCI counts during a high-intensity period with intensities around 4 MHz. Figure 5.10 displays the ratio between the counts from the left and right-side PMT. The left PMT clearly shows a faster efficiency decrease in the detected counts, while in the measurement before irradiation the left and right PMTs showed the same amount of counts. Usually a coincidence signal of the left and

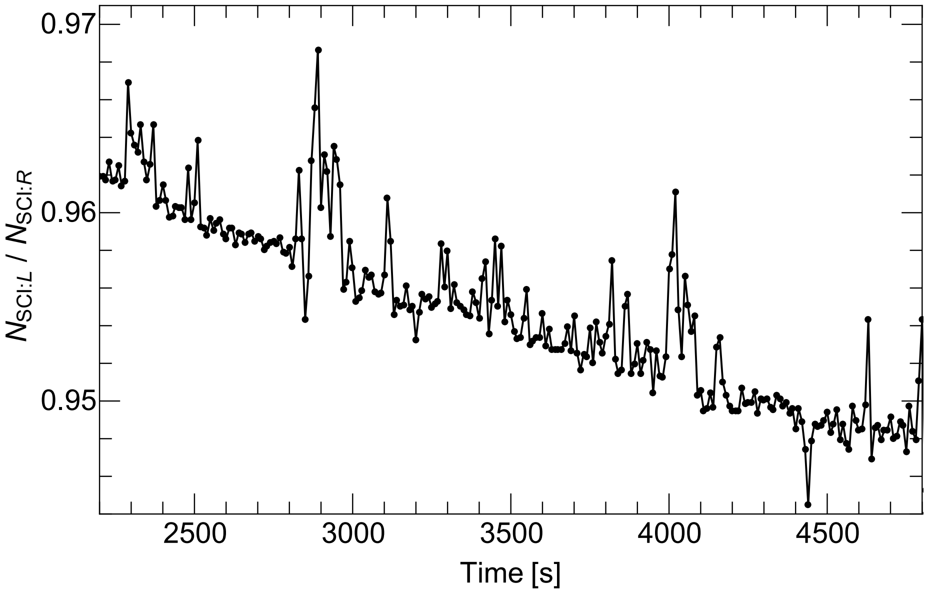

Figure 5.10.: Ratio between the measured counts of the left and right side photo-multiplier tubes of the SCI after absorbing a dose of above 30 kGy. All data points were averaged over 10 s.

right PMTs is taken for the count rates of a SCI. Due to the observed dose dependent efficiency for all further considerations the counts of the right PMT were taken. Nevertheless, comparing the measured counts of the SC-DD and the SCI (right-hand side PMT) with the counts by the calibrated SEM showed a continuous decrease in SCI efficiency. Count-rate ratios of the SC-DD and SCI versus the SEM are shown in Figure 5.11 in black and blue, respectively, for the same conditions and time period as in Figure 5.10. The average count-rate ratio was determined by applying a linear fit to the data. Since the data were recorded at rates above the linear operation region of both detectors and the SCI and SC-DD absorbed a dose of at least 30 kGy and 25.5 kGy, respectively, a count ratio below 1 was expected. While the ratio of the SC-DD versus the calibrated SEM was nearly constant, the efficiency of the SCI drops with time. Therefore, the efficiency of the SC-DD can be at least considered much slower decreasing at high intensities than the efficiency of the SCI. I.e., in addition to the increasing asymmetry between left and right PMTs, the overall efficiency decreased when compared to the SEM, which was not affected by saturation effects. Conclusively, SC-DD and SCI showed the same efficiency before irradiation and the SC-DD efficiency was less affected by on-going irradiation. Therefore, the SC-DD was considered as reference detector for all further ion intensity measurements.

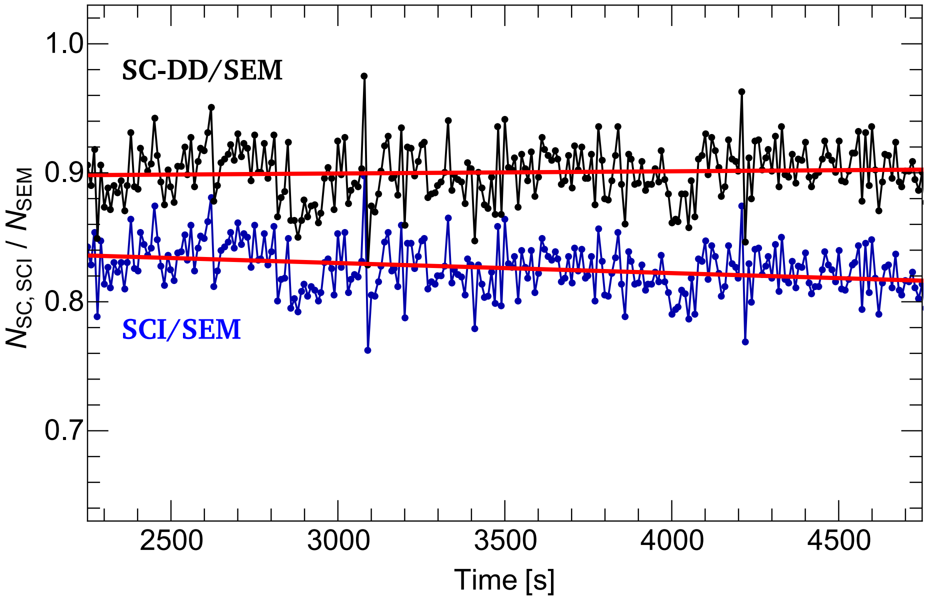

Figure 5.11.: Count-rate ratio of N_{SC}/N_{SEM} in black and N_{SCI}/N_{SEM} in blue (cal. of SEM in chapter 5.5) at rates around 4 MHz and in the same time period as Figure 5.10. Average ratios, provided by linear fits of the data, are indicated by red lines. All data points were averaged over 10 s.

5.5 SEM performance and calibration

Calibration

After showing that the SC-DD can be used as reference detector, the SEM was calibrated with respect to the SC-DD. Before calibrating the SEM, the electronic noise was measured and subtracted from the SEM-data. In Figure 5.12 the average electronic noise of the current digitizer is shown for data when

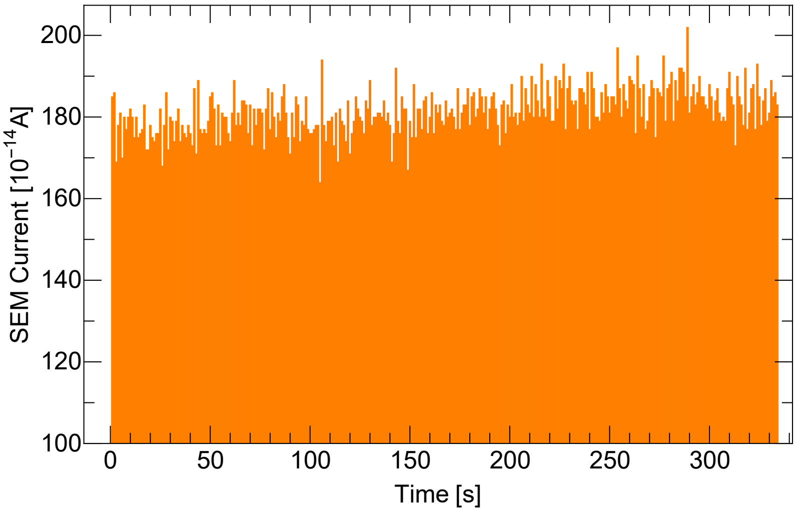

Figure 5.12.: Noise of the current digitizer while the beam was turned off. The noise was in the order of the signal strength with beam turned on. A detailed plot of the noise fluctuations is shown later in Figure 5.15. Binning: 1 s.

80 V was applied to the SEM, but the ion beam was turned off. The noise level was in the same order as the recorded and already noise-corrected current of the later performed calibration measurement which is presented in Figure 5.13. Calibration data were obtained by recording data at several intensities from a few kHz up to a few MHz, obtained by varying the beam attenuation and slit opening sizes. The final calibration plot of the SEM, showing the SC-DD counts vs. the noise-corrected SEM current is shown in Figure 5.13. The beam intensity arriving at the diamond detectors during this test experiment showed large fluctuations. Therefore, the recorded data were not integrated over a certain time period as in the analysis of the experiment in 2015. Instead, all recorded events, independent from their time of record, were ordered by the SC-DD ion rate. After ordering the events, the rates of all detectors were integrated and averaged in ranges of 5 kHz with regard to the SC-DD rate. A strictly linear response of the SEM current versus the SC-DD counts was found for rates of 0.15 MHz to 1.25 MHz. At higher rates a non-linear decrease of the correlation between SC-DD counts versus the SEM current was observed. This non-linear behavior was most likely induced by signal pile-up, leading to one large peak instead of two peaks being registered by the LED. The error bars of the calibration plot were given by statistical errors and the standard deviation of the averaged counts. Since the integration ranges were given by the SC-DD, the integrated points of the SC-DD differed by 5 kHz at most, and it's standard deviation was smaller than 5 kHz. The statistical uncertainties were of negligible scale when compared to the SC-DD count rates, too. In the case of the SEM, the measured number of counts of the current digitizer was relatively small leading to statistical uncertainties of comparable magnitude. Furthermore, the current digitizer was operated at its highest sensitivity to read out the SEM. Consequently, the electronic noise showed large fluctuations and varied at smallest disturbances of the detector or cables. Significant fluctuations of the SEM current were observed when the rate of the SC-DD remained stable. Since the integration range of the averaged data only depended on the rates given by the SC-DD, these SEM current fluctuations led to a large standard deviation of the averaged data points, significantly increasing

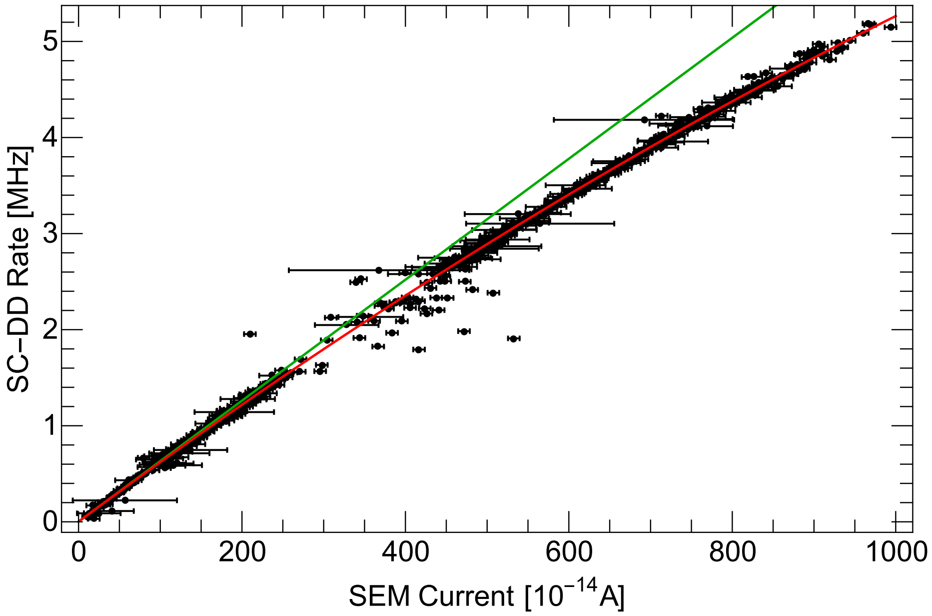

Figure 5.13.: Count rates of the SC-DD vs. the digitized current of the SEM. A second degree polynomial fit function was applied to the data, shown by the red line. The green line is just the linear part of this fit function.

the error bars of the SEM current in the calibration plot. The calibration of the SEM was performed by applying a second-order polynomial fit to the data

$$N_{\mathrm{SC}} = a \cdot I_{\mathrm{SEM}}^2 + b \cdot I_{\mathrm{SEM}} + c_1. \tag{5.2}$$

The resulting fit function is indicated by the red line in Figure 5.13. The total number of ions traversing the detectors N_{ions} with respect to the measured current was given by the calibration factor. This factor was provided by the linear parameter $b = (6295 \pm 320) \cdot 10^{14}$ ions/A of the fit

$$N_{\mathrm{ions}} = b \cdot I_{\mathrm{SEM}}. \tag{5.3}$$

Equation (5.3) is presented by the green line in Figure 5.13. The relative uncertainty of b, estimated to be 5.1 %, was not provided by the uncertainty of the linear fit but by graphical error estimation. In Figure 5.14 two linear fits

$$N_{\mathrm{SC,\,lin}} = b_2 \cdot I_{\mathrm{SEM}} + c_2 \tag{5.4}$$

of the same data as in Figure 5.13, but for different data ranges, are shown. The intervals of the fits were chosen to fit data with current uncertainties as small as possible. In Figure 5.14(a) data in the range of 0.2-0.55 MHz were fitted, in Figure 5.14(b) data in the range of 0.75-1.25 MHz. Linear calibration factors of $b_{2,\mathrm{red}}=6622 \cdot 10^{14}$ ions/A and $b_{2,\mathrm{green}}=5983 \cdot 10^{14}$ ions/A were obtained, respectively. They had an average uncertainty of $320 \cdot 10^{14}$ ions/A in b. Since both fits were in the region, where the SC-

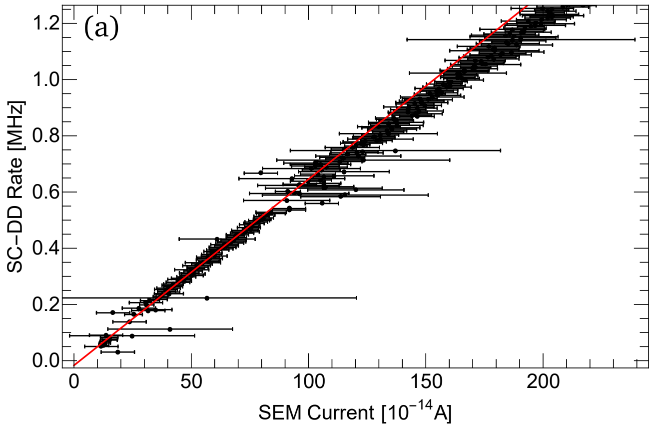

Figure 5.14.: Linear calibrations of the SEM current with respect to the SC-DD counts. Data in the range of 0.2-0.55 MHz (a) and 0.75-1.25 MHz (b) were fitted. Ranges were chosen to exclude points of very large current fluctuations.

DD was assumed to show a linear response versus beam intensity, the observed deviation from the linear relation was estimated as the uncertainty of the calibration factor b.

A possible explanation for the large differences of the fits are fluctuations of the SEM's electronic noise, measured at the current digitizer. Subtracting the average SEM noise level from the data in Figure 5.12 results in the data depicted in Figure 5.15. Within about 5 minutes the average noise level changed by about $9 \cdot 10^{-14}$ A.

Even despite the intensity fluctuations, most of the data used to obtain the green and red fit in Figure 5.14 were recorded at different attenuation factors of the ion beam and thereby, at different times. The beam records took more than 30 minutes at each attenuation factor. The change of noise level presented in Figure 5.15 was already comparable with the signal strength after a few minutes. In the

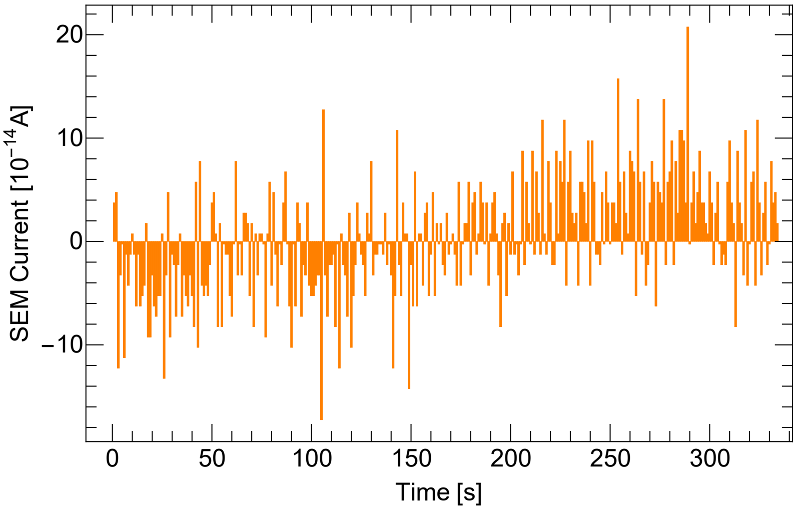

Figure 5.15.: Fluctuations of the CD noise. The spectrum was obtained by subtracting the average noise from Figure 5.12. Changes of the noise level were comparable to the measured SEM current with beam and were observed in time scales of a few minutes. Binning: 1 s.

experiment the noise level was checked after each full set of beam records with all attenuation stages, thus, every two hours or even more. Therefore large changes of the noise level between two attenuation stages were not recorded and the corresponding data could not be corrected for changes. The noise level before and after the presented calibration plot changed by about 10^{-12} A. Thus, the change of noise was in the same magnitude as the signal strength itself. Consequently, it was not possible to estimate to which extend the two linear fits were affected by the change of noise and which of them was describing the characteristic count-per-current yield of the SEM, and thereby its calibration factor, correctly. For this reason, the variances of the linear parameters $b_{2,\mathrm{red}}$ and $b_{2,\mathrm{green}}$ from the linear parameter b were taken as lower and upper limit of the calibration factor.

As the SEM signal depends on the energy loss of the ions in the SEM foils, ions that are faster, less charged, or lighter than the 62 MeV/nucl. $^{12}\mathrm{C}^{6+}$ ions of this experiment will produce smaller signals. This will prove a reliable SEM calibration more difficult and less accurate when omitting an IC as intermediate step. For the $^{238}\mathrm{U}^{28+}$ reference beam at FAIR with 1.5 GeV/nucl., a considerably larger energy loss is expected that renders a precise calibration of the SEM current directly from the SC-DD count rate feasible.

5.5.1 Benchmarking the calibration

To benchmark the calibration factor b another calibration of the SEM was extracted from a specific run shown in Figure 5.16. It was forfeited to be taken as reference, due to a lack of data in the rate regions below 0.7 MHz. Nevertheless, a linear fit of the whole data range yielded a linear factor of $b_2 = (6242 \pm 71) \cdot 10^{14}$ ions/A. The calibration factors b (Equation (5.2)) and b_2 (Equation (5.4)) were consistent within their error margins, supporting the choice of b as dedicated linear calibration factor for the data analysis.

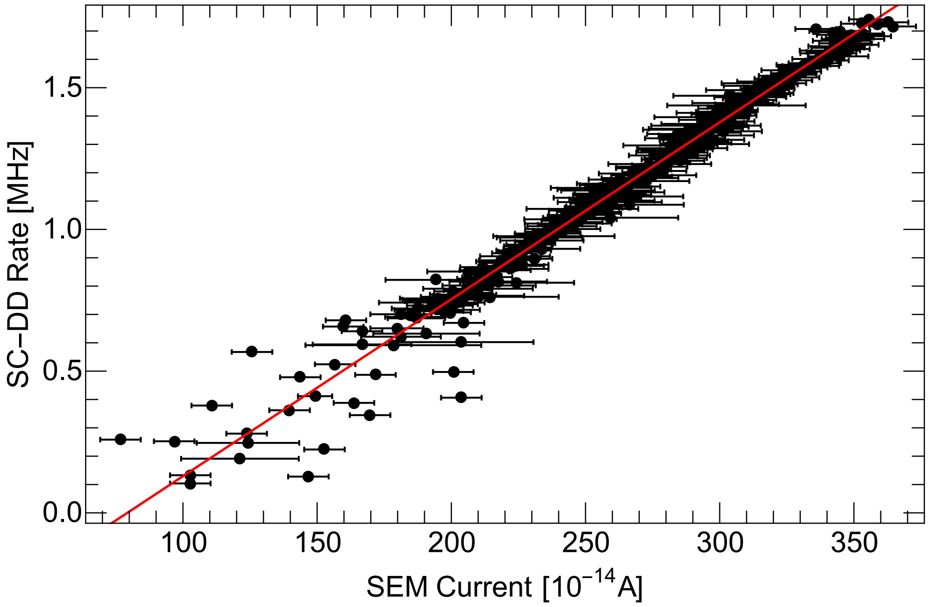

Figure 5.16.: Linear calibration of the SEM-prototype. This data set did contain nearly no data in the lower rate region.

A further benchmark was possible by crosschecking the measured secondary electron yield the SEM foils with results of earlier experiments. The secondary electron yield in a metal foil I_{sec} and the incident ion rate I_{prim} are related through the linear calibration of the SEM

$$\frac{I_{\text{prim}}}{I_{\text{sec}}} = b \cdot e, \tag{5.5}$$

with the electron charge e. The calibration, in turn, includes the secondary electron emission yield factor Y according to Equation (2.8). The secondary electron yield of this SEM-prototype was measured before at GSI by P. Boutachkov [73]. Those results, as well as yields measured with the old GSI-SEM, are shown in Figure 5.17. All secondary electron yields obtained with the old GSI SEM and the new prototype are comparable. Furthermore, the yield factor determined by P. Boutachkov and the yield factor obtained in this experiment are nearly identical. These results improved the confidence in the determined calibration factor. In spite of the difficulties discussed above, the acquired accuracy is comparable to Refs. [73] and [88].

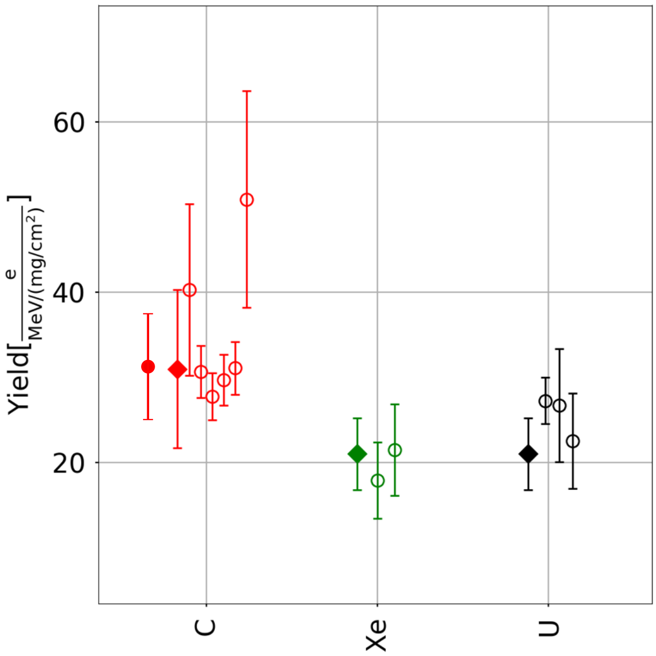

Figure 5.17.: Secondary electron yields, measured with C, Xe and U. Filled circle: Data from this work using the new FAIR-PDC-SEM measured at LNS 2017. Filled-Rhombus: Same SEM, data obtained at 300 MeV/nucl., measured at GSI, Ref. [73]. Open-circles: Data from the GSI-SEM, Ref. [88], obtained at energies between 270 MeV/nucl. and 1095 MeV/nucl. Figure adapted from [73].

5.6 Deposited Dose

In the first configuration of the setup, when the SEM was mounted behind the collimator, it was used to estimate the dose deposited at the diamond detectors. After placing the SEM in front of the collimator, the dose delivered to the diamond detectors were derived from the counts provided by the SC-DD. The

SC-DD counts showed a non-linear decrease at higher rates. To deduce an ion rates, less affected by the non-linear count-rate decrease, the measured counts were corrected by a reverse calculation of the polynomial fit from the SEM calibration

$$N_{\mathrm{SC}}(I_{\mathrm{SEM}}) = a \cdot I_{\mathrm{SEM}}^2 + b \cdot I_{\mathrm{SEM}} + c_1. \tag{5.6}$$

With

$$N_{\mathrm{ions}} = b \cdot I_{\mathrm{SEM}}, \tag{5.7}$$

and the dimensionless fit values of the calibration fit from Equation (5.2)

$$a = -1.033, \tag{5.8}$$

$$b = 6295, \text{ and} \tag{5.9}$$

$$c = 1928, \tag{5.10}$$

the count rate N_{ions} was derived from Equation (5.6) with respect to the measured count rate N_{SC} to be

$$N_{\mathrm{ions}} = \frac{-b^2 + \sqrt{b^4 - 4ab^2c + 4ab^2 \cdot N_{\mathrm{SC}}}}{2a}. \tag{5.11}$$

The determined number of ions that traversed the diamond detectors is shown in Figure 5.18(a). In the first 11 h the integrated counts were provided by the SEM, after that by the reverse calculated counts. The corrected SC-DD counts are a lower limit regarding the number of ions that traversed the detectors. The calibration fit was performed, before the SC-DD suffered radiation damage. As will be shown in the

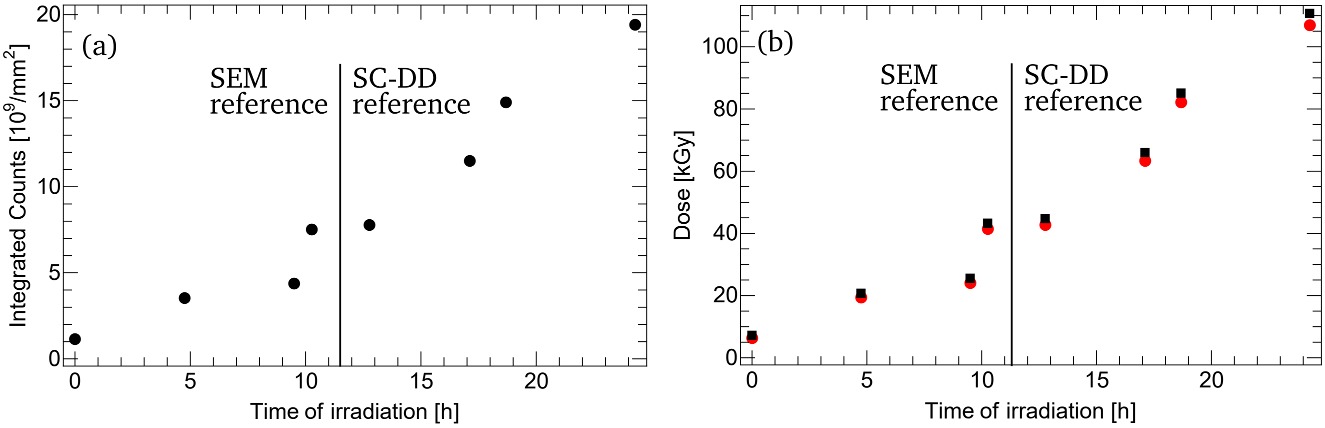

Figure 5.18.: Integrated counts per mm^2 that traversed the diamond detectors (a). The corresponding deposited doses (b) for the PC-DD (black squares) and SC-DD(red circles). The area of the beam spot had approximately been the same at both of the detectors.

next section, the SC-DD suffered radiation damage. Thereby, later measured counts were affected by a decrease of the SC-DD's efficiency. The resulting deposited dose D was calculated to be

$$D = N_{\text{ions}} \cdot \frac{E_{\text{loss}}}{A \cdot \rho x}, \tag{5.12}$$

where x is the detector material's thickness, ρ its density, and A the area of the beam spot at the diamond detectors and E_{loss} the energy loss of the ions in the material. LISE++ simulations suggested the beam spot at the SC-DD and PC-DD to be approximately of the same size with a spot radius of $r = 1.25$ mm and a flat intensity distribution. The simulation estimated an energy loss of about 19.4 MeV in the SC-DD and 37.3 MeV in the PC-DD. The doses absorbed by the detectors are shown in Figure 5.18(b). Since the corrected SC-DD counts are a lower limit of the ion number, the corresponding doses present a lower limit, too.

5.7 Efficiency of diamond detectors

5.7.1 Single-crystal diamond detector

To estimate the efficiency of the diamond detectors beyond the efficiency of the single-crystal diamond detector (chapter 5.4) the charge collection efficiency (CCE) was taken as an indication of the evolution of the detector characteristics with on-going irradiation. The CCE allowed to estimate if and at which scale the detector material was damaged. Oscilloscope records of the SC-DD waveforms were taken to analyze the detector's signal and thereby its CCE. Before analyzing the waveforms a BLA (cf. chapter 3.7) was performed. The constant signal background noise was subtracted by fitting the signals baseline and subtract the found value from the whole waveform. The corrected waveforms were integrated to obtain the collected charge of each signal. In Figure 5.19 the resulting charge distributions of the SC-DD before (a) and after (b) absorbing a dose of 25 kGy are shown. In both cases a large peak at

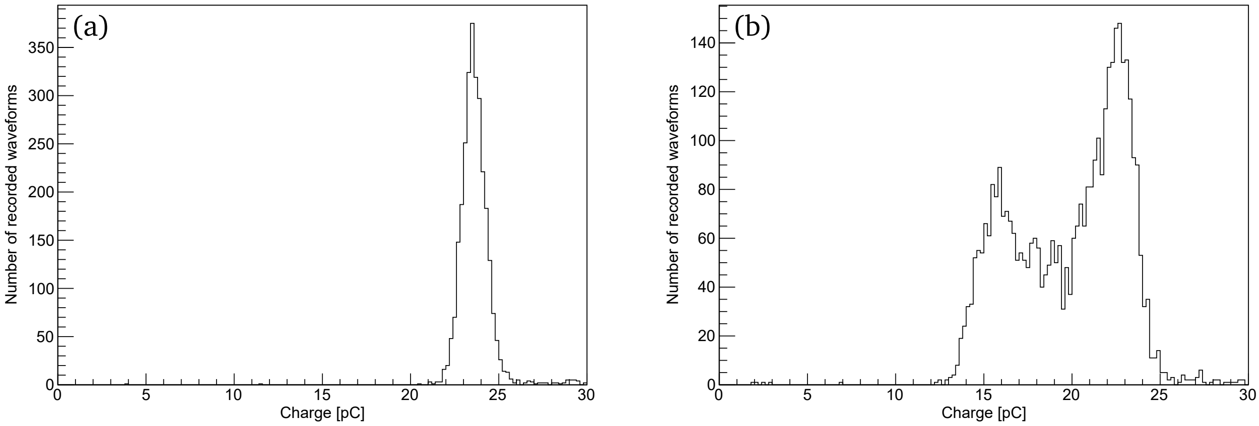

Figure 5.19.: Collected charge of the SC-DD before (a) and after (b) absorbing 25 kGy. The charge of each distribution was derived from 4000 waveforms records taken with the oscilloscope.

about 23.6 pC can be seen. In the distribution recorded after irradiation a second peak with a smaller charge collection had formed. This peak most likely formed due to ions traversing damaged areas of the SC-DD. Some areas of the material were still fully functioning and behaving like a SC-DD, while other parts were already damaged and showed a similar behavior like a PC-DD (cf. chapter 3.7). The average collected charge before irradiation and after absorbing 25 kGy decreased from (23.54 ± 0.05) pC to (19.46 ± 0.10) pC. The charge values were used to calculate the charge-collection-efficiency of the SC-DD. It can be calculated if the theoretically induced charge, the signal attenuation in the connecting cables and the DBA amplification are known. Signals coming from the diamond detectors suffered an attenuation in the cables of

$$A = -20 \cdot \log_{10}\left(Ch_{\text{out}}/Ch_{\text{in}}\right). \tag{5.13}$$

Vice versa the charge value before traversing the cable Ch_{in} could be calculated if the attenuation factor A of the cable and the charge after the cable Ch_{out} were known.

$$Ch_{\text{in}} = \frac{Ch_{\text{out}}}{10^{-A/20}} \tag{5.14}$$

Ch_{out} was given by the analysis of the waveforms, recorded with the oscilloscope which was connected to the SC-DD via a cable to the pre-amplifier. Hence, the reverse calculation was performed in three steps. The first step was to calculate the charge value directly behind the pre-amplifier using the measured charge and Equation (5.14). The next step was to calculate the charge before the pre-amplifier, by using the amplification of the DBA

$$A_{\text{DBA}} = \frac{Ch_{\text{out}}}{Ch_{\text{in}}}, \tag{5.15}$$

$$\Rightarrow Ch_{\text{in}} = \frac{Ch_{\text{out}}}{A_{\text{DBA}}}. \tag{5.16}$$

Finally, the attenuation of the charge in the cable, connecting DBA and the diamond detector was determined, again using Equation (5.14). The variables Ch_{out} and Ch_{in} denote the charge before and after the considered electronic device or cable. The BNC-cable connecting oscilloscope and DBA had an attenuation factor of $A_{\text{BNC}} = 0.58$ dB, the DBA a gain of $A_{\text{DBA}} = 42$ dB and the SMA-cable connecting DBA and diamond detector an attenuation factor of $A_{\text{SMA}} = 1.3$ dB. Theoretical values of the charge created in the diamond material were obtained using the energy loss in the material provided by LISE++ simulations and an average energy to create one electron-hole pair of 13 eV. Taking the charge values at the beginning of the experiment ((23.54 ± 0.05) pC) and after absorbing a dose of 25 kGy ((19.46 ± 0.10) pC), CCEs of $99.6 \pm 0.3\%$ and $82.2 \pm 0.5\%$ were obtained, respectively. These were the only waveforms of the SC-DD, recorded with the pre-amplifier model DBA-III. Further radiation effects could not be quantified due to a later change of the electronics setup.

Due to the large area of the unsegmented PC-DD and thus, the large capacitance of its active area, the electronics had problems correctly processing all signals. The large pulse heights demanded a delicate adjustment of the LED threshold, and the signal width over threshold was very long. Hence, the output pulse had to be adjusted properly to manage proper read-out by the VULOM3 scaler module. Proper electrode voltage had to be chosen, to collect the charge carriers fast enough, but not to induce a too large leakage current.

The final settings of the PC-DD electronics were only found after having irradiated the diamonds with $4.5 \cdot 10^9$ ions/mm^2. During the experiment, several DBAs failed. The DBA boxes used in the experiment did not have any surge protection [70] to improve their timing properties and reduce saturation effects at high rates of incoming signals. Especially the fluctuations of the intensity behind the collimator could have induced large and sudden amounts of charge carriers in the diamond material, leading to very large signals. Another explanation is a sudden charge release, possible happening in the PC material on a random basis. Charge carriers can be trapped in holes or defects or other positions due to field effects of the electrodes. If enough charge carriers get released in one shot, eventually a signal of too large amplitude and charge gets induced at the detector electrodes and damages the DBA [70]. Nonetheless, these effects can not be fully explained, yet, and are part of on-going studies.

Only three sets of data, comparing the PC-DD and the SC-DD count rates, were recorded. These sets are shown in Figure 5.20. The rate-dependent efficiency of the PC-DD with respect to the SC-DD was

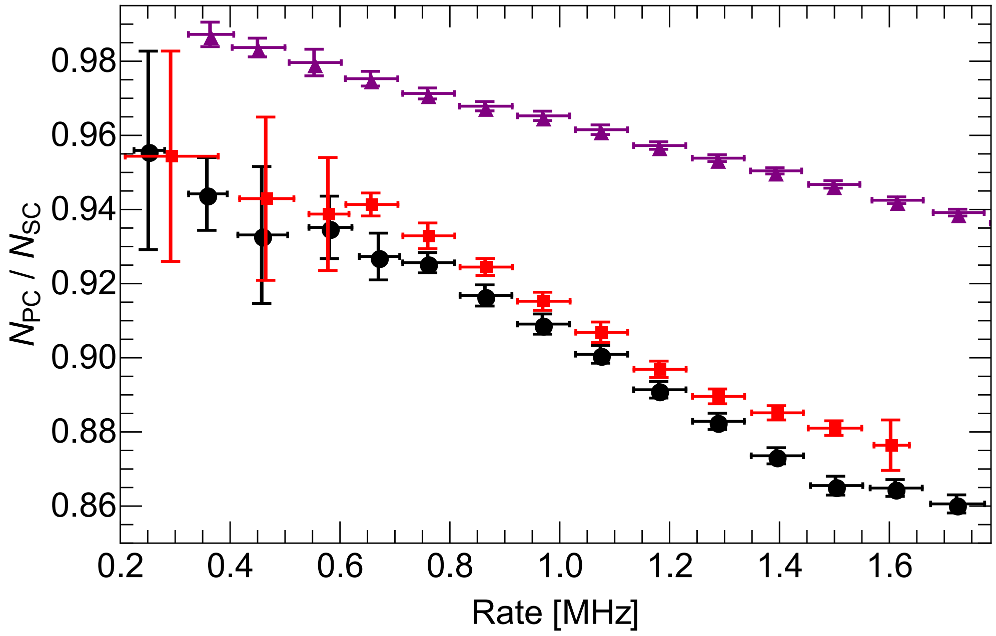

Figure 5.20.: Rate-dependent efficiency ratio of the PC-DD with respect to the SC-DD. Efficiencies (a) of the PC-DD are shown for records taken after absorbing a dose of $4.5 \cdot 10^9$ ions/mm^2 (black), $7.9 \cdot 10^9$ ions/mm^2 (red) and $15 \cdot 10^9$ ions/mm^2 (purple). The seemingly higher efficiency of the PC-DD (purple dots) is likely to be induced by a decreasing efficiency of the SC-DD with on-going irradiation. Error bars of the efficiency and rate are given by the FWHM and integration range, respectively.

obtained by calculating the ratio of their integrated counts.

It is notable that the ratio N_{PC}/N_{SC} increased with on-going irradiation. As the first experiment at the LNS in 2015 showed, the PC-DD characteristics were nearly unchanged after applying a dose in the order of MGy, the efficiency of the SC-DD likely decreased. This damage can be seen in the purple curve of the efficiency plot. Count rates of SC and PC nearly show the same count response concerning the beam intensity, indicating an advanced damage of the SC material. At small rates, both detectors work reliably, but in the PC-DD the charge needs longer to be collected completely (about 14 ns) compared to the smaller SC-DD (about 3 ns), and the probability for pile-up effects increases with increasing rate. Due to the electronics problems described above, a further analysis of the PC-DDs efficiency at even higher rates was not possible.

The efficiency of the PC-DD showed a strong rate dependence. Therefore, it's efficiency was determined at lower rates below 700 kHz at which a slightly weaker rate dependence was observed. To improve statistics the data used for the black and red points in Figure 4.1 were combined (see appendix B. 4). Determining the average of all data points below 700 kHz, one finds an efficiency of the PC-DD of (94.8 ± 2.5[18]) %. This corroborates, that, while not as high as a SC-DD, a PC-DD has a high count efficiency, too. Hence, PC-DDs may be used as a part of a particle intensity monitor. At the same time the characteristic curve of the PC-DD has to be carefully reviewed in convenient time intervals, to minimize any uncertainty, contributing to the overall uncertainty of the intensity monitor. Since the first experiment showed a high radiation hardness of the PC material, these time intervals can be assumed to be in the order of weeks or months, rather than days.

5.8 Cable length

SEM

Similarly to chapter 4.4 where the influence of connecting the IC-prototype to the current digitizer with a long cable was discussed, the SEM calibration was studied using two different cable lengths (3 m BNC vs. 50 m BNC-ecoflex). Data recorded using the setup with the short and long cable are shown in Figure 5.21(a) and (b), respectively. In both cases, linear fits were performed for data in the range of 0.75-1.25 MHz. Linear slopes of $5983 \cdot 10^{14}$ ions/A (a) and $6094 \cdot 10^{14}$ ions/A (b) were found. Although the current digitizer was already working at the highest possible sensitivity setting and the beam had a relatively low intensity and charge, the secondary SEM current still showed a linear response versus the beam intensity after exchanging the cables. However, the signals at low rates with the long cable proved very weak. Similar to the same test, concerning the IC, the SEM data only showed a slightly larger signal attenuation in the long cable compared to the short cable. Hence, the SEM read-out electronics can be placed far away from the SEM without jeopardizing the functionality of the detector.

---

[18] FWHM.

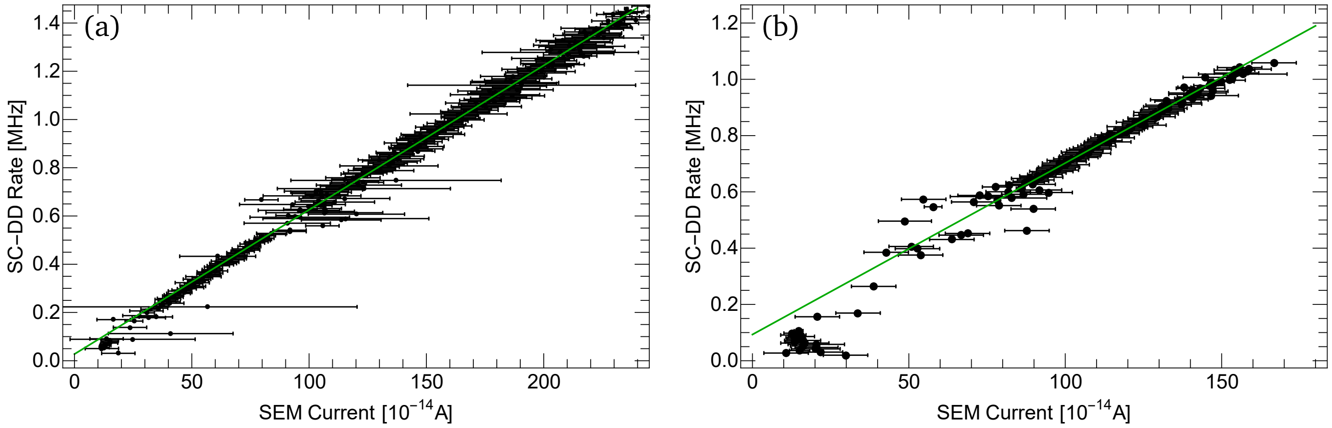

Figure 5.21.: Influence of a longer cable on the calibration of the SEM. A 3 m standard-BNC cable (a) and a 50 m ecoflex-BNC cable (b) were used to connect SEM and CD. Both fits were performed in the range of 0.75-1.25 MHz.

Single-crystal diamond detector

Similar studies were carried out with respect to the shape of the diamond signals. In this case the short cable between SC-DD and pre-amplifier was exchanged for a long cable. At first the waveforms of the SC-DD before and after exchanging the cables were recorded with the oscilloscope. The corresponding charge distributions are shown in Figure 5.22(a) and (b), respectively. The signal read-out was properly working using the long cable. An attenuation of the pulse height was observed, indicated by a decrease of the signal amplitude as well as the average measured charge. The decreases amounted to about 9%. A quantitative determination of the cable length’s influence on the measured ion rate was not possible.

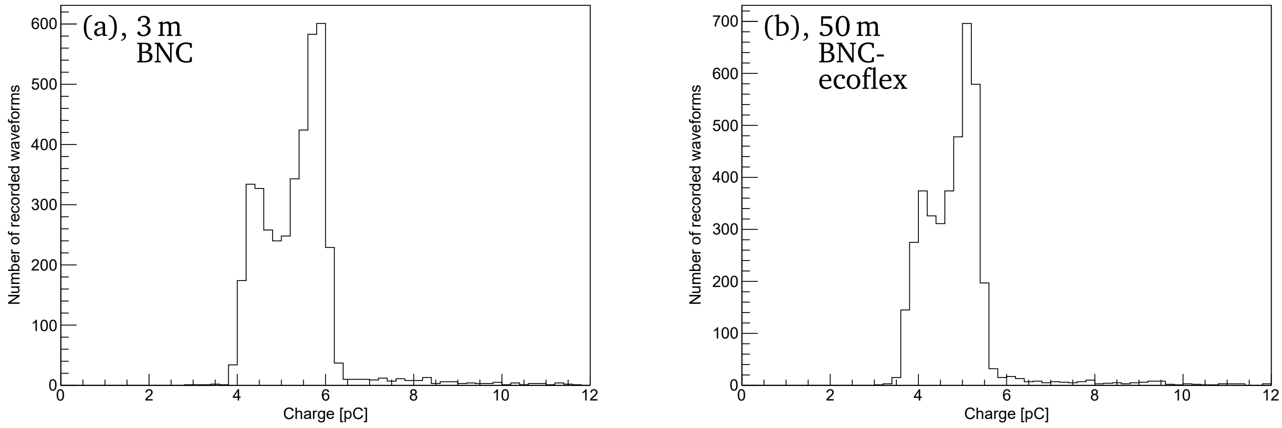

Figure 5.22.: Charge distribution of the SC-DD with a 3 m BNC cable (a) and a 50 m ecoflex-BNC cable (b) connecting SC-DD and pre-amplifier.

5.9 Summary

The experiment performed at the LNS in 2017 used again a ^{12}C beam at 62 MeV/nucl. Comparisons between a single-crystal diamond detector, polycrystalline diamond detector, plastic scintillator and a prototype of an aluminum-foil based secondary electron transmission monitor, yielded the following results:

- The SC-DD showed a linear response with respect to the SEM current at rates of 0.15 MHz to 1.25 MHz. At lower rates the SEM worked at the detection limit, while at higher rates SC-DD and SCI showed signs of pile-up and saturation.
- The SC-DD showed an efficiency of about 100 % compared to the measured SCI counts. The SC-DD showed less radiation damage than the SCI.
- The PC-DD showed a efficiency of $(94.8 \pm 2.5)\,\%$ when compared to the measured SC-DD counts at rates below 700 kHz.
  → A strong rate dependence of the PC-DD efficiency demands careful evaluation.
- A direct calibration of the SEM, using the SC-DD as a reference, was possible with an uncertainty of 5.1 %.

While theoretical estimations (Figure 1.1) predicted a limit for reliable SEM operation at 10 MHz, the device under test was found to functioning already at rates of a few hundred kHz. Because the current digitizer had to be operated at its highest possible sensitivity setting the noise level was non-negligible. Nevertheless, the results show that the SEM-prototype can be used as part of an intensity monitor. If a direct or a two-step calibration should be performed has to be carefully evaluated, depending on the charge and energy of the used ion beam and the maximal tolerated uncertainty of the calibration factor.

The results regarding the SC-DD proved that it is an adequate replacement for a SCI for the use as absolute reference intensity monitor. While both detectors showed the same efficiency at the beginning of the experiment, the SC-DD suffered less damage due to irradiation.

The results regarding the large-area PC-DD are not yet fully convincing. The detector showed an efficiency of about 95 % at lower rates. At the same time the efficiency showed a strong decreasing dependence at increasing intensities of the ion beam. A careful investigation of the rate dependence of the PC-DD has to be performed at periodic intervals to reduce large uncertainties of the intensities. Furthermore, the large capacitance of the PC-DD caused operational difficulties that may be solved when, e.g., reducing the effective area through electric segmentation.

6 Conclusion of the test experiments

Three test experiments were carried out. Studies regarding single- and polycrystalline diamond detectors, an IC prototype, and a SEM prototype were performed.

Diamond detectors

Results concerning the SC-DD proved, that it is an equal, if not a better replacement for the use as absolute particle intensity monitor, compared to plastic scintillators. While both detectors showed the same count efficiency before irradiation, the higher radiation hardness of the SC material favored the diamond detector to be used as reference detector for absolute particle counts. When using a fully stripped ^{12}C-beam at 62 MeV/nucl. a linear response of the SC-DD counts versus increasing intensities was found for rates of up to 1.25 MHz. The SC material started to show signs of radiation damage after absorbing a dose of about 25 kGy: A second peak at a lower charge appeared, indicating a differentiation of the detector into a damaged and undamaged area. On-going irradiation led to a fully damaged detector after about 80 kGy. From this point the SC-DD showed a similar behavior like a PC-DD regarding efficiency and evolution of detector properties with on-going irradiation. However, single crystal diamond detectors are only available with small active areas though. As part of an intensity monitor at the Super-FRS it will eventually suffer large and not controllable geometrical losses. This can be avoided by either focusing the beam at the detector or use a collimator. In general the beam is focused at the production target and using a collimator would negate one of the main objectives of FAIR, to reach higher beam intensities. Therefore both options are rather unrealistic.

The PC-DD on the other hand is available at much larger sizes and showed a higher radiation hardness. No signs of significant radiation damage were found, even after depositing a dose larger than 4 MGy. Up to 1.5 MGy even some hints of pumping, an increase of signal quality of the PC-DD was observable. The performed studies revealed a higher radiation hardness but in turn a lower efficiency of the PC-DD when compared to the SC-DD. An efficiency of $(95 \pm 2)\,\%$ was found when compared to an (undamaged) SC-DD. Additionally a strongly rate dependent efficiency of the PC-DD efficiency was found for ion rates above 700 kHz. Efficiency studies were performed using a large-area PC-DD with single planar electrodes on both sides of the detector. The large area, and consequently a too long charge collection time, are possible explanations for the strong rate dependence. For reliable read-out of the PC-DD the use of detectors with segmented electrodes is recommended.

In summary the high radiation hardness of polycrystalline diamond detectors makes them a good choice for operation as part of a PDC in the Super-FRS. They can be assumed to have a stable efficiency at a given intensity for a long period of irradiation. But their count efficiency below 100 % will afford periodic monitoring of its rate-efficiency curve, using a SC-DD or another detector performing at a count efficiency of 100 %. Due to the high radiation hardness of the PC-DD such checks should be sufficient to be carried out a few times per year, or before experiments requiring a very low uncertainty. Furthermore better read-out electronics could possibly decrease non-linear effects and increase the efficiency of both detector types at higher rates. Therefore the fabrication of good electronics is mandatory for the operation of diamond detectors. Decreasing detector properties, e.g., signal amplitude due to radiation damage can partly be compensated by further increasing the bias voltage of the detector. So far, electronic devices, electrodes, etc. of sufficient properties cannot be operated at high enough voltages to sufficiently compensate these effects [70].

FAIR-IC prototype

Investigations for a FAIR-IC prototype proved its full operational readiness. The ideal working range regarding the supply voltage of this design was found to be at about 900 V. A linear correlation between the absolute particle intensity, as given by the SC-DD, and the secondary current of the IC was found at rates between a few kHz up to a few MHz. Even at a few kHz the noise level was insignificant compared to the measured secondary current. As no ion beam with $Z = Q < 6$ was investigated it is not completely clear for what range of rates, e.g., a proton beam the IC features linear behavior. Including statistical and systematic uncertainties, a calibration of the IC with respect to the absolute particle intensity, as given by a SCI, was achieved within an uncertainty of $\lesssim 1\,\%$. Conclusively the FAIR design of the IC-prototype has proven to be working properly as particle monitor within the mentioned uncertainty and is suitable to be used as a part of the Super-FRS PDC.

FAIR-SEM prototype

Similar to the IC, the SEM was investigated at rates between a few hundred kHz up to a few MHz, using a diamond detector as reference detector. The secondary current of the SEM showed a linear behavior between about 150 kHz and several tens of MHz. At the lower intensity limit average electronic noise levels were at the same order as the signal strength of the secondary current. Thus, a direct calibration of the SEM using diamond detectors is approximately at its lower limit when irradiating the detectors with ions of charge $Z = 6$. The measurements allowed a calibration of the SEM, using the SC-DD as reference, with an uncertainty of about 5 %. For ion beams of higher charge a SEM calibration will become possible with smaller uncertainties. Performing a two step calibration DD→IC→SEM at different more suitable rate regions would eventually yield a lower uncertainty, too. Especially for very light ions this should hold true.

The SEM-prototype showed its operational readiness to be used as a part of the FAIR-PDC. Besides working below the theoretical limit for reliable operation, the SEM showed a linear correlation concerning different ion intensities at an uncertainty of about 5 %. Electron yields per unit of energy loss in the SEM foils were of the same order as for the older GSI-SEM design. One of the remaining main questions is, how well this SEM-design will behave in long-term irradiation.

Influence of cable length

All three detectors were working properly using a 50 m read-out cable. At the Super-FRS electronics, which will not be able to stay in the near of the detectors, can be placed further away in less radiative environments.

Conclusively all investigated detectors proved their full operation readiness as parts of a particle detector combination along the beam line of the Super-FRS. But characteristic properties of the detectors, such as efficiency and counting behavior at different rates, have to be verified in periodic intervals or after large dose depositions. Careful evaluation of these properties will allow operation of radiation hard detectors at low uncertainties and thus less beam shutdowns due to physical detector maintenance. The most recent Super-FRS PDC specifications for a PDC at FPF0 and FPF4 at the Super-FRS were stated in August 2018 and are available on request [89]. While IC and SEM prototypes are close in design for the detectors needed for the Super-FRS PDC, one of the remaining challenges is the realization of diamond detectors covering at least $20 \times 20\,\mathrm{mm}^2$ according to Super-FRS specifications [11].

Appendix

A One-Nucleon Removal Reaction Cross Sections from Carbon Isotopes

1 Target composition

The target composition was given by the data sheet of PF-60 foils from the company materion [90]. The quality level warrants a percentage of at least 99% ^{9}Be in the target material. The other contaminants are listed in Table 1.1.

All contaminant proportions are given as maximum percentage. Their sum exceeds 1%. Due to the lack of knowledge of the real distributions of the compositions, except for the maximum value given in the data sheet, for each component an uniform distribution was assumed. This leads to a mean value of each component of $\frac{\text{Maximum \%}}{2}$. Hence, a percentage of 0.4% of BeO was estimated leading to a total percentage of Be in the target of 99.2%. The total sum of the contaminants percentages by taking

Element	Maximum%	Molar mass [g/mol]
Beryllium oxide	0.8	9.012(Be) | 15.999(O)
aluminum	0.05	26.982
Boron	0.0003	10.811
Cadmium	0.0002	112.411
Calcium	0.01	40.078
Carbon	0.06	12.011
Chromium	0.01	51.996
Cobalt	0.001	58.933
Copper	0.01	63.546
Iron	0.08	55.845
Lead	0.002	207.200
Lithium	0.0003	6.941
Magnesium	0.049	24.305
Manganese	0.01	54.938
Molybdenum	0.002	95.960
Nickel	0.02	58.693
Nitrogen	0.03	14.007
Silicon	0.04	28.086
Silver	0.001	107.868

Table 1.1.: List of contaminants in the 99% Beryllium target. Taken from the data sheet for PF-60 targets from the company Materion [90].

half the maximum is 0.5654%. The remaining 0.4346% were uniformly filled by an evenly mixture of all materials present in the target material. The error of each contaminant was given by the standard deviation of an uniform distribution.

$$\sigma = \frac{\text{Maximum }\%}{\sqrt{12}} \tag{1.1}$$

The same error was estimated for the evenly mixture. All errors were quadratically summed up and squared to find the final $1\sigma = 0.265\%$ error of the composition. Thus, the molar mass of the reaction target was estimated to be

$$A = (9.03508 \pm 0.02396)\,\mathrm{g/mol}$$

The dimensions and mass of the reaction target were measured by the target laboratory of GSI [33]. The dimensions measured are

$$V = x \times y \times z = 206 \times 50 \times 26.11\,\mathrm{mm}^3,$$

with an uncertainty of 0.1 mm per dimension. The mass of the reaction target was given by a high precision scale. Thus, the density and corresponding areal density of the reaction target were estimated to be

$$t\rho = (4925.9 \pm 21.4)\,\mathrm{mg/cm}^2$$

2 Graphical selection plots - ^{9}Be $\left(^{11}\mathrm{C}, ^{10}\mathrm{C}\right)$ x

Example of all graphical plots required to estimate the corrected reaction probability of one-neutron knockout from ^{11}C, see Figures 2.1–2.4. In all figures the three dimensional Z vs. A/Z distribution and the corresponding graphical selection plot are shown. In Figure 2.1 and 2.1 the surviving ^{11}C projectiles were transmitted to S3, with and without reaction target in, respectively. In Figure 2.3 and 2.4 the ^{10}C reaction residues were transmitted to S3, with and without reaction target in, respectively.

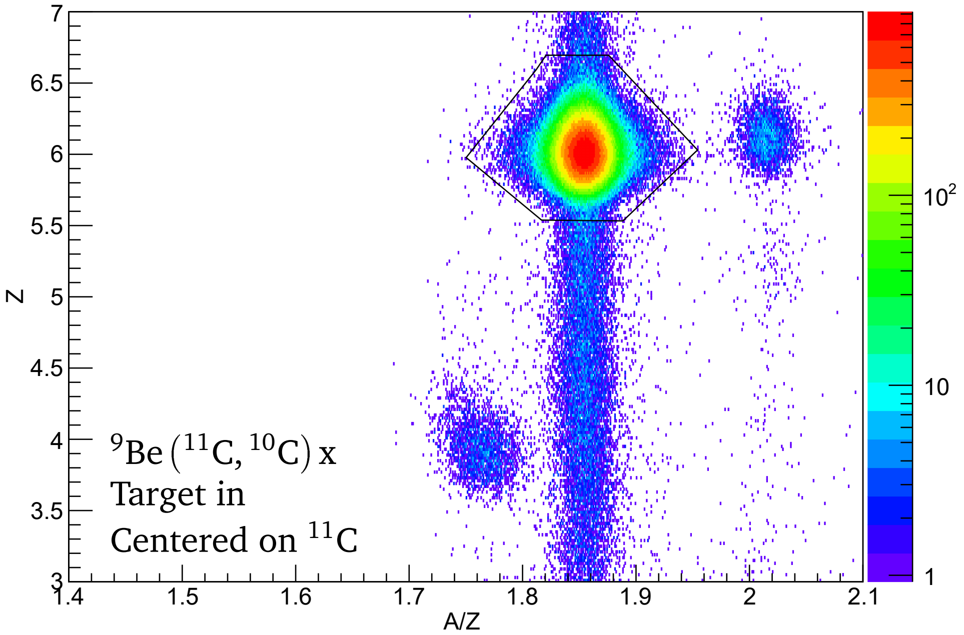

Figure 2.1.: Particle identification histogram showing the three dimensional Z vs. AoZ distribution at S3 for the reaction $^{9}\mathrm{Be}\left(^{11}\mathrm{C},{}^{10}\mathrm{C}\right)\mathrm{x}$ with secondary target in. The magnetic field setting of dipole D3 was centered on the ^{11}C reaction residues. The polygon indicates the graphical cut selecting ^{11}C

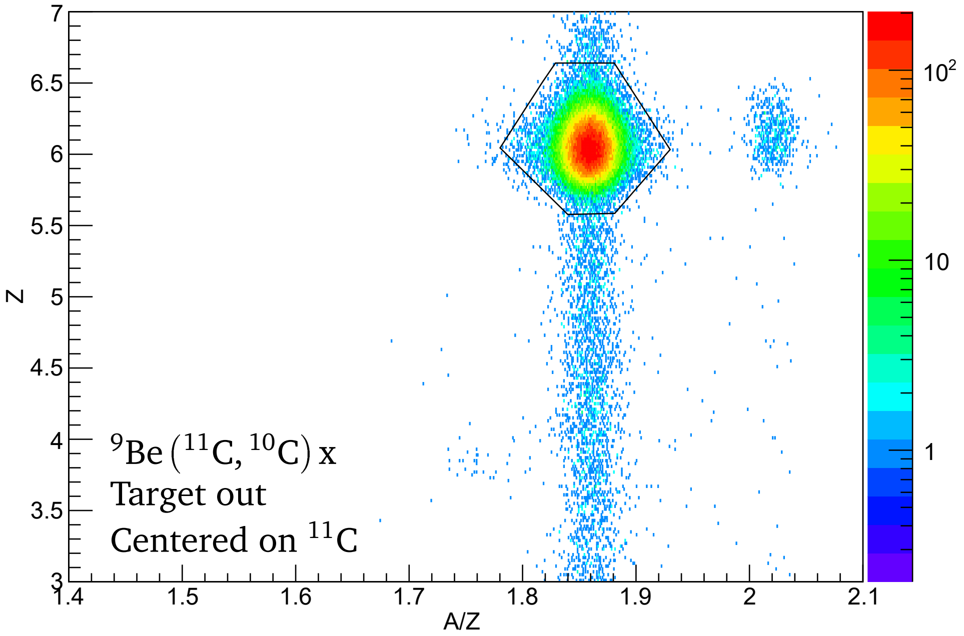

Figure 2.2.: Particle identification histogram showing the three dimensional Z vs. AoZ distribution at S3 for the reaction $^{9}\mathrm{Be}\left(^{11}\mathrm{C},{}^{10}\mathrm{C}\right)\mathrm{x}$ with secondary target out. The magnetic field setting of dipole D3 was centered on the ^{11}C reaction residues. The polygon indicates the graphical cut selecting ^{11}C

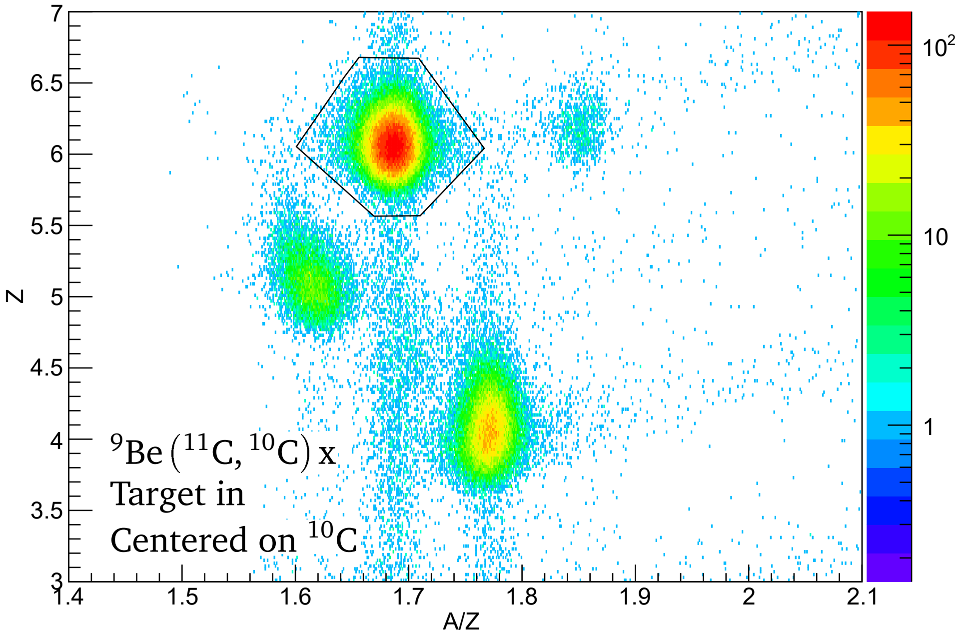

Figure 2.3.: Particle identification histogram showing the three dimensional Z vs. AoZ distribution at S3 for the reaction $^9\mathrm{Be}\left(^{11}\mathrm{C},{}^{10}\mathrm{C}\right)\mathrm{x}$ with secondary target in. The magnetic field setting of dipole D3 was centered on the ^{10}C reaction residues. The polygon indicates the graphical cut selecting ^{10}C

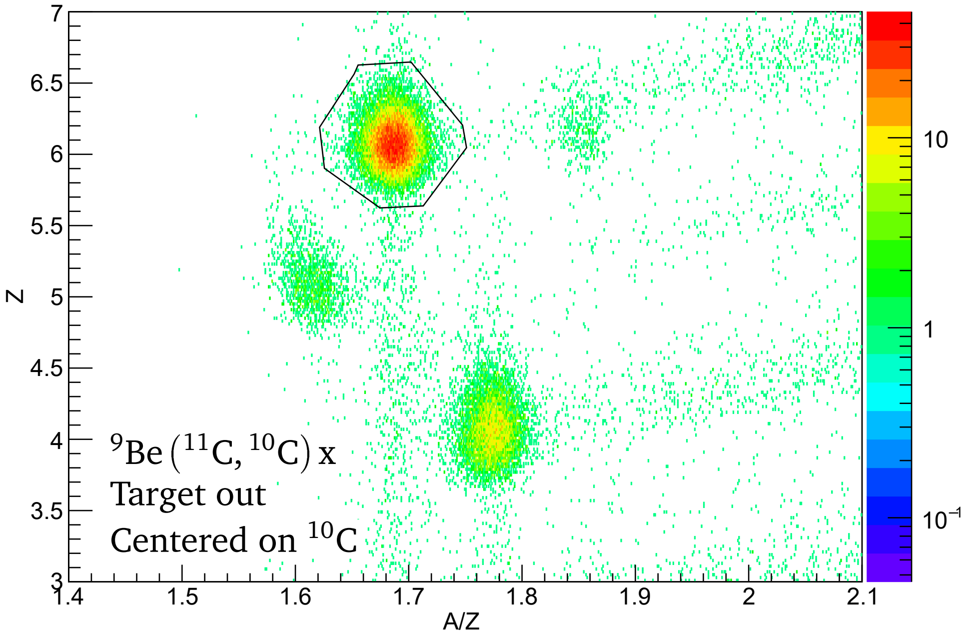

Figure 2.4.: Particle identification histogram showing the three dimensional Z vs. AoZ distribution at S3 for the reaction $^9\mathrm{Be}\left(^{11}\mathrm{C},{}^{10}\mathrm{C}\right)\mathrm{x}$ with secondary target in. The magnetic field setting of dipole D3 was centered on the ^{10}C reaction residues. The polygon indicates the graphical cut selecting ^{10}C

B Development of a Particle Detector Combination for the Super-FRS

1 Vacuum Chamber

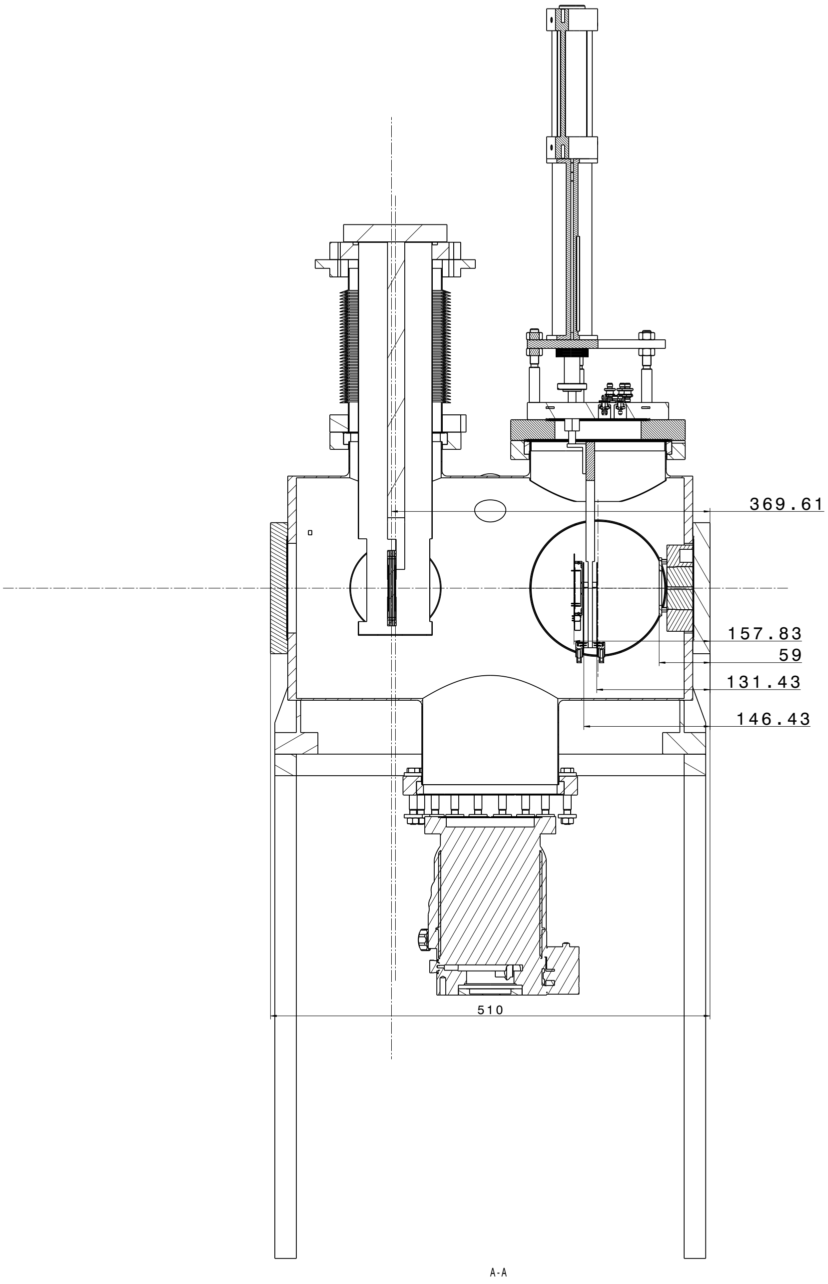

Figure 1.1.: Technical drawing of the vacuum chamber, used to mount all detectors in the test experiment at the LNS in Catania, 2015. Drawing provided by the mechanical workshop of the FRS-department at GSI. All units in mm.

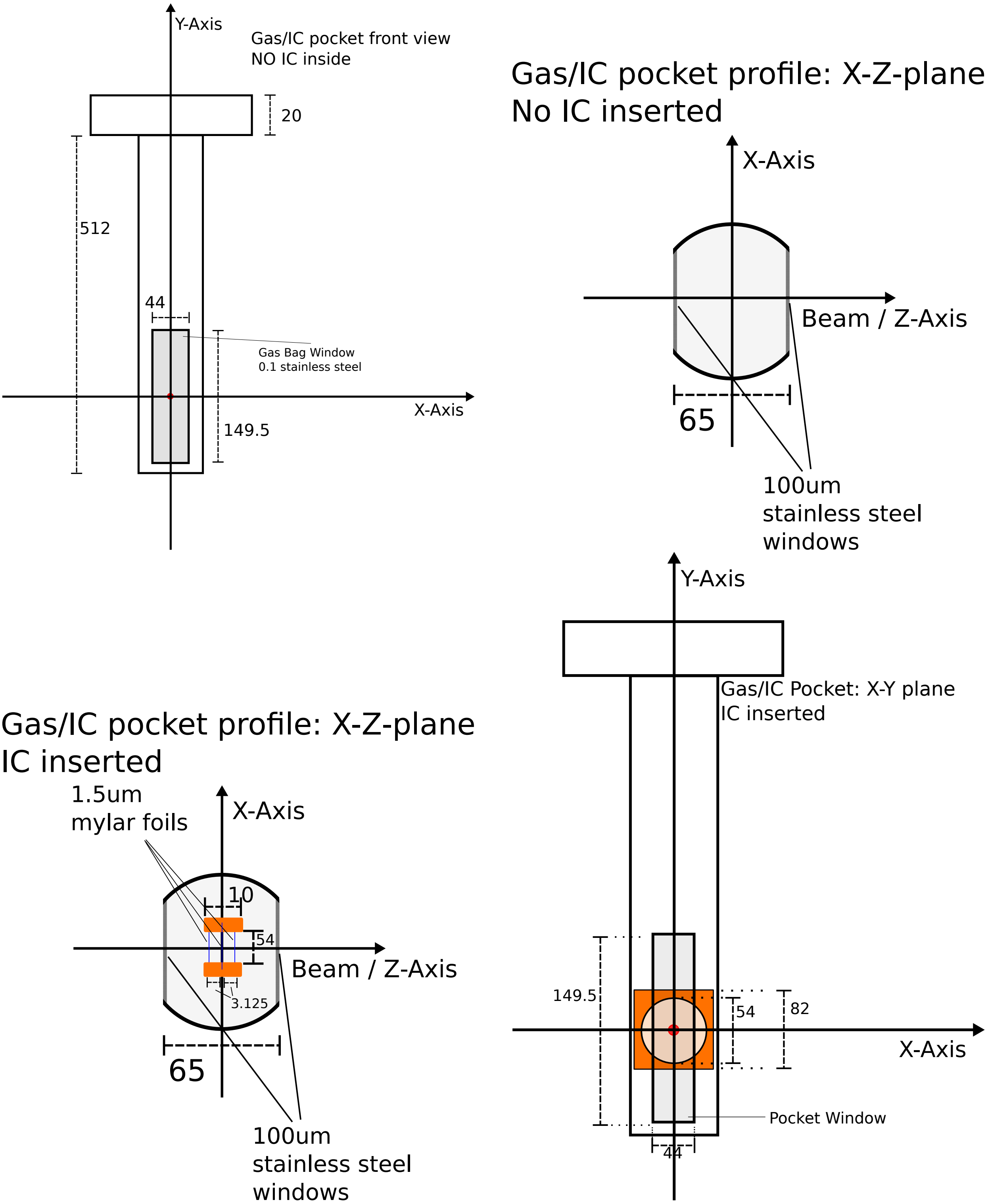

Figure 2.1.: Drawings and dimensions of the gas-pocket, used to mount the prototype of the FAIR-PDC, tested in the experiments at LNS and Catania in 2015 and 2016, respectively.

3 Design of the diamond detectors - Catania 2017

Drawings and pictures of the SC-DD and PC-DD used in the experiment at LNS in 2017. Detectors were designed and produced at the GSI detector laboratory.

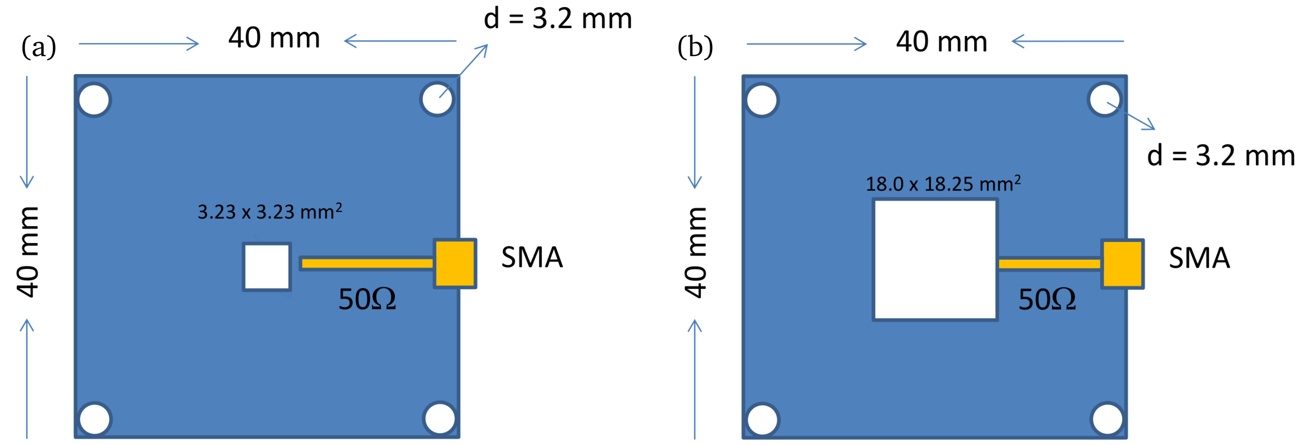

Figure 3.1.: Design of the SC-DD (a) and the PC-DD (b). The diamond material (white), acting as active detection area, was mounted on PCB-boards (blue). The electrodes of the diamond material were connected by SMA plugs. Drawings provided by F. Schirru from the Super-FRS dept. at GSI.

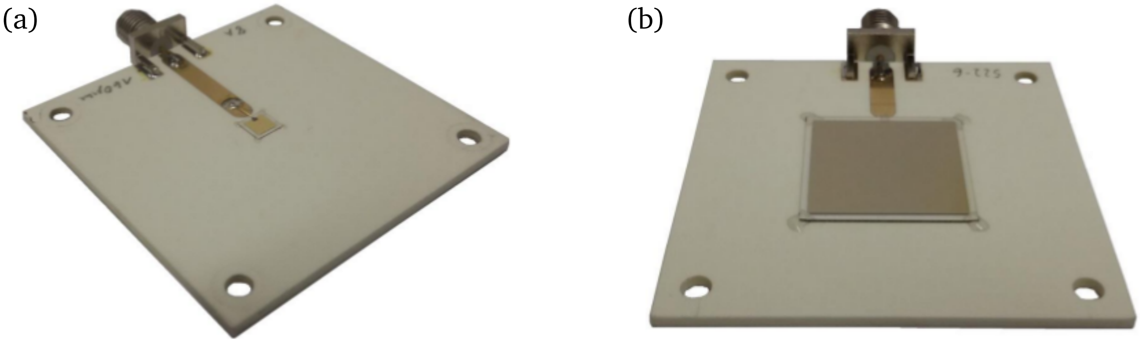

Figure 3.2.: Pictures of the SC-DD (a) and the PC-DD (b) showing the connection between SMA plugs and electrodes. Diamond material and connections are mounted on a PCB board. The active area and electrode are indicated by the slightly darker square in the center. Pictures provided by F. Schirru from the Super-FRS dept. at GSI

The shown efficiency curve was obtained by combining the data of the red and black points shown in Figure 4.1.

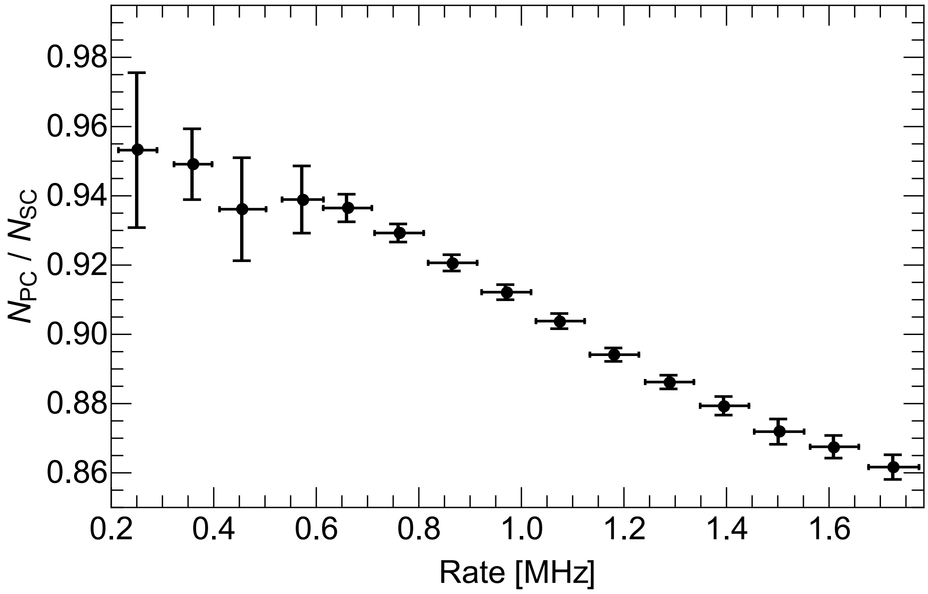

Figure 4.1.: Rate-dependent efficiency ratio of the PC-DD with respect to the SC-DD. To improve statistics below 1 MHz, the data of the red and black points from Figure4.1 were combined. Error bars of the efficiency and rate present the FWHM and integration range, respectively.

Bibliography

[1] E. Rutherford. *Philosophical Magazine* 21:669–688, 1911. `https://doi.org/10.1080/14786440508637080`

[2] J. Chadwick. *Nature* 129:312, 1932. `https://doi.org/10.1038/129312a0`

[3] B.A. Brown. *Nucl. Phys. A* 704:11–20, 2002. `https://doi.org/10.1016/S0375-9474(02)00761-3`

[4] I. Sick and P. deWitt Hubertus. *Comments Nucl. Part. Phys.* 20:177–1195, 1991. `http://inspirehep.net/record/1406038/files/v20-n4-p177.pdf`

[5] H. Esbensen and G.F. Bertsch. *Phys. Rev. C* 64:014608, 2001. `https://doi.org/10.1103/PhysRevC.64.014608`

[6] A. M. Crisp et al. *Phys. Rev. C* 77:044315, 2008. `https://doi.org/10.1103/PhysRevC.77.044315`

[7] `https://www.gsi.de`, last visit: November 2018

[8] B. Franczak, 1987. `https://www.gsi.de/fileadmin/PSchwab/Dokumentationen_Berichte/Beschleunigeranlage/SIS18/sis18_parameterliste.pdf`

[9] H. Geissel et al. *Nucl. Instr. Meth. B* 70:286–297, 1992. `https://doi.org/10.1016/0168-583X(92)95944-M`

[10] `http://www.fair-center.eu/`, last visit: November 2018

[11] H. Geissel et al. Technical Design Report on the Super-FRS, 2008. `http://repository.gsi.de/record/54552/files/GSI-2013-05264.pdf`

[12] T. Mayer-Kuckuk. *Teubner Studienbücher, Physik*, 1994.

[13] E.K. Warburton and B.A. Brown. *Phys. Rev. C* 46:923, 1992. `https://doi.org/10.1103/PhysRevC.46.923`

[14] E. C. Simpson and J. A. Tostevin. Direct and indirect one-nucleon and two-like-nucleon removal from carbon isotopes at relativistic energies, 2012. Unpublished.

[15] R.E. Julies, W.A. Richter and B.A. Brown. *South African Jour. Phys.* 15:35, 1992. `https://people.nscl.msu.edu/~brown/brown-all-papers/135-1991-npa.523.325.pdf`

[16] S. Cohen and D. Kurath. *Nucl. Phys. A* 101:1, 1967. `https://doi.org/10.1016/0375-9474(67)90285-0`

[17] D. Warner. *Nature* 425:570–571, 2003. `https://doi.org/10.1038/425570a`

[18] P.G. Hansen and J.A. Tostevin. *Annu. Rev. Nucl. Part. Sci.* 53:219–261, 2003. `https://doi.org/10.1146/annurev.nucl.53.041002.110406`

[19] G. Audi, A.H. Wapstra and C. Thibault. *Nucl. Phys. A* 729:3–128, 2003. `https://doi.org/10.1016/j.nuclphysa.2003.11.001`

[20] J.A. Tostevin. *Nucl. Phys. A* 682:320–331, 2001. `https://doi.org/10.1016/S0375-9474(00)00656-4`

[21] Valentina Maddalena. Dissertation, Michigan State University, 2000. `https://groups.nscl.msu.edu/nscl_library/Thesis/Maddalena,%20Valentina.pdf`.

[22] J.A. Tostevin. *J. Phys. G* 25:735, 1999. `http://stacks.iop.org/0954-3899/25/i=4/a=026`

[23] R.J. Glauber. *Interscience* 1:315.

[24] B.A. Brown, P.G. Hansen, B.M. Sherrill and J. A. Tostevin. *Phys. Rev. C* 65:061601, 2002. `http://dx.doi.org/10.1103/PhysRevC.65.061601`

[25] J.A. Tostevin and A. Gade. *Phys. Rev. C* 90:057602, 2014. `https://doi.org/10.1103/PhysRevC.90.057602`

[26] A.E.L. Dieperink and T. de Forest. *Phys. Rev. C* 10:543–549, 1974. `https://doi.org/10.1103/PhysRevC.10.543`

[27] A. Gade et al. *Phys. Rev. Lett.* 93:042501, 2004. `https://doi.org/10.1103/PhysRevLett.93.042501`

[28] G. Münzenberger. *Nucl. Instr. Meth. B* 70:265–275, 1992. `https://doi.org/10.1016/0168-583X(92)95942-K`

[29] `https://www-win.gsi.de/frs/technical.asp`, last visit: November 2018

[30] `https://www-win.gsi.de/frs-setup/`, last visit: November 2018

[31] `https://www.gsi.de/work/forschung/appamml/atomphysik/anlagen_und_experimente/esr.htm`, last visit: November 2018

[32] Glenn F. Knoll. *Radiation Detection and Measurement, Third Edition* p.30, 1999. `http://users.lngs.infn.it/~dimarco/Radiation%20Detection%20and%20Measurement,%203rd%20ed%20-%20Glenn%20F.pdf`, last visit: November 2018.

[33] H. Weick. Private communication, 2018.

[34] H. Weick. `https://www-win.gsi.de/frs/technical/FRSsetup/detectors-new.asp`, last visit: November 2018

[35] H. Weick. `https://web-docs.gsi.de/~weick/frs/mwpc.html`, last visit: November 2018

[36] A. Prochazka, 2008. `https://www-win.gsi.de/frs/technical/FRSsetup/detectors/tpc/tpcmanual.pdf`, last visit: November 2018

[37] H.G. Essel and N. Kurz. `https://www.gsi.de/work/forschung/experimentelektronik/datenverarbeitung/datenerfassung/mbs.htm`, last visit: November 2018

[38] `http://www.caen.it/csite/CaenProd.jsp?parent=11&idmod=30`. last visit: November 2018.

[39] J. Adamczewski-Musch et al. `www.gsi.de/en/work/research/experiment_electronics/data_processing/data_analysis/the_go4_home_page.htm`, last visit: November 2018

[40] Rene Brun and Fons Rademakers. *Nucl. Inst. Meth. in Phys. Res. A* 389:81–86, 1997. `https://doi.org/10.1016/S0168-9002(97)00048-X`

[41] M. Berz et al. `https://web-docs.gsi.de/~weick/gicosy/`, last visit: November 2018

[42] S. Kox et al. *Phys. Rev. C* 35:1678–1691, 1987. `https://doi.org/10.1103/PhysRevC.35.1678`

[43] Geant4 Collaboration. `http://geant4-userdoc.web.cern.ch/geant4-userdoc`, last visit: November 2018

[44] H. Geissel et al. `https://web-docs.gsi.de/~weick/mocadi/`, last visit: November 2018

[45] M. Holla et al. Not published, 2018.

[46] `https://www.nndc.bnl.gov/chart/`, last visit: November 2018

[47] C.A. Bertulani and A. Gade. *Computer Physics Communications* 175:372–380, 2006. `https://doi.org/10.1016/j.cpc.2006.04.006`

[48] `https://www.nndc.bnl.gov/ensdf/`, last visit: November 2018

[49] I. Brida, Steven C. Pieper, and R. B. Wiringa. *Phys. Rev. C* 84:024319, 2011. `https://doi.org/`

10.1103/PhysRevC.84.024319

[50] G.F. Grinyer et al. *Phys. Rev. C* 86:024315, 2012. `https://doi.org/10.1103/PhysRevC.86.024315`

[51] G.F. Grinyer et al. *Phys. Rev. Lett.* 106:162502, 2011. `https://doi.org/10.1103/PhysRevLett.106.162502`

[52] L. Lapikás, J. Wesseling, and R.B. Wiringa. *Phys. Rev. Lett.* 82:4404, 1999. `https://doi.org/10.1103/PhysRevLett.82.4404`

[53] D. Bazin et al. *Phys. Rev. Lett* 102:232501, 2009. `https://doi.org/10.1103/PhysRevLett.102.232501`

[54] T. Aumann. *Eur. Phys. J. A* 26:441, 2005. `https://doi.org/10.1140/epja/i2005-10173-4`

[55] J. Lee et al. *Phys. Rev. C* 83:014606, 2011. `https://doi.org/10.1103/PhysRevC.83.014606`

[56] N.K. Timofeyuk. *Phys. Rev. C* 81:064306, 2010. `https://doi.org/10.1103/PhysRevC.81.064306`

[57] N.K. Timofeyuk. *Phys. Rev. C* 88:044315, 2013. `https://doi.org/10.1103/PhysRevC.88.044315`

[58] F. Flavigny. *Phys. Rev. Lett.* 110:122503, 2013. `https://doi.org/10.1103/PhysRevLett.110.122503`

[59] T. Aumann, C.A. Bertulani, and J. Ryckebusch. *Phys. Rev. Lett.* 88:064610, 2013. `https://doi.org/10.1103/PhysRevC.88.064610`

[60] T. Wakasa. *Phys. Rev. C* 96:014604, 2017. `https://doi.org/10.1103/PhysRevC.96.014604`

[61] C. Nociforo et al. Detailed Specification of Particle Detector Combination for HEBT and SFRS, 2013. Unpublished.

[62] P. Forck. *Lecture Notes on Beam Instrumentation and Diagnostics*, 2012. `https://pdfs.semanticscholar.org/4bdf/2876d65df0c1887e591d9b7cea365f72ca34.pdf`

[63] E. Kozlova et al. *Nucl. Instr. Meth. B* 266:4275–4279, 2008. `https://doi.org/10.1016/j.nimb.2008.05.141`

[64] Felix Bachmair. Dissertation, ETH Zürich, 2016. `https://cds.cern.ch/record/2232048/files/CERN-THESIS-2016-163.pdf`

[65] Chris J.H. Wort and Richard S. Balmer. *Materials Today* 11:22–28, 2008. `https://doi.org/10.1016/S1369-7021(07)70349-8`

[66] C. Canali et al. *Nucl. Instr. Meth.* 160:73–77, 1979. `http://dx.doi.org/10.1016/0029-554X(79)90167-8`

[67] P. Moritz et al. *Diamond and Related Materials* 10:1765-1769, 2001. `https://doi.org/10.1016/S0925-9635(01)00434-4`

[68] SIMON RAMO. *Proceedings of the I.R.E.* 27:584–585, 1939. `https://doi.org/10.1109/JRPROC.1939.228757`

[69] F. Schirru et al. *J. Phys. D: Appl. Phys.* 49:215105, 2016. `http://stacks.iop.org/0022-3727/49/i=21/a=215105`

[70] F. Schirru. Private communication, 2018.

[71] K.A. Olive et al. *Chin. Phys. C* 38:090001, 2014. `https://doi.org/10.1088/1674-1137/38/9/090001`

[72] E.J. Strenglass. *Phys. Rev.* 108:1, 1957. `https://doi.org/10.1103/PhysRev.108.1`

[73] P. Boutachkov. GSI Scientific Report, 2017-1:465, 2017. `http://dx.doi.org/10.15120/`

GR-2017-1

[74] `http://teledynelecroy.com/oscilloscope/waverunner-6zi-oscilloscopes/waverunner-620zi`, last visit: November 2018

[75] `http://www.caen.it/csite/CaenProd.jsp?parent=12&idmod=119`, last visit: November 2018

[76] M. Ciobanu et al. *IEEE Trans. Nucl. Sci.* 58:2073–2083, 2011. `https://doi.org/10.1109/TNS.2011.2160282`

[77] M. Ciobanu et al. *IEEE Trans. Nucl. Sci.* 61:1015–1023, 2014. `https://doi.org/10.1109/TNS.2014.2305999`

[78] J. Hoffmann. `https://www.gsi.de/work/forschung/experimentelektronik/digitalelektronik/digitalelektronik/module/vme/vulom/vulom3.htm`, last visit: November 2018

[79] Current Digitizer CD101x Documentation. GSI Electronics Module Pool Catalogue.

[80] CD1011 Current Digitizer. GSI Electronics Module Pool Catalogue.

[81] `https://www.originlab.com/`, last visit: November 2018

[82] `https://www.wolfram.com/mathematica/`, last visit: November 2018

[83] `http://lise.nscl.msu.edu`, last visit: November 2018.

[84] H. Geissel et al. `https://web-docs.gsi.de/~weick/atima/`, last visit: November 2018

[85] `https://www-win.gsi.de/charms/seetraminfo/calibration.htm`, last visit: November 2018

[86] B. Juradon, K.-H. Schmidt and K.-H. Behr. *Nucl. Instr. Meth.* 483:603–610, 2002. `https://doi.org/10.1016/S0168-9002(01)01931-3`

[87] Sven Löchner, Jochen Frühauf, Michael Witthaus. ITEE Palaver, 2014. `https://wiki.gsi.de/foswiki/pub/EE/POLAND/ITEE_29042014.pdf`

[88] A. Peters P. Forck, P. Heeg. *AIP Conf. Proc.* 390:433, 1997. `https://doi.org/10.1063/1.52298`

[89] C. Nociforo et al. Detailed Specification of the Particle Detector Combination at the Super-FRS, 2018. EDMS Nr. 1906089. Unpublished.

[90] `https://materion.com/-/media/files/electrofusion/eqf3007_pf60.pdf`, last visit: November 2018

Credits

Mein größter Dank richtet sich an Prof. Joachim Enders. Einen engagierteren und hilfsbereiteren Doktorvater kann sich kein Student wünschen. Ohne seine fachliche und moralische Unterstützung wäre diese Arbeit niemals zustande gekommen.

Weiteren Dank möchte ich an Chiara Nociforo, Helmut Weick, Fabio Schirru und die vielen weiteren Kollegen an der GSI und dem IKP richten, die mir hilfsbereit zur Seite standen.

Zuletzt gilt mein Dank auch meiner Freundin Kristina Weber, die es in der Phase meiner Promotion nicht immer leicht mit mir hatte.

Diese Arbeit wurde mit Mitteln des BMBF (Kennzeichen: 05P15RDFN1) und durch den GSI-TU Darmstadt-Kooperationsvertrag unterstützt.

Curriculum Vitae

Personal Data

Name: Steffen Erich Schlemme

Birthdate: 19.08.1987

Birthplace: Büdingen (Germany)

Nationality: German

Education

11.2014 – today	Doctorate in Physics, Technische Universität Darmstadt
04.2012 – 09.2014	Master of Science in Physics, Technische Universität Darmstadt • Master Thesis: Test and considerations for spin-correlation measurements with massive, relativistic fermions
04.2008 – 03.2012	Bachelor of Science in Physics, Technische Universität Darmstadt • Bachelor Thesis: Aufbau eines Teststandes, Reparatur und Testmessung der QCLAM-Vieldrahtdriftkammern der dritten Generation
1998 – 2007	Secondary School: Gesamtschule Konradsdorf (Ortenberg)
1994 – 1998	Primary School: Grundschule Ortenberg

Lebenslauf

Persönliche Daten

Name:	Steffen Erich Schlemme
Geburtsdatum:	19.08.1987
Geburtsort:	Büdingen (Deutschland)
Nationalität:	Deutsch

Ausbildung

11.2014 – jetzt	Promotion in Physik, Technische Universität Darmstadt
04.2012 – 09.2014	Master of Science in Physik, Technische Universität Darmstadt • Master Thesis: Test and considerations for spin-correlation measurements with massive, relativistic fermions
04.2008 – 03.2012	Bachelor of Science in Physik, Technische Universität Darmstadt • Bachelor Thesis: Aufbau eines Teststandes, Reparatur und Testmessung der QCLAM-Vieldrahtdriftkammern der dritten Generation
1998 – 2007	Abitur: Gesamtschule Konradsdorf (Ortenberg)
1994 – 1998	Grundschule: Grundschule Ortenberg